FACHBEREICH PHYSIK
BERGISCHE UNIVERSITÄT
GESAMTHOCHSCHULE WUPPERTAL

High Precision Measurements of the LEP Center-of-Mass Energies during the 1993 and 1995 Z Resonance Scans

Kirsten Angelika Drees

Wuppertal, April 1997
WUB-DIS 97-5

Abstract

The calibration of the LEP beam energy is a substantial part of the determination of the Z mass and Z width. In principle, the LEP beam energy can be determined with a high precision of 200 keV using the technique of resonant depolarisation. However, the use of this technique is restricted to accelerator conditions without colliding beams, typically only at the end of a physics fill. In order to follow the evolution of the energy throughout a fill, a model, which will provide the instantaneous energy based on a set of corrections, is needed. The development of this model as well as the elaboration of the corrections during the 1993 and 1995 Z resonance scan will be described. In particular, the progress made in the 1995 scan compared to the model used in 1993 is presented. This progress is mainly based on the larger fraction of calibrated fills, energy calibrations at the beginning of physics fills and on an improved instrumentation to monitor the LEP dipole field in 1995. The later allowed the discovery of a significant energy rise during the physics fills. The rise is partially caused by temperature changes of the dipole cores, which were underestimated in the 1993 scan, and by leakage currents arising from trains in the Geneva area. In addition, the interaction point specific corrections to the energy evolution in 1995 are very different from earlier scans. The corrections in 1995 arise from a modified RF configuration, which include a significant fraction of super conducting RF cavities, and from opposite sign vertical dispersion induced by the bunch train scheme for the operation of LEP. Although the corrections per interaction point exceed easily 10 MeV, their related systematic errors are not dominant. In particular, the errors of the dispersion correction are small, indicating the success of the program, which was developed to cope this potentially troublesome source of uncertainty.

The contributions from the energy uncertainty to the errors on M_Z and Γ_Z, which are common for all LEP experiments, are:

$$\Delta M_Z = 1.5 \text{ MeV (exp.: 1.3 MeV)},$$
$$\Delta \Gamma_Z = 1.5 \text{ MeV (exp.: 2.0 MeV)}.$$

The errors in brackets are those arising from the statistical and experimental uncertainty of the cross section measurements.

Contents

Chapter 1

Introduction

In 1989, the **L**arge **E**lectron **P**ositron collider LEP was commissioned at CERN[1] to investigate the Standard Model of electroweak and strong interactions and to search for new particles and rare processes. The LEP collider accommodates four large experimental detectors: ALEPH [1], DELPHI [2], L3 [3] and OPAL [4]. All detectors are multi purpose detectors with almost 4π solid angle coverage. During the first LEP operation period (LEP I), from 1989 to 1995, electrons and positrons collided with a beam energy close to the Z resonance[2] in the four equipped interaction regions. Since the end of 1995, LEP is devoted to operation at higher energies up to approximately 90 GeV per beam (the "LEP II" program).

The LEP I studies profited from the clean environment of an e^+e^- collider and the large number of events around the Z resonance. The Z particle is a fundamental particle of the electroweak theory of the Standard Model. In bubble chamber experiments at CERN some evidence for the existence of the Z particle was already found in 1973 [5]. In 1983 [6] its existence was likewise proved at CERN by the experiments UA1 and UA2. An important part of the LEP I program is the precise determination of M_Z and the width of the Z resonance, Γ_Z, which are based on accurate cross section measurements at several beam energy settings around the Z resonance by the four experiments. The task of the determination of the Z parameters requires a careful calibration of the LEP energies and an elaborate investigation of the associated uncertainties. In 1986, three years before the startup of LEP, it was predicted that the main limitation of the uncertainty on the Z mass, ΔM_Z, would arise from the determination of the absolute energy scale [7]. The educated guess at that time was a precision of $\Delta E/E \simeq 1 \cdot 10^{-4}$ or $\Delta M_Z \simeq \pm 10$ MeV. For this accuracy, the implementation of an energy scale determination by electron-spin calibration (resonant depolarisation technique) was required. In this dissertation it will be shown how the precision of the energy determination could be reduced even further by about a factor of 10.

[1] Conseil Europeen pour la Recherche Nucleaire
[2] about 91.2 GeV

The operation of LEP at collision energies around the resonance was extended from 1989 till the end of 1995. During this period energy scans, in which the collision energy is varied around the resonance value, were performed in 1989, 1990, 1991, 1993 and 1995 to determine the line shape of the Z pole as precisely as possible. The precision achieved till 1991 was about 6 MeV uncertainty in the mass and about 5 MeV in the width of the Z [8]. Starting with the first observation of the predicted transverse polarisation at LEP in August 1990 significant progress has been made in exploiting polarisation as a tool to calibrate the LEP beam energy scale. This progress inspired the high statistic energy scan in 1993 with the goal to measure the Z mass and the width with an uncertainty of less than 3 MeV. During the 1993 energy scan some evidence of an unknown behaviour of the LEP dipole field and likewise the beam energy could be observed but not explained. The lack of explanations motivated a further energy scan, which was performed in 1995. The monitoring of the dipole field was considerably upgraded for this scan in order to improve further the accuracy of the Z line shape parameters and to confirm the results achieved in 1993. In the light of many additional systematic studies associated with the 1995 energy scan, former energy determinations and earlier results had to be revised. To my mind, the 1995 energy scan finally reached the limit of the feasible accuracy of the beam energy measurements at LEP.

In this thesis the realisation and results of the latest two energy scans performed in 1993 and 1995 will be discussed. The dissertation will review all known effects acting on the beam energy and center-of-mass energy and summarises the results for M_Z and Γ_Z. Among these topics I will focus on my own contributions to the 1993 and 1995 energy scans. Chapter 2 will give a short introduction to the determination of the Z mass and width and summarises the results achieved prior to the 1993 energy scan. Chapter 3 introduces some basic concepts of accelerator physics and briefly describes the LEP collider. Various tools, needed to determine the beam energy are introduced in the next chapter. Chapter 5 is the core of this thesis. It explains the determination of the average beam energy and discusses all effects, which are known to affect the beam energy. Chapter 6 summarises effects, which lead to local shifts of the center-of-mass energies. Further studies and an attempt to verify the results obtained in chapter 5 using data from cross sections measured by the experiments are described in chapter 7. Finally, in chapter 8 estimates of the various systematic error contributions to the definitive uncertainty on the LEP energy will be given.

Chapter 2

Energy Scans around the Z Resonance

An important part of the LEP I operation period was devoted to energy scans around the Z resonance. The performance and acceptance of the four detectors and their luminosity monitors give the experimental access of the Z parameters, the Z mass and the Z width. To date 5 energy scans have been realised. After the first three successful energy scans in 1989, 1990 and 1991, the profit of an additional energy scan was not evident. The precision of the results achieved till 1991 was limited by the error on the beam energy calibration. Requirements for further energy scans had to be worked out to ensure a significant gain in the precision of the measurements of the Z mass and the width. Once the practicability of the requirements had been carefully checked, it was decided to scan again around the Z resonance in the year 1993 and later in 1995. The available data sample from either of the additional energy scans in terms of delivered integrated luminosity is about the same whereas the luminosity weighted fraction of calibrated physics fills has been significantly larger in 95 than in 93.

2.1 The Z Resonance

The investigation of the characteristics of the Z particle, the Z mass and the Z width, was one of the main purposes of the LEP I running period. The Z boson is produced by electron positron annihilation and decays into a fermion anti-fermion pair. Only the annihilation of the initial e^+e^-pair via photon or Z particle (Fig. 2.1) has to be considered in the case, the final state is no e^+e^-pair. The presence of the t-channel complicates the treatment of the process $e^+e^- \rightarrow e^+e^-$. In the Minimal Standard Model with one iso-doublet of complex Higgs field, the lowest order predictions for the process $e^+e^- \rightarrow f\bar{f}(f \neq e)$ can be described with only 3 free parameters, which have to be determined from measurements. The most obvious choice is α, the electromagnetic coupling constant, G_F, the Fermi constant and M_Z because these quantities are measured with the highest accuracy. For the process $e^+e^- \rightarrow f\bar{f}(f \neq e)$ the total cross section near $\sqrt{s} = M_Z$ is dominated by the exchange of the Z and can therefore, neglecting the

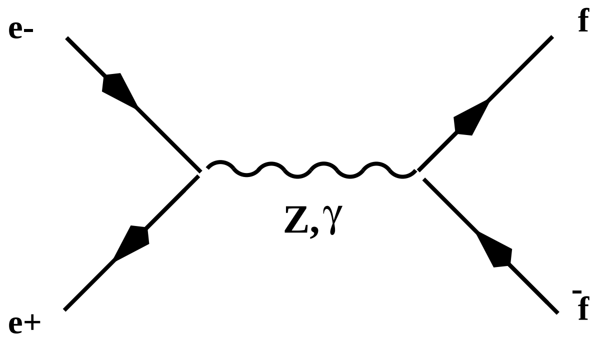

Figure 2.1: *Feynman graph of e^+e^- annihilation into a $f\bar{f}$ final state via a Z boson or a photon. The $f\bar{f}$ pair consists either of e^+e^-, $\mu\bar{\mu}$, $\tau\bar{\tau}$, $q\bar{q}$ or neutrinos.*

fermion masses, be written in Born's approximation [9] as:

$$\sigma_{f\bar{f}}(\sqrt{s} \simeq M_Z) \simeq \sigma^0_{f\bar{f}} \cdot \frac{s \cdot \Gamma_Z^2}{(s - M_Z^2)^2 + M_Z^2 \Gamma_Z^2} + \sigma_{\gamma,\gamma Z} \qquad . \tag{2.1}$$

$\sigma^0_{f\bar{f}}$ denotes the cross section for this process at $\sqrt{s} = M_Z$ and $\sigma_{\gamma,\gamma Z}$ corresponds to small contributions from the photon exchange and from the $\gamma - Z$-interference. At $\sqrt{s} \simeq M_Z$ the term $\sigma_{\gamma,\gamma Z}$ is of the order of 1%. Fig. 2.2 shows the total cross section for $e^+e^- \rightarrow$ hadrons as a function of the center-of-mass energy $\sqrt{s}$. The pole cross section is extremely large compared to the 1/s dependence of the pure γ exchange in QED (dashed line). Approximate energy ranges of other e^+e^-colliders are also indicated. The contribution of the Z cross section to the total cross section is relatively small for the earlier e^+e^-accelerators while it became dominant for LEP and SLC energies.

For $\sqrt{s} = M_Z$, where the interference term vanishes and the photon contribution is very small, the lowest order pole cross section $\sigma^0_{f\bar{f}}$ can be written in terms of the partial decay widths Γ_{ee} and Γ_{ff} [14]:

$$\sigma_{f\bar{f}} \simeq \frac{12\pi}{M_Z^2}\frac{\Gamma_{ff}\Gamma_{ee}}{\Gamma_Z^2} = \frac{12\pi}{M_Z^2} \cdot BR(Z \rightarrow e^+e^-) \cdot BR(Z \rightarrow f\bar{f}) \qquad , \tag{2.2}$$

where the total width Γ_Z of the Z is the sum of the partial decay width into fermions $\Gamma_Z = \sum_f \Gamma_f$ with $M_f < M_Z/2$. In the Standard Model [10] the partial widths of the Z are no free parameters but can be written in terms of vector and axial-vector coupling constants, g_v^f and g_a^f, of the Z whereby $\alpha = e^2/4\pi$ is the electromagnetic coupling constant and Θ_W is the weak mixing angle relating the masses of the heavy gauge bosons with $\cos\Theta_W = M_W/M_Z$:

$$\Gamma_{ff} = N_c^f \frac{\alpha M_Z}{12 \sin^2\Theta_W \cos^2\Theta_W} \left[(g_v^f)^2 + (g_a^f)^2\right] \qquad , \tag{2.3}$$

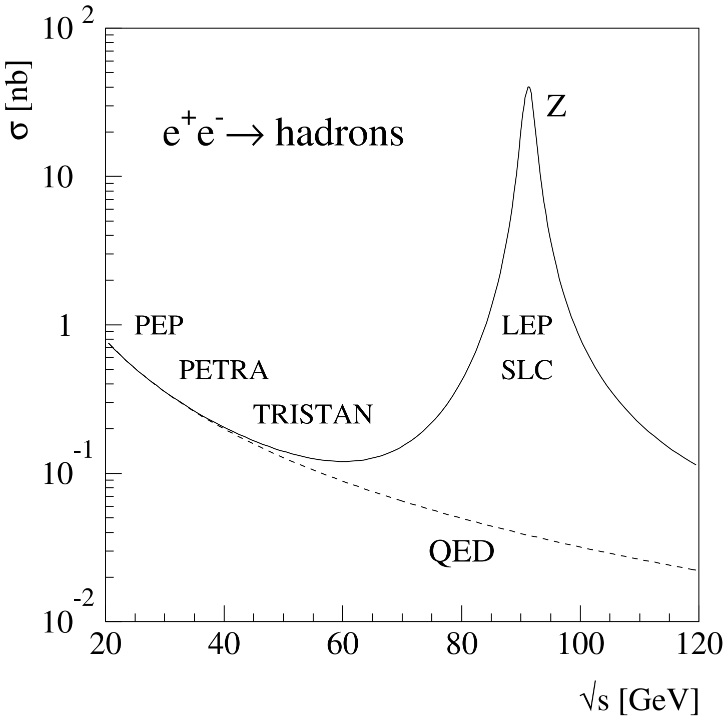

Figure 2.2: *Cross section for $e^+e^- \to$ hadrons in lowest order as a function of the center-of-mass energy $\sqrt{s}$.*

$$N_c^f = \begin{cases} 1 \text{ for leptons} \\ 3 \text{ for quarks} \end{cases} \quad . \tag{2.4}$$

According to Eq. 2.2 the peak cross sections can be expressed as the product of the branching ratios of the Z decaying into $e^+e^-$and $f\bar{f}$times the prefactor $12\pi/M_Z^2$. At the peak the cross section takes in its maximum value which is possible without violating the unitary limit [11]. About 20% of the Z boson decay into neutrinos and are therefore undetectable with the exception of $e^+e^- \to \nu\bar{\nu}\gamma$ events. Approximately 70 % of the Z bosons decay into hadrons. All four LEP detectors provide a high efficiency for hadron detection and are thus suitable for precision measurements of the Z mass and the width.

2.2 Experimental Access of the Z Parameters

The experiments yield the cross section via the relation:

$$\sigma = \frac{N_{sel} - N_{bgd}}{\epsilon \int \mathcal{L} dt}. \tag{2.5}$$

N_{sel} denotes the number of events passing the selection cuts and N_{bgd} represents the number of background events in the selected event sample. ϵ accounts for the selection efficiency of the experimental detectors and $\int \mathcal{L} dt$ for the accumulated luminosity. Several quantities can be derived from the fit of the cross section measurements as a function of the center-of-mass energies:

- M_Z from the position of the peak value of the distribution,
- Γ_Z from the peak width,
- the partial widths $\Gamma_{had}, \Gamma_{\tau\tau}, \Gamma_{\mu\mu}$ and Γ_{ee} from the peak height $\sigma_h^0 \sim \Gamma_{ee}\Gamma_{had}/\Gamma_Z^2$ and $R_l = \Gamma_{had}/\Gamma_{ll}$, for $l = e, \mu, \tau$.

These quantities are the free parameters of a fit using a “Breit-Wigner” approach. Considering lepton universality the number of free parameters is reduced to four: the mass and total width of the Z, M_Z and Γ_Z, and the partial widths Γ_{had} and Γ_{ll}. Two software packages (i.e. ZFITTER [12] and MIZA [13]) are used by the experiments to perform the fits and to implement correction terms. Other important parameters such as $\Gamma_{inv} = \Gamma_Z - \Gamma_{had} - 3\Gamma_{ll}$, the number of Neutrino types N_ν[1] $= \frac{\Gamma_{inv}}{\Gamma_{ll}} \left(\frac{\Gamma_{ll}}{\Gamma_{\nu\nu}}\right)_{SM}$ or α_s from QCD corrections to Γ_{had} can be derived.

The experimental systematic errors on cross section measurements are small and similar for the four detectors. The error on the cross section $e^+e^- \rightarrow$ hadrons is typically smaller than 0.1% [14] excluding the contribution from luminosity measurements. Tab. 2.1 shows the typical experimental uncertainties (from 1994) for the different cross section measurements.

	hadrons	muons	taus	electrons
ALEPH	0.073	0.26	0.32	0.48
DELPHI	0.1	0.3	0.6	0.5
L3	0.051	0.31	0.65	0.23
OPAL	0.16	0.15	0.46	0.24

Table 2.1: *1994 experimental uncertainties of the cross section measurements in per cent.*

2.2.1 Event Selection

In principle the selection of hadronic events in the LEP experiments is straight forward. Z boson decays into hadronic final states are discriminated from background events by a few basic cuts:

- charged multiplicity N_{ch}:
  leptonic events and cosmic ray events are rejected if $N_{ch} \geq N_{ch}^{cut}$,
- deposited energy and energy balance:
  rejection of 2-photon and beam-gas events.

Tab. 2.2 shows the number of selected[2] events between 1989 and 1995. For background

	ALEPH	DELPHI	L3	OPAL	total
N_{sel}	4164	3556	3358	3357	14435

Table 2.2: *The selected number of hadronic events from 1989 to 1995 in units of* 10^3.

suppression and reduction of systematic errors complete detector simulations are elaborated using the MONTE CARLO method. The simulated data are compared with the data themselves. The results of this comparison is used to fix the particular setting of the selection cuts. The remaining background in the sample of hadronic events amounts to approximately 0.1% [9]. This order of magnitude is about the same for all four experiments.

2.2.2 Luminosity Measurements

Ideally the luminosity is obtainable from beam parameters. In case of head-on collisions of the electron and positron beams and no crossing angle, the luminosity at the interaction point (IP) between k bunches of electrons and positrons can be calculated from the beam currents (I_{e^+} and I_{e^-}) and the horizontal and vertical emittances (ε_x and ε_y) of both beams:

$$\mathcal{L} = \frac{1}{2\pi e^2 k f_{rev}} \cdot \frac{I_{e^+} I_{e^-}}{\sqrt{\beta_x^* \beta_y^* (\varepsilon_x(e^+) + \varepsilon_x(e^-))(\varepsilon_y(e^+) + \varepsilon_y(e^-))}} \quad . \tag{2.6}$$

where f_{rev} is the revolution frequency of the particles and $\beta_{x,y}^*$ are the horizontal and vertical betatron functions at the interaction point. However, these parameters are

[2] Not all experiments have yet analysed the full data set.

not known with sufficient precision. A more precise determination of the luminosity can be obtained from Eq. 2.5, not counting hadronic decays of the Z boson but events from a process with a well known cross section. For this purpose all experiments use the process of small angle Bhabha scattering $e^+e^- \rightarrow e^+e^-$. The cross section as well as the angular distribution of the final state e^+e^- of this process can be computed from QED [15]. For accurate luminosity measurement the acceptance region of the particular luminosity monitor has to be taken into account. The polar angle region, covered by the luminosity detectors, is typically between 25 mrad and 120 mrad. In this range the differential cross section for Bhabha scattering is given by:

$$\frac{d\sigma_{Bhabha}}{d\Theta} \simeq \frac{32\pi\alpha^2}{s\Theta^3} \qquad . \tag{2.7}$$

The integration of Eq. 2.7 from the lower limit of the luminosity monitor acceptance, Θ_{min}, to the upper limit, Θ_{max}, gives:

$$\sigma_{Bhabha} \simeq \frac{16\pi\alpha^2}{s}\left(\frac{1}{\Theta^2_{min}} - \frac{1}{\Theta^2_{max}}\right) \qquad . \tag{2.8}$$

Thus the precise measurement of the acceptance is mandatory for an accurate determination of the luminosity. The uncertainty of the inner radius, e.g. $r_{min} = 10$ cm, limits the accuracy of the luminosity measurement as:

$$\frac{\Delta\mathcal{L}}{\mathcal{L}} \simeq \frac{2\Delta\Theta_{min}}{\Theta_{min}} \simeq 2\% \cdot \Delta r_{min} \qquad . \tag{2.9}$$

Until the end of 1992 the experimental systematic error in the luminosity was typically about 0.5%. With improved luminosity monitors, which are based on silicon technology and operated since the 1993 run, the error is reduced to about 0.1%. Tab. 2.3 shows typical experimental uncertainties (from 1994). In addition a common theoretical error

	ALEPH	DELPHI	L3	OPAL
$\Delta\mathcal{L}$	0.073	0.090	0.078	0.079

Table 2.3: *1994 experimental uncertainties for luminosity measurements in per cent.*

of 0.11% at the Z peak, arising from the theoretical calculation of the low angle Bhabha scattering cross section [15], contributes to the total error on the luminosity.

2.3 Results Achieved up to 1991

The cross sections and fit results obtained in 1989-1991 have already been published (see Refs. [16]- [27]). Since the year 1992 was devoted to high statistics running at the peak of the Z resonance, no new results on M_Z and Γ_Z could be obtained including the 1992 data into the analysis. All results from the first three years are presented in Table 2.4. The combined values in 1990 and the value for M_Z in 1991 are taken from [28] and [8], respectively. Γ_Z in 1991 is simply averaged based on the numbers given in the table. 1989 no combined results were published by the experiments. The values presented in Table 2.4 are based on an weighted average assuming no correlation between the experiment, giving a fairly good estimate of the combined value of M_Z and Γ_Z. The LEP errors, which are common to all experiments, are published in [29], [30] and [31]. In 1989 no LEP error was assigned to Γ_Z. However, the LEP error would have been negligible small compared to the experimental one. The statistical error could

Year	Exp.	M_Z [GeV]	± exp. err. [GeV]	± LEP err. [GeV]	Γ_Z [MeV]	± exp. err. [MeV]	± LEP err. [MeV]
1989	ALEPH	91.174	0.055	0.045	2680	150	-
	DELPHI	91.09	0.08	0.045	2420	210	-
	L3	91.132	0.057	0.045	2588	137	-
	OPAL	91.01	0.05	0.045	2600	130	-
	comb.	**91.10**	**0.03**	**0.045**	**2584**	**80**	-
1990	ALEPH	91.182	0.009	0.025	2484	17	5
	DELPHI	91.177	0.01	0.025	2465	20	5
	L3	91.181	0.01	0.025	2501	17	5
	OPAL	91.156	0.009	0.025	2496	17	5
	comb.	**91.175**	**0.005**	**0.025**	**2487**	**10**	**5**
1991	ALEPH	91.187	0.007	0.006	2501	12	4
	DELPHI	91.186	0.007	0.006	2486	12	4
	L3	91.195	0.007	0.006	2494	10	4
	OPAL	91.181	0.007	0.006	2483	11	4
	comb.	**91.187**	**0.004**	**0.006**	**2491**	**6**	**4**

Table 2.4: *The table contains the results on M_Z and Γ_Z obtained from 1989, 1990 and 1991 data. The year 1990 and 1991 include the data from the years before. In the fits lepton universality was assumed. The experimental errors include statistical and systematic errors from the experiments.*

be reduced dramatically in 1990 and 1991. In the same year, 1991, the common LEP error on the Z mass could also be reduced significantly due to the introduction of the resonant depolarisation method [32], which will be described later. In the previous two years the energy of the beams was calibrated using a combination of protons circulated in LEP and magnetic field measurements. A brief description of the procedure [29] is as follows:

(a) Protons were injected into LEP at 20 GeV and the revolution time was measured. The beam energy at 20 GeV is calculated from the measured revolution time.

(b) The energy was extrapolated from 20 GeV to 45 GeV using magnetic measurements with the "fluxloop" [59].

(c) Magnetic field measurements in a reference magnet, powered in series with the main bending magnets, were used to compute the fill to fill variations [29, 30].

Besides the limited practicability the systematic error of the proton-injection method could not be reduced to better than 25 MeV [30]. In order to match the continuously decreasing statistical errors arising from the accumulating data sample, a more reliable method had to be looked for. A method like this was found with the resonant depolarisation, which replaced the energy calibration using the proton-injection method from 1991 onwards.

2.4 Requirements for the 1993 and 1995 Energy Scans

At the end of 1992 the "LEP Energy Working Group"[3] was left in a situation where the error on the Z mass due to the combined cross section measurements of the four LEP experiments was reduced to less than 4 MeV. At the same time the systematic error on the LEP energy, which could be achieved during the last energy scan in 1991, was about 6 MeV while the total error on the width was still dominated by the experimental errors. The systematic errors on the Z mass and width arising from the LEP energy calibration are related to a good approximation to the errors on the sum and the difference of the two center-of-mass (CM) energies by the following formula [33]:

$$\Delta M_Z \simeq 0.5 \cdot \Delta(E_{P+2} + E_{P-2}) \quad , \tag{2.10}$$

$$\Delta\Gamma_Z \simeq \frac{\Gamma_Z}{E_{P+2} - E_{P-2}} \cdot \Delta(E_{P+2} - E_{P-2}) \quad . \tag{2.11}$$

E_{P+2} and E_{P-2} are the luminosity weighted CM energies at the two off-peak points. After the third energy scan the precision to which the Z mass could be measured during the LEP I program was limited by the determination of the beam energy. Due to this reason, in the following energy scans in 1993 and later in 1995, considerable effort was

[3] A working team, founded to work on the energy calibration task, consisting of representatives of all four experiments and of the accelerator group.

made to measure the beam energy as often and accurate as possible. Additionally all parameters, which could possibly influence the beam energy, were monitored with a high rate in order to discover all important sources for beam energy changes. The parameters were monitored every 15 minutes during the 1993 as well as the 1995 scan, which was sufficiently often for energy calibration purposes. Mainly the calibration is performed in three steps:

- Instantaneous calibration of the absolute beam energy as often as possible via the resonant depolarisation method.
- Determination of the average beam energy on the time spot in samples of 15 minutes.
- Investigation of IP dependent corrections to calculate precise center-of-mass energies at each IP.

The LEP Energy Working Group judged this task to be feasible. Hence it was decided to perform an additional scan during the 93 LEP run. The analysis of the 93 data resulted in a LEP contribution to the error of the Z mass and width of:

$$\Delta M_Z = 1.4\ \mathrm{MeV} \qquad , \tag{2.12}$$
$$\Delta \Gamma_Z = 1.5\ \mathrm{MeV} \qquad . \tag{2.13}$$

The analysis and errors are published in [33]. At the time of the 1993 scan, the beam energy revealed various unexpected features. A few of them remained unexplained while others were understood and successfully implemented into an energy model. This lack of understanding, the implementation of a new LEP operation scheme at the end of the 1994 run and the desired accumulation of more off-peak data to reduce the statistical errors motivated finally a further energy scan in 1995. The new operation scheme, where LEP is operated with so called bunch trains, leads to possible center-of-mass energy shifts at the interaction points. This additional scan was considered to verify the stability of the center-of-mass energies against the operation scheme and to confirm the results achieved in the 1993 scan. The achieved accuracy on the Z mass and width could still be improved with the additional off-peak data in the probably last energy scan around the Z resonance at LEP. After all, the yield of knowledge in the 1995 energy scan led to a revisal of the 1993 data and finally to an enlargement of the 1993 LEP errors, which were already published in [33]. The detailed arguments for this change will be given in the following chapters.

2.4.1 Data Sample

An appreciable number of Z events should be delivered by LEP and collected by the experiments in order to obtain a statistical error on the Z mass and width matching the common systematic error arising from the energy measurements. Hence, an important part of the LEP operation period during the years 1993 and 1995 was devoted to a three point energy scan around the Z resonance at Peak-2, Peak and Peak+2 energy settings. Table 2.5 presents the accumulated luminosity of the various energy points and the according approximate energies. The total operation period of the 1993 scan

Year	LEP Setting	Beam Energy (GeV)	# of calibr. fills (total of fills)	$\int \mathcal{L}dt$
1993	Peak-2 ("P-2")	44.72	13 (38)	$\approx 10\ pb^{-1}$
	Peak ("P")	45.61	1 (57)	$\approx 20\ pb^{-1}$
	Peak+2 ("P+2")	46.52	11 (31)	$\approx 10\ pb^{-1}$
1995	Peak-2 ("P-2")	44.72	14 (26)	$\approx 10\ pb^{-1}$
	Peak ("P")	45.64	1 (18)	$\approx 18\ pb^{-1}$
	Peak+2 ("P+2")	46.49	13 (28)	$\approx 10\ pb^{-1}$

Table 2.5: *Definition of the three LEP settings, the corresponding approximate beam energies, the number of calibrated fills and the delivered integrated luminosities of the years 1993 and 1995.*

contains 126 fills while the 1995 energy scan consists of 72 fills.

The accurate calibration of the LEP beam energy at "P-2" and "P+2" energy settings in both years is provided by the resonant depolarisation technique [34]. In total, 25 fills in 1993 and 28 fills in 1995 are calibrated, corresponding to a luminosity weighted fraction of calibrated fills of about 35 % in 1993 and 70 % in 1995. The unexplained energy variations in 1993 required additional consistency checks. The improved operational control of the polarimeter in 1995 allowed the successful calibration of a few fills before the beams were put in collision (Beginning of Fill - BoF - calibrations). Standard calibrations were at the end of the fills (EoF calibrations). In addition some fills[4], devoted to studies of the accelerator performance, include frequent energy calibrations. Overall, 13 long term fills containing several calibrations could be collected in 1992, 1993, 1994 and 1995. These fills are listed in Table 2.6. From September 1995 onwards a conditioning of the bending magnets[5] was performed at the beginning of 32 fill.

[4]**M**achine **D**evelopements (MD)
[5]so called "bending modulation"

year	fill	E_{nom}	length (h)	t.a.r. (*) (h)	start day time (h)	end day time (h)	ΔE [MeV]	comment
92	1439	P+2	6.5	7.5	11-11 02:00	11-11 08:30	0.9	Tide exp. I, beams lost
	1440	P+2	10.5	3.5	11-11 14:00	12-11 00:30	-0.7	Tide exp. I, continued
93	1636	P-2	4	2.5	20-06 17:00	20-06 21:00	1.2	MD fit $C_{T_{class}}$
	1734	P-2	4.5	2	05-08 00:00	05-08 04:30	2.2	MD fit $C_{T_{class}}$
	1772	P-2	21.5	1.5	29-08 02:40	29-08 24:00	7.8	Tide exp. II, temp. exp.
	1811	P+2	5.5	21	12-09 14:00	12-09 19:20	-1.2	after physics
	1849	P-2	11	13.5	11-10 19:40	12-10 06:30	3.5	Tide exp. III, after physics
94	2234	Peak	10.5	12	25-07 10:20	25-07 21:00	0.5	jump in E_{fd}: 2.2 MeV
95	2929	P-2	9.5	4	24-08 19:10	25-08 04:45	1.9	MD
	3022	P+2	16	1.5	24-09 18:30	25-09 10:15	3.4	BoF/b.m./EoF calibr.
	3029	P+2	15.5	2	28-09 19:00	29-09 10:30	6.5	BoF/BoF/EoF calibr.
	3030	P-2	21	1	29-09 17:00	30-09 14:00	4.4	BoF/EoF calibr.
	3036	P+2	16	1	02-10 01:00	02-10 17:00	1.7	BoF/EoF calibr.
	3064	P+2	7	1	08-10 13:30	08-10 20:20	1.4	MD

Table 2.6: *Table of long term resonant depolarisation experiments since Nov. 1992. Experiments devoted to specific studies as the tide effect are included. Start and end time are the time of the first and last energy measurement respectively. No corrections except for tidal effects are applied to the measured energy differences (ΔE) between the first and last measurement.*
(*) time after ramp to final energy

Chapter 3

Introduction to Accelerators and to the LEP Collider

The LEP storage ring is designed to accelerate electrons and positrons, to keep them at the final beam energy in the ring for hours and to bring them into collision at the interaction points, which are equipped with experimental detectors. Bunches of electrons and positrons are injected into the vacuum chamber which passes through the magnet lattice. The lattice has focusing and defocusing properties driving all particles toward the circular design orbit. The coordinate system used to describe beam motions through the magnetic field is introduced in section 3.1. The guide field causes horizontal and vertical oscillations of electrons and positrons around the ideal closed orbit, so called betatron oscillations. Ideally the stationary and periodic magnetic guide field has only components transverse to the reference orbit $\vec{B} = (B_x, B_y, 0)$, whereas the nominal bending field $\vec{B_0} = (0, B_0, 0)$ has only a vertical component. If the vertical magnetic field differs from its nominal value or if there is some small horizontal field, the particles will follow a distorted closed orbit, which differs from the ideal closed orbit. During each revolution the particles lose a small fraction of their energy through synchrotron radiation This energy loss is compensated by a corresponding energy gain from **R**adio **F**requency (RF) cavities. The periodic accelerating field confines the particles into circulating bunches. Individual electrons or positrons inside a bunch oscillate in longitudinal direction and in energy. Oscillations of this type are called synchrotron oscillations.

The specifications for the operation of the LEP collider are briefly introduced at the end of this chapter.

3.1 Coordinate System

It is convenient to describe the coordinates of a particle using a local reference system (x, y) along the path length s on the ideal orbit. Fig 3.1 shows a schematic view of a particle at the azimuthal position S_0 displaced from the ideal orbit by dx (horizontal) and dy (vertical). Therefore any trajectory of a particle can be expressed by a set of coordinates (x,y,s), where x and y are coordinates related to the ideal orbit. The path

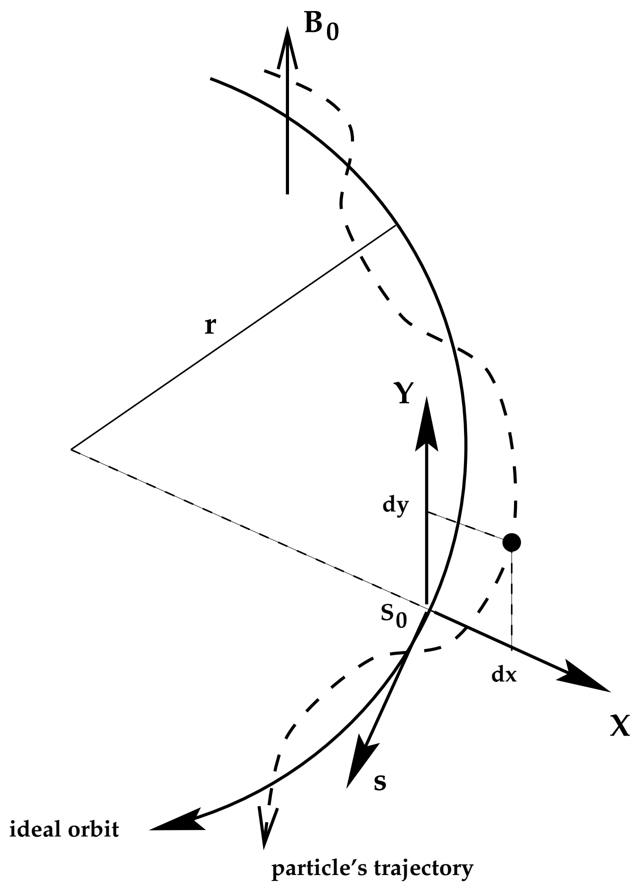

Figure 3.1: *The displacement of a particle from the ideal orbit can be described with the two transverse coordinates x (horizontal) and y (vertical). s denotes the path length along the LEP ring. B_0 is the vertical bending field.*

of a particle with the coordinates $x = y = 0$ denotes the ideal orbit. The validity range of s resides between $s_1 = 0$ and $s_2 = C_{LEP}$, where C_{LEP} corresponds to the circumference of LEP. The boundary condition from the LEP ring geometry constrains s_1 to be equal to s_2.

3.2 Betatron Oscillations

In a perfect circular machine the absence of horizontal dipole fields causes the ideal orbit to be confined to the (x, s)-plane. The curvature $\rho(s)$ of the particle trajectory, which is confined to the horizontal plane, is given by:

$$\frac{1}{\rho(s)} = \frac{e}{p} B_y(s) \qquad , \tag{3.1}$$

derived from the equality $F_L = F_c$, where $F_L = -ev_s B_y$ is the Lorentz force and $F_c = p^2/m\rho$ the centrifugal force. The bending radius $\rho(s)$ is the same in all of the standard bending magnets. The guide field is designed such that an electron with the nominal energy, once properly started, will move forever along the ideal orbit. In addition to the dipole magnets, providing the bending of the trajectories, accelerators also require magnets to focus the beams and to stabilise the particle orbits around the ideal orbit. For this purpose quadrupoles with focusing and defocusing properties are used. Quadrupoles are characterised by their horizontal and vertical field gradients:

$$\frac{\partial B_y}{\partial x} = \frac{\partial B_x}{\partial y} \qquad , \tag{3.2}$$

which give rise to a transverse field $\vec{b}$:

$$\vec{b} = \hat{e}_x \frac{\partial B_y}{\partial x} \cdot x \; + \; \hat{e}_y \frac{\partial B_x}{\partial y} \cdot y \qquad . \tag{3.3}$$

$\partial B_x/\partial y$ and $\partial B_y/\partial x$ are the field gradients in the particular quadrupole and x, y are the horizontal and vertical displacement of a particle in the quadrupole with respect to its centre. Owing to this structure, a quadrupole provides a focusing force in one plane and a defocusing force in the other plane. Apart from this property, which distinguishes quadrupoles from classical lenses for light optics, quadrupoles act on the particle beam like lenses on a light beam. Therefore the magnetic structure of an accelerator is referred to as "beam optics". Because of this characteristic, a magnet lattice of an accelerator is build up with alternating horizontally focusing and horizontally defocusing quadrupoles. The simplest magnet lattice is made of a periodic structure build from identical cells. Each cell consists of a horizontally focusing quadrupole, a dipole magnet and a defocusing quadrupole. This simple arrangement is called a "FODO" cell. An example is shown in Fig. 3.2. The strength of a quadrupole for a particle with the nominal energy E_0 is defined as [35]:

$$K(s) = -\frac{ec}{E_0} \left(\frac{\partial B}{\partial x} \right) \qquad . \tag{3.4}$$

The equation of motion for a particle circulating in a lattice of dipoles and quadrupoles is given by [35]:

$$\frac{d^2x}{ds^2} = -\left(\frac{1}{\rho(s)^2} + K(s) \right) \cdot x + \frac{1}{\rho(s)} \cdot \frac{\Delta E}{E_0} \qquad , \tag{3.5}$$

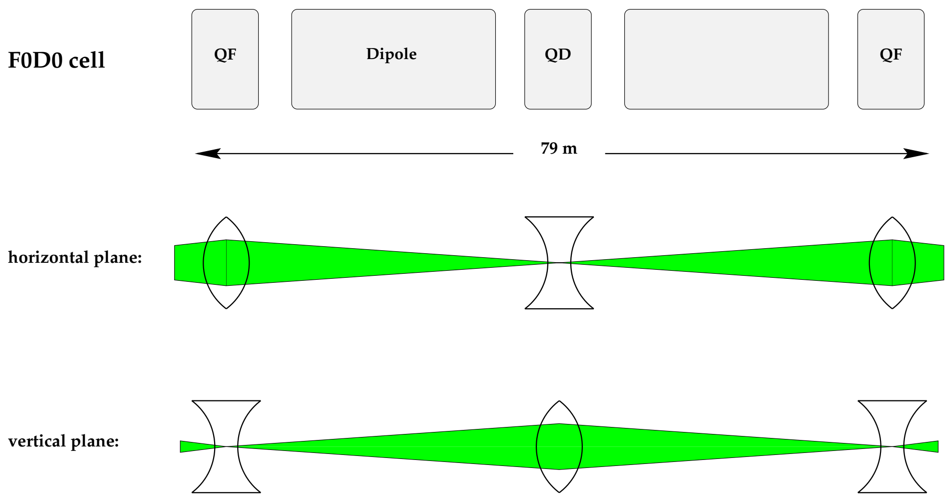

Figure 3.2: *Schematic view of a "FODO"-cell (top). Quadrupoles play the role of lenses for the particle beams.* **QF** *and* **QD** *denote quadrupoles with focusing respectively defocusing properties in the horizontal plane (centre). The optical properties of the quadrupoles are inverted in the vertical plane (bottom).*

$$\frac{d^2y}{ds^2} = K(s) \cdot y \qquad , \tag{3.6}$$

using Eq. 3.1 and Eq. 3.4. ΔE is the energy deviation of the particle from E_0. Eq. 3.5 is called "Hill's equation". If the term $\Delta E/E_0$ is neglected, Eq. 3.5 is the equation of a classical harmonic oscillator with varying strength. A general solution in either x or y coordinates can be written in the representative form:

$$x(s) = a\sqrt{\beta(s)}\,\cos(\phi(s) - \phi_0) \qquad . \tag{3.7}$$

This equation describes a pseudo-harmonic oscillation, called the **betatron oscillation**, of the particles in a storage ring. With the assumptions made, the motion is independent for the two transverse coordinates x and y with different functions $\beta(s)$ and $\phi(s)$ for the two planes. The function $\beta(s)$ is called the **betatron function**. It represents the focusing characteristics of the ring and describes the complete magnet configuration of the ring. According to Eq. 3.7, the amplitude of the betatron oscillation at a given position s along the ring is determined by $a \cdot \sqrt{\beta(s)}$. The phase function $\phi(s)$ is related to the betatron function by:

$$\phi(s) = \int_0^s \frac{ds'}{\beta(s')} \qquad . \tag{3.8}$$

The betatron function is periodic in s with the period L, the path length of one complete revolution along the ideal orbit. For a complete revolution the phase advances by:

$$\phi(s_0, s_0 + L) = \int_{s_0}^{s_0+L} \frac{ds}{\beta} = \oint \frac{ds}{\beta} = 2\pi Q \qquad . \tag{3.9}$$

This integral is independent of the position s_0 due to the periodicity of β. The phase advance increases by the same amount after any complete revolution and is written as $2\pi Q$. The **betatron tunes** Q are defined as:

$$Q_{x,y} = \frac{1}{2\pi} \oint \frac{ds}{\beta_{x,y}} \qquad . \tag{3.10}$$

$Q_{x,y}$ represents the number of betatron oscillations in the horizontal and vertical coordinate per turn. Typical values for the betatron tunes at LEP can be found in Table 3.1. If Q is an integer value, any imperfection in the guide field becomes a synchronous perturbation and leads to a resonant excitation of the oscillation and an exponential growth of the amplitude. Hence the betatron tunes should not be integer or any simple low order fraction. Tilted magnets cause coupling between the two transverse motions. Thus horizontal and vertical tunes, which satisfy the following equation, also lead to resonances (m, n, r integer):

$$m \cdot Q_x + n \cdot Q_y = r \qquad . \tag{3.11}$$

The strength of the resonance diminishes with higher orders of $|m| + |n|$.

3.3 The Closed Orbit

In a circular accelerator the individual particles perform betatron oscillations around the **closed orbit**. Since the closed orbit is unique and periodic, the horizontal position $x_{co}(s)$ along the closed orbit can be written as:

$$x_{co}(s_0) = x_{co}(s_0 + L) \qquad , \tag{3.12}$$

where L is the circumference of the ring. For a perfectly aligned machine the closed orbit coincides with the ideal orbit corresponding to $x_{ideal} = x_{co} = 0$ everywhere along the ring. If x represents the displacement from the ideal orbit at a certain position s_0, two components contribute to it:

$$x(s_0) = x_\beta(s_0) + x_{co}(s_0) \qquad , \tag{3.13}$$

where x_β is the betatron oscillation around the closed orbit. For a transverse magnetic field error ΔB in a small azimuthal interval Δs, the slope $\Delta x/\Delta s = \Delta x'$ of the particle is changed by:

$$\Delta x' = -\frac{ec}{E_0} \cdot \Delta B \cdot \Delta s \qquad . \tag{3.14}$$

Small transverse magnetic fields occur for example due to misaligned quadrupoles. The closed orbit is defined as a particular periodic trajectory. Hence $x_{co}(s)$ has to fulfil Hill's Equation (Eq. 3.5) and can according to Eq. 3.7 be written:

$$x_{co}(s) = a \cdot \sqrt{\beta(s)} \cdot \cos(|\phi(s) - \phi(s_0)| - \phi_0) \qquad , \tag{3.15}$$

$$a = \Delta x' \cdot \frac{\sqrt{\beta(s_0)}}{2\sin(\phi_0)} \qquad \text{with}\, \phi_0 = \pi Q \qquad . \tag{3.16}$$

This displays two features of the magnet lattice: (i) The displacement of the closed orbit is proportional to the field error and to the square root of the betatron function at the location of the error. (ii) The denominator of a in Eq. 3.16 vanishes and therefore no stable orbit is possible when the betatron tune adopts an integer value.

3.3.1 Dispersion Orbit

An energy deviation also leads to a displacement from the ideal orbit. The total displacement x of a particle at a certain position s_0 can be written as the sum of three parts:

$$x(s_0) = x_\beta(s_0) + x_{\Delta E}(s_0) + x_{co}(s_0) \qquad , \tag{3.17}$$

where x_β is the betatron oscillation, x_{co} the closed orbit and $x_{\Delta E}$ the displacement due to a deviation from the nominal energy E_0. $x_{co} + x_{\Delta E}$ is the closed orbit for a particle with an energy deviation, the **dispersion orbit**. The displacement is proportional to the energy deviation ΔE:

$$x_{\Delta E}(s) \;=\; D(s) \;\cdot\; \frac{\Delta E}{E_0}(s) \qquad , \tag{3.18}$$

where $D(s)$ is the dispersion function and describes the closed orbit displacement per unit energy deviation as a function of the azimuthal position. The dispersion as a function of s is bent towards the s-axis in focusing and repelled from this axis in defocusing quadrupoles. A dispersion orbit is unique for a certain energy deviation.

One important consequence of dispersion orbits is the associated change in the circumference of the closed orbit. Since the orbit displacement at a given energy has generally the same sign all around the ring, a non-vanishing path lengthening remains from energy oscillations. If L_0 is the orbit length of one complete revolution on the ideal orbit, the dispersion orbit is expected to differ from L_0 by ΔL. The change in the orbit length is related to the energy deviation:

$$\frac{\Delta L}{L_0} = \alpha \cdot \frac{\Delta E}{E_0} \qquad . \tag{3.19}$$

The momentum compaction factor α is a characteristic of the magnet lattice and thus of the design of a ring. See Table 3.1 for a typical value at LEP.

3.4 Synchrotron Oscillations

Stored electrons and positrons do not all have the nominal energy E_0, which is the design energy for a given setting of the magnet currents and fields. In general, the energy of a stored particle will deviate from the nominal energy and the particle will oscillate in its longitudinal position and its energy around the position of the 'nominal particle' in the centre of the bunch. The energy deviation is caused for instance by synchrotron radiation.

3.4.1 Synchrotron Radiation

Synchrotron radiation is emitted when charged particles are accelerated. The closer the particle's velocity is to the velocity of light the more frequently this happens. Electromagnetic radiation occurs whenever there are electric and magnetic fields with components orthogonal to each other. The power P_γ radiated by a unit charge of the energy E on a curved path with the bending radius ρ is given by [36]:

$$P_\gamma = \frac{cC_\gamma}{2\pi} \frac{E^4}{\rho^2} \qquad , \tag{3.20}$$

C_γ depends on r_c, the classical particle radius, and mc^2, the rest energy of the particle:

$$C_\gamma = \frac{4\pi}{3} \frac{r_c}{(mc^2)^3} = 8.8575 \cdot 10^{-5} \frac{m}{GeV^3} \qquad . \tag{3.21}$$

the energy loss E_s per turn of a particle is obtained from an integral of the radiation power along the circumference of the ring:

$$E_s(\mathrm{GeV}) = \oint P_\gamma ds = C_\gamma \frac{E^4}{\rho} \qquad . \tag{3.22}$$

The total energy loss due to synchrotron radiation scales like the fourth power of the particle energy and is inversely proportional to the bending radius. For a particle energy of about 45.6 GeV at LEP the energy loss is about 120 MeV per turn (s. Tab. 3.1). The strong dependence of the energy loss on the particle energy leads to practical limitations on the maximum achievable energy for circular e^+e^-accelerators.

3.4.2 Phase Focusing and Synchrotron Tune

Particle acceleration and storage is achieved with the help of longitudinal electric fields. Such fields can be generated in high quality resonators, so called **R**adio **f**requency (RF) cavities. In order to remain synchronous with the circulating bunches, the RF frequency f_{RF} has to be an integer multiple of the revolution frequency f_{rev}:

$$f_{RF} = h \cdot f_{rev} \qquad , \tag{3.23}$$

where h is called the harmonic number. The RF fields must be sufficient to compensate the energy losses per turn due to synchrotron radiation E_s. For a sinusoidal waveform of the accelerating voltage, the synchronous phase of the RF fields ψ_s is given by the condition:

$$E_s = e\, V_0 \, \cos\psi_s \qquad , \tag{3.24}$$

where V_0 is the sum of all accelerating voltages seen by a particle in one turn. While a particle with the nominal energy arrives at the RF cavity exactly at the synchronous phase ψ_s, most other particles arrive at a slightly different phases $\psi = \psi_s + \Delta\psi$. According to figure 3.3, the synchronous particle gains exactly the energy E_s needed to compensate the energy losses due to synchrotron radiation. Without fluctuations of E_s a nominal particle would arrive after the next turn at the same phase. At LEP, the ultra-relativistic particle is bend less if its energy exceeds the nominal energy E_0, i.e. $\Delta p/p > 0$, and will therefore arrive later at the cavity. The particle sees a lower voltage and gains less energy. After the next turn it will loose some energy and some of its time precedence. The opposite happens to a particle with less energy, i.e. $\Delta p/p < 0$. It arrives earlier at the cavity with respect to the synchronous particle and will gain more energy than needed to compensate for the energy losses of one turn. After the next turn its phase will be again closer to ψ_s. This **phase focusing effect** forces the particles to

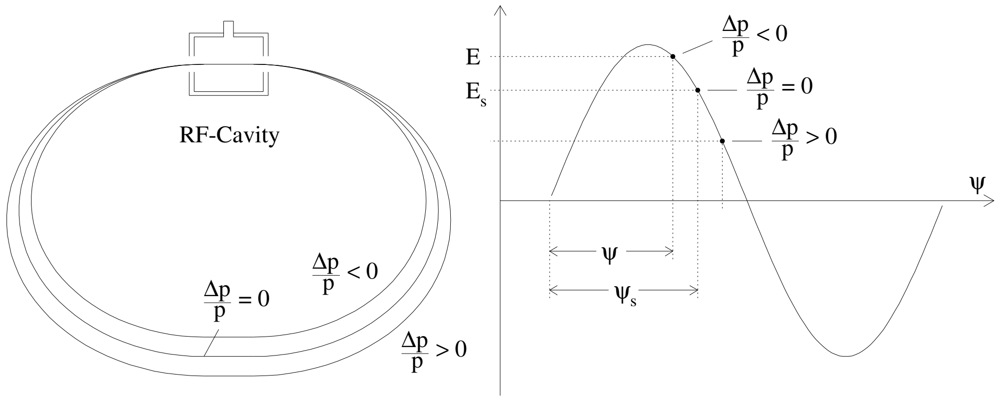

Figure 3.3: *Schematic view of the phase focusing principle of an RF cavity.*

perform longitudinal oscillations around the synchronous phase. This damped energy oscillation around the nominal energy is called **synchrotron oscillation**. The energy change ΔE_{n+1} after one turn is given by:

$$\Delta E_{n+1} = eV_0 \Delta\psi \cos\psi_s - \frac{d\omega}{dE}\Delta E_n \qquad . \tag{3.25}$$

ω is the oscillation frequency.

For small deviations $\Delta\psi \ll \psi$ from the synchronous phase, and thus small oscillation amplitudes, the "synchrotron frequency" ω_s is given by:

$$\omega_s^2 = \omega_{rev}^2 \cdot \frac{h\alpha e V_0 \cos\psi_s}{2\pi\beta^2 E_0} \qquad , \tag{3.26}$$

where α is the momentum compaction factor, h the harmonic number and E_0 the nominal energy. Similar to the betatron oscillation tunes the synchrotron (oscillation) tune Q_s can be defined as:

$$Q_s = \frac{\omega_s}{\omega_{rev}} \qquad . \tag{3.27}$$

Q_s represents the number of synchrotron oscillations per turn. Typical values at 45 GeV are between 0.06 and 0.07. A change of the total accelerating voltage would also change the synchrotron tune.

3.5 The LEP Collider

The LEP collider consists of eight circular arcs separated by straight sections including the eight **I**nteraction **P**oints (IPs). Arcs are also referred to as octant j, where j is an integer between 1 and 8. The notation used later is the following:

$$\mathrm{IP}_i \leftrightarrow \mathrm{IP}_j \equiv \mathrm{octant}\, j$$

$1 \leq i, j \leq 8$ denote the number of the IPs. In particular, the octant between IP8 and IP1 is defined as octant 1. Four interaction regions accommodate large experimental detectors. LEP is operated with two counter-rotating beams of electrons and positrons. In the standard operation cycle, the beams are injected and accumulated at an energy of approximately 20 GeV. As soon as a sufficient beam intensity has been accumulated, the beams are accelerated to the physics energy where they are brought into collisions at the IPs for several hours. One operation cycle, typically in the order of 10 to 15 hours, is called a fill. During the first LEP operation period (LEP I) electrons and positrons collided with a beam energy close to the Z resonance at about 45.6 GeV in the four equipped interaction regions (IP2, IP4, IP6, IP8). Fig. 3.4 presents a general overview of the LEP collider and the four experimental detectors. Typical values of important LEP operation parameters are listed in Table 3.1. Either the design parameters [37] or averaged values obtained during LEP I operation are given. Usually the LEP parameters are monitored in intervals of several minutes. This implies a continuous measurement and memorising of the various quantities within the various LEP operation modes. A complete standard operation cycle consists of:

- **filling**
  Electron and positron beams are injected from SPS to LEP at approximately 20 GeV.

- **accelerating**
  The beams are ramped from 20 GeV up to the desired energy working point (P-2,P,P+2).

- **adjusting**
  The machine is prepared for physics operation. The beam energy is already at nominal setting.

- **physics**
  This machine mode is devoted to physics data taking by the experiments. The beam energy is set to the nominal energy

- **calibration**
  The calibration mode is foreseen for energy calibration tasks, usually at the end of physics mode but not necessarily. The beam energy is set to the nominal energy.

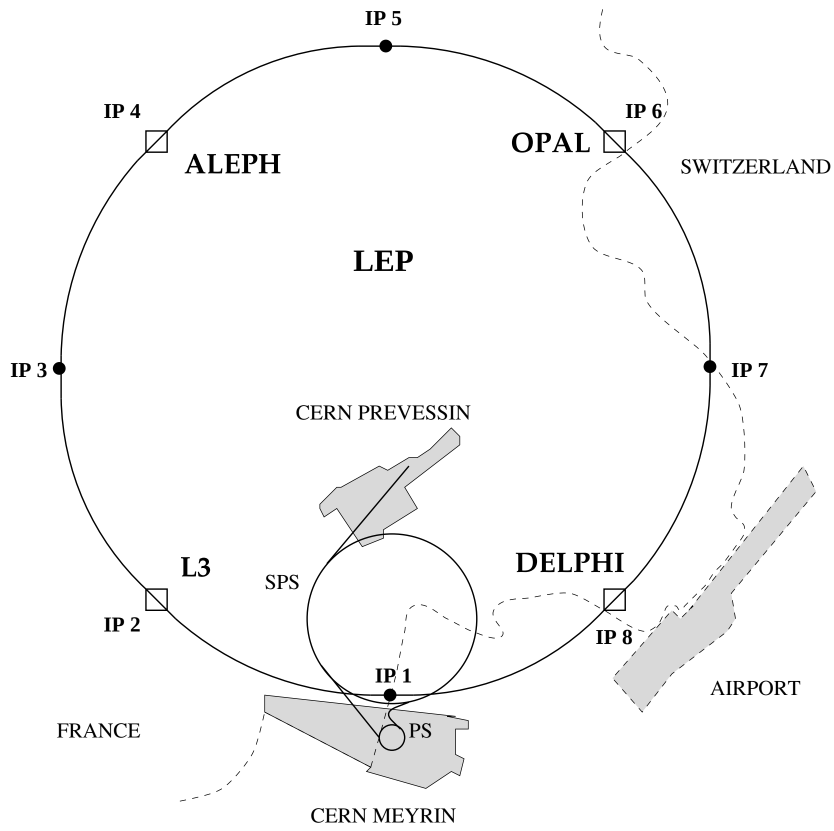

Figure 3.4: *The LEP collider with a circumference of about 27 km and its 8 interaction points (IP) underneath the French-Swiss border. 4 IPs are equipped with experimental detectors (L3, ALEPH, OPAL, DELPHI).*

- **dump_beam**
  The beams are dumped.

The "LEP logging database" is the device where all relevant quantities for LEP operation are saved with different periodicities. Frequency and number of parameters depend on the operation mode. In some cases missing values and records have been filled in by interpolating between previous and subsequent data points in a fill or are taken from various private logging systems.

3.5.1 LEP Operation Schemes

During the 1993 and 1994 run LEP was operated in the "pretzel" scheme. Each of eight bunches of electrons and positrons are equally spaced around the ring and collide at each of the four experimental interaction regions. The unwelcome additional parasitic collision points in the centre of the arcs are avoided by oscillations of the two

Description	synonym	value
Circumference (*)	C_0	$\simeq$ 26658.9 m
Average radius (*)		$\simeq$ 4242.9 m
Number of bunches	k_b	8 (1993)
		12 (1995)
Number of standard F0D0 cells (*)		244
Length of a standard F0D0 cell (*)		79 m
Length of a standard dipole (*)		5.748 m
Field of a standard dipole at 45.6 GeV (*)		0.049 T
Excitation current at 45.6 GeV		$\simeq$ 2000 A
Bending radius (*)	ρ	3096.4 m
Betatron phase advance per cell	ϕ_x, ϕ_y	$90^o, 60^o$
Betatron tunes	Q_x, Q_y	90.27, 76.19
Momentum compaction factor	α	$1.86 \cdot 10^{-4}$
RF frequency (*)	f_{RF}	352 254 170 Hz
Revolution frequency (*)	f_{rev}	11 245.5041 Hz
Harmonic number (*)	h	31 324
Nominal energy at "Peak-2" settings	E_0	44.7 GeV
at "Peak" settings		45.6 GeV
at "Peak+2" settings		46.5 GeV
Synchrotron radiation energy loss per turn at 45 GeV	E_s	124.6 MeV
Horizontal emittance at 45 GeV	ϵ_x	12 - 40 nm
Vertical emittance at GeV	ϵ_y	$\simeq$ 1 nm
Energy spread at 45 GeV	σ_E/E	about $1. \cdot 10^{-3}$
Synchrotron tune at 45 GeV	Q_s	0.06 - 0.075

Table 3.1: *A selection of the main parameters of LEP throughout the 1993 and 1995 energy scan. Values marked with * are taken from the design report. For the other parameters typical values obtained during LEP operation are given.*

beams in the horizontal plane created by horizontal electrostatic separators. Separators like this are also used to avoid the collisions in the odd IPs. Fig. 3.5 illustrates the horizontal "pretzel" oscillations of the positron beam in two arcs and one experimental interaction region centred between the two arcs. The phase difference between positron and electron beam amounts 180^o. The horizontal displacement is calculated by the LEP simulation program MAD [38]. The oscillation of the beams in the horizontal plane provide the required separation in the arcs to avoid the parasitic collision points. The horizontal orbit is flat in the straight sections around the even IPs.

In order to improve the achievable luminosity, LEP is since 1995 operated in a "bunch train" scheme [39]. Furthermore the new scheme was supposed to offer more flexibility for subsequent LEP II operation. During the operation this prognosis turned out to be too optimistic. The Bunch Train scenario implements four equally spaced trains, consisting of three bunches each. The trains are crossing at the four experimental

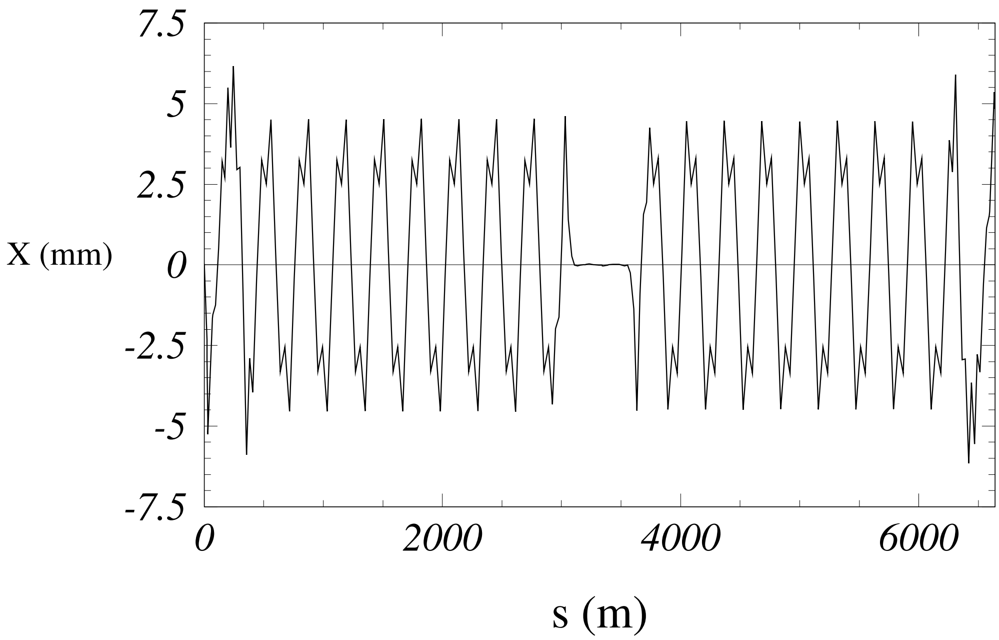

Figure 3.5: *The horizontal orbit as a function of the position s along the ring calculated with MAD. $s = 0$ corresponds to IP1. IP2 centred between two arcs is shown. In the arcs the "pretzel" oscillations reach about 6 mm horizontal displacement.*

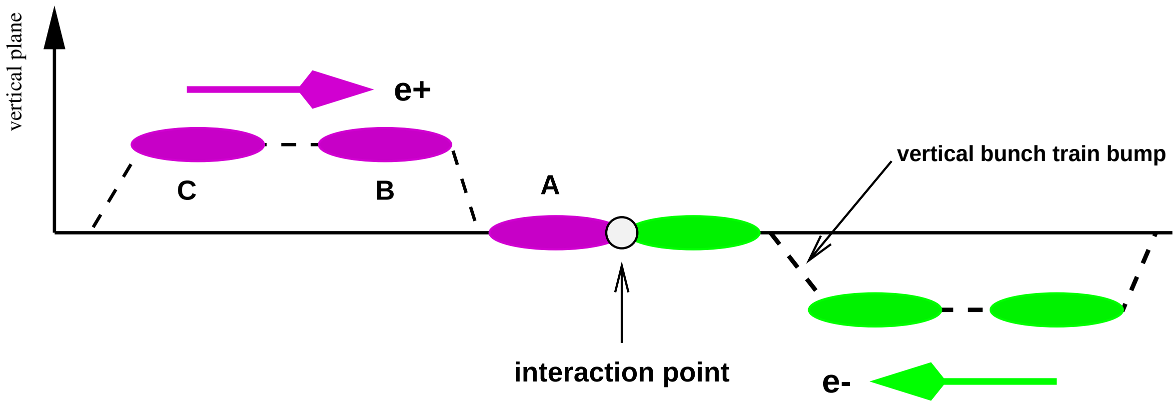

Figure 3.6: *Schematic view of the vertical bunch train bumps around the experimental areas. Both, electron and positron trains, consist of three bunchlets A,B and C.*

IPs. Inside a train the bunches were spaced by 247 ns, which corresponds to about 85 m. Vertical separation bumps are used to avoid the parasitic collisions around each of the eight IPs. Fig. 3.6 shows a schematic view of one electron and positron train colliding at an interaction point. The vertical separation bumps around the IP are indicated by dashed lines. The presence of the separation bumps creates opposite sign vertical dispersion of electrons and positrons at the position of the interaction point [40]. Vertical dispersion and effects arising from its presence at the IPs are discussed later.

Chapter 4

Tools for Beam Energy Measurements

The ultimate goal of the energy calibration for a Z resonance scan is to provide beam energies in intervals of about 15 minutes with the highest possible accuracy. Since the beam energy is a function of the integrated magnetic field along the closed orbit, the LEP dipole field has to be monitored throughout a fill as well as the mean horizontal orbit position in the quadrupoles. A substantial part of the energy calibration task is the determination of the absolute beam energy in order to calibrate the magnetic field measurements if possible in every fill. An accurate instantaneous measurement of the beam energy is realised by the principle of resonant depolarisation.

4.1 Beam Energy and Magnetic Field

The average beam energy is determined in a storage ring by the integrated magnetic field $B(s)$ along the closed orbit:

$$E_{beam} = \frac{ec}{2\pi} \oint B(s)ds \qquad . \tag{4.1}$$

For a beam energy of 45 GeV the integrated magnetic field is about $\oint B(s)ds \approx 10^3 Tm = 10^7 Gm$. The integral can be split into three components:

$$\oint B(s)ds = \oint B_{di}ds + \oint B_{quad}(x)ds + \oint B_{misc}ds \qquad , \tag{4.2}$$

where:

- B_{di} is the field of the dipole magnets. It usually accounts for $> 99.9\,\%$ of $\oint B(s)ds$.
- B_{quad} is the contribution of the quadrupoles. The quadrupole contribution basically depends on the transverse position of the beam.
- B_{misc} is the contribution due to other miscellaneous sources like sextupoles, corrector magnets (low field steering dipoles), the earth magnetic field etc. Not all of the sources are known. Commonly these terms are very small but cannot always be neglected.

The LEP dipole field is generated by 3280 standard dipoles, 32 low field dipoles around the straight sections and 24 strong injection dipoles [37]. In a perfect storage ring it is possible to choose the RF frequency value such that the beam moves through the centre of all quadrupoles (neglecting energy losses). The frequency, for which this condition is fulfilled, is called the "central frequency" f_c. At LEP, the central frequency is measured several times a year with a standardised procedure [41]. In a real machine, where the quadrupoles have some misalignment, the beam can only be centred on average in the quadrupoles. Along this "central orbit" the quadrupole contribution vanishes: $\oint B_{quad}(s)ds = 0$. When the RF frequency differs from the central frequency by Δf_{RF} the energy changes by:

$$\frac{\Delta E}{E} = -\frac{1}{\alpha}\frac{\Delta f_{RF}}{f_{RF}} \qquad , \tag{4.3}$$

where α is the momentum compaction factor and E the nominal energy. Distortions of the ring leading to a modification of the ring circumference C also cause energy shifts if the RF frequency is kept constant, which is usually the case at LEP. A change of the LEP circumference displaces the centre of the quadrupoles with respect to the beam orbit, whose length is fixed by the constant RF frequency. The related energy shift is:

$$\frac{\Delta E}{E} = -\frac{1}{\alpha}\frac{\Delta C}{C} \qquad . \tag{4.4}$$

To obtain an accurate measurement of the particle energy in samples of 15 minutes it is essential to measure continuously the dipole field and the additional quadrupole contributions around the ring. Therefore the reliability of the instruments is just as relevant as the understanding of magnetic field effects, which influence the beam energy.

4.2 The Principle of Resonant Depolarisation

The energy of a circulating particle is proportional to the precession frequency of the particles spin [42]. The resonant depolarisation technique [34] is based on a measurement of the spin polarisation combined with a subsequent resonant depolarisation of the beam. The technique uses the fact that electron and positron spins in a storage ring polarise spontaneously in the transverse plane. Once the beam is polarised, the possibility for very accurate measurements of the average beam energy is opened. The polarisation level is measured by a laser polarimeter [43, 32, 44]. The resonant depolarisation technique requires particular conditions for the LEP machine: separated beams and special settings of the machine parameters such as Q_x and Q_y. It is not possible to perform continuous energy calibrations during a fill because the interactions of the beam at the collision points are strongly depolarising.

The polarisation vector $\vec{P}$ is defined as the average of all spin vectors $\vec{s}$ for a group of particles (e^- or e^+ bunch). In an ideal machine, vertical polarisation can reach 92.4% due to the "Sokolov-Ternov effect" [45]. The maximum vertical polarisation is often reduced by magnetic fields, which bend the spins away from the vertical direction. The implementation of techniques to compensate for depolarising forces in the storage ring (for instance the experimental solenoids and optic imperfections) [46, 47, 48, 49] allowed the establishment of sufficient transverse polarisation for routine energy calibrations. Details about the procedure to establish transverse polarisation are published in [44]. Between the 1993 and 1995 polarisation levels between 5% and 20% could be reproduced in standard conditions for energy calibration purposes.

The laser polarimeter, which is used to measure the polarisation level at LEP, is a standard equipment in e^+e^-storage rings above 1 GeV. It is based on spin dependent Compton scattering of circularly polarised photons from the electron/positron beam. Circularly polarised photons are provided by a laser installed in an optical laboratory close to IP1. The spin dependent total Compton cross section differs for polarised beams illuminated by left- and right-hand circularly polarised laser light. The backscattered high energy photons travel towards a detector[1], which records their vertical angular distribution. If the beam is transversally polarised an up-down asymmetry in the γ-rate is present. The distributions of the left- and right-handed photons are then vertically shifted by Δy. The polarisation level P_e is directly related to the vertical shift and the light polarisation P_γ:

$$\Delta y \;=\; \xi \cdot P_e \cdot P_\gamma \qquad , \tag{4.5}$$

where the proportional factor ξ depends on the configuration of the laser polarimeter and needs to be determined from measurements. For the LEP polarimeter setup ξ is of the order of a few micrometer per percent polarisation.

The motion of the spin vector $\vec{s}$ of a relativistic electron/positron in electro magnetic fields $\vec{E}$ and $\vec{B}$ is described by the Thomas-BMT equations [42]:

$$\frac{d\vec{s}}{dt} = \vec{\Omega}_{BMT} \times \vec{s} \qquad , \tag{4.6}$$

[1] a W-Si calorimeter

$$\vec{\Omega}_{BMT} = -\frac{e}{\gamma m}\left[(1+a\gamma)\vec{B}_{\perp} + (1+a)\vec{B}_{||} - \left(a\gamma + \frac{\gamma}{1+\gamma}\right)\vec{\beta}\times\frac{\vec{E}}{c}\right] \quad , \tag{4.7}$$

where $\vec{\Omega}_{BMT}$ is the spin precession frequency. $\vec{B}_{\perp}$ and $\vec{B}_{||}$ are the transverse and parallel components of the magnetic field with respect to the particle velocity $\vec{\beta}c$. e and m correspond to the electron charge and mass respectively, a is the magnetic moment anomaly and γ the Lorentz factor. In a storage ring the spin vector of a particle precesses $a\gamma$ times in one revolution. The term $a\gamma$ is called the "spin tune" ν. For ideal machines the average spin tune of a bunch is proportional to its average beam energy E:

$$\nu = a\gamma = \frac{aE}{mc^2} = \frac{E\,(\mathrm{MeV})}{440.6486(1)} \quad . \tag{4.8}$$

To measure the spin precession frequency at LEP, a radial field with a strength of $\int b_x dl = 2$ Gm is used to rotate the spin vector of the particles by a small amount (140 μrad) per turn. If this field is in phase with the spin precession frequency, the rotations add up coherently from turn to turn. Under resonance conditions the polarisation vector is rotated into the horizontal plane after about 10^4 turns ($\simeq 1$ second). Figure 4.1 shows a schematic view of the depolarisation principle. The resonance condition for

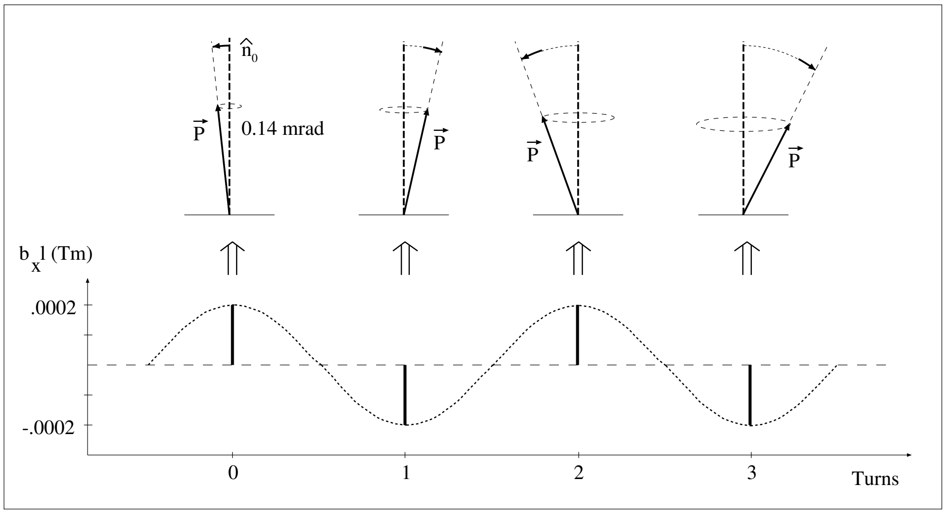

Figure 4.1: *Schematic view of the resonance condition between the spin precession (q_s = 0.5) and the radial perturbation from the kicker magnet. The figure is taken from [52].*

the kicker magnet oscillating with a certain frequency f_{dep} is:

$$f_{dep} = (k \pm \mathbf{q}) \cdot f_{rev} \quad . \tag{4.9}$$

f_{rev} is the revolution frequency of the electrons, k is an integer and $\mathbf{q}$ is the non-integer part of the spin tune. The integer part of the spin tune can easily be derived from the bending field measurements (Eq. 4.2). In figure 4.1 the resonance condition is illustrated for $\mathbf{q} = 0.5$. During the energy scans of 1993 and 1995 two possible settings of f_{dep} were used:

(a) $f_{dep} = \mathbf{q} \cdot f_{rev}$,

(b) $f_{dep} = (1 - \mathbf{q}) \cdot f_{rev}$.

In practice the depolarising frequency is slowly varied in a certain range until a depolarisation is observed. The width of this frequency interval Δf_{dep} limits the resolution of the method. In standard conditions $\Delta f_{dep} \simeq 22$ Hz $\Rightarrow \Delta q_{dep} = 0.002$ was used leading to RMS errors of $\sigma_q = \Delta q_{dep}/\sqrt{12} \Rightarrow \sigma_E \simeq 0.25$ MeV. Using Eq. 4.9 and Eq. 4.8 the spin tune and the corresponding value of the beam energy can be derived. However, this procedure is still ambiguous. A successful depolarisation is compatible with a measured non-integer part of the spin tune at both the $\mathbf{q}$ and the $(1 - \mathbf{q})$ setting. A depolarisation can also occur on "synchrotron satellites": $q_{satellite} = \mathbf{q} \pm Q_s$. To avoid these ambiguities, the procedure of resonant depolarisation is repeated several times while the beam energy and the synchrotron tune Q_s are varied deliberately. After a controlled change of the beam energy, settings (a) and (b) can be discriminated since the measured value of f_{dep} either increased (a) or decreased (b). Only the position of the true resonance does not change once the synchrotron tune has been varied while depolarisations, which occurred on a synchrotron satellite, move their position.

Using this method the **average** beam energy of the particles is obtained because the precession frequency of the polarisation vector is determined over many turns. Possible deviations from this value of the individual particles due to the beam energy spread [50, 51] or local energy variations do not bias this measurement. The accuracy of the energy calibration is limited by several effects such as the knowledge of the frequency of the kicker magnet and systematic shifts of the spin tune due to horizontal or longitudinal fields. The total systematic error on energy calibration by this method was calculated [52] to be $\Delta E = 0.2$ MeV at 45.6 GeV. Experiments to verify the systematic effects resulted in an upper bound of 1.1 MeV [52]. However, the statistical significance of these experiments was low. Due to the very limited accuracy of these studies the systematic error of the energy calibration was finally set to 0.2 MeV. Since the precision of this method is one order of magnitude better than that provided by other existing methods for absolute measurements [31], all energy calibrations during the 1993 and 1995 energy scans were based exclusively on the resonant depolarisation technique.

4.3 Measurements of the Dipole Field

According to Eq. 4.2 the dipole field gives the main contribution to the integrated magnetic field and thus to the beam energy. At LEP the bending field is measured simultaneously by a rotating induction coil (flip coil), several **N**uclear **M**agnetic **R**esonance (NMR) probes and eight induction wires (flux loops) covering an entire octant each. The NMR probes are installed in a "reference magnet" in a surface building and in the tunnel.

4.3.1 Instruments

Figure 4.2 shows the position of the available NMR probes around LEP. The flip coil and two NMR probes, called NMRREF and NMRVAC, are installed in the reference magnet. Two other NMR probes are installed in dipole magnets (M418 and M818) of the ring close to IP4 and to IP8. These two probes will later be referred to as NMR4 and NMR8, respectively. A detailed description of the working principle of the LEP NMR probes can be found in [53] and of induction coils for instance in [54].

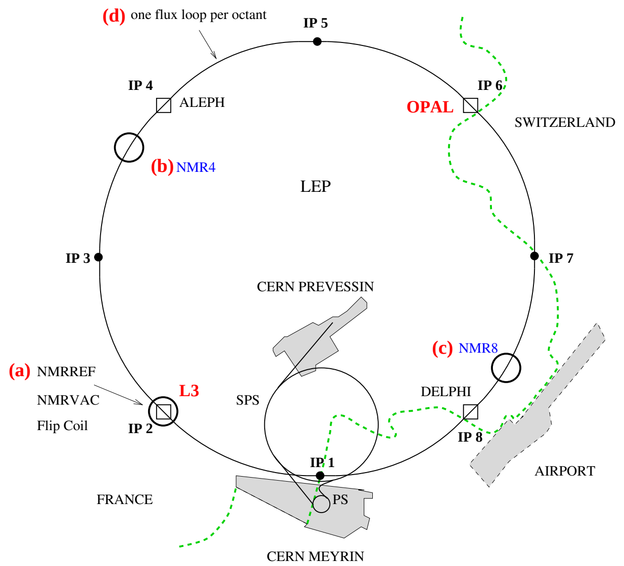

Figure 4.2: *The LEP ring with the positions of the 4 NMR probes. NMR4 (b) and NMR8 (c) are mounted in two tunnel bending magnets, M418 and M818. NMRREF, NMRVAC and the flip coil are installed in the reference magnet (a), located in a surface building and connected in series with the tunnel dipoles. Each of the eight octants includes one flux loop (d).*

- **NMR probes**
  The principle of nuclear magnetic resonance [55, 56] is based on the paramagnetism of atomic nuclei. The head of a NMR probe is composed of a proton sample (e.g. water) and two surrounding coils. One coil (rf-coil) applies a horizontal alternating field. The second coil is a vertical field modulation coil. By modulating the strength of the external field with the horizontal coil, the resonance condition of the NMR is varied. The NMR absorption signal is proportional to the energy deposited into the proton sample and recorded by the rf coil. The

phase difference $\Delta\phi$ of the modulating field to the phase of the absorption signal is detected. The resonance condition is fulfilled when $\Delta\phi = 0$. The resonance frequency of the rf coil signal is converted into a magnetic field measurement.
The NMRREF probe is used since the beginning of 1991. The other probes were installed after the 1993 energy scan in order to provide redundant measurements. The NMR probes are designed for a relative precision of $\Delta B/B = 5 \cdot 10^{-6}$ with a reproducibility of better than 2 mG [57]. To allow an estimate of the mean beam energy by a single NMR probe, a calibration of the instruments is done. The NMR probes are calibrated with resonant depolarisation measurements E_{pol}:

$$\kappa_B = \frac{E_{pol}}{B_{NMR}} \frac{(\text{MeV})}{(\text{G})} \qquad . \tag{4.10}$$

The magnetic field readings from the NMR probes is represented by B_{NMR}. To calculate κ_B for the four probes resonant depolarisation experiments at the start of 6 fills were selected. The magnetic field at the start of a fill is unaffected from all influences, which eventually change the magnetic field later in a fill. Table 4.1 summarises the results. The quoted errors correspond to the RMS scatter of the different conversion factors κ_B in the 6 fills. The results from Table 4.1 are used to convert the NMR readings from Gauss into MeV.

NMR probe	conversion factor κ_B [MeV/G]
NMRREF	54.712 ± 0.007
NMRVAC	52.777 ± 0.004
NMR4	91.295 ± 0.010
NMR8	91.311 ± 0.005

Table 4.1: *Conversion factors between the magnetic field in Gauss and the equivalent beam energy in MeV for all NMR probes.*

- **Flip coil**
  The flip coil is a device, which is rotated in the gap of the magnet. A flux change is induced by a change of the angle between the coil and the $\vec{B}$-field The flip coil is mounted on the reference magnet since 1989 and tracks the magnetic field with a precision of $\Delta B/B \simeq 5 \cdot 10^{-5}$ [31].

- **Flux loop**
  Flux loops [31, 59] are induction wires installed inside the gap of the magnet (see Fig. 4.3). An entire loop consists of many induction wires connecting every dipole magnet in an octant. Each of the LEP octants is covered by one independent loop. The flux loop records the magnetic field time derivative $\Delta B/\Delta t$. The total flux induced is integrated over a certain time period by the readout device and translated into a field change under the assumption of a constant cross section of the flux loops. In calibration experiments [58] all magnets are cycled from -2900

A up to +2900 A and the remanent magnetic field at the time of zero excitation current is deduced from the measurement. Flux loops determine the absolute dipole field of one complete octant with a precision of $\Delta B/B \simeq$ few10^{-4}. In 1995 no flux loop calibrations were performed.

Flux loops as well as the flip coil have the advantage that they are insensitive to the field quality, while the NMR probes need very homogeneous fields. However, the relative precision of the NMRs is superior to the precision of the other available devices, and therefore the determination of the magnetic field will be based on NMR measurements only.

4.3.2 Installation of the NMRs

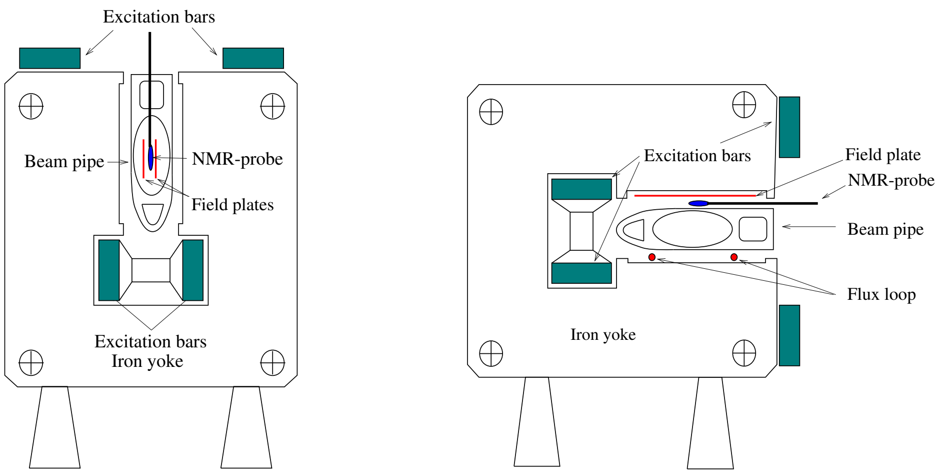

Figure 4.3: *NMR location in the bending magnets. Left: Transverse section of the reference magnet with the probe inside the vacuum chamber and field plates. Right: Tunnel bending magnet with the NMR probe installed in the slit between field plate and vacuum chamber wall. The induction wires of the flux loop are installed on the lower pole face.*

The installation of the NMR probes in the dipole magnets is illustrated in Fig. 4.3. The reference magnet is located in a temperature regulated ($\pm\ 1^o C$) room in a surface building close to the power converters. It is connected in series with the tunnel dipoles. It is a C-shaped magnet, made of laminated iron, and consists of 1.5 mm thick iron plates alternating with 4 mm air gaps. Both reference magnet probes (NMRREF, NMRVAC) and the rotating coil are centred in the gap of the yoke. The NMRVAC probe is surrounded by a piece of the LEP vacuum chamber (Fig. 4.3, left). The probes in the reference magnet need a minimum field of 800 Gauss for reliable operation. Since at 45 GeV the field in the magnets is only about 500 Gauss, 2 field plates are installed around each NMR to increase the field. The B-field in the reduced gap is then roughly 860 Gauss.

The standard tunnel dipole magnets have the same laminations as the reference magnet but the air gaps are filled with concrete [37]. The probes in the tunnel magnets are installed in a slit between the pole face of the magnet and the vacuum chamber wall (Fig. 4.3, right). At this off-centre position the field homogeneity is affected by the laminated structure of the yoke. To ensure the field homogeneity required for the operation of the NMRs, an iron plate (170 x 200 x 1.5 mm) had to be glued onto the pole face. This plate increases the field by about 1.5 %. Since the type of NMR probe installed in the tunnel dipoles requires a minimum field of 400 Gauss, no further gap reduction is necessary. Data from these probes are available for every fill in the 1995 scan with few exceptions only.

4.4 Beam Orbit Monitoring

On the central orbit, the beam passes through the centre of all quadrupoles. A particle moving on this orbit is only deflected by the dipole magnets since on the centre position ($\Delta x = 0$) the contribution from the quadrupole field cancels on average. When a particle is passing off-centre through the quadrupoles, it receives additional deflections (Fig. 4.4). The energy of the particles is then given by the nominal bending field

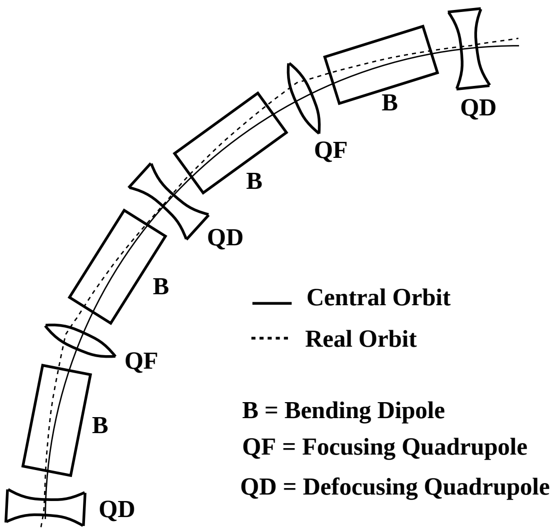

Figure 4.4: *A sequence of bending dipole magnets interleaved with focusing and defocusing quadrupole magnets. The solid line corresponds to the central orbit passing through the centre of all quadrupoles, the dashed line denotes an off-centre orbit where particles receive additional deflections in the quadrupoles.*

($\Rightarrow E_0$) plus an energy change ΔE due to the quadrupole contribution to the total deflection. The radial displacement Δx of this particle from the central orbit in the horizontal plane is related to ΔE through:

$$\Delta x(s) = D_x(s)\frac{\Delta E}{E_0} \qquad . \tag{4.11}$$

$D_x(s)$ is the horizontal dispersion. Since the horizontal dispersion vanishes in the straight sections of LEP, the mean horizontal displacement Δx_{arc} must be monitored in the arcs. In the LEP arc cells 240 **B**eam **O**rbit **M**onitors (BOM) [60, 61] are installed on quadrupole magnets to monitor the transverse position of the beam with respect to the centre of the quadrupole. These capacitive pickups measure the positions of electrons and positrons with a relative precision of a few microns. The mean horizontal orbit position Δx_{arc}, which is measured by the BOM system, is related to an energy change at $E_0 = 45.6$ GeV by [62]:

$$\Delta x_{arc} \;=\; D_x^{BOM} \frac{\Delta E}{E_0} \simeq (13.0 \pm 0.3) \left(\frac{\mu\mathrm{m}}{\mathrm{MeV}}\right) \cdot \Delta E\,(\mathrm{MeV}) \qquad , \tag{4.12}$$

where D_x^{BOM} denotes the mean horizontal dispersion at the beam orbit monitors. A value of 59 cm for D_x^{BOM}, calculated from the simulation program MAD [38], was used in Eq. 4.12. Measurements of D_x^{BOM} agree with this value within 2%. Fig. 4.5 shows the correlation between the mean horizontal position of the orbit in the arcs and the energy measured by resonant depolarisation during the 1993 and the 1995 energy scans. In both years the dependence of the energy measurements from the mean horizontal position agrees well with the expected relation of 1 MeV / 13μm. The predicted value of the correlation factor is indicated by a dashed line. Other effects influencing the beam energy smear the relation between energy measurements and the orbit position. The scatter of the data points around the predicted slope is somewhat larger in 1995 than in 1993. The reproducibility of the horizontal orbit position measurements was determined from 1993 and 1994 data. Within fills it amounts to 8 μm while the fill to fill reproducibility is between 20 μm (1993) and 10 μm (1994). The fill to fill reproducibility corresponds to an uncertainty of the beam energy of 1.2 MeV and is used as the estimate for the absolute precision of the X_{arc}-measurement for one fill.

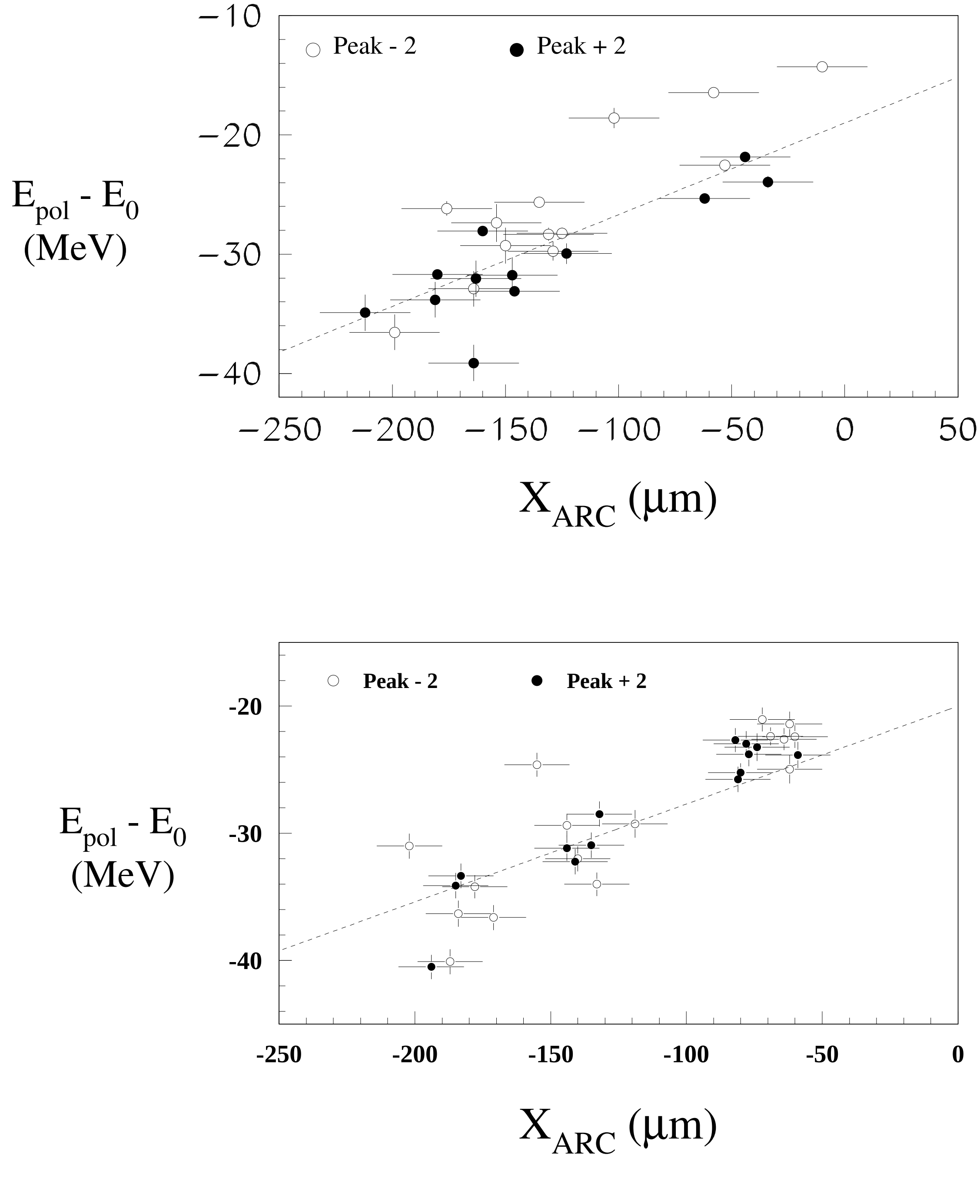

Figure 4.5: *Correlation between the horizontal position of the orbit in the arcs and the energy measured by resonant depolarisation during the 1993 energy scan (top, figure is taken from [63]) and the 1995 energy scan (bottom). The error of the mean horizontal orbit position is 20 μm in 1993 and 15 μm in 1995. A constant value (E_0), depending on the energy setting, is subtracted from the calibration data (E_{pol}) to combine the peak-2 and peak+2 data. The dashed line shows the expected relation between the orbit position and the beam energy.*

Chapter 5

Sources of Beam Energy Variations

All presently known parameters affecting the average beam energy have to be implemented into a basic model to obtain a realistic prediction for the LEP beam energy behaviour during entire fills. Table 5.1 gives an overview about these effects (IP dependent corrections are not taken into account here, they are discussed later). There are mainly two types of magnetic field effects contributing to the common corrections: dipole corrections and quadrupole corrections. The detailed effects influencing

type	source	remarks
dipole	temperature	the temperature of the magnet cores
		affects the magnetic dipole field
	humidity	humidity affects the permeability μ
		of the magnetic dipole material
	trains	train leakage currents perturb
		the dipole magnetic field
quad	moon	the moon influences the average horizontal orbit
		position due to earth tides
	rain	geological rock movements change the LEP
		circumference
amb.	hor.	settings of the horizontal correctors modify
	corr.	the bending or contribute to orbit
		lengthening effects ($\Rightarrow$ quadrupole part)

Table 5.1: *Listing of the presently known effects acting on the LEP average beam energy. The effects are arranged according to their contribution to the average beam energy (either* **dipole** *part,* **quad***rupole part or* **amb***iguous).*

the magnetic field of LEP will be discussed according to their type of magnetic field contribution (dipole or quadrupole). The Effect of horizontal corrector magnets is included in the section of the quadrupole field contributions.

5.1 Dipole Fields

The absolute beam energy calibration in both years was obtained by the resonant depolarisation method. The most important progress in the monitoring of the dipole field evolution during entire fills was the installation of NMR probes in two tunnel magnets in the first period of 1995. Due to the absence of magnetic field measurements in the tunnel, the dipole field evolution could not be verified in 1993. Some doubts remained on the interpretation of such field changes observed in 1993. Therefore, in the final energy determination (see Ref. [33]) an additional error was assigned to the beam energy results. In 1995 a method to anticipate this behaviour, the bending modulation, was invented. The analysis of the 95 data revealed a puzzling behaviour of the LEP tunnel magnets, which could be related to train leakage currents. It turned out that this effect together with the core temperature plays an important role for the understanding of the B-field evolution inside a fill. Environmental effects influence the magnetic field on a fill to fill basis.

5.1.1 Unexplained Field Changes in 1993

Because of the missing instrumentation, some observations remained unexplained after the 1993 Z resonance scan. There were indications for 2 **sudden energy jumps** [52] in a long term energy calibration experiment performed on August 29th, 1993, shown in Fig. 5.1. These jumps could not be explained inside the current understanding of the LEP energy behaviour, which was considered to be affected by temperature changes only. Figure 5.1 shows the long term energy calibration experiment in fill 1772. The two jumps happened between 06:30 and 08:00 in the morning and between 10:00 and 12:30. Certainly neither the prediction of the temperature model nor the evolution of the NMRREF readings were able to explain this. However, the temperature model prediction fits well the energy calibration data if it is shifted (indicated by dashed lines) by the same amount as the jumps. This experiment was excluded from the 1993 analysis.

The analysis of the 1993 data from the **N**uclear **M**agnetic **R**esonance (NMR) probe in the **reference magnet showed unexpected jumps** of up to +5 MeV between two consecutive readings. Jumps were observed in 5 to 10 % of all physics fills. Figure 5.2 shows a fill with two jumps. In 1994, during a polarisation experiment, a jump in the reference magnet was observed and its effect on the beam energy could be checked by the energy calibrations. Figure 5.3 shows these measurements during fill 2234. The energy calibration data saw the same jump but obviously only 50% of the amplitude.

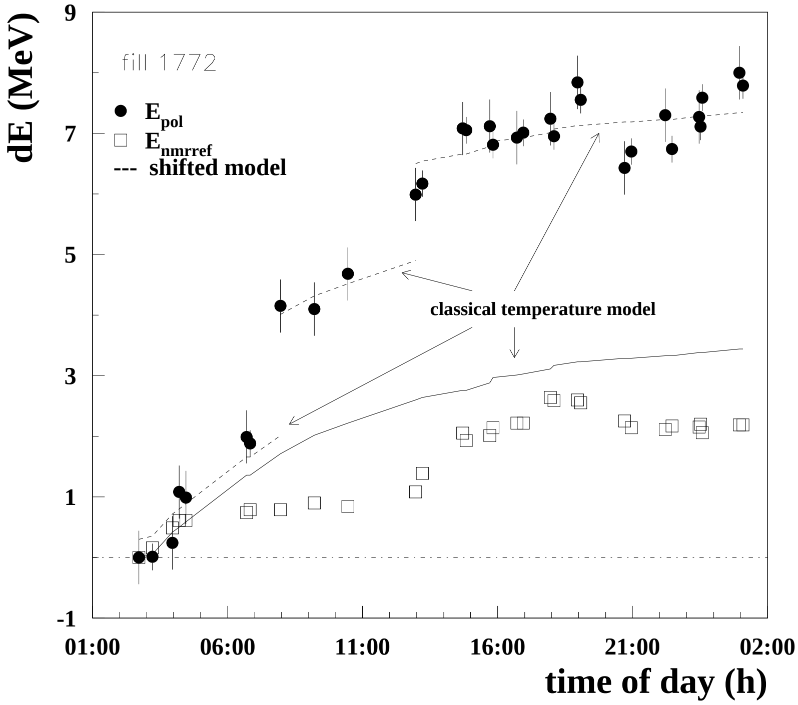

Figure 5.1: *Relative beam energy changes with respect to the first energy calibration measurementas a function of time during fill 1772. Energy calibration data and readings from the NMRREF probe are shown. The prediction from a temperature model is plotted as a solid line. The dashed lines correspond to the same model prediction but shifted by a certain amount in order to match with the* E_{pol} *data.*

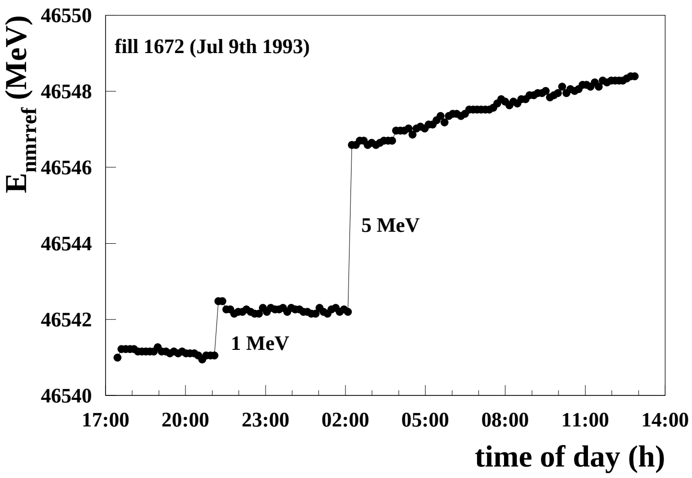

Figure 5.2: *In fill 1672 two jumps of different sizes occurred. The readings of the NMRREF probe are converted into units of beam energy using the conversion factor of the flip coil.*

It could not be verified if all jumps were related to real field variations. It remained unclear why the beam energy change was reduced by a factor of 2 with respect to the reference magnet probe. Following this observation, the 1993 LEP energy model took into account only 50% of the drifts seen in the reference magnet.

Besides sudden jumps, the NMR showed upward **field drifts** during fills. These drifts could reach a few MeV after some hours. Figure 5.4 shows data from fill 1849, in October 11th, 1993, with frequent energy calibration measurements. The readings

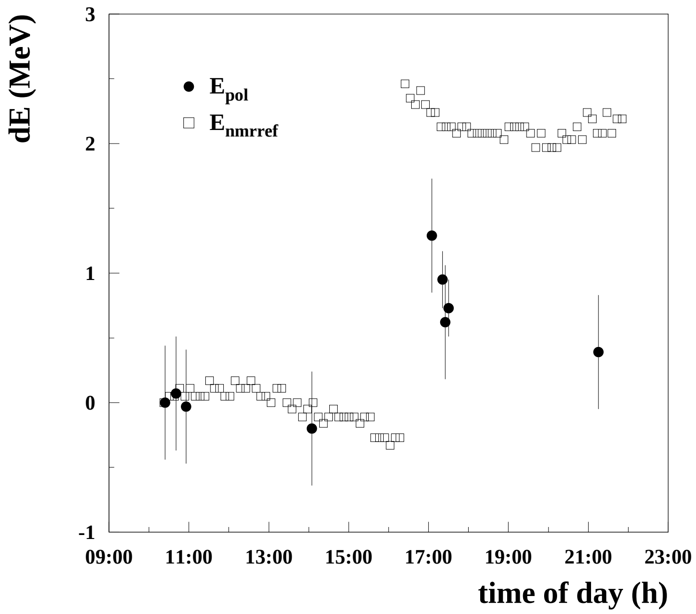

Figure 5.3: *Energy calibration data (E_{pol}) and NMRREF probe readings (E_{nmrref}) during fill 2234. The NMR readings are normalised to the first energy measurement. Only relative changes after the first measurement are shown. Around 16:30 a jump in the reference magnet is recorded. 30-50% of its amplitude was confirmed by the energy calibration measurement.*

from the NMRREF probe indicate a slow drift up to > 2 MeV throughout the fill. The first energy measurement in this fill took place more than 13 hours after the ramp to the final energy. The drift of the E_{pol} data reached 3.6 MeV after about 10 hours

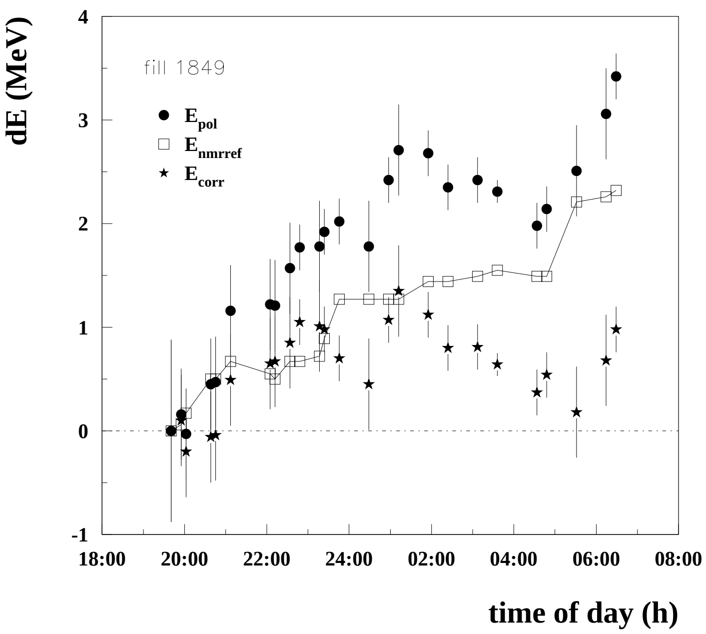

Figure 5.4: *Evolution of the relative beam energy as a function of time in fill 1849. Data from resonant depolarisation (E_{pol}), the probe in the reference magnet (E_{nmrref}) and E_{pol} corrected for the E_{nmrref}-drift (E_{corr}) are shown. All points are normalised to the first measurement. The depolarisation data are corrected for energy variations due to tides. During that fill the temperature did not change.*

while no drifts were expected after correction for tide and temperature effects since no further effects were known. This discrepancy became much smaller when the data were corrected for the drift seen by the NMRREF probe. The remaining rise of the corrected data sample E_{corr} was 1 MeV after 10 hours. The current of the bending magnets, which is monitored with a resolution of $\Delta I/I \simeq 2 \cdot 10^{-5}$ by DCCTs[1] [64],

[1]Direct Current Current Transformer

showed no change in this fill.

5.1.2 Conditioning of the Bending Magnets

Studies [65] performed during the 1993 energy scan to understand the jumps and drifts of the field in the reference magnet showed, that a series of current spikes applied to the magnets lead to an increase in the field which saturates after a few spikes. The field

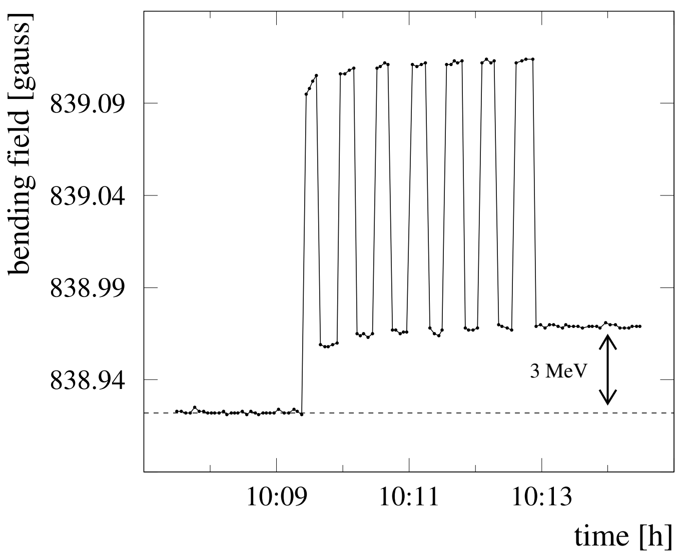

Figure 5.5: *Magnetic field (NMRVAC) as a function of time during a bending modulation test. The figure is taken from [53].*

variation shakes the magnetic domains of the bending magnets. In the (H,B) plane of the magnet hysteresis [66], an increase of the current causes the magnet to increase its B-field. After the excitation a non zero shift $\Delta B = \Delta B_{final} - \Delta B_{inital}$ remains due to the nonlinearity of the hysteresis loop. When such a cycle is repeated for many times, the magnetic field stabilises at a slightly higher level. This behaviour suggested the possibility to stop or reduce the increase of the field in the dipoles by applying a few deliberate current spikes at the beginning of each fill. Following some tests in the first part of the scan this technique (called **bending modulation**) has been applied to the magnets at the beginning of all fills starting with fill 2948. Figure 5.5 shows the readings of the NMRVAC probe during a bending modulation test in 1995. Each modulation pulse is clearly visible in the form of a peak in the magnetic field. The saturation [66] after the second excitation pulse is evident. The level change of the magnetic field after the bending modulation is different for the 4 probes [53]. Tab. 5.2 presents the average increase for each probe. The response of the reference magnet is roughly a factor of 2 larger than the effect in the tunnel magnets. The factor 2 is caused by the field doubling plates, which are mounted in the reference magnet. The response in units of equivalent beam energy (MeV) is about the same for all probes inside the quoted uncertainties. The scatter of the result of NMR8 is a factor of 2 enlarged with respect to NMR4. Both reference magnet probes record about 50% of the scatter of NMR4. The different size of the scatter indicates a different reproducibility of the

	$\Delta B \cdot 10^{-2}$ (G)	ΔE (MeV)
NMRREF	6.3 ± 1.0	3.5 ± 0.5
NMRVAC	5.5 ± 0.7	3.0 ± 0.4
NMR4	2.5 ± 1.0	2.3 ± 1.0
NMR8	3.0 ± 2.4	2.7 ± 2.2

Table 5.2: *Field increase due to the magnet conditioning measured by the four NMR probes. Errors correspond to the RMS scatter of the data sample.*

readings of the particular probes. More details and results on bending modulation are given in [67, 53].

5.1.3 Systematic Studies of the Dipole Field in 1995

This chapter attempts to classify the behaviour of the four different NMR probes. The measurements from the four NMRs show a distinct time dependence. An example is given in Fig. 5.6. In contrary to the tunnel NMR probes, the NMRs in the reference magnet do not display any significant variations of the B-field with time. Fill 2969 demonstrates all typical features of the tunnel probes: A **quiet period** in the early morning hours, a **short term behaviour** with fast field fluctuations and a **long term behaviour** with a slow upward drifts of the magnetic field.

5.1.3.1 The Quiet Period

The tunnel NMRs show fast fluctuations between 04:30 and 24:00. In the remaining period of time no perturbation can be seen. This quiet period starts every day around midnight and ends between 04:00 and 05:00 in the morning. This pattern is observed with an uncertainty of ± 30 minutes in all fills which covered this particular period of time and could be confirmed with flux loop measurements [53]. Figure 5.7 shows for each NMR probe the fluctuation as a function of day-time. It is averaged over all physics fills of the 95 scan. The difference of the magnetic field readings has been converted into the equivalent change of the beam energy ΔE. The fluctuation in both reference magnet probes is always very small ($\Delta E < 0.2$ MeV/h). The exceptional but still small peak in the distribution between 15:00 and 16:00 corresponds to the data from 2 fills where a jump in the magnetic field of the reference magnet occurred. The fluctuations of NMR4 and NMR8 are much larger except during the period from

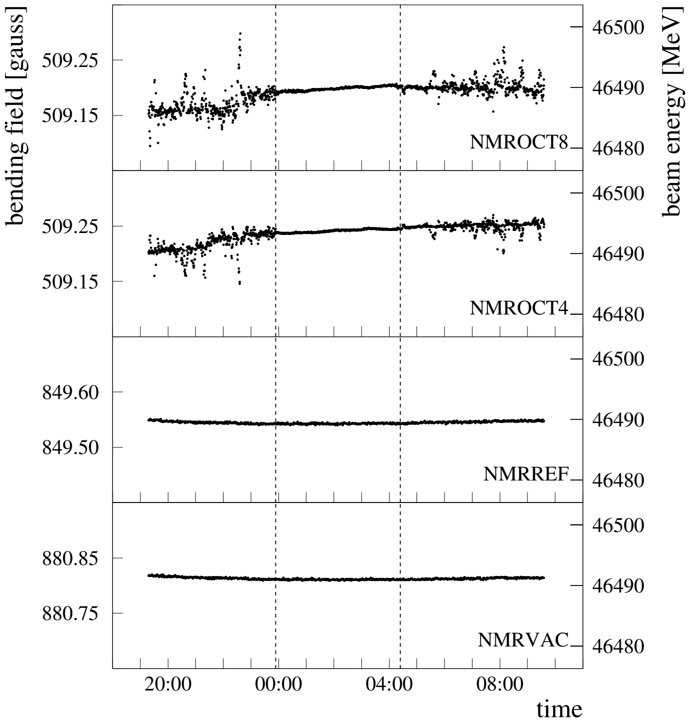

Figure 5.6: *Bending field in Gauss of all NMR probes in fill 2969 (p+2). The dotted lines denote the beginning and the end of a quiet period between 23:55 and 04:25. Out of this period both NMRs in the tunnel show fast field fluctuations whereas the probes in the reference magnet record no time dependence.*

00:00 to 05:00. Both probes fluctuate by about 0.1 MeV/h during this period, which is consistent with the fluctuation seen by the reference magnet probes. After 06:00, the perturbation in the tunnel dipoles increases roughly by one order of magnitude.

5.1.3.2 Short Term Behaviour

The two tunnel NMR show fast and large fluctuations outside the quiet period. The day-time structure is similar for NMR4 and NMR8: the two distributions have the same daily peak distribution (around 08:00, between 11:00 and 14:00, around 18:00 and 23:00). They differ in the amplitudes by a factor of approximately 1.5. The correlation of the two distributions, which are visible in Fig. 5.7 (c) and (d), is illustrated in Fig. 5.8. The solid line corresponds to a fit with a slope parameter of 1.5 ± 0.4 indicating a different amplification factor of the perturbation. The large fluctuations origin from sudden changes of up to 10 MeV equivalent beam energy, which are recorded outside the quiet period in the tunnel magnets. The duration of these fast field fluctuations is of the order of a few minutes (Δt $\leq$ 5 minutes) and the largest slope is about 0.3 MeV/s. The short term perturbation consists of field fluctuations with low frequency components of less than 1 Hz. Fig. 5.9 shows that the difference between two consecutive readings (ΔB) of the tunnel NMRs is strongly anti-correlated with a slope of -1.7. The amplitude $\mathcal{A}$ of the perturbation at the two locations, around NMR4 and NMR8, is related by a factor:

$$\mathcal{A}_{NMR8} \simeq -1.7\, \mathcal{A}_{NMR4} \quad . \tag{5.1}$$

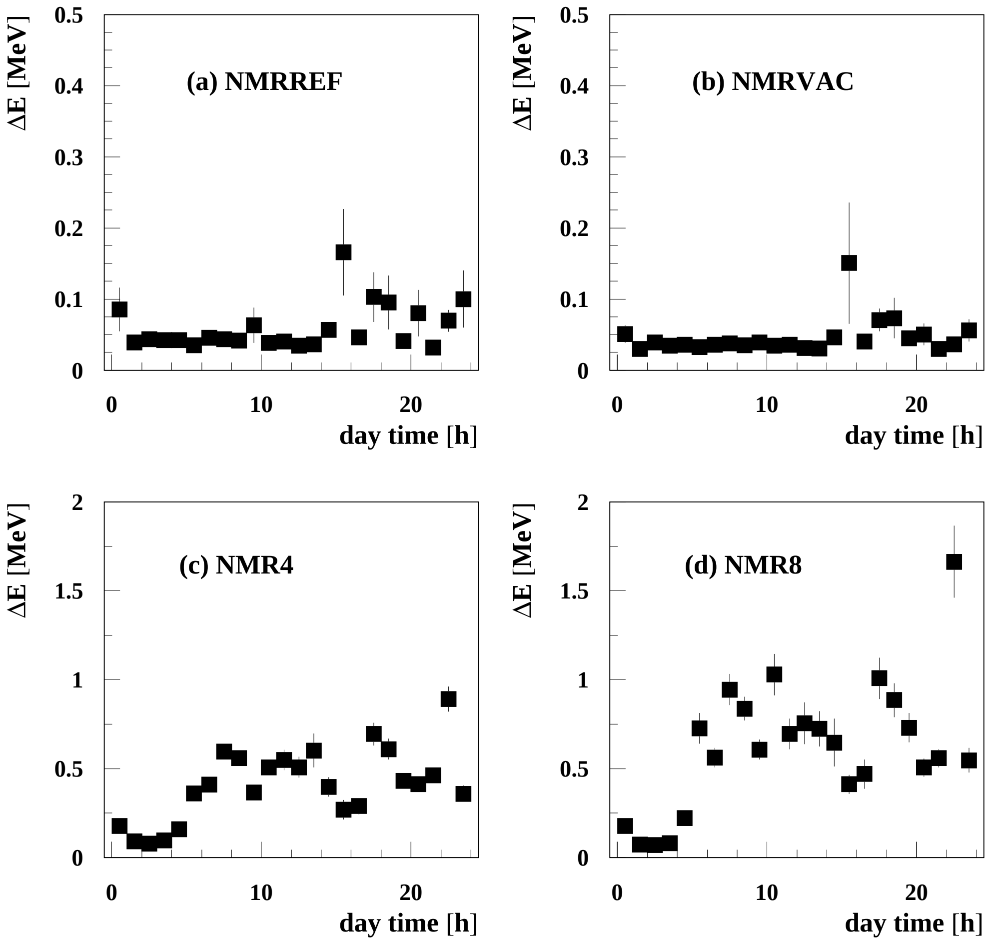

Figure 5.7: *Average variation of the absolute value of two consecutive magnetic field readings as a function of the day time for all NMR probes (in units of equivalent beam energy).* ΔE *is the absolute value of the difference between two readings. The errors of the mean are displayed for every bin. The first 4 bins correspond to the quiet period. Note the different scales in the top and bottom plots.*

The factor -1.7 agrees well with the slope obtained from Fig. 5.8, which is not sign sensitive. The anti-correlation is confirmed with flux loop measurements [53].

No equivalent short term behaviour is observed for the reference magnet. Jumps, as demonstrated in Fig. 5.2, occur rarely. In cases where jumps are recorded for all probes it is considered to be due to current spikes in the main bending power converter. Fig. 5.10 presents a fill, where such a coincident jump in all NMR probes occurs. NMRREF records a jump of 6 MeV while NMRVAC records a 2 MeV level change.

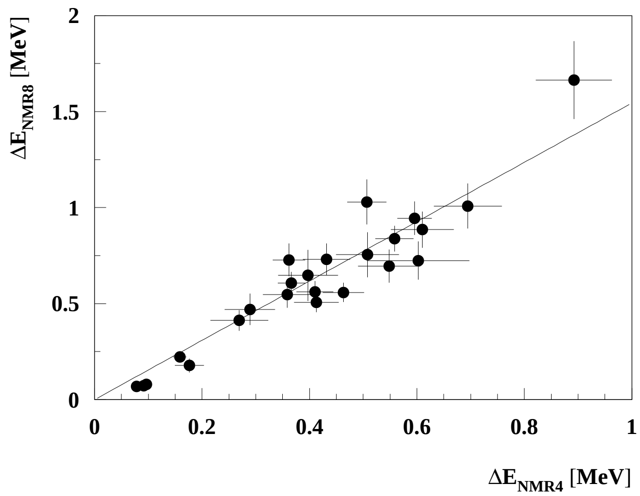

Figure 5.8: *Correlation of the day-time structure of NMR4 (Fig. 5.7, (c)) and NMR8 (Fig. 5.7, (d)). Data from the whole scan period is included. The field measurements are converted into units of beam energy. The solid line illustrates the result of a linear fit to the data with the slope* 1.5 ± 0.4.

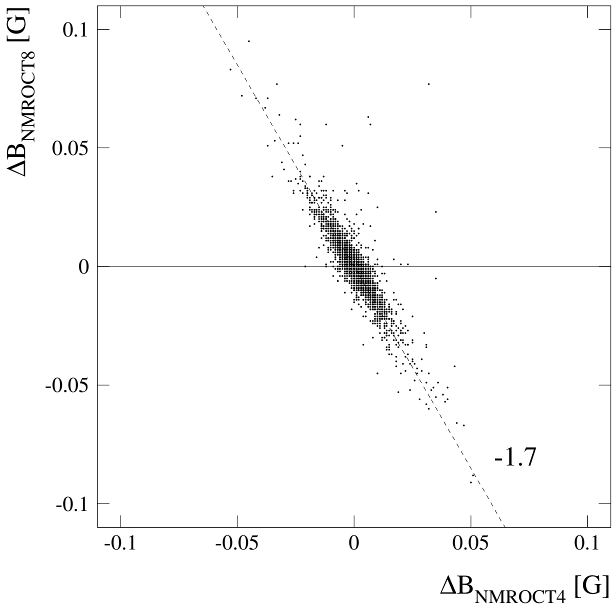

Figure 5.9: *Correlation of the difference* ΔB *of two consecutive readings for NMR4 and NMR8. The data consist of readings from 3 fills. The slope is -1.7.*

The size of the jump recorded by the probe installed inside the vacuum chamber, NMRVAC, is reduced by a factor of about 3 with respect to NMRREF. The reduction of the jump sizes is due to the vacuum chamber surrounding NMRVAC.

5.1.3.3 Long Term Behaviour

On a time scale Δt larger than a few hours the tunnel NMR probes record a rise of the magnetic field regardless of the superimposed perturbation (Fig. 5.6). This pattern can be observed in many fills. Since in 1993 only the reference magnet was equipped with a NMR probe, no data from the magnetic field drifts in the tunnel could be recorded. Field drifts in the reference magnet were observed in 1993 and 1995. Data taken during the 1993 scan from the NMRREF probe and the flip coil installed in the reference magnet are presented in Fig. 5.11. Both instruments record an average drift

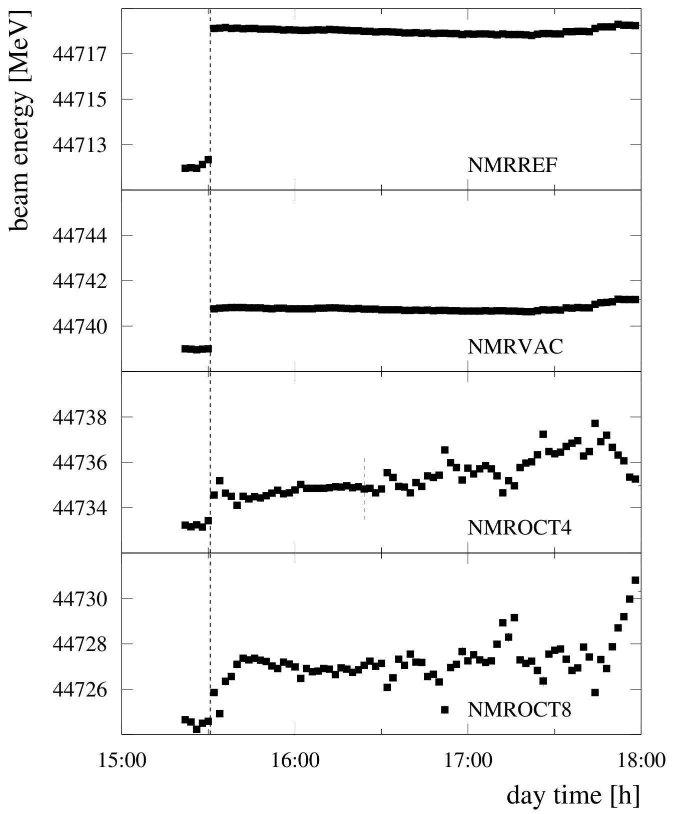

Figure 5.10: *Bending field in units of equivalent beam energy in fill 2856 as a function of day time. The coincident jump happens around 15h30 during the afternoon. The level change seen by NMRVAC is reduced by a factor of 3 compared with NMRREF.*

of about 1.5 MeV after 14 hours. Averaged recordings from the tunnel magnets are

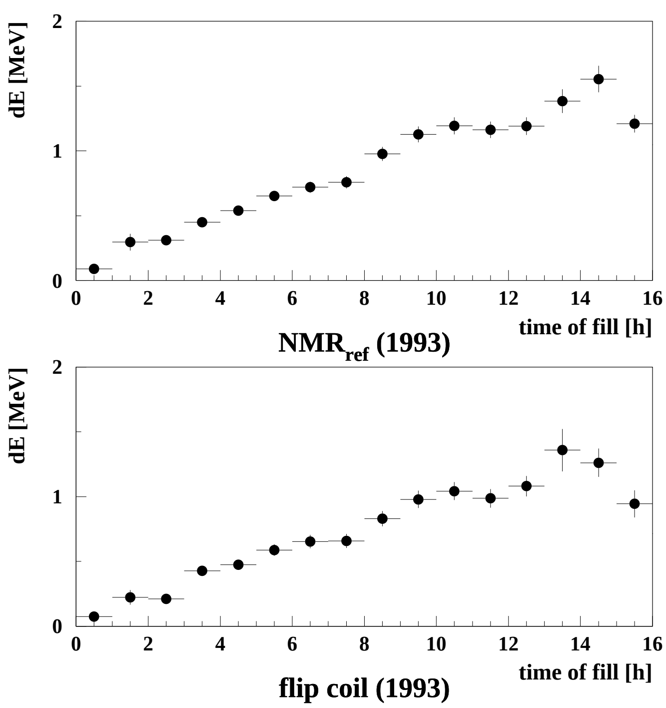

Figure 5.11: *Beam energy changes with respect to the start value as a function of the time in fill. Top: Averaged data recorded by the NMR-REF probe during the 93 scan. Bottom: Averaged data recorded by the flip coil during the 93 scan. Error bars correspond to the error of the mean in every bin.*

presented in figure 5.12, together with the data from the NMRREF and NMRVAC probes. The data taken during the 95 scan were divided into two samples with and without bending modulation at the beginning of the fill. The start time of a fill was considered to be the time the ramp to the final energy is terminated, while for a fill with bending modulation it was the time the conditioning of the magnets is finished. In figure 5.12 the results for the two data samples are superimposed. Consistently with

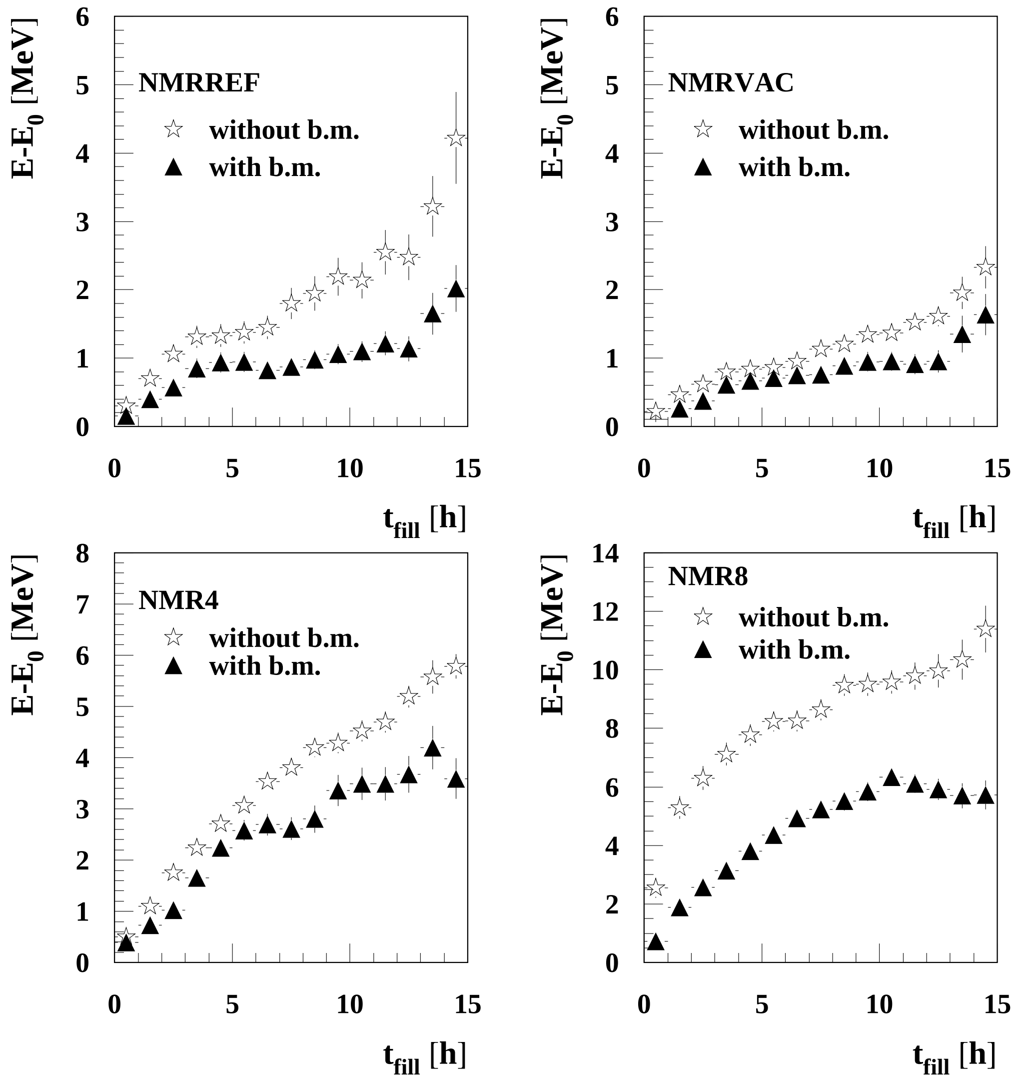

Figure 5.12: *Variation of the B field (in units of beam energy) for fills with and without* **b***ending* **m***odulation (b.m.) as a function of time after the ramp to the final energy and the time after the realisation of a bending modulation respectively. E_0 denotes the initial beam energy.*

1993 NMRREF and NMRVAC show an increase of the energy by $\simeq 0.2$ MeV/hour if no bending modulation is applied. The bending modulation considerably reduces this rise. The NMR probes in the tunnel observe a larger rise than those in the reference magnet. It is different for both probes and amounts roughly 0.5 MeV/hour and 1 MeV/hour for NMR4 and NMR8, respectively. Introducing bending modulations again reduces the increase. However, a significant rise remains. For NMR4 it is reduced by roughly 30% while for NMR8 is is reduced to 50%. The time dependence is also different for both magnets. Without bending modulation the field rise seen by NMR4 does not

selected data	NMRREF [MeV/h]	NMRVAC [MeV/h]	NMR4 [MeV/h]	NMR8 [MeV/h]
all	0.20 ± 0.03	0.13 ± 0.02	0.37 ± 0.04	0.74 ± 0.08
00:00-04:00	0.11 ± 0.02	0.09 ± 0.01	0.17 ± 0.03	0.03 ± 0.02
without b.m.	0.32 ± 0.04	0.08 ± 0.01	0.42 ± 0.05	0.91 ± 0.14
with b.m.	0.08 ± 0.03	0.01 ± 0.01	0.30 ± 0.06	0.49 ± 0.08
P-2	0.14 ± 0.02	0.11 ± 0.01	0.29 ± 0.08	0.70 ± 0.16
P	0.20 ± 0.02	0.15 ± 0.02	0.44 ± 0.09	0.75 ± 0.17
P+2	0.19 ± 0.05	0.14 ± 0.03	0.40 ± 0.06	0.71 ± 0.15

Table 5.3: *Mean of the average B-field rise measured by the four NMR probes during the 1995 energy scan. The error is the statistical error of the mean.*

saturate after 15 hours of a fill and the magnetic field increases more or less linearly up to about 6 MeV. The same magnet tends to saturate slightly after 15 hours in a fill if it was conditioned at the beginning. The rise during the first few hours is again linear. NMR8 saturates in both cases after a rise of about 10 hours up to approximately 6 MeV and 10 MeV respectively. The drift behaviour in the first hours cannot be described by a linear approximation and it is significantly different in the two octants. The bending modulation, as it was applied in 1995, is not sufficient to suppress the drifts in the tunnel magnets efficiently. Table 5.3 summarises the results for data subsamples selected with different criteria:

- **all**
  All fills from the scan period 95 are selected without cuts. Drifts are small in the reference magnet and a factor of 2 respectively 4 larger in the two tunnel magnets. The ratio between the drifts seen by NMR4 and NMR8 is about 2.

- **00:00-04:00**
  Only data from the "quiet period" between midnight and 04:00 are taken into account. Residual drifts ($\simeq$ 50 % of the "all"-data values) are measured in the reference magnet and the tunnel magnet M418. The drift vanishes at NMR8 only. The drifts in the reference magnet are consistent with the drift measured in 1993 (see figure 5.11).

- **without/with bending modulation (b.m.)**
  Fills with and without magnet conditioning at the beginning, as shown in Fig. 5.12, are selected. The mean rise in the magnetic field is always larger for

fills without bending modulation than for fills which started with bending modulation. With bending modulation the drift vanishes in the reference magnet and is reduced by about 30% and 50% in the tunnel magnets.

- **P-2, P, P+2**
  All fills at one energy point are averaged including all fills with and without bending modulations. The rise is slightly larger at the Peak setting because most of these fills were made at the beginning of the scan period before bending modulation became a standard procedure. NMR4 sees a slightly smaller mean rise at "P-2" energy setting rather than at "P+2", but these deviations are not significant.

5.1.4 Train Leakage Currents

Investigations to understand the behaviour of the NMRs installed in the LEP tunnel showed that a current of up to a few amperes was circulating on the vacuum chamber and on all parallel conductors in LEP as for instance the ground cable, which is installed along the vacuum chamber and connected to earth at the 8 IPs. The origin of these currents [68] is in fact a well-known problem of DC railroads [69]. In principle, the current supplied by the power stations to the locomotive should return to the power stations via the railroad tracks. In fact, a certain fraction of this current (up to 25 %) leaks into the ground and flows back to the generator along other "roads". The currents affecting LEP are mainly due to the railroad line between Geneva and Bellegarde which is powered with DC voltage (1500 V). The Swiss CFF[2] lines, using 15000 V AC, do not contribute for two reasons: (i) For the same electrical power the DC line requires 10 times higher currents. (ii) The diffusion depth into the earth of DC leakage currents is large while AC leaks are confined around their source [70]. In the case of LEP, some of

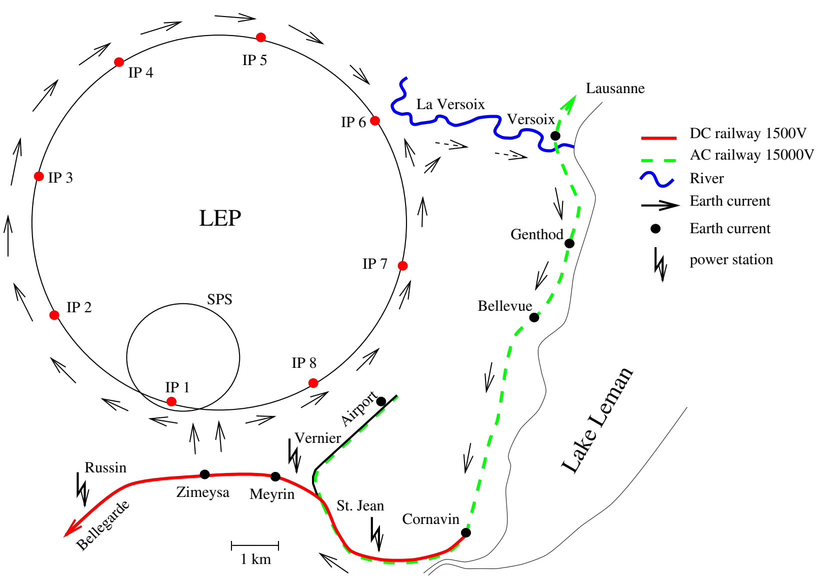

Figure 5.13: *Schematic View of LEP with the 8 interaction points and the railroads in the Geneva area. The arrows indicate the direction of the current flowing in the LEP environment and along the vacuum chamber in the tunnel.*

[2]Swiss railroad company: Chemin de Fer Fédéraux

the return currents from trains passing on that railroad line flow back to the generator via the "good conductors" installed in LEP: the ground cable, the vacuum chamber and the metallic struts in the concrete of the tunnel wall itself. Fig. 5.13 illustrates the way of the current flow in the LEP environment and along the beam pipe. In a

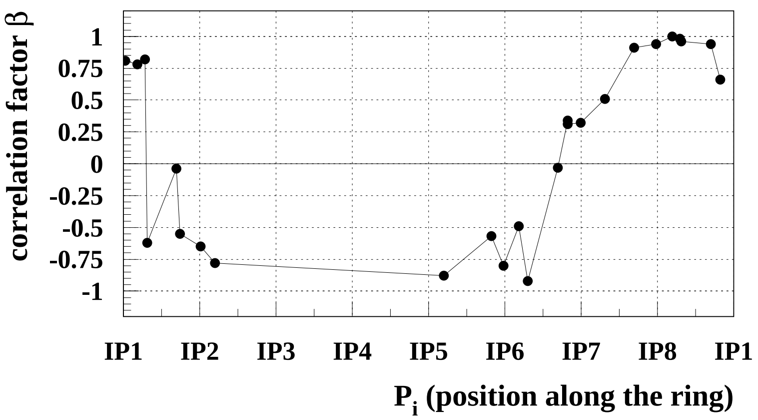

Figure 5.14: *The correlation factor β of the leakage currents with respect to the position of NMR8 as a function of the position along the ring P_i.*

dedicated experiment the current flow was measured simultaneously close to NMR8 and at 25 positions along the ring. The duration of the data acquisition at the various positions was about 3 hours. For each position P_i the recorded current flow $I(P_i)$ and the simultaneously measured flow at the reference position $I(P_{NMR8})$ was analysed. The correlation factor β at a certain position P_i along the ring was calculated such that:

$$I(P_i) = \beta(P_i) \cdot I(P_{NMR8}) \qquad . \tag{5.2}$$

At the reference position P_{NMR8} β is equal to 1 by definition. Fig. 5.14 presents the results of the correlation measurements. The correlation factor changes sign around the injection lines (i.e. close to IP1) and the interaction point IP6. This indicates that the leakage currents enter and leave the LEP ring through the transfer lines from the SPS around IP1 and over a relatively large zone around IP6. A controlled experiment was performed during the LEP high energy run after the 95 scan period to confirm the effect of the train leakage currents. The potential difference between rails and ground, the voltage on the vacuum chamber and the magnetic field in the tunnel were measured simultaneously. A typical result over 15 minutes is shown in figure 5.15 during a busy afternoon when a "TGV" type train is passing. The correlation between the three quantities is evident. The understanding of the perturbation mechanism of the Train Effect is the following: A current circulating on the vacuum chamber produces B-field lines which are transverse to the beam pipe. The field lines are trapped by the iron yoke of the bending magnet because of its high permeability. The transverse field depends on the current profile (i.e. evolution with time and amplitude height) on the vacuum chamber. The **short term** fluctuation of the magnetic field is explained by a superposition of the transverse field produced by the leakage currents and the nominal LEP dipole field. At least a part of the **long term** behaviour can be modelled

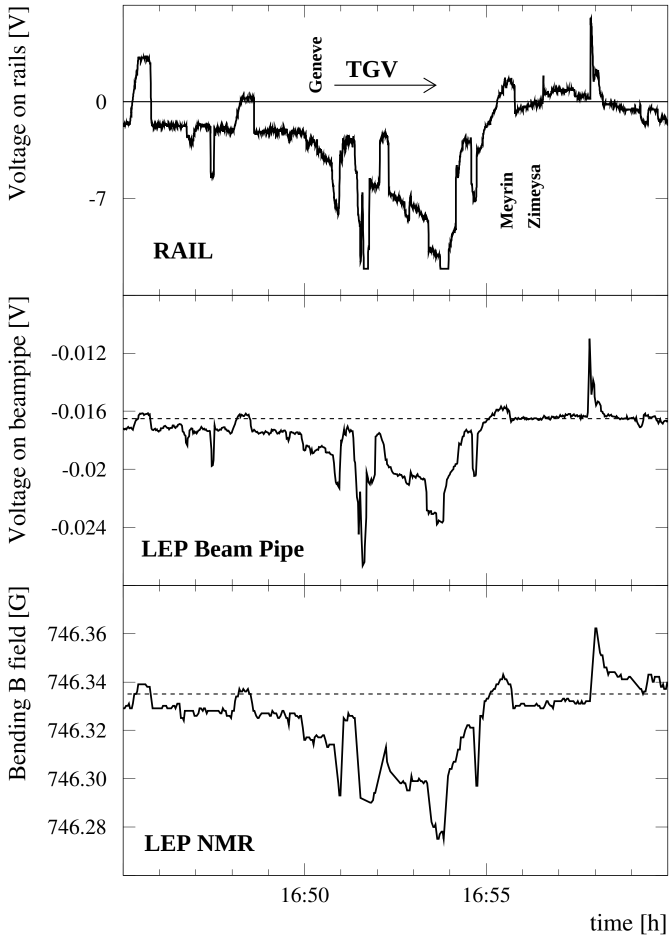

Figure 5.15: *The potential difference between the rails and a reference ground were measured simultaneously with the magnetic field in the tunnel and the voltage on the vacuum chamber for 15 minutes during a "busy" afternoon. The figure is taken from [53].*

with nonlinear effects of the iron hysteresis. The same effect is used for the successful application of the bending modulation procedure. Thus the train leakage currents explain several features of the magnetic field at the same time. The approach based on the train leakage currents will later be referred to as the **Train Effect**.

- **Quiet Period**
  The observed quiet periods between 00:00 and 04:00 correspond to a time window, where no DC trains circulate.

- **Short Term Behaviour**
  The short term fluctuations of the magnetic field are explained by a superposition of the train leakage currents and the LEP dipole field. The anti-correlation of the fluctuations is due to the fact that the sign of the current is opposite in the two parts of LEP (relative to the direction of the main bending current) where the NMR probes are located. At IP1 the CERN injectors seem to catch the train leakage currents and propagate it in the LEP tunnel. Leakage currents circulate clockwise from IP1 via NMR4 towards IP6 and counterclockwise in the other branch. There, between IP6 and IP7, the Versoix river presumably provides a

good local ground conductivity and the leakage current circuit is closed by the CFF line Geneva-Lausanne. Thus LEP is separated into two branches with a length ratio of 5/3. These two parts behave like a parallel resistor system [68], which explains the amplitude ratio of $1.7 \simeq 5/3$ between the field fluctuations seen in NMR4 and NMR8. The anti-correlated short term fluctuations are not supposed to affect the average beam energy since the current integrated over the two branches cancels.

- **Long Term Behaviour**
  The saturation of the magnetic field rise with the number of excitation cycles is the approach to the understanding of the long term field behaviour, which is the most important consequence of the Train Effect on the beam energy. This consequence is equally valid for the 93 beam energies. The 93 data had to be revised in the light of the new perception, since the Train Effect has not been taken into account at the time of the submission of the 93 final energy values to the experiments. Some part of the total rise in the field is related to the profile and the amplitude of the current flow and the history of the magnets. The Train Effect cannot explain the discrepancy between the NMR4 and NMR8 drift behaviour during the first hours of a fill. Furthermore it is not clear why the conditioning of the magnets could not efficiently prevent the magnetic filed rise. Eventually the simultaneous superposition of the Train Effect and the bending modulation reduced the efficiency of the bending modulation but a further unknown source of drifts might also explain the discrepancy. The behaviour of a magnet, which is continuously affected by small excitation cycles, could not be studied.

Based on the NMR measurements the change of the energy due to the Train Effect can be determined and thus included in the LEP energy model. This implies a parametrisation of the ring bending field as a function of time. The parasitic currents split LEP into two unequal branches of 3/8 and 5/8 of the total length. The splitting suggests a superposition of two NMR probes, i.e. NMR_{48}[3] to obtain a measurement, which is equivalent to the integral magnetic field of the ring:

$$NMR_{ring} \equiv NMR_{48} := \frac{5}{8} \cdot NMR4 + \frac{3}{8} \cdot NMR8 \qquad . \tag{5.3}$$

Eq. 5.3 and its application to the 93 data are based on the following basic assumption: the magnetic field measured by NMR4 and NMR8 is representative for the magnetic field of the 5/8 branch and the 3/8 branch of LEP. The assumption is valid for magnetic field drifts caused by the Train Effect only.

[3] In the following the subscription 48 indicates a superposition of octant 4 and 8.

5.1.5 The Classical Temperature Correction

The magnetic field of a dipole magnet can be affected by environmental effects like the core temperature. Depending on the specific properties of the magnet material, a rise in temperature leads to a lengthening of the magnet and to an increase of the (transverse) gap size. The lengthening of the bending magnets increases the integral field around the ring and therefore causes an increase of the beam energy. The opening of the gap reduces the B-field in the gap and causes thus a decrease in the beam energy. Both effects compensate each other to some extent. Because of the particular construction of the tunnel dipoles (iron-concrete structure instead of the iron-air layers of the reference magnet) further effects can be considered to cause a temperature dependence.

5.1.5.1 The Cooling System during the 93 and 95 Scans

Bending magnets are heating up due to the power dissipation of the coils and the deposition of energy by synchrotron radiation. To anticipate overheating as well as thermal effects on the bending field the dipoles need to be cooled in a controlled way. The LEP cooling system for the dipole magnets is consists of 8 independently regulated cooling circuits for the 8 octants. In each octant four magnet cores are equipped with temperature probes, the water temperature and the supply temperature are monitored. A schematic view of the LEP cooling system is given in Fig. 5.16. While the cooling

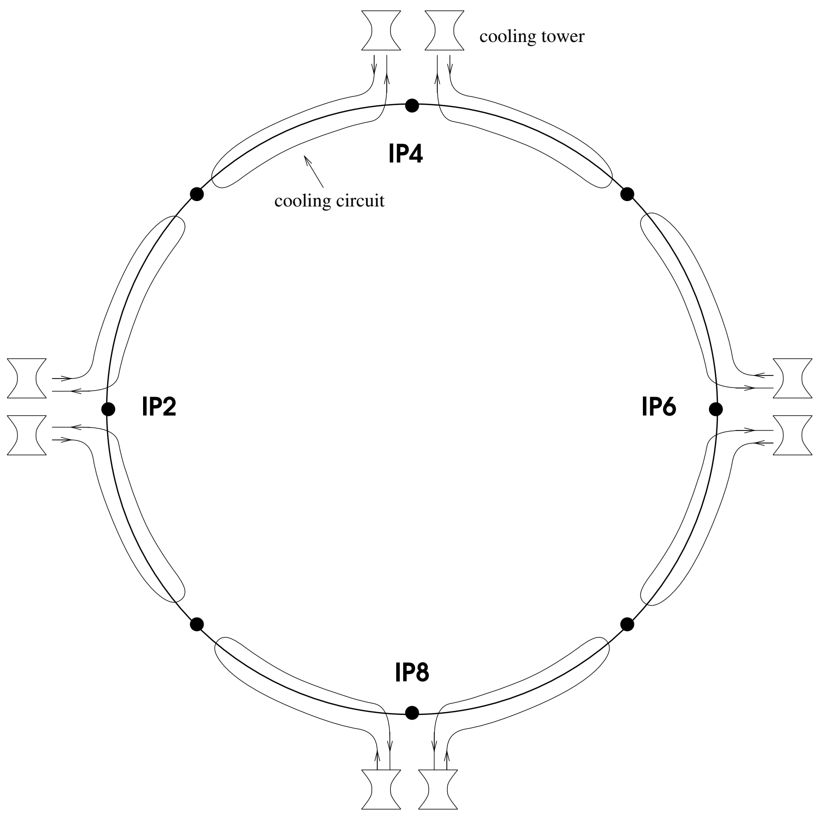

Figure 5.16: *Schematic view of the LEP cooling system. The cooling system is arranged in 8 independent cooling circuits, one per octant. The cooling towers are located at the even IPs.*

regulation during the 93 scan was based on sensors measuring the temperature of the cooling water, the regulation during the 95 scan was based on the temperature probes in the magnet cores. For this reason, the mean temperature as a function of time since the start of a fill is systematically different for the two scan periods. Figure 5.17 presents the averaged core temperature behaviour during the 93 and the 95 scan. The

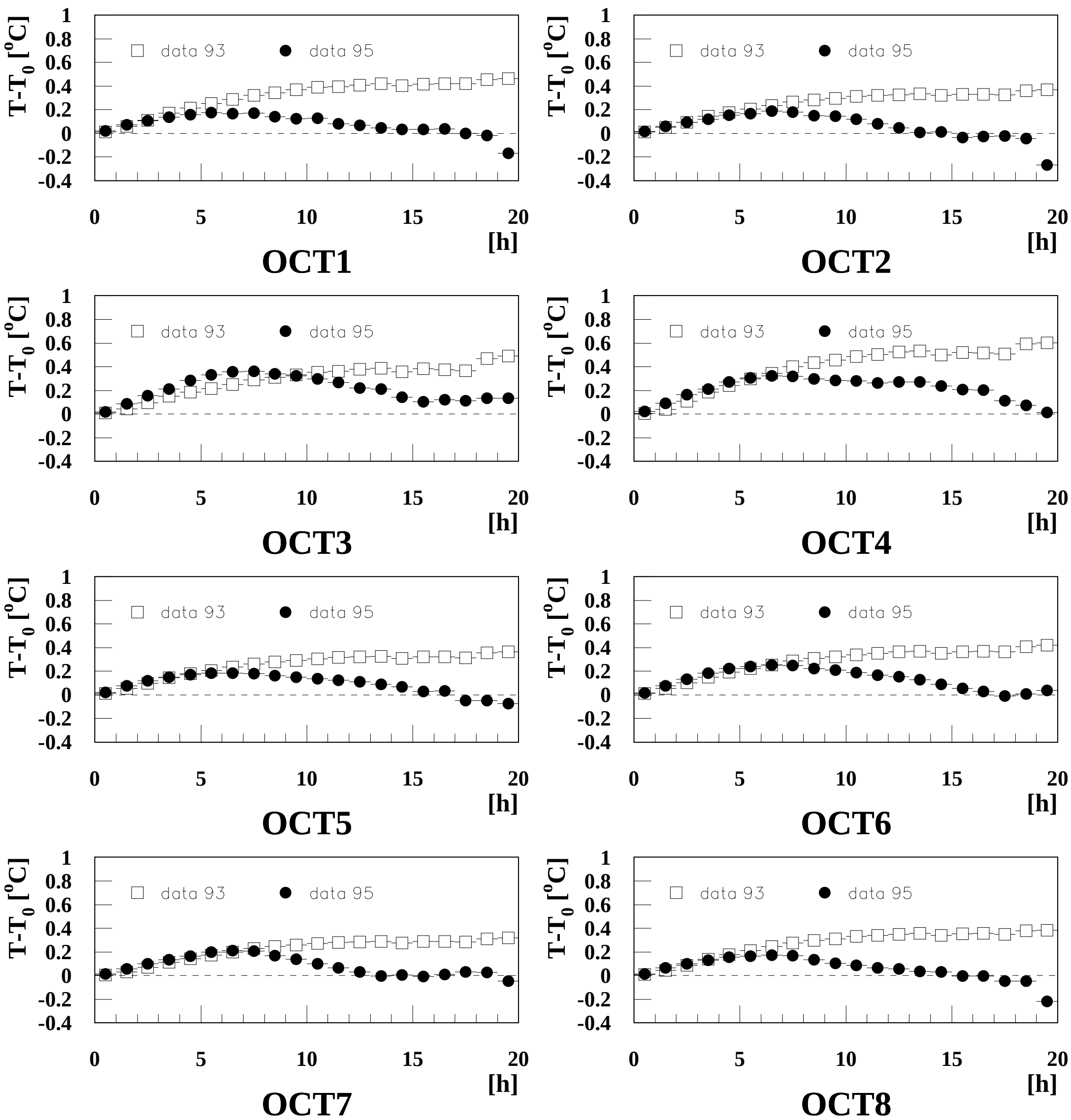

Figure 5.17: *Mean core temperature deviation with respect to the start value T_0 per octant as a function of time in a fill. The calculation of the mean is based on the 4 temperature probes installed in every octant. The temperature evolution per fill is averaged in the two scan periods, corresponding to "data 93" and "data 95". The RMS scatter per bin is smaller than the size of the data points.*

cooling feedback used in the 1993 scan was designed to keep the water temperature stable. Typically in the 93 scan the temperature rises by about 0.5 ^{o}C in a fill followed by a saturation. The octant to octant variations are small. The cooling feedback was changed between the 93 and the 95 scan to keep the magnet core temperatures as stable as possible. On average the mean temperatures rises during the first 6 to 7 hours in a fill and decreases again later. After about 15 hours it was stabilised around the start value. Due to the initial increase and the later decrease, the total temperature variation in 95 fills is larger than in 93 fills. The maximum excursion (OCT3 and OCT4) is about 0.4 ^{o}C, whereas the typical rise in the other octants is about 0.2 ^{o}C. Neither regulation of the cooling system could maintain the core temperatures stable for all magnets.

5.1.5.2 Classical Temperature Coefficients

The effect of a temperature change on the magnetic field or the beam energy can be described by a "classical" approach, where the temperature coefficient C_{T_c} is defined as:

$$C_{T_c} = \frac{1}{E}\frac{\Delta E}{\Delta T} = \frac{1}{\int Bdl}\frac{\Delta(\int Bdl)}{\Delta T} \qquad , \tag{5.4}$$

where T is the temperature of the magnet core and E the nominal energy given by the integral dipole field.

For the **reference magnet**, which is not filled with concrete, one assumes that the expansion temperature coefficient ($+1.5\ 10^{-5}$) is given by the elongation/expansion coefficient of the yoke steel. The magnetic field temperature coefficient for the expansion of the gap has the opposite sign and the same size ($-1.5\ 10^{-5}$). To first order the field integral $\int Bdl$ remains unaffected by the temperature. The NMR probes located in the gap of the reference magnet measure the local B-field which varies with the gap size. Therefore all B-field measurements from the reference magnet NMR probes have to be corrected with a temperature coefficient of $-1.5\ 10^{-5}$ to correct for the gap change.

The magnetic characteristics of 12 **LEP dipole magnets** were measured in 1991 in a laboratory setup. Table 5.4 shows the various coefficients derived from the tests with the 12 dipoles. The errors on the coefficients are obtained from the RMS scatter of the dipole sample. $C_{T,gap}$ denotes the measured transverse expansion coefficient of the gap, $C_{T,length}$ the longitudinal expansion coefficient, $C_{T,dipole}$ the temperature coefficient of the magnetic field in the centre of the dipole and $C_{T,beam}$ the estimated beam energy temperature coefficient. $C_{T,beam}$ has to be applied to the NMR readings to obtain a field measurement, which is representative for the integral bending field seen by the beam. The measurements [31] show that large B-field changes with temperature can not be explained by the longitudinal and transverse expansion of the material. The large value of $C_{T,dipole}$ can be explained [71] by the variation of the mortar induced stresses, which occur if the thermal expansion coefficient of mortar is different from that of steel. For the specific mortar used in the LEP dipole cores the expansion coefficient is most likely much larger than for regular concrete and larger than the coefficient of steel [71].

	mean value $[10^{-4}/^oC]$	RMS $[10^{-4}/^oC]$	remark
$C_{T,gap}$	0.11	0.03	gap size effect
$C_{T,length}$	0.13	0.01	elongation effect
$C_{T,dipole}$	1.20	0.25	field in the centre of the dipole
$C_{T,beam}$	1.28	0.25	estimated $C_{T,beam} = C_{T,dipole} + 0.63\ C_{T,length}$

Table 5.4: *Details of the different components of the dipole temperature coefficient. These results were obtained in laboratory measurements in 1991 with 12 LEP dipole cores.*

A correlation between flux loop measurements [72] and the measured temperature was clearly demonstrated by a controlled experiment in 1991. A temperature correction to the flux loop measurements of $1.01 \pm 0.25\ 10^{-4}$ per ^oC was obtained at 45 GeV. To compare this result with the other measurements it has to be corrected for the change of the flux loop surface and 63 % of the longitudinal expansion of the magnets. This leads to a **temperature coefficient of the ring** $C_{T,Ring} = 0.79 \pm 0.25\ 10^{-4}$. In 1993, the ring temperature coefficient was extracted from three dedicated resonant depolarisation experiments with the result [52]:

$$C_{T,Ring} = (1.07 \pm 0.3) \cdot 10^{-4} \qquad , \tag{5.5}$$

The coefficient was evaluated from the first two temperature experiments only, since the third experiment was excluded from the 1993 analysis. The value from 5.5 has been used for the analysis of the 1993 data in [33] and in [52]. Figure 5.18 shows the two experiments in fill 1636 (left) and 1734 (right). This result is in good agreement with the laboratory measurements in 1991. In the third experiment the measured temperature coefficient reached $2.5\ 10^{-4}$ with a good correlation between energy and temperature. However, when the beam energy measurements were corrected with the coefficient obtained from the first two experiments, the time evolution of the beam energy for this experiments became flat apart from two sudden jumps (Fig. 5.1). Since this experiment was the only evidence in 1993 for sudden jumps in the energy evolution and a possible explanation for the origin was unknown, it was not used to compute the average temperature coefficient for the ring. Today the data from the third experiment may be interpreted to be the evidence of two jumps due to the Train Effect.

5.1.5.3 Limits of the Classical Approach

To disentangle the effect of temperature from the Train Effect in 1995, only data from the quiet period (00:00 - 04:00) have been selected to extract the field derivative $\Delta B/\Delta T$. To improve the quality, it was requested that data were available for the

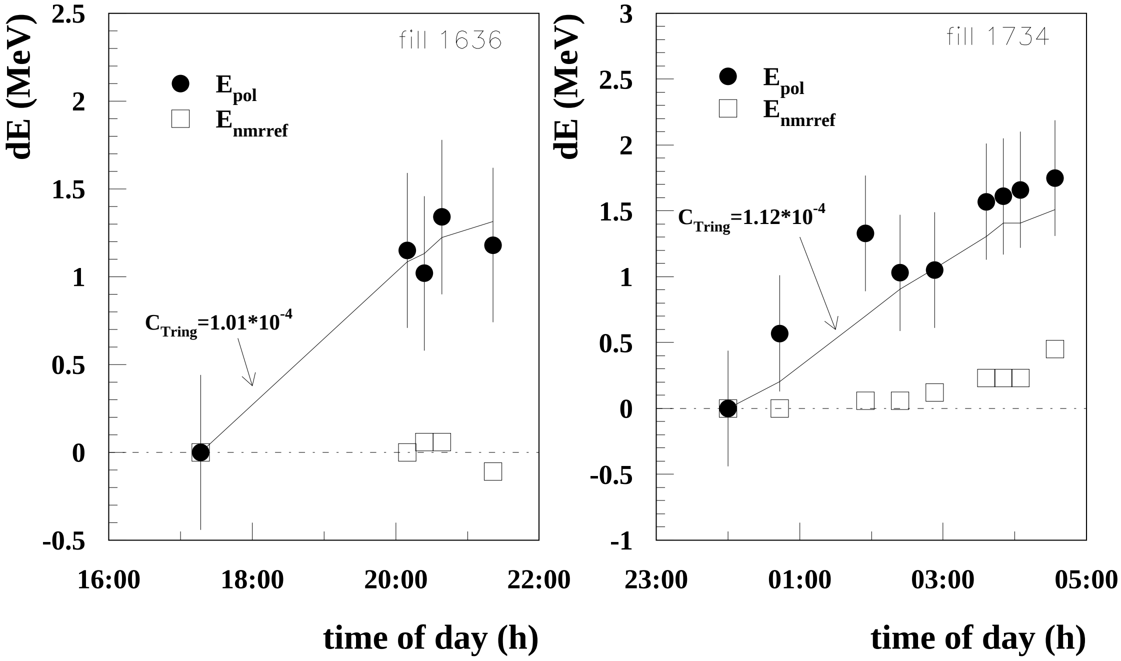

Figure 5.18: *Energy measurements with respect to the first successful calibration as a function of day time. Readings from the NMRREF probe are superimposed. The solid line corresponds to the prediction of a temperature model according to Eq. 5.4, which was constrained to be zero at the time of the first energy measurement. The coefficients are obtained from a fit to the data. In both plots the model prediction is constrained to be zero at the time of the first measurement.*

whole 4 hour period and a temperature difference of $\Delta T \leq -0.3^oC$ or $\Delta T \geq 0.4^oC$. The requirements are not necessarily fulfilled for both tunnel probes in the same fill since the temperature control systems for the octants are independent. After the cuts 7 fills were left to extract $\Delta B/\Delta T$ at NMR4 and 5 fills to extract it at NMR8. Figure 5.19 shows the fit results for both probes as a function of the fill number together with the mean (solid line) of all results. In average a value of $\Delta B/\Delta T \simeq 4.6$ MeV/^oC with a scatter of 2.1 MeV/^oC for NMR4 and a value of 2.2 MeV/^oC with a scatter of 1.4 MeV/^oC for NMR8 was obtained. This leads to the following coefficients of the particular magnets:

$$C_{T_c}^{M418} = 1.0 \pm 0.5 \cdot 10^{-4} \; /^oC$$
$$C_{T_c}^{M818} = 0.5 \pm 0.5 \cdot 10^{-4} \; /^oC.$$

The data seemed to prefer different coefficients for $\Delta T > 0$ and $\Delta T < 0$ [73]. However, taking into account the large scatter and the limited data sample the different trends were not significant. Later dedicated measurements of the variation of the magnetic

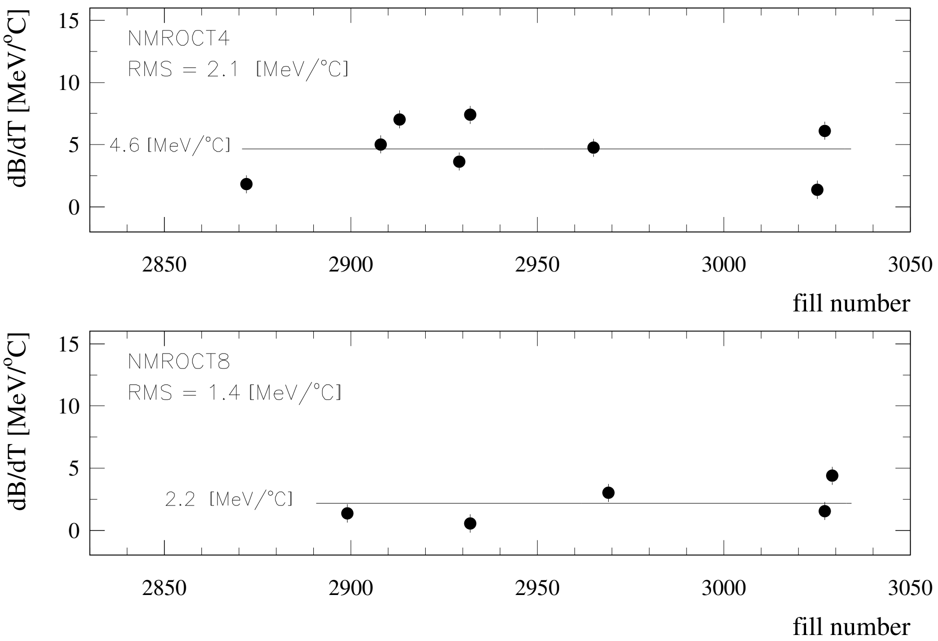

Figure 5.19: *$\Delta B/\Delta T$ at NMR4 and NMR8 respectively as a function of the fill number. Errors are estimated. The solid line corresponds to the unweighted mean.*

field with temperature during the operation of LEP after the scan without circulating beams lead to temperature coefficients covering a wide range of values:

$$0.2 \cdot 10^{-4} \leq C_{T_c}^{M418} \leq 1.4 \cdot 10^{-4} \,,$$
$$0.1 \cdot 10^{-4} \leq C_{T_c}^{M818} \leq 0.8 \cdot 10^{-4}.$$

The results are spread over roughly one order of magnitude for the same magnet. The large scatter and the inconsistency between negative and positive temperature variations cast some doubts whether this method can be used to compute the temperature coefficient of the particular magnets. They rather indicate that either the coefficient might have varied with time, that other unknown sources for magnetic field variations perturb the measurements of the temperature coefficient or that the measured temperature does not represent the temperature of the whole magnet core. Another possible explanation is that the simple approach of Eq. 5.4 does not parametrise the variation of the magnetic field with temperature and probably more parameters are needed.

5.1.6 Further Studies of the Temperature Influence

Motivated by the obvious limits of the classical parametrisation and due to the fact, that the average temperature variation in the tunnel in standard operation cycles did not exceed 0.4^o C, a magnet test bench was established 1996 in a laboratory. A standard LEP bending dipole was equipped with field and temperature monitoring devices. A total of 16 temperature sensors were installed in the test magnet, equally distributed in 3 rows along the longitudinal axis (s). A NMR probe was mounted such that its position along the longitudinal (s) and along the horizontal axis (x) could be varied. A controllable cooling circuit and water temperature sensors were installed. Electronic readout devices and a computer allowed to monitor and save all parameters continuously. In a long term experiment at Sep. 6th, 1996, the dipole was heated and cooled several times. Fig. 5.20 depicts the magnetic field, the core and the water temperature as a function of time during this experiment. During the experiment the magnet was degaussed 4 times, indicated by dashed vertical lines in Fig. 5.20. Degaussing includes 5 cycles of the magnet current from +300 A to +2900 A. It is a standard procedure at LEP between two fills. In the 5 cycles (marked with (I) to (V)), which lasted up to 52 hours, the core temperature was varied by controlling the water temperature. The water temperature was changed by up to 20^oC in order to force large changes of the core temperature. It turned out that the initial temperature, the minimal and maximal temperature of the core as well as the water temperature influence the magnetic field. The following parametrisation for the drift of the magnetic field $B(t)$ caused by temperature changes could be extracted from the experiment [74]:

$$\begin{aligned} B_{Tmod}(t) &= B_0 \times [1 + C_{T_0} \cdot T_i + C_{T_{max}} \cdot (T_{max}(t) - T_i) \\ &\quad + C_{T_{min}} \cdot (T_{min}(t) - T_i) + C_T \cdot (T_c(t) - T_i) \\ &\quad + C_{T_w} \cdot (T_w(t) - T(t))] \qquad . \end{aligned} \tag{5.6}$$

The various terms correspond to:

- A constant nominal field B_0 is assigned to a certain excitation current.
- T_i is the initial temperature at the start of the operation cycle $t = 0$. While the other terms control the magnetic field variations throughout a fill, the first term affects only fill to fill variations, which are caused by temperature changes.
- $T_{max}(t)$ is the maximum temperature at time t. For a monotonic increasing field it corresponds to the core temperature. In fills, where initially the temperature rises, the term $T_{max} - T_i$ stays constant if the temperature decreases again. It is the main contribution in the new parametrisation.
- $T_{min}(t)$ is the minimum temperature of a fill. When the temperature is increasing monotonically, it is equal to the initial temperature. Unless the core temperature falls below the initial temperature T_i, the term $T_{min} - T_i$ does not contribute.

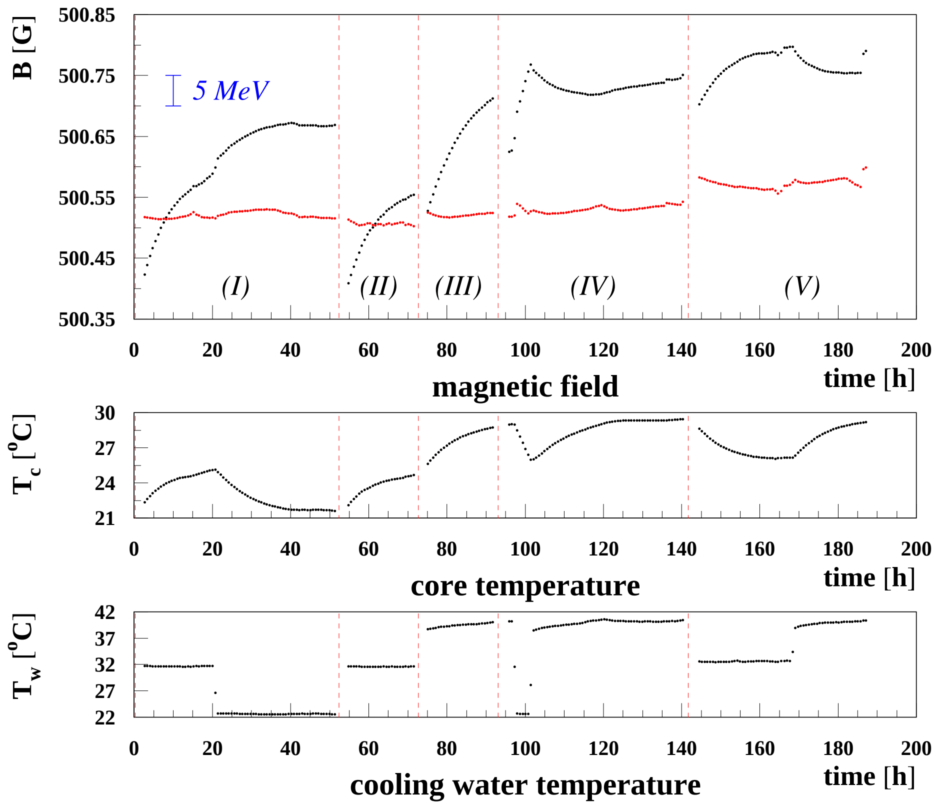

Figure 5.20: *Uncorrected and corrected magnetic field (top), core temperature (centre) and water temperature (bottom) as a function of time during the long term temperature experiment at Sep. 10th, 1996. The vertical dashed lines indicate the degaussing of the magnet. The figure is taken from [74].*

- $T_c(t)$ is the temperature of the magnet core during the fill. Due to the negative sign of the coefficient, the term $T_c(t) - T_i$ reduces the contribution of the second term for increasing core temperatures. Once the temperature during a fill decreases again, this effect diminishes. If $T_c(t) < T_i$, it amplifies the effect of the second term.
- $T_w(t)$ is the temperature of the cooling water. Due to a relatively constant water temperature and a small coefficient, this term is usually negligible for physics fills.

If the core temperature increases monotonically from the start of the fill (like in 1993), the sum of the two terms $C_{T_{max}} \cdot (T_{max}(t) - T_i) + C_T \cdot (T_c(t) - T_i)$ is equivalent to the classical temperature coefficient as defined in Eq. 5.4. The main difference between the effect of the classical approach on one hand and the new approach on the other hand is the prediction of a B-field increase while the temperature is decreasing. The five coefficients were adjusted [74] to describe the magnetic field evolution during a fill. The coefficients are listed in Tab. 5.5. The “effective coefficient” for an increasing temperature is then:

$$C_T^{eff} = C_{T_{max}} + C_T \simeq 12 \cdot 10^{-5} \qquad . \tag{5.7}$$

This coefficient in the new parametrisation is in good agreement with the coefficients listed in Tab. 5.4 and the result obtained from fits to 1993 data given in Eq. 5.5.

	C_{T_0}	$C_{T_{max}}$	$C_{T_{min}}$	C_T	C_{T_w}
$\cdot 10^{-5}/^oC$	6.4	15	-5	-3.3	-0.4

Table 5.5: *The coefficients for the new temperature parametrisation as they result from the long term experiment at Sep. 10th, 1996.*

Based on the new parametrisation the contribution of the various terms to the change of the beam energy were derived from temperature data stored in the LEP logging database during the 95 scan. The contributions are calculated separately for each term in Eq. 5.7 and converted into beam energy units at 45 GeV. Fig. 5.21 presents the energy change of each individual term as a function of the time in a fill at NMR4 and NMR8. According to the new parametrisation NMR8 is less affected by temperature effects than NMR4. In both octants the $C_{T_{max}}$-term dominates the temperature-induced rise. The C_T-term contributes about 15% only. Looking at the 93 data, the contribution from $(T_{min}(t) - T_i)$ is negligible since the temperature variations are always upwards during a fill. The cooling system 93 was designed to keep the water temperature constant. The water temperature contribution vanishes with the small coefficient.

Only the contributions arising from the $C_{T_{max}}$- and C_T-terms are large enough to be potentially obtained from the tunnel data directly. However, with the 1995 data sample alone the two temperature coefficients cannot be derived reliably, since the core temperature variations during fills are too small. In 1996, during the LEP high energy runs at centre-of-mass energies of 161 GeV and 172 GeV, the core temperature was always increasing. Typical rises of about 1.5^oC - 2^oC, which are caused by the high magnet excitation current and the deposition of synchrotron radiation, allow a reliable determination of the **effective temperature coefficient**. Since no temperature decrease occured during 1996 fills, the effect of $C_{T_{max}}$ and C_T cannot be disentangled. The following results for C_T^{eff} are derived from the high energy data [75]:

$$\text{OCT4: } C_T^{eff} = (14 \pm 5) \cdot 10^{-5}/^oC$$

$$\text{OCT8: } C_T^{eff} = (9 \pm 5) \cdot 10^{-5}/^oC$$

$$\text{ring: } C_T^{eff} = (9.5 \pm 2.5) \cdot 10^{-5}/^oC$$

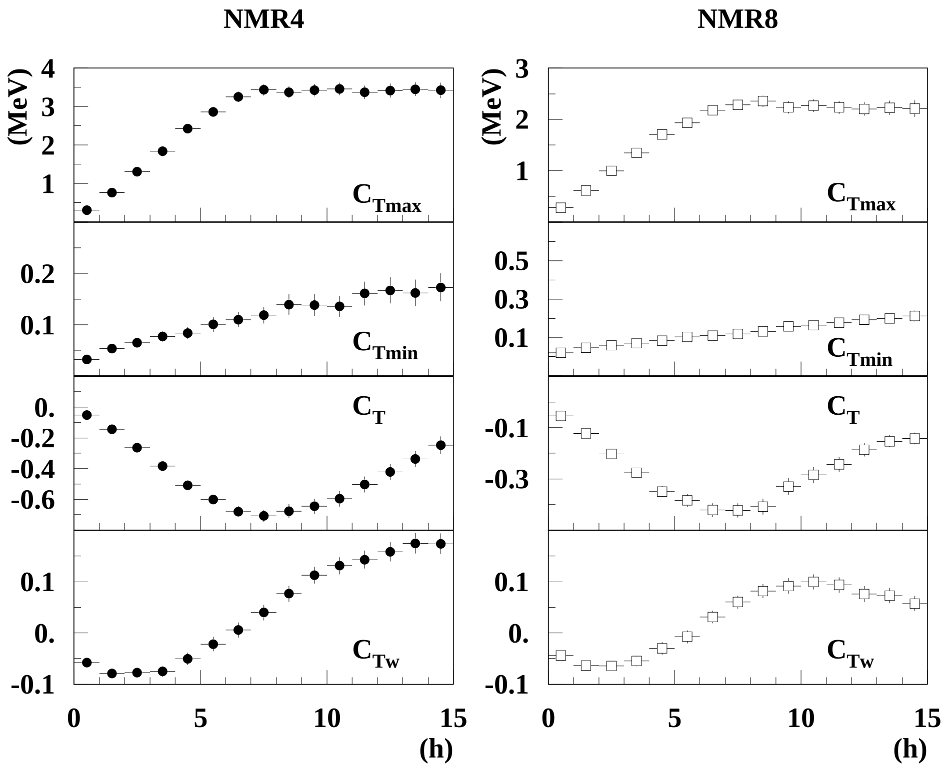

Figure 5.21: *The average contribution for the coefficients of the new parameterisation as a function of time. The contribution is calculated from the core and water temperature readings at NMR4 and NMR8 respectively during the 1995 energy scan. Errors correspond to the RMS scatter.*

The coefficients obtained from fits to the 1996 data agree reasonably well with the values determined from the test experiment in the laboratory (Tab. 5.5) and with the ring temperature coefficient obtained in 1993 (Eq. 5.5).

The **initial coefficient** C_{T_0} for the two tunnel magnets can be derived with a limited accuracy from 1995 NMR4 and NMR8 data. At each energy setting separately the field at the start of a fill was fitted as a function of the initial temperature. Fig. 5.22 shows the results for the two tunnel probes. The NMR4 and NMR8 readings are corrected for various known effects as for instance the effect of the magnet conditioning at the beginning of a fill. The data points and the fit results of the NMR8 readings scatter much more than the NMR4 readings and results. This can be explained by the different train current perturbation in the two octants, leading to less reliable field readings at NMR8. In fact, the fits to the peak and peak-2 data at NMR8 are meaningless and only the result from the fit to the peak+2 data is relevant. The resulting temperature coefficients are:

NMR4: $C_{T_0} = (10 \pm 1) \cdot 10^{-5}$

NMR8: $C_{T_0} = (6 \pm 2) \cdot 10^{-5}$

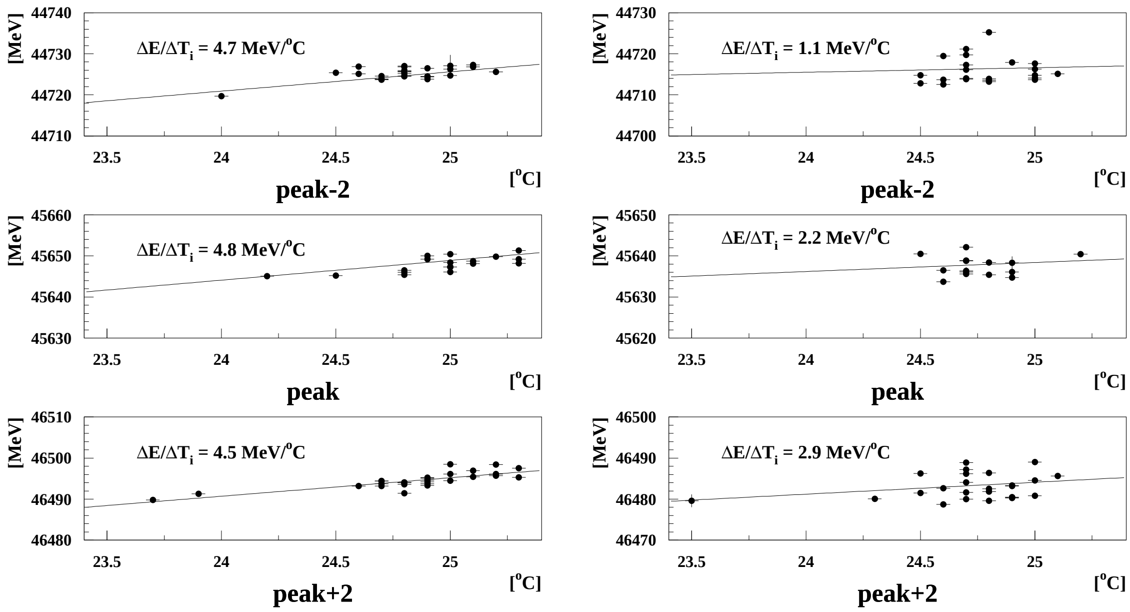

Figure 5.22: *The magnetic field measured by NMR4 and NMR8 at the start of a fill converted into beam energy units as a function of the initial temperature T_i. Error bars correspond to statistical errors only.*

The quoted errors are estimates. Since only C_{T_0} and C_T^{eff} could be extracted directly from data, values for the other coefficients, which are derived from the test experiment, are used for later data analysis.

5.1.6.1 Implications of the new Parametrisation

The prediction for the rise of the beam energy based on the new parametrisation is different for each year. During the 1996 high energy operation of LEP, data from 13 fills around the Z resonance were acquired. None of the 13 fills lasted more than 10 hours. The 1996 peak fills are included into the data analysis since they have simultaneous measurements of the temperature and the magnetic field in the tunnel. Fig. 5.23 shows the energy change prediction for octant 4 and 8 separately as well as for the combination of both and the whole ring. “Ring” denotes an unweighted superposition of all LEP octants, while “octant 48” corresponds to the weighted combination of octant 4 and 8 according to Eq. 5.3. In Fig. 5.23 the predictions for the years 1993, 1995 and 1996 are superimposed. Because the magnet cooling is different for the three years, variations of the temperature induced rises are expected. In 96 the cooling was stronger to cope with larger power dissipations in the coils during the high energy runs. As a consequence small temperature variations occur during the peak fills and the predicted 1996 energy changes due to temperature are very small. Typically the temperature in 1995 decreases again after a few hours, leading to more integral temperature variations than in 1993 and causing a higher predicted energy rise. The predicted energy drift

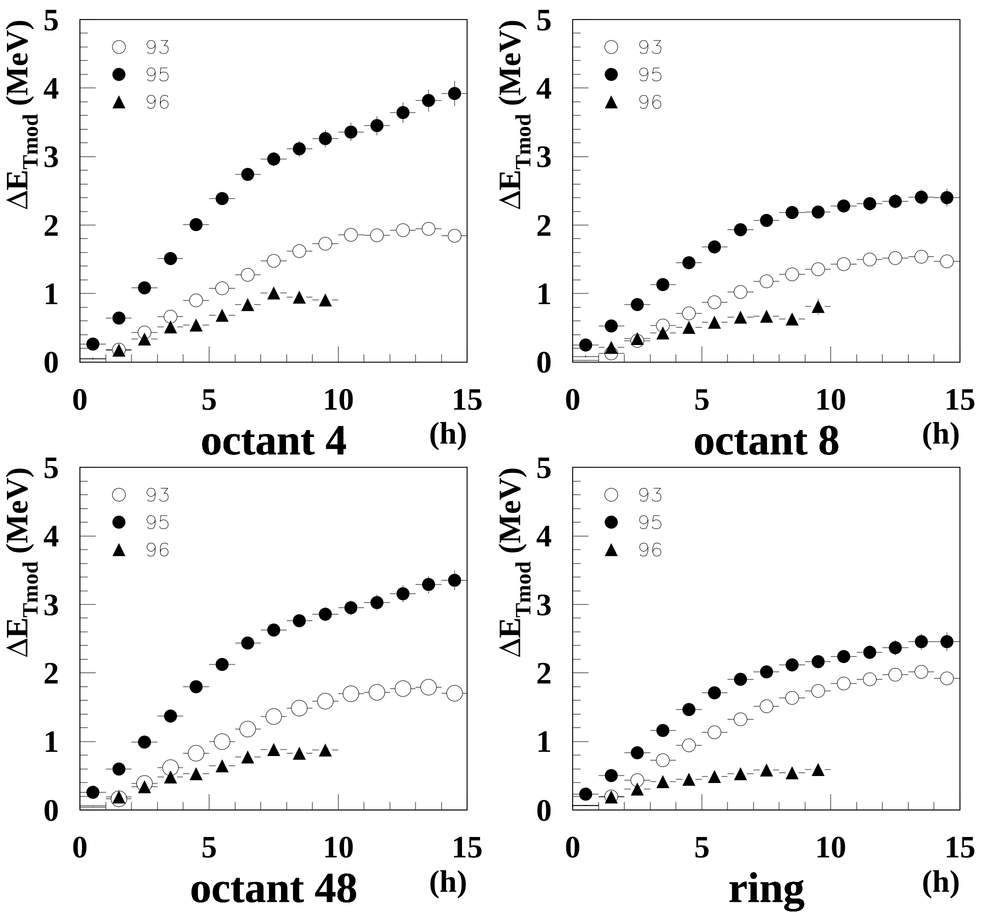

Figure 5.23: *The predicted energy change due to temperature variations as a function of time in the fill. The prediction is calculated from the new temperature parametrisation according to Eq. 5.7. Only statistical errors are shown.*

for octant 4 in 1995 is a factor of 2 larger than in octant 8, which is explained by the typical temperature variation in the two octants. In the other years this difference between octant 4 and 8 is much less significant. In 1995 the temperature drifts for octant 3 and 4 only exceed the value of $T - T_0 = 0.2^oC$, which is typical for all other octants. Therefore the energy drifts in OCT3 and OCT4 are not representative for the 5/8 branch of LEP. This explains the discrepancy between the octant 48 prediction and the prediction for the whole ring.

The 1993 energy drift prediction from the new temperature parametrisation cannot be compared with the behaviour of the magnetic field, since it was not monitored. A comparison of the field and the temperature prediction is shown for the 1995 fills and the 1996 peak fills in Fig. 5.24. The temperature prediction and the 1995 NMR4 data sample with magnet conditioning agree perfectly. The agreement between temperature prediction and the NMR data without magnet conditioning is similar in both years. Neither the 1995 nor the 1996 NMR8 data agree with temperature prediction from the corresponding year. The shape of the 1995 and 1996 evolutions differ significantly.

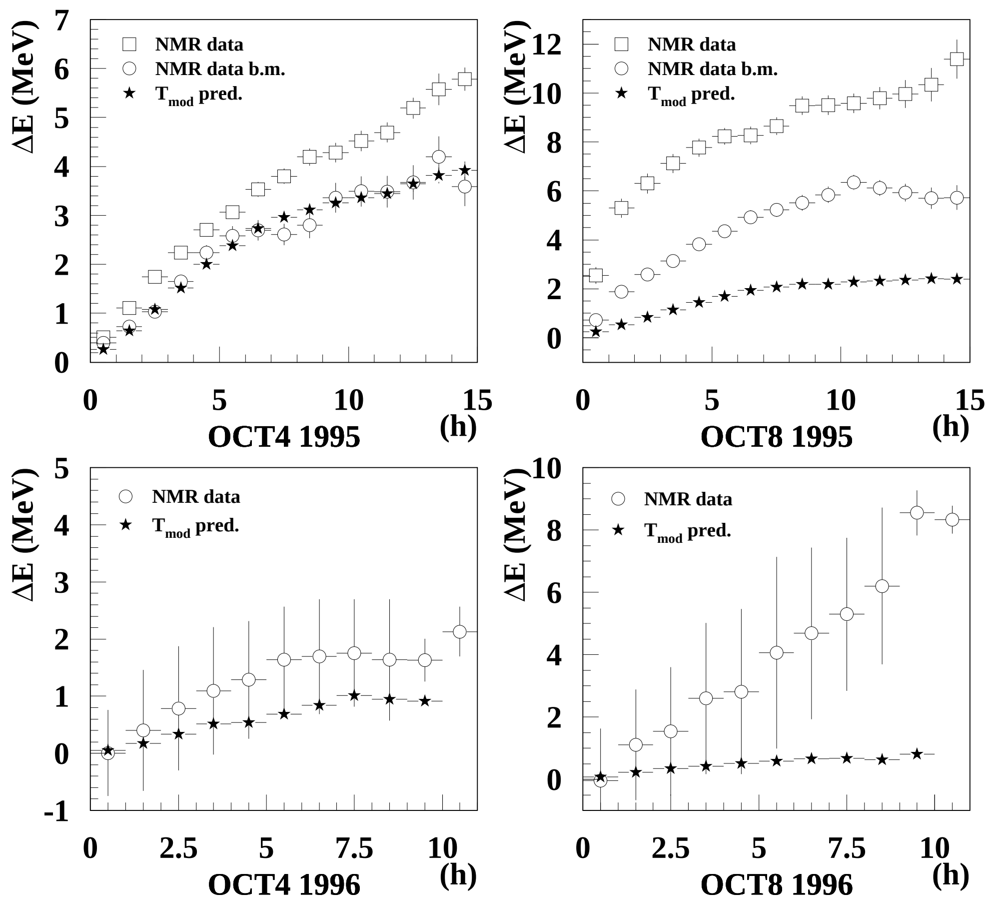

Figure 5.24: *Magnetic field variation in units of beam energy and energy rise predictions from the temperature model as a function of time. The 1995 data sample (top) includes NMR data with (NMR data b.m.) and without (NMR data) magnet conditioning. The errors bars of the 96 NMR data correspond to the the RMS scatter of the data sample. All other errors correspond to the errors of the mean.*

The agreement between the temperature prediction and the NMR4 data leads to the conclusion that the energy rise remaining after bending modulation in octant 4 arises from temperature effects only. To verify the conclusion, the temperature prediction was subtracted from the 1995 NMR data without bending modulation and from the 1996 NMR data. Since in 1996 no bending modulation was applied at the start of the fills, the 1995 fills without magnet conditioning should be equivalent to the 1996 fills. Fig. 5.25 shows the results. While for octant 4 the data of the two years agree very well, there is a striking discrepancy for octant 8. They disagree not only by the amount but also by the shape of the evolution. Possible explanations are:

- NMR4:
  The average B-field rise in octant 4 is due to a superposition of a temperature rise and the Train Effect. It shows that bending modulation in 1995 efficiently suppressed the part of the rise, which is caused by the Train Effect. Typical drifts

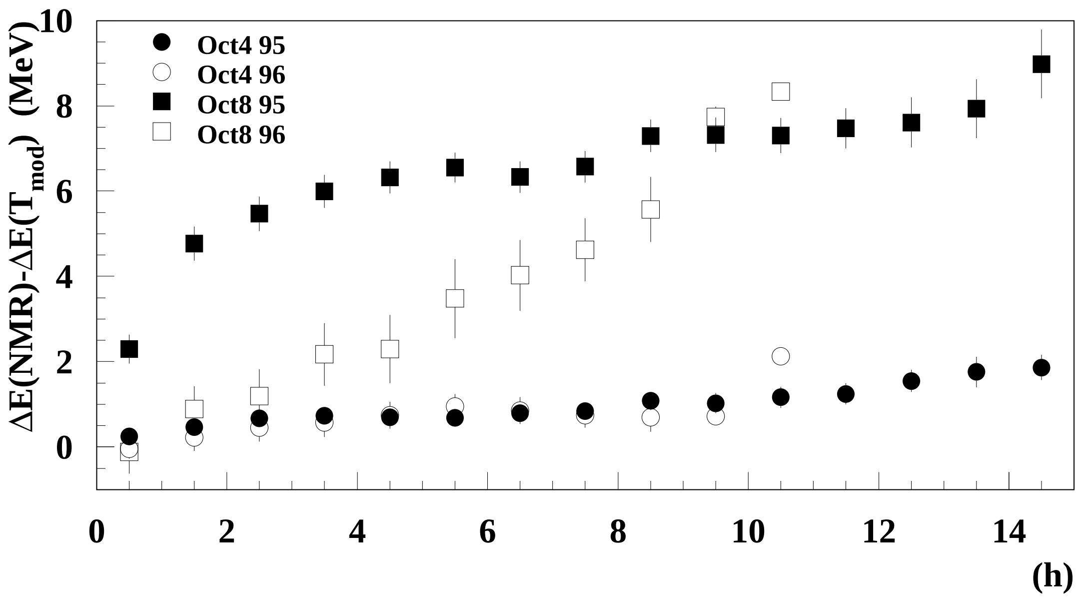

Figure 5.25: *Difference between NMR data and temperature prediction in 1995 and 1996 as a function of time. Errors are statistical.*

in 1993, ΔE_{1993}, can be calculated by adding the temperature prediction of 1993 $\Delta E(Tmod_{1993})$ to the difference distribution:

$$\Delta E^i_{1993} \simeq \Delta E^i_{1995} - \Delta E^i(Tmod_{1995}) + \Delta E^i(Tmod_{1993}) \qquad , \tag{5.8}$$

where $i = 2, 3, 4, 5, 6$ represents the octants in the 5/8 branch of LEP.

- NMR8:
  The average B-field rise in octant 8 does not consist of a linear superposition of the temperature part and the Train Effect. This difference with the behaviour of NMR4 is not yet understood. The different shape of the average energy drift in 95 and 96 excludes an extrapolation to 1993 and typical drifts cannot be calculated according to Eq. 5.8. It contributes to the uncertainty of the estimate for the 1993 energy rise in a fill.

5.1.7 Fill to Fill Variations

The NMR probes in the tunnel allow to monitor the time dependence of the mean magnetic field on a fill to fill basis, which is shown for 1995 in Fig. 5.26. Since several years a continuous weakening of the magnetic field in octant 4 was recorded by the horizontal orbit monitoring. This evolution could be confirmed for 1995 by NMR4, which shows a weakening of about 10-20 MeV with respect to the first fill of the scan. The magnetic field at NMR8 does not show a drift but a level change of approximately 0.07 Gauss ($\simeq$ 6 MeV) between fill 2900 and fill 2930. At this time the probe was

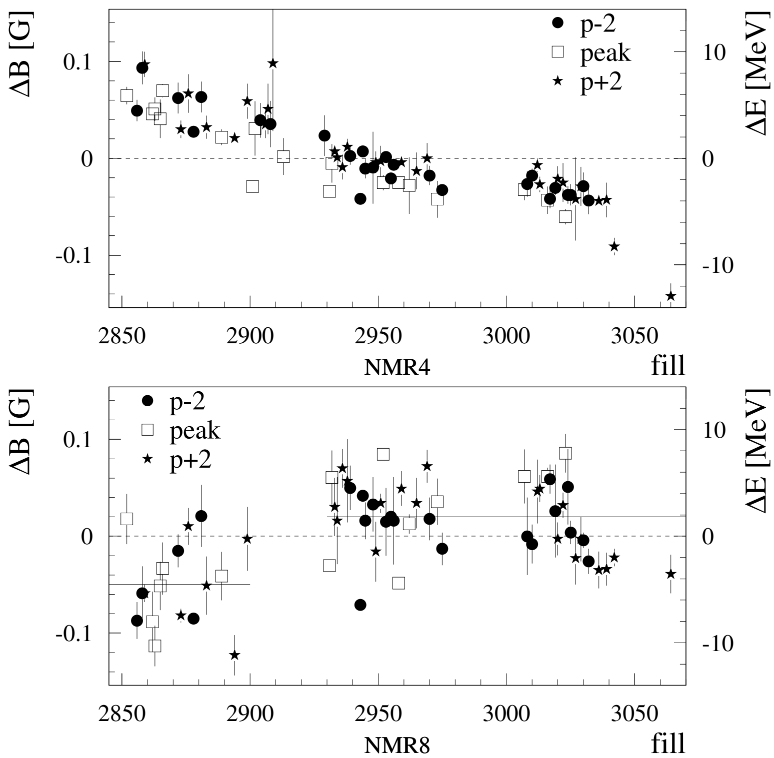

Figure 5.26: *Evolution of the average magnetic field as a function of the fill number. The mean values are normalised to the mean field per energy setting. Errors correspond to the RMS scatter inside the fill. The left scale corresponds to the relative change in the magnetic field in Gauss whereas the scale given on the right side is the equivalent change of the beam energy in MeV. The mean value of the fills at each energy point is set to 0 Gauss and 0 MeV respectively. The solid lines in the bottom plot indicate the fitted average in the two periods before and after removing the NMR8 probe.*

removed and reinstalled. The scatter around the two averages is due to different core temperatures at the start of the fills. While the drift of the dipole field in octant 4 could be related to humidity, the jump of the field measurements in octant 8 is due to a displacement of the probe relative to the position of the field plate.

5.1.7.1 Humidity

The air humidity is not constant along the ring but has a structure, illustrated in Fig. 5.27. The octants 4 and 5 are significantly drier during operation than the others. In both octants water is infiltrating the LEP tunnel and the air ventilation is intensified to keep the two octants as dry as possible. Fig. 5.28 shows the relative air humidity in three octants as a function of time for 1995. The humidity evolution in the other octants is the same as in octant 8. During the shut down period the air ventilation is switched off. This leads to a significant increase of the humidity during the winter months in octant 4, where water from the Jura mountains enters the LEP tunnel. In octant 4 the difference between the humidity in winter months (75%-80%) and the humidity in operation months (30%-35%) is significantly larger than in all other octants. Because of this large difference, concrete of the dipoles in octant 4 is most likely drying out during the months of operation. Since the concrete volume is modified during the drying process the pressure on the iron shut varies. The change of the pressure leads to

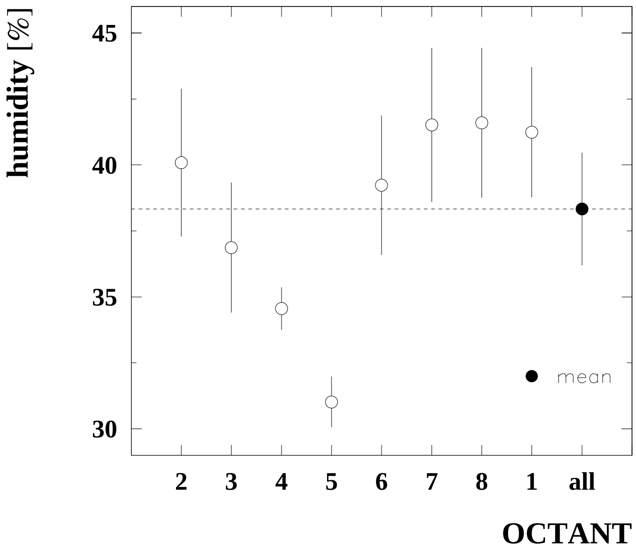

Figure 5.27: *Mean humidity of the air as a function of the number of the octants along the LEP ring. Octant 1 corresponds to the octant between IP8 and IP1, octant 2 to the octant between IP1 and IP2 and so on. Quoted errors are the RMS values of the statistical distributions.*

a variation of the iron magnetic permeability and thus of the field in the dipoles [76]. Fig. 5.29 shows the change of beam energy at 44 GeV as a function of the humidity, which varies by 14 MeV when the humidity changes from 35% to 80%. This agrees with the drift seen by the NMR4 probe. The field drifts in octant 4 might therefore be related to the drying of the dipole concrete in this arc.

The phenomena of the continuous drift in octant 4 was confirmed by measurements of the mean horizontal orbit position in the arcs. In an octant, whose field differs from the mean field by ΔB, the beam has to move on a dispersion orbit since its energy is not matched to the dipole field. The difference of the horizontal beam position with respect to the average position is given by:

$$\Delta x = -\frac{7}{8} \cdot D_x \cdot \frac{\Delta B}{B} \qquad . \tag{5.9}$$

Since the magnetic field is related to the horizontal beam orbit position, the correlation of the two devices, NMR and BOM, can be derived. Figure 5.30 shows the magnetic field measured by NMR4 as a function of the relative horizontal orbit position in octant 4 measured by the BOM system. A fit of the field derivative $\Delta B/\Delta X_{ARC}$ leads to a correlation factor of 12 ± 3 μm/MeV. The fitted correlation factor agrees well with the result from Eq. 4.12, which was calculated from predictions for the horizontal dispersion. Thus the drift of the horizontal orbit in octant 4, seen by the BOM system since 1994, confirms the results from the NMR4 fill to fill analysis.

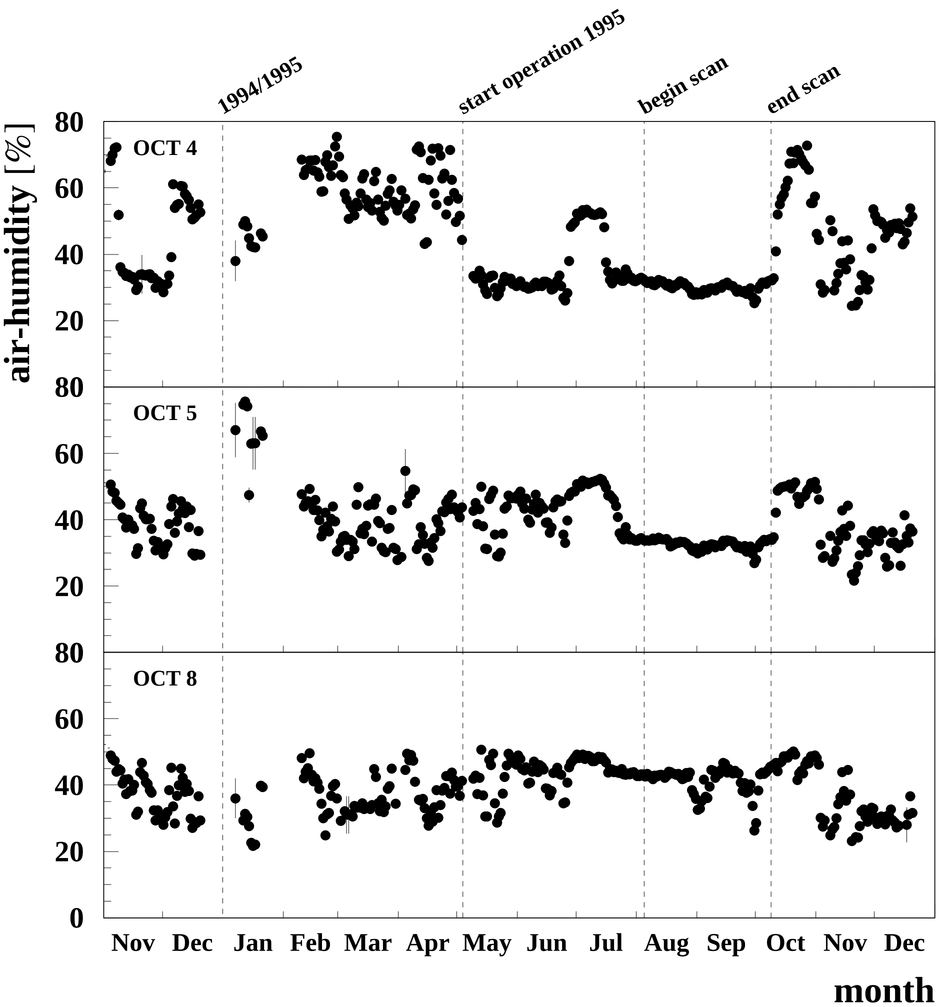

Figure 5.28: *Relative air humidity as a function of time in 1995 for LEP octant 4, 5 and 8. One data point corresponds to the average humidity over one day, error bars correspond to the RMS value. The change of the year, the end of the shut down and the start and end of the scan period are indicated by dotted lines.*

5.1.7.2 The Field Plate

The operation of NMR probes in LEP dipoles requires a field plate to improve the field homogeneity. Both NMR probes are installed between iron plates with dimension $(170 \times 200 \times 1.5)$ mm^3. The magnetic field seen by a probe installed inside a field plate depends on the distance of the probe head to the centre of the plate. The field variation as a function of the longitudinal (along s) and transverse (along x) position of the probe was measured using the magnet test bench [74]. Fig. 5.31 shows the results of various measurements. The measurements along the x-axis were repeated at several longitudinal positions. In both dimensions the field variation can be expressed by a

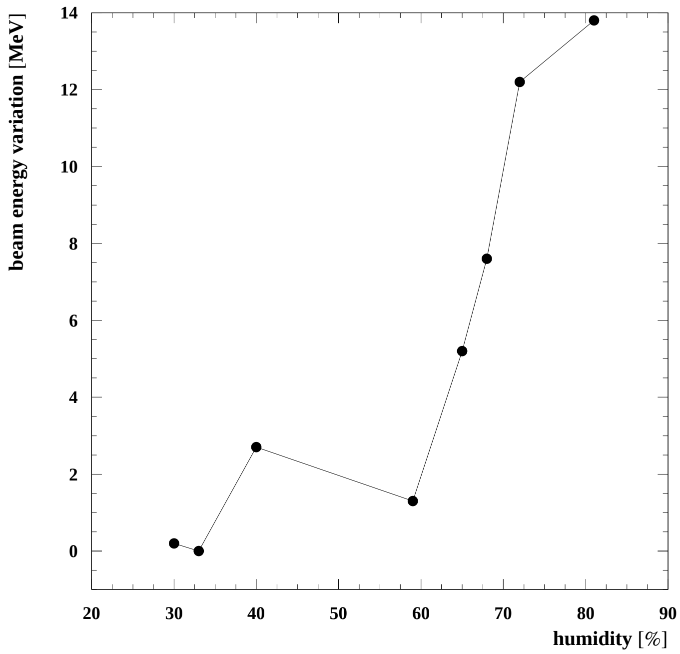

Figure 5.29: *The change of the beam energy caused by variations of the magnetic field at 44 GeV as a function of the relative humidity.*

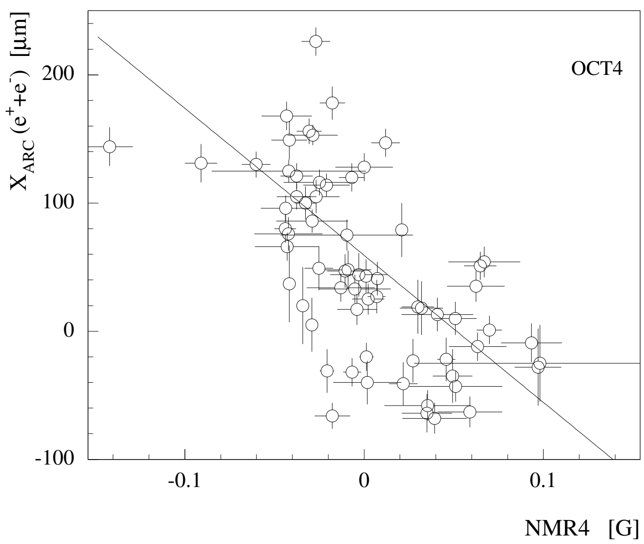

Figure 5.30: *Correlation between the magnetic field at NMR4 and the horizontal orbit position measured by the BOM system in OCT4 with respect to the average position in the whole ring during the 95 scan. The solid line is a fit to the data. The beam energy in octant 4 changes by 1 MeV for a $12 \pm 3\,\mu m$ transverse movement of the beam relative to the centre of the quadrupoles.*

second order polynomial:

$$\Delta B(s) = b_1^s \cdot s + b_2^s \cdot s^2 \quad , \tag{5.10}$$
$$\Delta B(x) = b_1^x \cdot x + b_2^x \cdot x^2 \quad . \tag{5.11}$$

The linear terms are negligible. The second order terms in the two directions differ by one order of magnitude, leading to $b_2^s \simeq 0.7 \cdot 10^{-4}\,\mathrm{G/mm^2}$ and $b_2^x \simeq 0.8 \cdot 10^{-3}\,\mathrm{G/mm^2}$. The NMR8 probe was removed for about 9 days from Aug 16th, 1995, to Aug 25th, 1995. The difference in the average field before and after the removal is approximately 0.07 G. Such a shift can easily be explained by a small displacement in x or s of the probe position after the re-installation with respect to the original position. The total

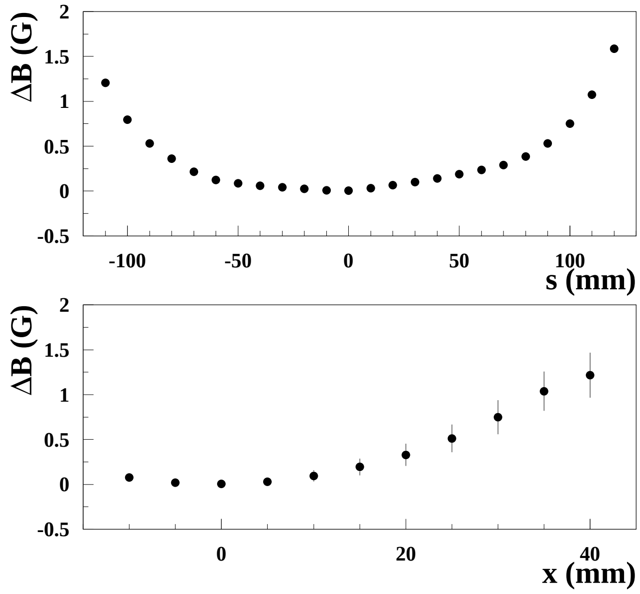

Figure 5.31: *Variation of the magnetic field as a function of the longitudinal (top) and transverse (bottom) position of the probe with respect to the centre of the field plate. The magnetic field is normalised to the field measurement at the centre position. The error bars in the bottom plot correspond to upper and lower limits from several series of measurements at different s positions.*

effect of such a displacement depends on the initial distance x_0 and s_0 from the centre of the field plate. Possible position shifts necessary to accommodate such a deviation are in the range of 1 to 30 mm depending on the initial position and on the direction. At the time of the second installation the probe was not realigned to the initial position. However, large displacements with respect to the initial position are excluded since the mounting of the probe fixes its position to a few millimetres in s and x. The field is more sensitive to small shifts in x direction. Therefore most likely a small displacement in the order of a few mm in the transverse direction occurred while mounting the probe again after the removal.

5.2 Quadrupole Fields

Particles going off-centre through a quadrupole magnet see a magnetic field proportional to the offset. Energy and beam orbit position are therefore related (Eq. 4.12). Since the length of the orbit is fixed by the RF frequency, relative movements of the beam with respect to the centre of the quadrupoles can be caused by a change of this frequency or by a change of the mean radius of LEP. The RF frequency was kept constant during the two scans, but ground motions due to geological and gravitational effects lead to radial deformations of the ring and thus to a change of the mean radius. While ground motions change the position of the quadrupoles with respect to the beam, variations of the orbit corrector settings can change the position of the beam with respect to the centre of the quadrupoles.

5.2.1 Radial Deformations of the Ring

Gravitational effects are caused by the moon and the sun, which move the Earth surface up and down. The lateral components of this motion modify the LEP circumference by about 1 mm. Earth tides act on a short term time scale with gradients of $\Delta E_{tide}/\Delta t \simeq 1 MeV/h$. The observed variations can be predicted from a precise tide model. Geological effects change the mean radius of LEP on a long term time scale leading to seasonal effects, which can be monitored using the LEP BOM system. Seasonal variations change the average beam energy on a fill to fill basis.

5.2.1.1 Earth Tides

The gravitational attraction from the moon and the sun is not uniform over the Earth surface because of the $1/r^2$ dependence of the gravitational force. The radius r represents the distance between the source of the gravitational force and a point on the surface of the Earth. An interference of the moon and the weaker sun tides produce tide bumps on the Earth surface which can reach up to 25 cm at the location of the LEP ring [77]. The motion of the Earth crust modifies the circumference of the ring by at the most $\pm$ 0.5 mm, which corresponds to a relative variation of $3 - 4 \cdot 10^{-8}$. Fig. 5.32 shows a schematic view of the tidal deformation of the Earth crust due to the gravitational forces of the moon. The crust deformation has the same origin than the well known water tides of the oceans. Numerous periodicities including eccentricity

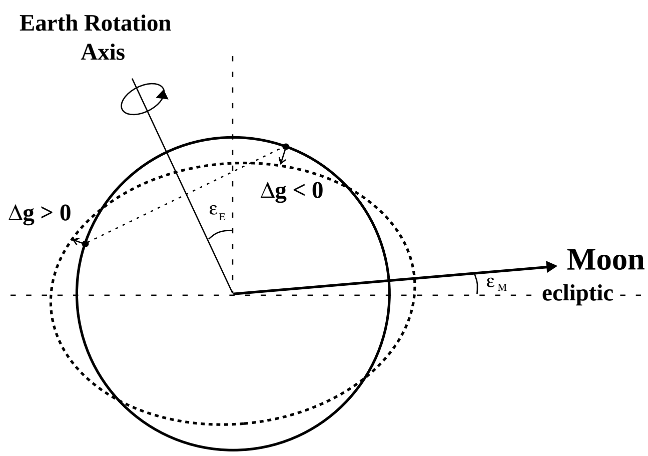

Figure 5.32: *A schematic view of the Earth, misshaped due to the gravitational forces of the moon. The gravity variations Δg caused by the tidal deformations are indicated at two antipodal locations at a latitude of about 45°. At a location far from the equator the tide amplitudes are asymmetric because of the inclination of the Earth rotational axis (ϵ_E = 23°26′) and of the lunar orbital plane (ϵ_M = 5°8′). Plot taken from [77].*

and oscillations of the terrestrial and lunar orbit lead to a large number of harmonics of the tide frequency spectrum. To analyse the experimental beam energy data predictions for the tide amplitudes based on a Cartwright-Tayler-Edden (CTE) potential [78], including 505 main harmonic components of the tide potential, are used. Energy variations are related to gravity changes Δg through a sensitivity coefficient

κ_{tide}:

$$\frac{\Delta E(t)}{E_{tide=0}} = \kappa_{tide} \cdot \Delta g(t) \quad . \tag{5.12}$$

The effects of the terrestrial tides on the beam energy were observed on various occasions and three dedicated experiments with stable beams over a long period. Fig. 5.33 shows the evolution of the beam energy with time and a prediction from a CTE tide model. A beam energy variation of up to 220 ppm corresponding to 10 MeV was observed in the 1992 tide experiment, which was performed at full-moon. The largest energy variation at full-moon corresponds to a ring modifications by about 1 mm (according to Eq. 4.4). The agreement between data and model prediction is excellent. The data were used to fit the sensitivity coefficient leading to [77]:

$$\kappa_{tide} = -0.86 \pm 0.08 \text{ ppm}/\mu\text{gal} \; (1\, gal = 1\, cms^{-2}) \quad . \tag{5.13}$$

Additionally, the tide coefficient has been derived from beam orbit studies [79] using 1994 and 1995 data from the LEP BOM system. The BOM analysis lead to a smaller value of $\kappa_{tide} = -0.83 \pm 0.03$ ppm/μgal. The BOM measurement is dominated by systematic errors while the accuracy of the coefficient from energy calibration measurements is limited by statistical uncertainties. Both values agree reasonably well with the expected value of -0.9 ppm/μgal from [78]. The uncertainty on the coefficient is so small that it may be neglected for the calculation of the total error on the beam energy calibration.

5.2.1.2 Seasonal Effects

In addition to the regular tide motion, slow ring deformations were observed during the LEP operation. It was first revealed by unexpected variations of the beam energy and could be traced back to slow changes of the ring circumference. The analysis of the long term beam orbit evolution is based on beam orbit measurements by the BOM system [62]. Fig. 5.34 and Fig. 5.35 show the average horizontal beam positions as a function of time for each LEP fill with valid data for the years 1993 and 1995 after correction of tidal effects. The beam energy measurements by the resonant depolarisation method are also shown (top). The orbit measurements are converted into units of beam energy using Eq. 4.12. The absolute scale of the orbit data is shifted with respect to the first energy calibration measurement in the scan period. One data point correspond to the average horizontal orbit position in a fill. In both years the shape of the beam energy evolution is in a good agreement with the shape of the orbit evolution. The orbit measurements reveal variations of up to 20 MeV, which are confirmed by energy calibrations. According to Eq. 4.4 energy changes of 20 MeV correspond to circumference changes of 2 mm. Since orbit measurements by the BOM system are

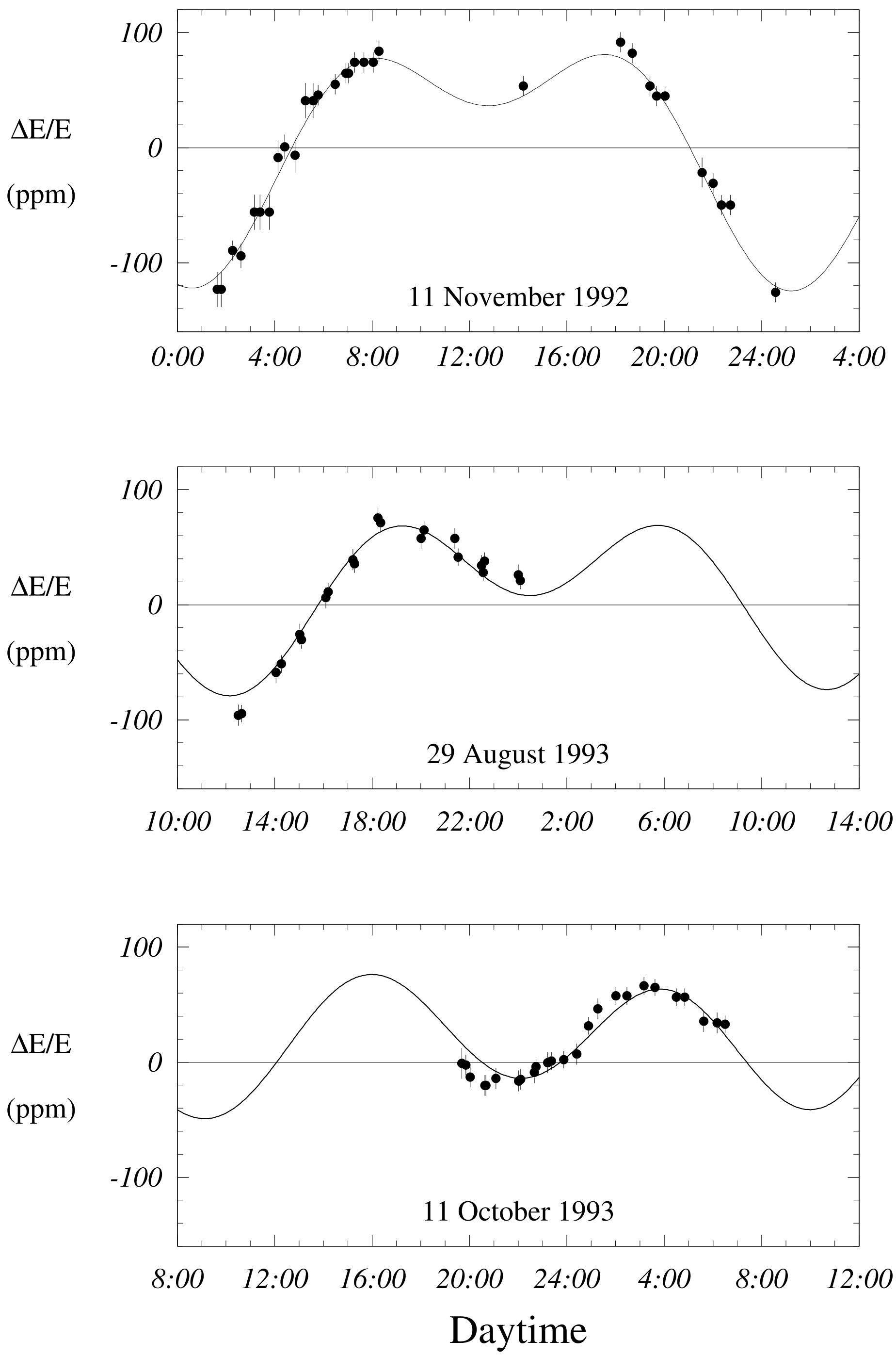

Figure 5.33: *Relative beam energy variation due to terrestrial tides as a function of time in three dedicated experiments. The solid line corresponds to a prediction calculated from a CTE model. The figures are taken from [77].*

available for almost all fills, they can thus be used to interpolate between fills with and without a beam energy calibration to calculate the fill to fill energy variations.

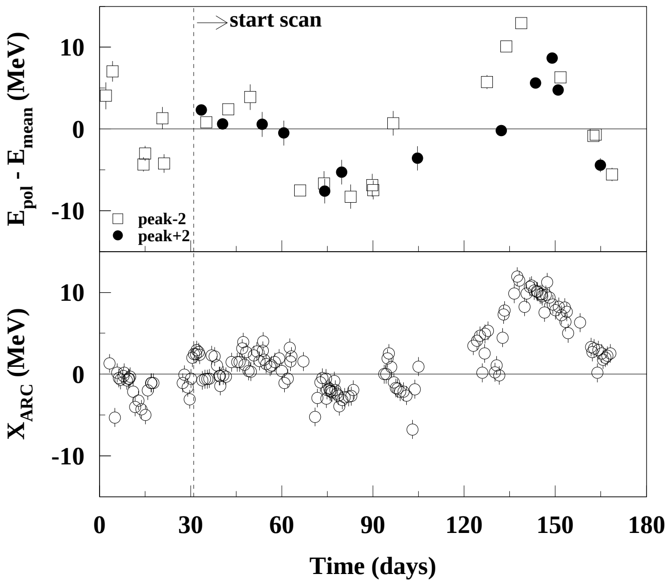

Figure 5.34: *Evolution of the beam energy (top) and the average horizontal beam orbit (bottom) in the arcs as a function of time in the year 1993. Day 0 corresponds to Jun 1st, 1993. The energy measurements are normalised to the mean value per energy point. The orbit measurements are converted into equivalent energy changes. Errors correspond to 20 μm. X_{ARC} data are normalised to the first beam energy calibration in the scan period. The start of the scan period 1993 is indicated by a dashed line.*

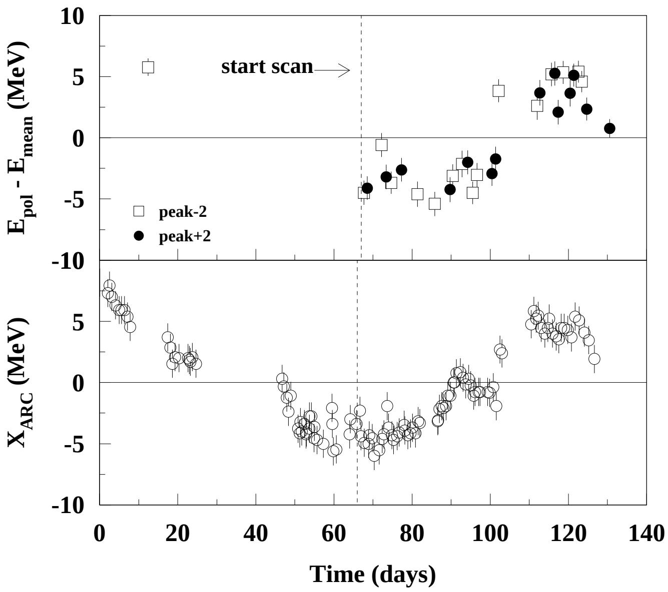

Figure 5.35: *Evolution of the Beam energy and the average horizontal beam orbit in the arcs as a function of time in the year 1995. Day 0 corresponds to Jun 1st, 1995. The energy measurements are normalised to the mean value per energy point. The orbit measurements are converted into equivalent energy changes. Errors correspond to 15 μm. X_{ARC} data are normalised to the first beam energy calibration in the scan period. The start of the scan period 1995 is indicated by a dashed line.*

The change in the circumference during the years 1993 and 1994 seems to be correlated with large amount of rainfall and a rise in the underground water level under the Jura. The agreement between the rainfall data and the orbit measurements is satisfactory but not all details can be explained [80]. Furthermore there is some evidence that the water level of the Lake Leman could be a substantial cause of the circumference changes. Fig. 5.36 shows the level of the water in the Lake Leman in 1993 and 1994. Water level and LEP circumference are obviously correlated in May, where the water level changes rapidly because of the melting water from the Alps. The correlation disappears for a large part of the year where the water level is almost constant. The major part of the LEP ring is positioned in the molasse of the Lemanic Plain and the remainder in the limestone of the Jura. A deformation of the molasse because of the mass of the water could cause the ring extensions. Looking to the water level data from 1995 [81] give rise to doubts about the correlation between water level and LEP

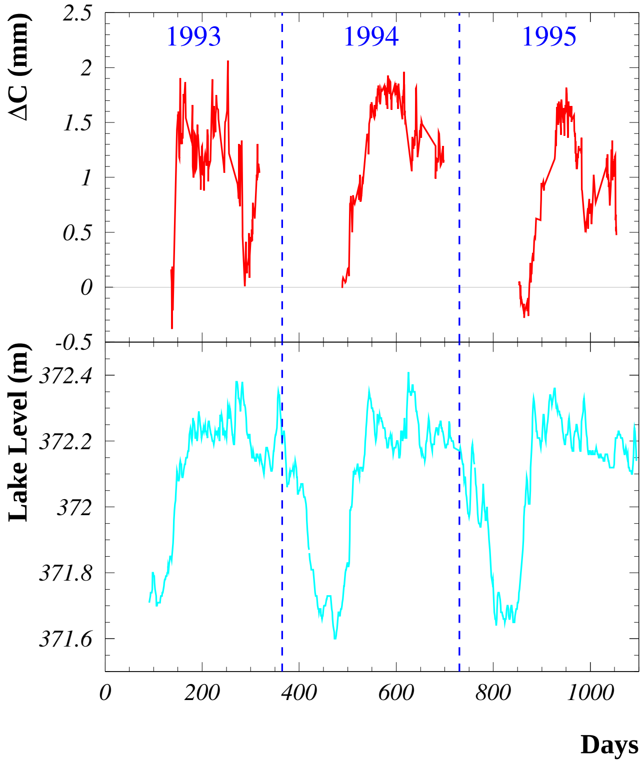

Figure 5.36: *Evolution of the water level in the Lake Leman and the circumference variations of the LEP ring as a function of time in the years 1993-1995. The circumference data are calculated from BOM orbit measurements. The 1993 and 1995 distribution correspond to Fig. 5.34 and Fig. 5.35 respectively. Plot taken from [81].*

circumference. The significant increase of the water level is shifted by about 2 weeks with respect to the orbit changes.

Using the LEP BOM system it is possible to observe circumference variations of LEP with good accuracy. Over a period of 3 years the circumference showed periodic fluctuations of about 2 mm. These variations are confirmed by energy calibrations with resonant depolarisation. Hence measurements of the beam position can be used to interpolate between calibrated fills and to reduce the uncertainty of the fill to fill energy variation. In 1993 and 1994, there is some evidence that the water level of the Lake Leman could cause the circumference changes. This conclusion could not be confirmed with the 1995 water level data. However, the origin of these changes does not matter to predict the related energy shifts.

5.2.2 Orbit Corrector Magnets

At LEP approximately 260 horizontal and 320 vertical corrector magnets are used to control the position of the beam orbit. Horizontal correctors consist of dipole magnets with a vertical magnetic field. The direction of the the horizontal corrector field and the bending field is the same. Each of the corrector magnets can be controlled individually. Two simple models can be used to describe the effects of orbit distortions and corrector kicks on the beam energy [82]: (i) Orbit lengthening and (ii) Dipole effects.

- Quadrupole effect
  The corrector magnet kicks Θ lead to a distorted orbit and possibly to a change of the average beam energy. The correctors affect the beam orbit positions, which are derived from the BOM system. The orbit lengthening contribution of the corrector magnets to a beam energy change is given by a change of the orbit length ΔL with respect to the length of the ideal orbit L_0:

$$\frac{\Delta E_{length}}{E} = -\frac{1}{\alpha} \cdot \frac{\Delta L}{L_0} \quad , \tag{5.14}$$

  In a real machine, where sextupoles are used to compensate the momentum dependence of the tunes, ΔE receives an additional contribution from the sextupole deflections Θ_s:

$$\frac{\Delta E_{sext}}{E} = -\frac{\Sigma \Theta_s}{2\pi} \quad . \tag{5.15}$$

  The total change of the average beam energy ΔE is finally given by:

$$\frac{\Delta E}{E} = \frac{\Delta E_{length}}{E} + \frac{\Delta E_{sext}}{E} \quad . \tag{5.16}$$

  If the LEP energy evolution in a fill is determined including a correction for X_{ARC}, some double correction may be introduced.

- Dipole effect
  In a case where the corrector pattern is very asymmetric, it is possible to imagine that the fields of (some) horizontal corrector magnets contribute to the total bending field. The energy change is then related to a corrector kick Θ by:

$$\frac{\Delta E}{E} = -\frac{\Theta}{2\pi} \quad . \tag{5.17}$$

Usually, horizontal correctors contribute to beam energy changes through both channels. To understand more precisely the contribution of the horizontal correctors to the average beam energy, a simulation of LEP with the MAD [38] program was carried out. Furthermore, the influence was tested experimentally during two fills in 1996. Fig. 5.37 shows the two experiments and the correlation of measured and predicted values. The experiments proved that corrector magnets can influence the beam energy. In both experiments the measured effect of a change in the corrector configuration agreed well with the energy change predicted from calculations. The agreement leads to a correlation factor of $\rho = 1.3 \pm 0.2$ between measured and predicted energy variation. The experiments did not favour one of the two approaches.

In general, corrector magnet settings were changed going from physics mode to calibration mode, to flatten the horizontal beam orbit. A flat horizontal orbit is considered to be helpful to establish transverse polarisation. Hence methodical shifts between the measured energy and the beam energy in physics mode are likely. The settings of the

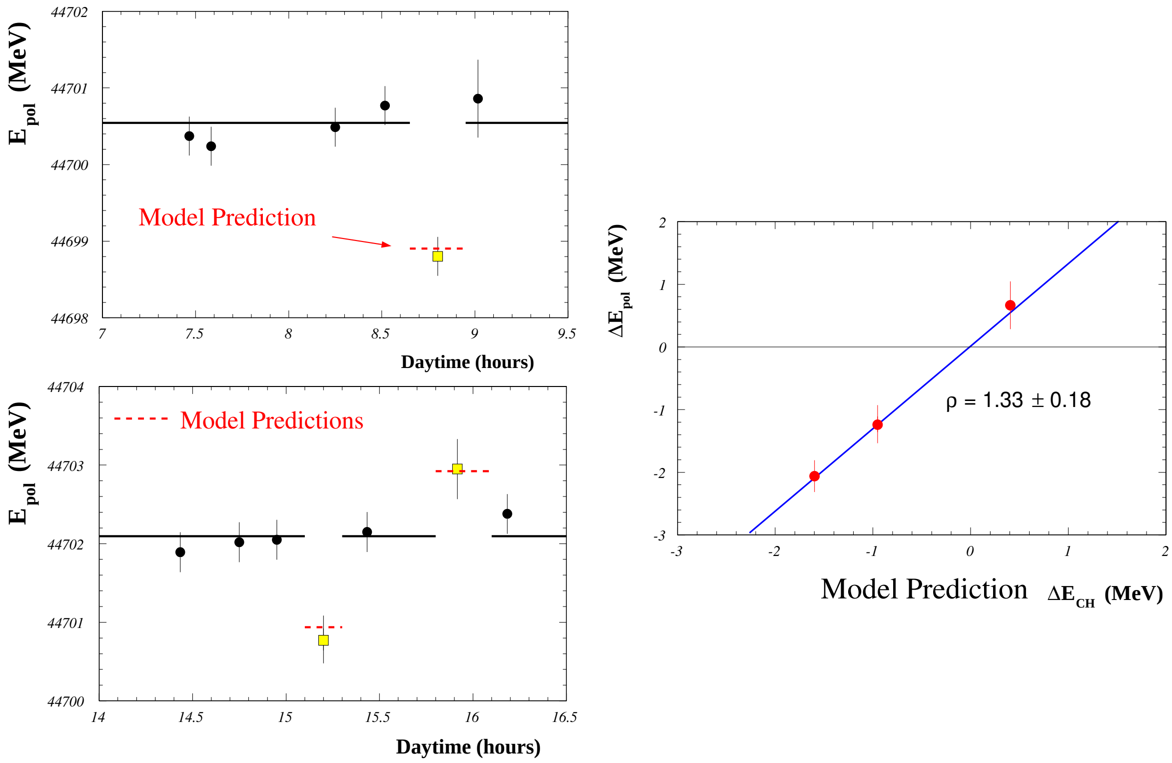

Figure 5.37: *Left: Energy measurements with resonant depolarisation in two experiments as a function of time. The closed circles correspond to energy calibrations at the initial setting of correctors. The mean energy value is indicated by a solid line. The squares correspond to energy calibrations at the time of deliberate changes of the corrector settings. The model prediction is indicated by a dashed line. Right: Energy measurements as a function of the model prediction. The fitted slope is 1.33. The figures are taken from [82].*

corrector magnets were logged in the LEP database since 1993. Hence the energy shifts predicted by both approaches can be reconstructed for the two energy scans. The difference of energy shifts predicted by the two methods can be used as estimates for the systematic errors. The RMS scatter of this difference is roughly $\Delta E/E \simeq 1.5 \cdot 10^{-5}$.

5.3 Analysis of Long Term Energy Calibration Experiments

The Analysis of the 1995 long term experiments will be presented first since they include NMR data from the tunnel. The conclusions made will be tried to verify using the data, which were acquired in 1993 mainly.

5.3.1 1995

Several energy calibrations were performed throughout 6 fills from the 1995 data taking. Besides the first fill (2929), all other fills start with a bending modulation. Data from these fills are available to prove the assumptions made above. Various methods have been applied to correct the energy calibration data E_{pol}. The effect of temperature changes on the entire ring has been calculated according:

$$B_{Tmod}^{ring}(t) \;=\; \frac{1}{8} \cdot \sum_i B_{Tmod}^{oct^i}(t) \qquad , \tag{5.18}$$

where $i = 1, ..., 8$ denotes the eight octants of LEP. $B_{Tmod}^{octi}(t)$ accounts for the prediction of temperature caused B-field rise in a particular octant according to the new parametrisation (Eq. 5.7).

(1) Only tide corrections are applied to E_{pol}.

$$E_{raw}(t) = E_{pol}(t) + \Delta E_{tide}(t) \tag{5.19}$$

(2) E_{pol} is corrected for the horizontal corrector settings. In fill 2929 and 3064 the settings did not change since in both fills the machine mode was not varied.

$$E_{hc}(t) = E_{raw}(t) + \Delta E_{hor.corr.}(t) \tag{5.20}$$

(3) E_{raw} is corrected for the variation of the beam orbit position during the fill. $\Delta E_{X_{ARC}}$ is applied after correction of tidal effects to avoid double-compensation.

$$E_X(t) = E_{raw}(t) + \Delta E_{X_{ARC}}(t) \tag{5.21}$$

(4) E_{raw} is corrected for horizontal corrector settings and for temperature drifts according to the classical approach.

$$E_{hc+T_c}(t) = E_{raw}(t) + \Delta E_{hor.corr.}(t) + \Delta E_{T_{class}}(t) \tag{5.22}$$

(5) E_{raw} is corrected for horizontal corrector settings and for temperature drifts according to Eq. 5.18.

$$E_{hc+T_n}(t) = E_{raw}(t) + \Delta E_{hor.corr.}(t) + \Delta E_{T_{new}}(t) \tag{5.23}$$

(6) The energy calibration measurements are corrected for orbit changes during a fill and for temperature drifts according to the classical approach.

$$E_{X+T_c}(t) = E_{raw}(t) + \Delta E_{X_{ARC}}(t) + \Delta E_{T_{class}}(t) \tag{5.24}$$

(7) Corrections for the horizontal beam positions during the fill calculated from the BOM system and the new temperature model are taken into account.

$$E_{X+T_n}(t) = E_{raw}(t) + \Delta E_{X_{ARC}}(t) + \Delta E_{T_{new}}(t) \tag{5.25}$$

(8) Corrections for corrector magnets, horizontal beam positions and temperature drifts according to the classical approach are applied.

$$E_{hc+X+T_c}(t) = E_{raw}(t) + \Delta E_{hor.corr.}(t) + \Delta E_{X_{ARC}}(t) + \Delta E_{T_{class}}(t) \tag{5.26}$$

(9) Corrections for corrector magnets, horizontal beam positions and temperature drifts according to Eq. 5.18 are applied.

$$E_{hc+X+T_n}(t) = E_{raw}(t) + \Delta E_{hor.corr.}(t) + \Delta E_{X_{ARC}}(t) + \Delta E_{T_{new}}(t) \tag{5.27}$$

(10) Corrections for corrector magnets and temperature drifts according to Eq. 5.7 are applied.

$$E_{hc+T_{eff}}(t) = E_{raw}(t) + \Delta E_{hor.corr.}(t) + \Delta E_{T_{eff}}(t) \tag{5.28}$$

B-field drifts recorded by the reference magnet are negligible small in all fills. The difference ΔE between the last and the first energy measurement after applying the various methods is presented in Tab. 5.6. The number in each row indicates the type of correction as listed above. The mean value and the RMS scatter of the variation of ΔE with the fill number is shown in the last two lines. The mean value indicates the remaining shift, which could be attributed to the Train Effect. The RMS value is a measure of the quality of the applied method to correct the energy data.

The correction for corrector magnets only (2) reduces the scatter by a significant amount compared to a correction for beam orbit positions (3). A "classical" temperature correction added to the corrector magnet correction (4) gives an RMS of about 0.8 MeV, the same results as (2). A significant reduction of both, the mean and the RMS, is achieved by applying correction function (5), a combination of horizontal correctors and the new temperature model according to Eq. 5.7. The results are highlighted in Tab. 5.6. The RMS value achieved here is 0.5 MeV. Using the same correction function but instead of the complete new temperature model a reduced approach, which is based on an effective temperature coefficient according to Eq. 5.7, the RMS value is slightly decreased to 0.4 MeV (10). The mean value in this case amounts 1 MeV. The detailed results for this approach are not listed in Tab. 5.6. The application of the classical temperature correction based on a correction for the beam position (6) causes an significant increase of the RMS compared to (5). The scatter is reduced to 1.7 MeV by using the new temperature model (7) instead of the classical approach. A combination of corrections for corrector magnets, beam position and temperature results in RMS values of 1.6 MeV (8) and 1.1 MeV (9). The negative mean value in the last case indicates a kind of "over-compensation" of horizontal orbit drifts in the data, if both, corrector magnet compensation and compensation for the beam orbit

		fill number							
	method	2929	3022	3029	3030	3036	3064	mean	RMS
1	ΔE_{raw}	1.9	2.1	6.5	4.4	1.7	1.4	3.0	1.8
2	ΔE_{hc}	1.9	0.8	3.4	1.8	2.1	1.4	1.9	0.8
3	ΔE_{X}	2.0	1.3	5.0	4.3	-0.7	0.9	2.1	2.0
4	ΔE_{hc+T_c}	2.6	1.7	3.1	2.0	2.1	0.5	2.0	0.8
5	ΔE_{hc+T_n}	**1.4**	**0.2**	**0.6**	**-0.2**	**0.2**	**0.3**	**0.4**	**0.5**
6	ΔE_{X+T_c}	2.7	1.1	4.7	4.5	-0.7	0.	2.0	2.1
7	ΔE_{X+T_n}	1.5	-0.4	2.2	2.3	-2.6	-0.2	0.5	1.7
8	ΔE_{hc+X+T_c}	2.7	0.9	1.6	1.9	-2.2	-0.2	0.8	1.6
9	ΔE_{hc+X+T_n}	1.5	-0.6	-0.9	-0.3	-2.2	-0.2	-0.5	1.1
10	$\Delta E_{hc+T_{eff}}$	1.5	1.3	1.2	1.1	0.6	0.5	1.0	0.4

Table 5.6: *Difference in MeV between the last and the first energy calibration measurement in the 6 long term experiments of 1995. The 10 lines correspond to different applied correction method.*

position, are applied. It implements that the contribution of the corrector magnets to beam energy changes is mainly given by a lengthening of the distorted orbit.

The data from the 6 long term experiments in 1995 favour a compensation for corrector magnet effects together with a correction for temperature effects according to the new parametrisation. Fig. A.9 to Fig. A.14 in Appendix A show the uncorrected and corrected energy and NMR data of the 6 fills. The upper part of the six figures gives the uncorrected readings from the two NMR probes and the E_{raw}-data as a function of time. Superimposed as a solid line is the prediction for the energy variation due to temperature effects according to Eq. 5.18. The temperature correction of the NMR readings is calculated according to Eq. 5.7 for the particular octants 4 and 8. The corrected NMR data are shown in the lower part of the 6 figures. The energy measurements are corrected using method (5). The dashed lines indicate a “perfect model” without any drifts. The evolution of the corrected energy measurements and the NMR data recorded in the 6 fills are interpreted as follows:

- **Fill 2929** (Fig. A.9)
  Between 18:00 and 22:00 energy data and NMR data do not record any significant deviation from the dashed line. Energy measurements confirm the rise seen by the NMR4 probe after 23:00. Shortly before 23:00 the huge scatter of the NMR

readings indicates a large perturbation by train leakage currents. Because of the good agreement between energy and NMR data the remaining difference of 1.4 MeV at the end can be considered to be caused by the Train Effect.

- **Fill 3022** (Fig. A.10)
  Energy data and NMR readings agree well at the start of the fill before 20:00. At that time a bending modulation was performed leading to an increase of about 1.3 MeV at NMR4 and NMR8. All B-field and energy measurements which happen to be later than the bending modulation are shifted by 1.3 MeV in order to compensate for the effect of the magnet conditioning. No remaining drifts are recorded by neither the NMR probes nor the energy measurements. Thus the Train Effect can be neglected in this fill.

- **Fill 3029** (Fig. A.11)
  Between 22:00 and 23:00 a Train Effect caused jump happens which affects the magnetic field recorded by NMR8 only. Considering a 5/8 * NMR4 + 3/8 * NMR8 distribution of the train leakage currents around the ring, the remaining ΔE of 0.6 MeV agrees perfectly with the Train Effect approach.

- **Fill 3030** (Fig. A.12)
  All drifts in this fill can be explained by temperature and corrector magnet effects. The temperature effect in octant 4 seems to be slightly over-compensated by the temperature correction. The energy difference between first and last measurements of $\Delta E = 0$ agree with the NMR data within less than 1 MeV.

- **Fill 3036** (Fig. A.13)
  Between 05:00 and 06:00 a passing train causes a jump in the NMR8 data. The NMR4 readings record a very weak decrease while the NMR8 readings are slightly increasing during the fill. A value of $\Delta E = 0.2$ MeV at the end of the fill agrees well with the (5/8 * NMR4 + 3/8 * NMR8) approach of the Train Effect.

- **Fill 3064** (Fig. A.14)
  Neither the NMR4 data nor the energy measurements reveal a deviation from the initial value during this fill. Only NMR8 seems to be affected by a Train Effect caused jump around 17:00. $\Delta E = 0.3$ MeV agrees with the Train Effect approach of (5/8 * NMR4 + 3/8 * NMR8) within less than 0.5 MeV.

Combining all 6 fills it can be concluded that the effect of the train leakage current in octant 4 is not scaled down by a factor of 1.7 but vanishing in 5 out of 6 cases. All other drifts recorded by NMR4 can easily be explained by temperature caused effects. NMR8 is affected by the train leakage currents in 3 out of 6 cases. The remaining variations agree entirely with the predictions from the new temperature model and corrector magnet settings. The change of the beam energy, which can be attributed to the Train Effect, is in all cases less than 1.4 MeV and in average about 0.4 MeV (method 5). Using a slightly modified parametrisation, which is based on the effective ring temperature coefficient, the remaining drifts are for all fills less than 1.5 MeV and in average 1 MeV (method 10). Hence about 30% of the average raw rise can be attributed to the Train Effect. The difference between the two mean values accounts for the uncertainty in the prediction of the Train Effect caused rise.

5.3.2 1992, 1993 and 1994

The same exercise has been performed for the available energy calibration data sample in the years before. Unfortunately no B-field measurements in the tunnel were acquired. Data, from 2 fills in 1992, 5 fills in 1993 and 1 fill in 1994, which cover more than 4 hours, are available for a verification of the above assumptions. In the following discussion the two fills in 1992, which are presented in Fig. A.1 and Fig. A.2, are excluded. At that time, the newly developed resonant depolarisation method was set in for energy calibrations and nobody was experienced in its operation. The NMRREF probe was installed in the reference magnet without the field plates causing less reproducible readings. Thus both data sets record large fluctuations, which are not meaningful. Various methods have been applied to correct the energy calibration data E_{pol}:

(1) Only tide corrections are applied to E_{pol}.

$$E_{raw}(t) = E_{pol}(t) + \Delta E_{tide}(t) \tag{5.29}$$

(2) E_{raw} is corrected for temperature drifts according to Eq. 5.7:

$$E_{T_{eff}}(t) = E_{raw}(t) + \Delta E_{T_{eff}}(t) \tag{5.30}$$

(3) E_{raw} is corrected for temperature drifts according to Eq. 5.18:

$$E_{T_n}(t) = E_{raw}(t) + \Delta E_{T_{new}}(t) \tag{5.31}$$

(4) E_{raw} is corrected for drifts recorded by NMRREF only.

$$E_{REF}(t) = E_{raw}(t) + \Delta E_{NMRREF}(t) \tag{5.32}$$

(5) E_{raw} is corrected for temperature drifts according to Eq. 5.18 and for drifts recorded in the reference magnet.

$$E_{REF+T_n}(t) = E_{raw}(t) + \Delta E_{T_{new}}(t) + \Delta E_{NMRREF}(t) \tag{5.33}$$

Data from the horizontal corrector magnets are available for most of the 1993 scan data. Since only minor changes are recorded, a correction for the corrector settings has been neglected. Data from the horizontal orbits are not available for these fills. The difference ΔE between the last and the first energy measurement after applying the various methods is listed in Tab. 5.7. The number in each row indicates the type

		fill number							
	method	1636	1734	1772	1811	1849	2234	mean	RMS
1	ΔE_{raw}	1.2	2.2	7.8	-1.2	3.5	0.5	2.3	2.8
2	$\Delta E_{T_{eff}}$	-0.1	0.8	5.0	-1.2	3.5	0.4	1.4	2.1
3	ΔE_{T_n}	-0.3	0.5	4.3	-1.2	3.4	0.4	1.2	2.0
4	ΔE_{REF}	1.3	1.75	6.5	-0.3	1.2	-0.1	1.7	2.3
5	ΔE_{REF+T_n}	**-0.2**	**0.**	**3.1**	**-0.3**	**1.1**	**-0.2**	**0.6**	**1.2**

Table 5.7: *Difference in MeV between the last and the first energy calibration measurement in the 6 long term experiments of 1993 and 1994. The 5 rows correspond to different applied correction methods.*

of correction method as listed above. The mean value and the RMS scatter of the variation of ΔE with the fill number is shown in the last two columns. The mean value indicates the remaining average rise, which can be attributed to the Train Effect. The scatter of the raw energy differences in Tab. 5.7 is somewhat larger than in Tab. 5.6. While in 1995 all long term fills start with an energy calibration, most of the 1993 and 1994 calibration data are acquired at the end of the fill after several hours of operation in physics mode. The scatter is reduced by about 30% once a temperature correction is applied (method 2 and 3). No significant difference appears between the effective (2) and complete (3) new temperature approach. An application of method 4 (NMRREF only) gives slightly worse results. Applying both, a correction for reference magnet drifts and temperature drifts, reduces significantly the RMS scatter. The results from this method are highlighted in Tab. 5.7. The small scatter seems to implement that the reference magnet records true bending field drifts, which affect the beam energy. It is not known, which kind of effect could be related to field changes in the reference magnet on one hand and to variations of the beam energy on the other hand. However, the mean drift of 0.6 MeV, which remains, is consistent with the result from the 1995 data. The RMS scatter is enlarged by a factor of 2 with respect to the favourite method in 1995.

The data from the 8 long term experiments in 1992, 1993 and 1994 favour a compensation for field drifts in the reference magnet in combination with a correction for temperature effects according to the new parametrisation. Fig. A.1 - Fig. A.8 in Appendix A show the uncorrected and corrected energy and NMRREF data of the 8 fills. The upper part of the figures shows the readings from the NMRREF probe and the E_{raw}-data as a function of time. Superimposed as a dashed line is the prediction for the energy variation due to temperature effects according to Eq. 5.18. The corrected and uncorrected energy calibration data are shown in the lower part of the 8 figures. The energy measurements are corrected using the favoured method (5). The dotted lines indicate a “perfect model” without any drifts. The evolution of the corrected energy measurements in the 8 fills are interpreted as follows:

- **Fill 1439** (Fig. A.1)
  The fluctuation of the energy data as well as the NMRREF data in this fill is consistent with small temperature caused drifts only. Since only the mean ring temperature was recorded, the temperature behaviour is parametrised according to the effective temperature model. Although the NMRREF readings without field plate are less reliable, a correction according method 5 does not change the scatter of the data points around the perfect model significantly.

- **Fill 1440** (Fig. A.2)
  The fluctuation of the energy data as well as the NMRREF data in this fill is consistent with small temperature caused drifts only. Since only the mean ring temperature was recorded, the temperature behaviour is parametrised according to the effective temperature model. Although the NMRREF readings without field plate are less reliable, a correction according method 5 does not change the scatter of the data points around the perfect model significantly.

- **Fill 1636** (Fig. A.3)
  The whole drift seen by the energy calibration measurements can be explained by temperature variations only. No drifts of the field in the reference magnet are recorded for this fill.

- **Fill 1734** (Fig. A.4)
  The whole drift seen by the energy calibration measurements can be compensated by applying a temperature correction. Only very small drifts of the field in the reference magnet are recorded for this fill.

- **Fill 1772** (Fig. A.5)
  About 50% of the rise recorded by the energy data can be compensated by temperature effects. The NMRREF drifts do not exceed 1 MeV and are negligible. A significant change of the beam energy remains with indications for two jumps at 07:00 and 12:00. This fill is the only evidence for a Train Effect caused drift in 1993.

- **Fill 1811** (Fig. A.6)
  This fill is the only case with decreasing energy calibration measurements. No temperature changes occur. The first data point is acquired after more than 21 hours. Both, energy calibration measurements and NMRREF readings, have the same trend.

- **Fill 1849** (Fig. A.7)
  This data sample is equivalent to the third tide experiment (Fig. 5.33, bottom). The energy calibration measurements record a total integrated rise of about 3.5 MeV. About 75% of it, a rise of 2.5 MeV, is seen in the reference magnet. Temperature changes in this fill are very small. The NMRREF data

record 2 small jumps around 24:00 and around 05:00. It cannot be seen how far these two jumps are associated with beam energy changes. For the analysis of the terrestrial tides acting on the LEP beam energy, the resonant depolarisation data has been corrected for the drift recorded by the NMRREF device. Fig. 5.33 includes this correction. It indicates that the reference magnet drifts are related to true beam energy changes. Since the bending current does not change it is not known which effect could cause a rise in the reference magnet and the tunnel magnets simultaneously.

- **Fill 2234** (Fig. A.8)
  Around 16:30 a jump of 2.2 MeV, recorded by the NMRREF probe, occurs. This jump is considered to be due to a current spike in the main bending power converter. About 30% of this jump can be confirmed by energy calibration data. It is consistent with the effect of reduced jump sizes recorded by the NMRVAC probe with respect to NMRREF. The reduction is due to the vacuum chamber surrounding the beam.

Combining all 8 fills it can be concluded that the Train Effect accounts for about 30% of the average raw rise seen in all fills. It is consistent with the results from the 1995 data, although in 1993 no rise could be attributed to horizontal corrector settings as it is in 1995. The change of the beam energy, which can be attributed to the Train Effect, is in one case about 3 MeV and in average 0.6 MeV (method 5). The remaining variations agree entirely with the predictions from the new temperature model combined with correction for reference magnet drifts. It remains unclear, which relation could exist between the observed reference magnet drifts and the beam energy.

5.4 Summary of Beam Energy Variations

The analysis of the 1995 energy scan data revealed an additional and important source of beam energy variations, which was not known previously. Other already known effects have been carefully reevaluated and some were found to be negligible. The results have been discussed in detail in this chapter and may be summarised as follows:

- The Train Effect contributes significantly to the mean energy rise during a fill. An increase of 1 to 2 MeV in a fill could be verified with the long term experiments.
- The effect of temperature changes was underestimated in 1993. New insight into the temperature dependence of the dipole field allows much more reliable corrections. The predicted effect for the whole LEP ring is a drift of about 2 MeV in a typical fill in 1993 as well as in 1995.
- The effect of horizontal correctors could be studied empirically and by simulation in 1996. In 1993 the full effect was taken as an error. Now it could shown that

this effect is as predicted by simulation and the assigned uncertainty could be reduced significantly. Occasionally this effect can amount up to 3 MeV in certain fills.

- The observed orbit drifts during fills are most likely only partially related to real energy changes. There is some evidence that the horizontal correctors account already for these drifts. Therefore orbit drifts inside fills will not longer be corrected for and an error will be assigned to this uncertainty. The mean horizontal orbit in a fill is still used to calculate fill-to-fill fluctuations of the mean beam energy.

- Except for variations of the bending current, drifts in the reference magnet are not considered to reflect changes of the beam energy. The correction for NMRREF drifts, as done in 1993, will be omitted and the uncertainty induces a systematic error[4].

The various contributions to the beam energy variation during fills were combined to a beam energy model. The model will be described in the last chapter of this thesis. In order to be able to predict IP dependent energy variations, effects which are discussed in the following chapter have to be taken into account. The systematic errors on the beam energy, which are related to the various model ingredients, result from a comparison between the model prediction and the energy calibration data from resonant depolarisation. The complete model and the resulting systematic errors will be discussed in the last chapter.

[4]Doubts remain for this conclusion, since in some cases in 1993 correlations were seen between the beam energy and the NMRREF readings. However, during 1995 the shifts observed in the reference magnet are negligible for almost all fills.

Chapter 6

Local CM Energy Corrections

Because of energy losses from synchrotron radiation, the energy of the beam depends on the longitudinal position along the ring. Energy calibrations by resonant depolarisation give the average energy of the bunches and are insensitive to local deviations. Local effects can cause shifts of the centre-of-mass energies at the experimental interaction points: the centre-of-mass energies then no longer correspond to twice the average beam energy. There are two known sources for centre-of-mass energy shifts at the IPs:

- **The RF System**:
  Misaligned cavities and phase errors give rise to local changes of the centre-of-mass energy.

- **Dispersion**:
  Under certain circumstances, vertical dispersion at the IPs leads to shifts of the centre-of-mass energy if the beams collide with some transverse offsets.

The energy corrections at the IPs depend on LEP machine parameters, which have to be monitored to be able to compute the accurate centre-of-mass energies for each experiment. The desired sampling rate for all quantities affecting the average beam energy is approximately 15 minutes. The relevant information about the vertical offsets at the IPs and the RF system was monitored automatically and stored in a database. Due to logging problems some gaps in this database had to be filled by interpolating between valid reading.

6.1 Effects of the RF System on the CM Energy

As bunches move along the ring, they loose energy due to synchrotron radiation, which is compensated by acceleration in RF cavities. Since the RF cavities are not distributed homogeneously along the ring, the beam energy depends on the longitudinal position along the ring. The centre-of-mass energy (E_{cm}) is the sum of the two local beam energies and is not necessarily constant along the circumference. Resonant depolarisation is only sensitive to the average energy of the beams in the fraction of the machine which is equipped with bending magnets. Additional corrections to E_{cm} are needed to take local deviations from the average into account. This chapter describes an analysis of E_{cm} shifts at the four IPs, which are caused by the interplay of the LEP beams with the RF system and other LEP components. Systematic errors are estimated by comparing the agreement between model predicted and measured LEP parameters.

6.1.1 Position of the RF Cavities

The energy loss due to synchrotron radiation was compensated in 1993 by a set of copper cavities (CU-RF), symmetrically distributed along the straight sections around IP2 and IP6. Copper cavities are operated at room temperature. In 1995 the superconducting RF cavities (SC-RF), foreseen for LEP II, were tested during the energy scan. For a large fraction of 1995, LEP was operated with a highly asymmetric RF configuration, since the SC cavities were being tested at high accelerating gradients and most of them were installed around IP6. Fig. 6.1 shows a schematic view of the

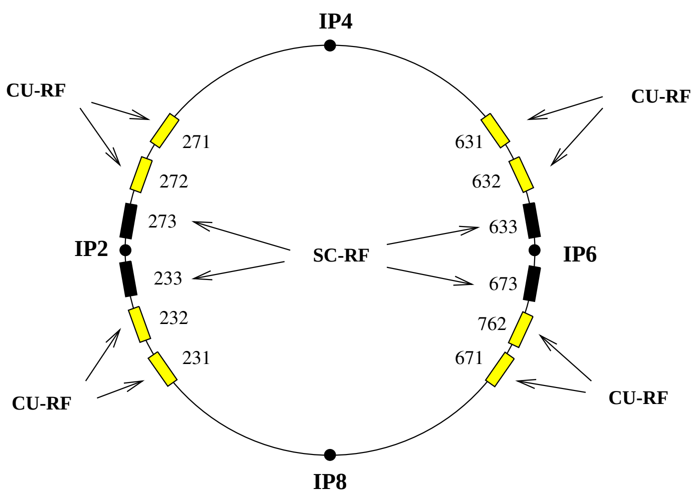

Figure 6.1: *Graphical view of the LEP RF configuration in a large fraction of 1995. SC cavities around IP2 and IP6 are drawn.*

RF configuration of LEP at the end of the 1995 scan. The SC cavities around IP2 were used for the last part of the scan only.

6.1.2 The RF Model

The deviations from the average E_{beam} as a function of the position along the ring are drawn schematically in Fig. 6.2. The beam looses energy due to synchrotron radiation

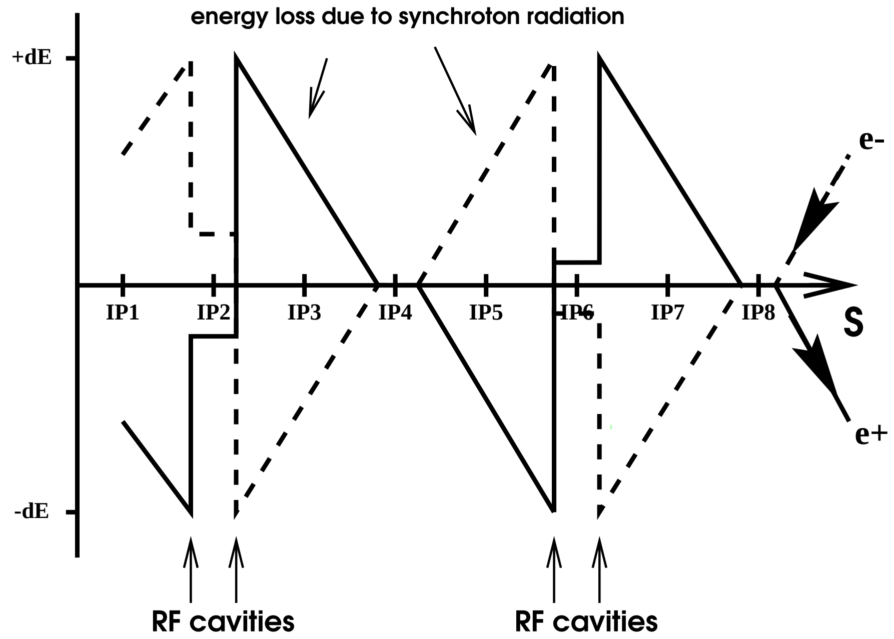

Figure 6.2: *Schematic view of the energy deviation from the nominal beam energy as a function of the position along the ring. Because of its shape this distribution is called the "energy sawtooth". Energy losses are due to synchrotron radiation and gains originate from the RF cavities located around IP2 and IP6.*

in the LEP arcs between the positions of the RF cavities, which provide the necessary energy gain per turn. Because of its typical shape this effect is referred to as the "energy sawtooth". Ideally the sum of the electron and positron energy does not depend on the azimuthal position because of the symmetry of the sawtooth. However, due to misaligned cavities or phase errors local shifts of the centre-of-mass energy occur at the interaction points. Hence corrections to the average beam energy must be applied to obtain the correct value of E_{cm} at the IPs. The shifts are calculated by a **RF model** from the difference in energy gain on the incoming side and on the outgoing side. In the simulation of this RF model the average stable phase angle of each bunch is determined by setting $E_{loss} = E_{gain}$ per turn. The energy loss is given by the bending radius of LEP, the beam energy and the wiggler currents. The energy gain in the cavities depends on the RF voltage, their phases, the cavity positions and the bunch currents. The modelling of the corrections at each IP is carried out by an iterative calculation of the synchronous RF phase angle ψ_s incorporating all of the known energy losses and gains of the circulating beams. Energy shifts calculated by the model are relative to the average beam energy, which is measured by resonant depolarisation.

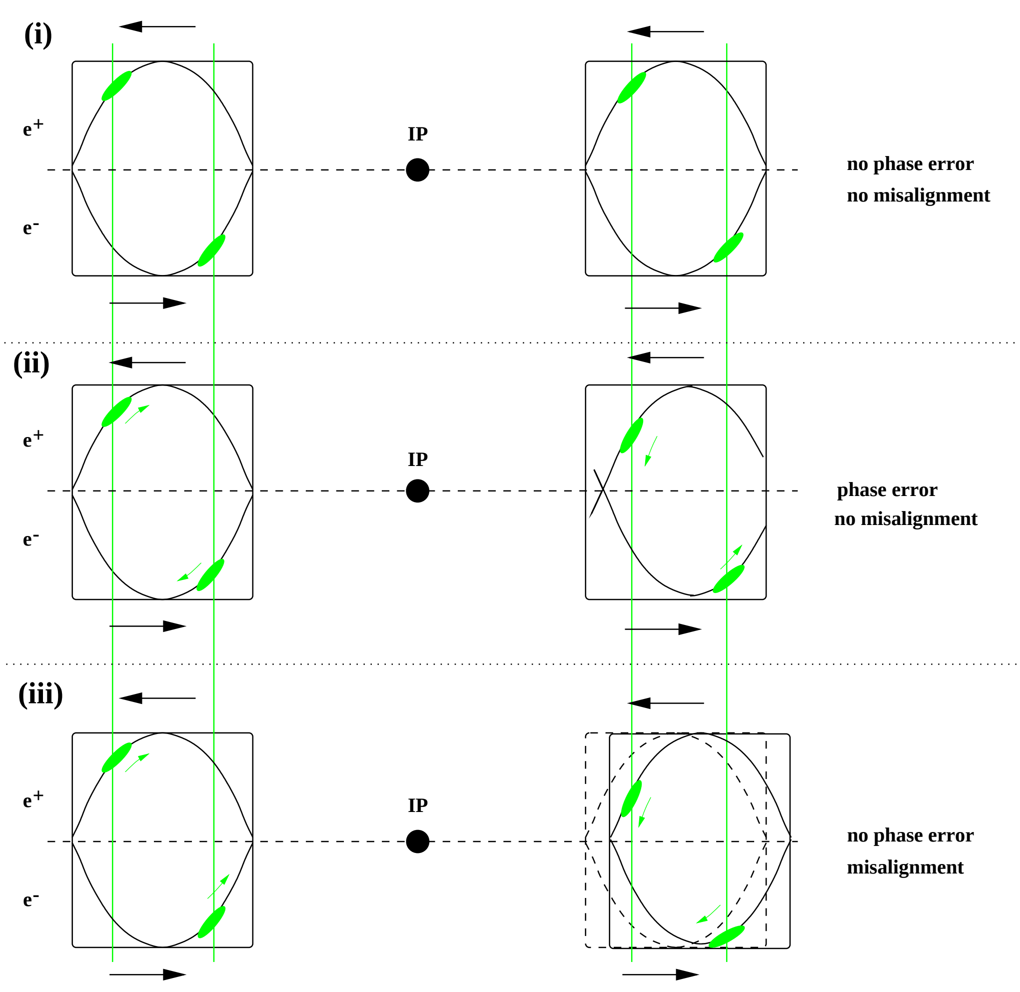

Figure 6.3: *Schematic view of two cavities with an illustration of the RF voltage curve around an IP. The vertical lines indicate the nominal phases of the incoming and outgoing bunches. (i) No phase error and no misalignment. Both counter-rotating bunches gain the same energy. (ii) Right cavity with phase (timing) error. The instantaneous effect on E_{cm} is compensated after a few turns by a change of the bunch phases on both sides, indicated by small arrows. No energy shift remains since the beam gains more energy on one side and looses energy on the other. (iii) Right cavity misaligned. The bunches move in phase, indicated by small arrows. The incoming electron bunch gains less energy causing a negative shift of E_{cm} at the IP. This effect cannot be compensated.*

In the model calculation various parameters and related effects were incorporated, which influence the size of the energy shifts. Most of them are caused by cavity misalignment. In the following a detailed account of the individual sources of energy offsets is given:

- **Cavity Misalignment**
  Ideally, in a case of a perfect RF system without any misalignment of the in-

dividual cavities, no E_{cm} shifts would occur. See Fig. 6.3, (c), to illustrate the effect. By mistake, the CU-RF units were aligned with respect to the lower of two frequencies, f_1 and f_2, at which the copper cavities of LEP are operated. In the copper cavities, the microwave energy oscillates between the storage cavities and the accelerating cavities with a frequency corresponding to the difference between these frequencies. It is eight times the revolution frequency of the beams. The actual RF-frequency seen by the beams is the average of f_1 and f_2: $\overline{f_{RF}} = \frac{1}{2}(f_1 + f_2)$. Therefore the cavities appear to be placed too far from the interaction point. The particle bunches arrive too early in the first set of cavities with respect to the phase of the accelerating voltage and gain an energy which is higher than the energy gain in the second set of cavities on the other side of the interaction point, where they are late in phase. Due to this effect, an average phase error ψ_e of about -10^o appears. ψ_e depends on the distance of the centre of the RF units from the interaction point and the accidental alignment of the cavities to f_1 instead of $\overline{f_{RF}}$. The energy offsets per beam at the interaction point can be calculated from the difference of the accelerating voltage, U_{RF}, on the incoming and outgoing side and the phase angles:

$$\Delta E_{beam}(IP) = \frac{1}{2}\left(U_{RF}^{in}\sin(\psi_1 + \psi_e) - U_{RF}^{out}\sin(\psi_1 - \psi_e)\right) \quad . \tag{6.1}$$

ψ_1 is the stable phase angle of the bunches with respect to f_1 and was about 150^o during the 1993 running period. The RF voltage $U_{RF}^{in} \simeq U_{RF}^{out}$ was typically 260 MV at the peak energy. Inserting the numbers, one obtains an energy offset of $E_{beam}(IP) \simeq 9$ MeV [33]. Variations in the RF configurations can lead to shifts in the z vertex position at the interaction points, which can be used to verify the model. In addition to this systematic misalignment all RF units are also subject to random alignment tolerances.

- **Phase error**
  As a consequence of phase (timing) errors the beam has to adapt its stable phase in all cavities in order to balance energy gains and losses. The beam will sit at a different phases for each cavity (Fig. 6.3, (b)). No CM energy shift appears for symmetry reasons. However, at the presence of some misalignment, the collision energy is affected by the phase error.

- **RF Voltage**
  The total active RF voltage at a given time is normally set to obtain a certain value of Q_s giving the best luminosity. The trip of one or more RF cavities changes the integral voltage seen by the beam or leads to a modification of the RF distribution to compensate the local losses. The individual voltages of the RF units are the most important input parameter of the model. Voltage induced into the switched off cavities by the beam reduces the available voltage (**beam loading effect**). The voltage V_0^{left}, which is left in a cavity after the passage of a bunch that enters the straight section, is given by:

$$V_0^{left} = \sqrt{V_0^2 - I_b \cdot h \cdot \sin\psi_s \cdot C_{unit}} \qquad , \tag{6.2}$$

where V_0 is the initial peak voltage, ψ_s is the synchronous phase (according to Eq. 3.24), h is the harmonic number and I_b the bunch current. C_{unit} is a constant depending on the impedance of the particular RF unit. The effective voltage seen by the bunch is $V_0^{eff} = \frac{1}{2} \cdot (V_0 + V_0^{left})$. A bunch leaving the straight section sees a reduced effective voltage, because the cavity filling time is long compared to the time between the passage of two counter-rotating bunches. The reduced voltage corresponds to V_0^{left}, leading to small shifts in E_{cm} (about 0.5 MeV) at IPs surrounded by RF cavities.

- **Beam Current**
  The effective voltage in cavities, which are switched on, as well as the induced voltage in switched off cavities depends on the current of the bunch passing through the cavity. Since the effective voltage depends on the amount of energy taken out of the RF system, Q_s also varies with the bunch current.

- **Wiggler Current**
  Wiggler magnets consist of an arrangement of many short dipoles with alternating polarity. At collision with high beam currents they are used to blow up the transverse bunch sizes to control the strength of the beam-beam interaction. The current in the wiggler magnets (wiggler current) is varied with the bunch current. At low bunch currents (i.e. about 200 μA per bunch) LEP can be operated without wigglers. The wiggler magnets increase the synchrotron radiation losses, affect the shape of the energy sawtooth and vary the synchrotron tune Q_s (Eq. 3.27).

- $\Delta l_{2\leftrightarrow 6}$
  $\Delta l_{2\leftrightarrow 6}$ is the effective path length difference between IP2 and IP6 along the two half-circles of LEP. In the case of asymmetric RF power at IP2 and IP6, the effective path lengths of electrons and positrons become different, leading to different RF phases. The effect is equivalent to moving all of the cavities towards or away from the interaction points. This leads to small energy shifts at interaction points IP2 and IP6. ($<$ 0.1 MeV). If $\Delta l_{2\leftrightarrow 6}$ is large, the effect reaches about 1 MeV at IP4 and IP8.

The model contains some "free" parameters, the phase of each RF unit ($\pm 10^o$ max.), the voltage calibration scale ($\simeq$ 2 %) and the overall reference point of the RF unit z-position (arbitrary). The 1995 RF model includes additional features, which are specific to the running conditions and diagnostic tools during the 1995 scan:

- The bunch train scheme implied the simulation of ψ_s for each bunch in a train. The spacing and the different positions on the RF voltage envelope are taken into account.

- The SC-RF are implemented including their individual alignment and calibration constants.

- Because the total available voltage was much larger than the required 260 MeV some CU-RF units were left off. A model was therefore required to describe the interaction of the beams with unused cavities.
- A new diagnostic tool was implemented with the BOM data.

6.1.3 Constraints on the RF Model

Mainly three quantities are used to tune the agreement between the RF model and LEP data:

1. The measured value of Q_s is compared to the value calculated from the model.
2. The calculation of the so called R_{BOM} has been implemented into the model as a new diagnostic tool. The measured size of the difference between electron and positron orbits on both sides of IP2 and IP6 is compared to the predicted one.
3. Longitudinal shifts of the collision point in the IPs along the beam axis, the z vertex position, can be predicted from the model. A comparison of the predicted shifts with the measured shifts provides another way of cross-checking the model's validity.

Any correction applied to the phasing of RF units has to improve the agreement between calculated and measured Q_s. Knowing the phase angles in each cavity, the synchrotron tune Q_s can be calculated from the sum of the energy derivatives of all Nb bunchlets:

$$Q_s = \sqrt{-\frac{h\,\alpha_c}{2\pi\, E_{beam}} \sum_i^{Nb} \frac{dE^i}{d\psi_s^i}} \quad , \tag{6.3}$$

where h is the harmonic number, α_c is the momentum compaction factor and $dE/d\psi_s$ is the gradient of the bunchlet energy with respect to the stable phase angle ψ_s for that bunchlet. The gradient is the part, which is actually calculated by the model. The comparison of the calculated and the measured Q_s is one of the most powerful constraints on the predictions of the RF model. It provides an important cross-check on the consistency of the input parameters. It is used to calibrate the RF voltages and it is the final arbitrator when more than one correction is possible and no other phasing information is available. The precision of the measured Q_s values is about 1 Hz for a typical synchrotron frequency of 700 Hz. The expected average difference $\Delta Q_s = < Q_s^{meas} - Q_s^{calc.} >$ for a perfect model is zero. Table 6.1 lists the values obtained in 1993 [83] and 1995 [84]. Fig. 6.4 shows the difference between the 1995 measured Q_s and that calculated from the updated RF model. The RMS of the distribution is used

model	ΔQ_s	RMS
1993	$0.7 \cdot 10^{-3}$	$0.4\ 10^{-3}$
1995 data, tuned model	$< 1 \cdot 10^{-4}$	$0.8\ 10^{-3}$

Table 6.1: *The average difference between the measured and the calculated Q_s for 1993 and 1995.*

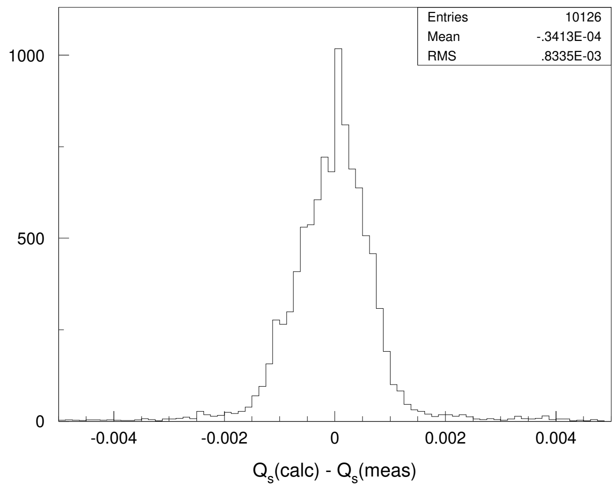

Figure 6.4: *The difference between the measured Q_s and the value, which is calculated from the tuned RF model. Only 1995 data are taken into account. The plot is taken from [84].*

to estimate the systematic error. The mean value, which is close to zero, demonstrates the good agreement between model prediction and data. The RMS value is twice as large as in 1993 because the modelling of the SC cavities and the switched off CU cavities seems not to be good enough.

Orbit measurements with the LEP BOM system are used to cross-check the RF model in 1995. They allow to monitor the energy sawtooth. The R_{BOM} parameter combines the measured size of the difference of the electron- and positron-orbit ΔX on both sides of IP2 and IP6:

$$R_{BOM} = \frac{|\Delta X_{IP2,left}| + |\Delta X_{IP2,right}|}{|\Delta X_{IP6,left}| + |\Delta X_{IP6,right}|} \quad . \tag{6.4}$$

R_{BOM} is sensitive to the relative phase of the RF between IP2 and IP6 only. It can also be calculated within the RF model. Typically 4 BOM pickups are averaged to determine ΔX. The resolution achieved with R_{BOM} is approximately 3 % and corresponds to a sensitivity of less than 3^o on the relative phases. In the calculation, R_{BOM} is based on the modelled energy gains and losses. The ratio of the calculated and the measured R_{BOM} reveals whether or not the phases of the RF cavities, which are input parameters to the model, are correct. During the process of the model tuning

R_{BOM} is used to check the RF phasing in the model and any discrepancies are removed once they are understood. The expected result of a perfectly tuned model is a R_{BOM} ratio of 1 for the combined data sample. Fig. 6.5 shows the ratio distribution for the

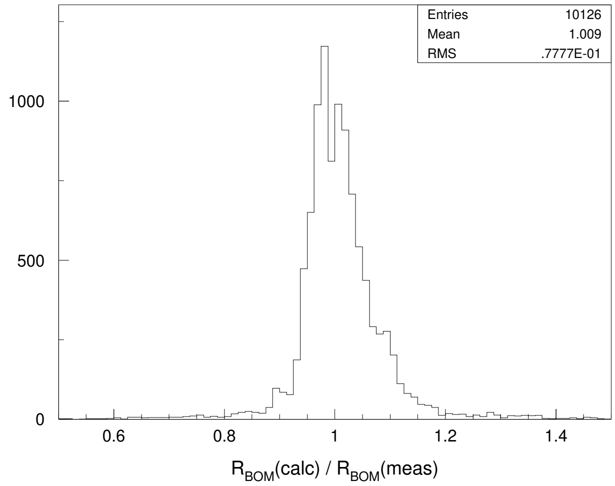

Figure 6.5: *The ratio between the measured R_{BOM} value and the value calculated from the RF model. The ratio is derived from the 1995 data only. The plot is taken from [84].*

1995 scan. The mean of the distribution has been tuned to 1 giving a RMS value of 0.08, which is much larger than the resolution indicating some intrinsic weakness of the model.

Since energy gains of electrons and positrons are different in the presence of alignment errors and RF voltage asymmetries, the two beams move to different stable phase angles in response to voltage changes. This implies a shift of the collision point of the two bunches, which is the same at all interaction points. Such shifts of the vertex position can be measured by the experiments and predicted by the model. A comparison between experimental results and the RF model predictions for the position of the luminous region in z for the individual bunchlets was made. Fig. 6.6 shows the average vertex position in z as a function of time. In this overview the agreement between the measured average vertex position from the four LEP experiments and the predictions of the RF model is reasonably good. However, at the end of the scan period, between day 266 and 270, discrepancies of approximately 1 mm occur. Various effects, which could cause such a large vertex shift, were considered and investigated but most of them could be excluded. Two possible effects remain, which cannot be verified easily: (i) A shift of approximately 0.5 cm of all SC cavities towards the IP. (ii) A path length difference $\Delta l_{2\leftrightarrow 6}$ of 0.85 cm. In principle, the uncertainty on the SC cavity alignment is too small to explain the effect and only very small arc length differences are suggested by the alignment data. Therefore further studies will be necessary to obtain a self-consistent answer. For the time being this residual discrepancy is taken as a systematic error. The position of the individual bunchlet vertices can also be predicted by the model. Fig. 6.7 shows a summary of the model-data agreement on the collision points of the three bunches A, B and C. In the data bunchlet B is much closer to C than to A before day 266, later the spacing is more symmetric. The bunch spacing in the model is produced by an asymmetric RF configuration and the fact that the

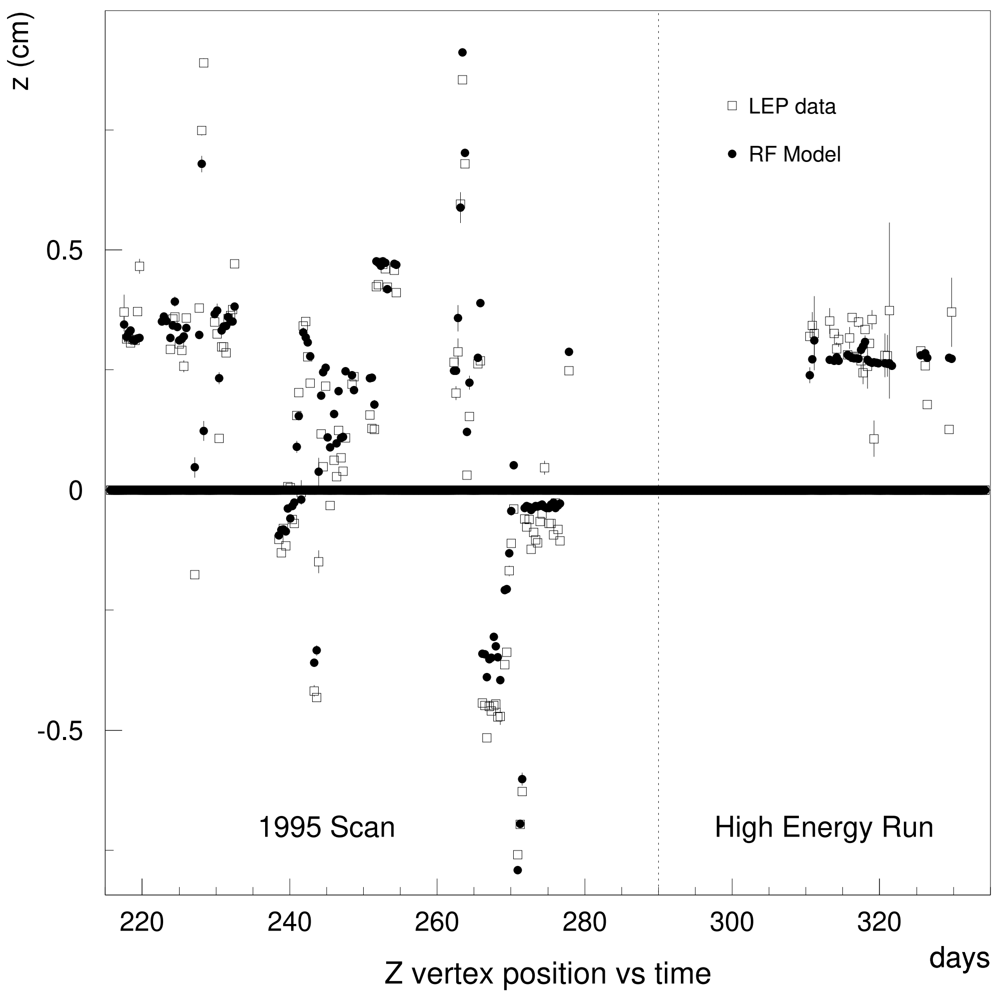

Figure 6.6: *Measured and predicted positions of the average z vertex for all of the 1995 running as a function of time. Data from the LEP high energy run at 65-68 GeV are also included. The LEP data are represented by the mean of the four experiments. The RF model corresponds to the 1995 version. The figure is taken from [84].*

voltage envelope of the CU cavities cannot be at maximum for all bunchlets passages. Although the model predicts the correct trend, it fails to describe the magnitudes of the bunchlet spacing. The largest deviation from the simulation of the effect, was first taken as an estimate of the residual systematic error. The effect of the longitudinal shifts is simulated in the RF model by constraining the difference in stable phase angle. The new studies and the procedure are described in [85]. After these studies the systematic error, which is assigned to this effect, could be reduced slightly.

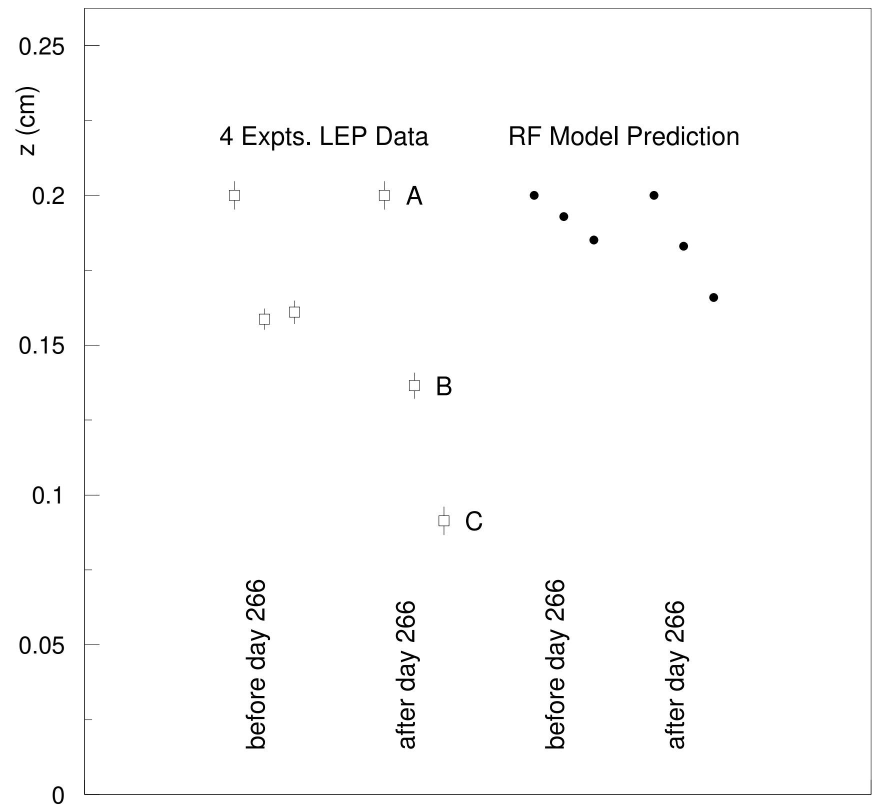

Figure 6.7: *Measured (squares) and predicted (closed circles) positions of the average z position of the collision points of the three bunchlets in a train. The bunchlets are labelled A, B and C. The data sample is split into two periods, one before and one after day 266. After day 266 the SC-RF became dominant. The figure is taken from [85].*

6.1.4 Energy Shifts and Systematic Errors

The energy shifts to be applied for both scans are listed in table 6.2 for each IP and the two off-peak energy points [83, 84]. A comparison between 1995 results and the RF model prediction of the collision point shows some deficiencies in the 95 model. The mean collision point and the z vertex position of the individual bunchlets cannot be predicted by the model adequately. These discrepancies are part of the remaining systematic error in the centre-of-mass energy. The effects of varying the corrections within some reasonable bounds of Q_s-agreement are considered as a systematic error. In detail, the following sources of systematic uncertainties were taken into account:

1. the shifts of the mean z vertex position (1995 only),
2. the difference $Q_s(e^+) - Q_s(e^-)$,
3. missing data,

	1993		1995	
IP	ΔE_{cm}(P-2)	ΔE_{cm}(P+2)	ΔE_{cm}(P-2)	ΔE_{cm}(P+2)
2	19.0	19.9	14.7	14.7
4	0.0	0.0	0.8	1.3
6	19.5	20.1	4.3	4.5
8	0.0	0.0	-0.9	-1.4

Table 6.2: *The corrections in MeV to E_{cm} for each IP and the two off-peak points arising from the 1993 and 1995 tuned RF model.*

4. the uncertainty in the difference of the path length between IP2 and IP6 along the two half-circles, $\Delta l_{2\leftrightarrow 6}$, (IP4 and IP8),

5. the voltage scale (for IP2 and IP6),

6. the RF misphasing (for IP2 and IP6),

7. the CU-RF misalignment (± 1 mm, 1993 + 1995), and the SC-RF misalignment (for IP2 and IP6, only 1995),

8. the shifts of the individual bunchlet z vertex position (1995 only), calculated for IP4/IP8 and IP2/IP6,

9. discrepancies between the predicted and the measured energy losses,

10. the uncertainty in the momentum compaction factor.

Tab. 6.3 gives the magnitude of each of the systematic errors. The numbering in the table corresponds to the numbers in the listing. If the error was estimated to be negligible small, no error is assigned.

Combining the various sources results in an uncertainty of about ± 0.8 MeV for IP2 and IP6 and ± 0.3 MeV for IP4 and IP8 in 1993 [33, 85]. A detailed analysis [84, 85] of the 1995 data leads to an error on the individual centre-of-mass energies at the experiments of approximately 0.6 MeV for IP4, IP6 and IP8. The energy offsets at IP2 have an error of about 1.1 MeV due to the large uncertainty in the position of the individual bunchlet z vertex. To obtain the precise overall errors the correlations between the various years, between the experiments and between the energy settings have to be taken into account.

error	IP	1993 ΔE_{CM} (MeV)	1995 ΔE_{CM} (MeV)
1	all	-	0.1
2	all	0.2	0.2
3	all	0.1	0.1
4	IP4,8	0.1	0.1
5	IP2	0.2	0.4
	IP6	0.2	0.1
6	IP2	0.3	0.1
	IP6	0.3	-
7	IP2	0.4	0.6
	IP6	0.4	0.5
8	IP2	-	0.8
	IP4,8	-	0.6
	IP6	-	0.1
9	IP2	0.6	0.3
	IP6	0.6	-
10	IP2,6	0.1	0.1

Table 6.3: *Systematic error contribution arising from various sources in 1993 and 1995.*

6.2 Vertical Dispersion at the IPs

The simultaneous presence of vertical dispersion with opposite sign for the two beams and of vertical collision offsets at the IPs causes local energy shifts. Such a situation occurred in 1995, when LEP was operated in the "bunch train mode". Early estimates of the energy shifts indicated that the 1995 energy scan could only take place with a tight control of the collision offsets. However, prior to the scan techniques to minimise the dispersion effect were improved and became operational tools for the energy calibration task.

6.2.1 The Effect of Opposite Sign Dispersion

The qualitative effect of vertical dispersion combined with vertical collision offsets is explained by the drawing shown in Fig. 6.8.

(a) Electron and positron beams collide without offset. The dispersion function has the same sign for both beams. Particles with negative ($-\Delta E$) and positive ($+\Delta E$) energy deviation from the nominal beam energy collide with each

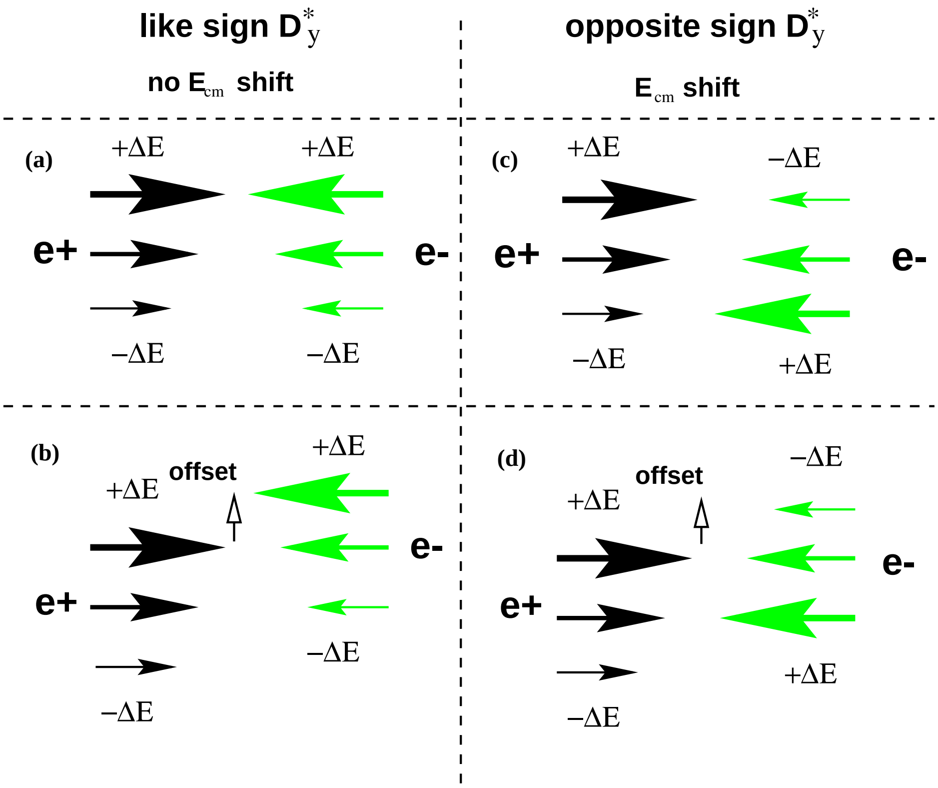

Figure 6.8: *Schematic view of the mechanism of energy shift at the presence of vertical dispersion at the IP. In the cases (a) and (c) without collision offset, no energy shift is introduced. In case (d) a collision offset coincides with opposite sign dispersion and an energy shift results. No shift arises in a situation of collision offsets at the presence of like sign dispersion (b).*

other. The nominal centre-of-mass energy is maintained:
$2 \cdot (-\Delta E) \; + \; 2 \cdot (+\Delta E) \; = \; 0 \qquad .$

(b) Electron and positron beams collide with an offset. The dispersion function has the same sign for both beams. Low energy particles of the e^+ beams and high energy particles from the e^- do not collide. Again no deviation from the nominal centre-of-mass energy is found:
$(-\Delta E) \; + \; (+\Delta E) \; = \; 0 \qquad .$

(c) Electron and positron beams collide without offset. The dispersion function has the opposite sign for both beams. The negative $(-\Delta E)$ energy deviation in one beam compensates the positive $(+\Delta E)$ energy deviation in the other beam and vice versa. On average e^+ and e^- collide at the nominal E_{CM}:
$(-\Delta E) \; + \; (+\Delta E) \; + \; (-\Delta E) \; + \; (+\Delta E) \; = \; 0 \qquad .$

(d) Electron and positron beams collide with offset. The dispersion function has the opposite sign for both beams. Low energy particles of both beams do not collide but the high energy particles do. The average energy deviates from the expected centre-of-mass energy, i.e. twice the nominal beam energy. In this simplified illustration the energy shift ΔE_{CM} is equal to ΔE.

$$\frac{1}{2} \cdot [(+\Delta E) \ + \ (+\Delta E)] \ = \ +\Delta E \qquad .$$

A quantitative estimate has been performed in [86]. The presence of opposite sign vertical dispersion ΔD_y^* of electrons and positrons at the IPs leads according to Eq. 3.17 to shifts in the centre-of-mass energy. The energy shift ΔE_{cm} is a function of the collision offset Δy:

$$\Delta E_{CM} = -2\Delta y \frac{\Delta D_y^* \sigma_E^2}{E_0 \sigma_b^2} \qquad . \tag{6.5}$$

σ_E is the energy spread, σ_b the vertical bunch size and E_0 the nominal energy. In our case, the vertical dispersion of opposite sign is created by the bunch train bumps. The size of the effect increases with the vertical dispersion, the collision offset and the energy spread. It is reduced when the vertical bunch size increases.

Tab. 6.4 gives an overview of the size of the rather dramatic effect, which was expected prior to the 1995 scan [86, 87]. In general, bunch currents of 300 μA were typical for the LEP operation during the 1995 scan. Since the maximum vertical separation Δy_{max} between the bunchlets of the two counter rotating trains is affected by beam-beam kicks, it scales with the bunch current. Collision offsets of about 1 μm still

I:	bunch current $I_b = 0.5$ mA			
	IP2	IP4	IP6	IP8
$< \Delta D_y^* >$ (mm)	2.00	-1.25	1.85	-1.10
3 Bunches/Train : a,b,c				
Δy_{max} (μm)	4.0	4.1	4.1	4.1
ΔE_{max} (MeV) [$\sigma_y^* = 5\mu$m]	24.8	17.0	23.6	15.6
ΔE_{max} (MeV) [$\sigma_y^* = 7\mu$m]	13.6	9.0	12.8	8.0
II:	bunch current $I_b = 0.3$ mA			
$< \Delta D_y^* >$ (mm)	2.0	-1.0	1.9	-0.9
3 bunches/train : a,b,c				
Δy_{max} (μm)	2.5	2.6	2.6	2.5
ΔE_{max} (MeV) [$\sigma_y^* = 5\mu$m]	18.4	10.8	18.4	9.4
ΔE_{max} (MeV) [$\sigma_y^* = 7\mu$m]	10.2	5.6	10.2	5.0

Table 6.4: *Shifts of the centre-of-mass energies at two different bunch currents and for two bunch sizes. A certain curved shape in the vertical plane of the bunch train is assumed for this calculations. σ_E/E was set to $1 \cdot 10^{-3}$. The size of the vertical dispersion at the IPs was predicted by theoretical calculations, using slightly different scenarios. y_{max} is the distance of the bunchlet, which is most displaced, from the optimal position. ΔE_{max} corresponds to the maximal difference in the CM energies between the different bunchlet collisions at the IP.*

lead to centre-of-mass energy shifts of several MeV in the scenario of the lower part of Tab. 6.4. An expected shift of several MeV due to the dispersion effect was finally evaluated in the preparation phase of the 1995 scan [88]. Some dispersion effect might also appear in Pretzel operation because of coupling or optic imperfections. The size of the energy shifts related to dispersion effects was reevaluated in 1995 [89]. The results of the reevaluation are given at the end of this section together with the 1995 results.

6.2.2 Minimisation of the Dispersion Effects

It is evident from Eq. 6.5 that the energy shift can be minimised by keeping Δy as small as possible. An obvious way to control Δy is to maximise the luminosity since Δy and $\mathcal{L}$ are correlated through the relation:

$$\mathcal{L} = \mathcal{L}_0 \cdot \exp\left[-\frac{\Delta y^2}{\sigma_b^2 + \Delta D_y^2 \sigma_E^2}\right] \quad , \tag{6.6}$$

where $\mathcal{L}_0$ gives the luminosity for $\Delta y = 0$. Maximisation of the luminosity was realised by regular beam separation scans, where e^+ and e^- beams are scanned relative to each other in the vertical plane. These scans were later called “Vernier Scans”[1]. They were performed using vertical electrostatic separators, which will be referred to as vernier separators. The luminosity was measured with the LEP luminosity monitors, which detect Bhabha pairs at small angles with $0.6\,\text{mrad} \leq \theta \leq 11.8\,\text{mrad}$ [90]. The scans were performed for each IP separately. A Gaussian fit is applied to obtain the optimal adjustment y_{opt} for a minimum collision offset (i.e. the Vernier setting at maximum luminosity). Fig. 6.9 shows the results for the three bunches in train of a typical Vernier Scan. In 1995, this technique was improved and successfully operated to control the opposite sign dispersion effect. The data for all three bunchlets are shown separately. The luminosity from bunchlets A, B, C can not be maximised simultaneously. However, the resulting average energy shift at $y = y_{opt}$ has been calculated to be less than 0.2 MeV [86] and can therefore be tolerated. To achieve an accuracy on the Z mass of better than 1 MeV, systematic offsets from y_{opt} larger than 0.3 μm need to be avoided. For this reason it was planned to perform 2 Vernier Scans per fill at each IP in 1995. This could be realised for about 70% of the off-peak fills. At the two off-peak energy points and at each IP 35 good Vernier Scans were performed. The total number of scans is 280. The typical statistical error was 0.2 to 0.3 μm [91].

Fig. 6.10 displays the stability of the optimal vernier setting at IP2 (P-2) during the 95 energy scan. Fluctuations of the optimal setting of up to several μm occur. The error on the mean optimal position per IP and off-peak point was found to be between 0.15 and 0.25 μm with a typical RMS value around 1 μm. Furthermore, the optimal position drifts by about 2 μm during a fill. Fig. 6.11 shows the drift of the optimal vernier setting at IP8 as a function of time in the fill. The optimal position is affected

[1] i.e. deduced from “vernier” = small scale adjustment

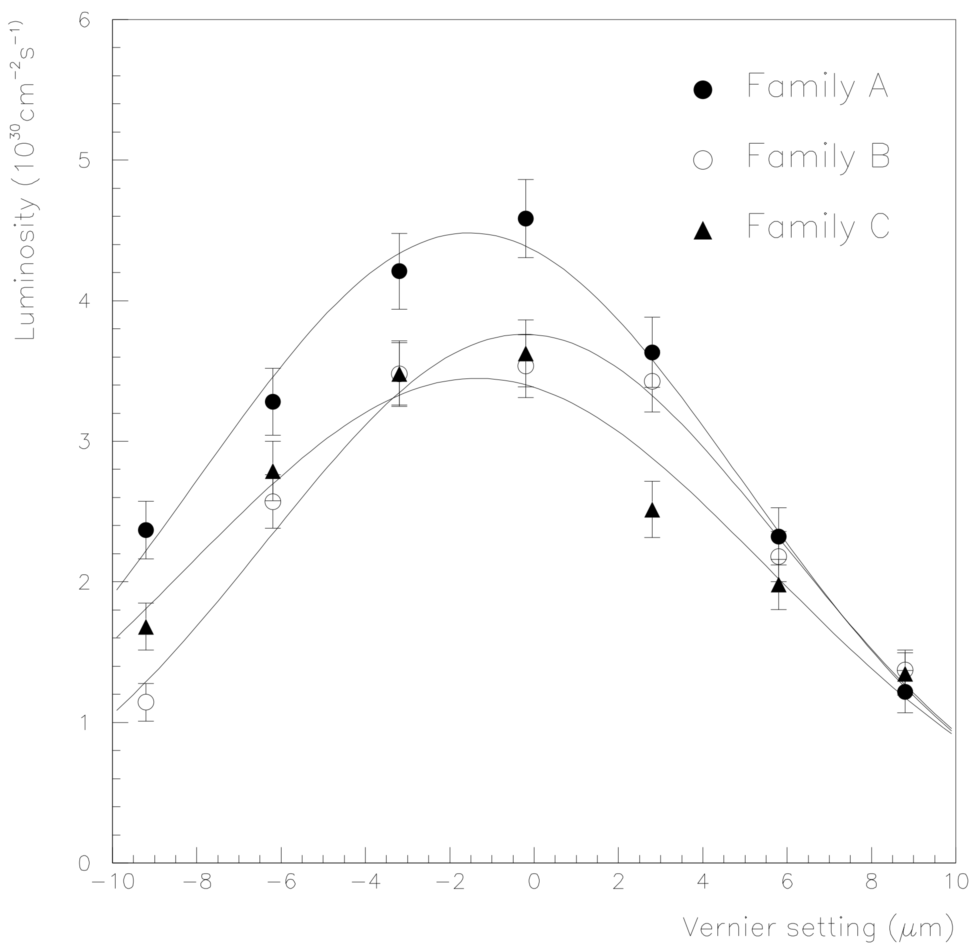

Figure 6.9: *A typical vernier scan at one IP for all three bunchlets in a train. Family A corresponds to the first bunch, family B to the second bunch and family C to the third bunch in a train. The solid lines correspond to Gaussian fits, which are applied to the luminosity measurements. Statistical errors from the luminosity measurements are assigned to the data points.*

by beam-beam interactions. Hence the continuous change of machine parameters as the vertical bunch sizes, the beam current or wiggler currents throughout a fill could be considered to cause such a drift of the optimal vernier settings. However, the evolution of the optimal position with time is dominated by irregular fluctuations in the order of some μm, which are caused by other important parameters like tunes, orbit changes or the RF distribution. For fills where no or only one scan was performed, errors have to be assigned to the optimal position, to take possible E_{CM} shifts into account. These errors are based on the fill-to-fill reproducibility of the optimal positions and typical drifts during a fill.

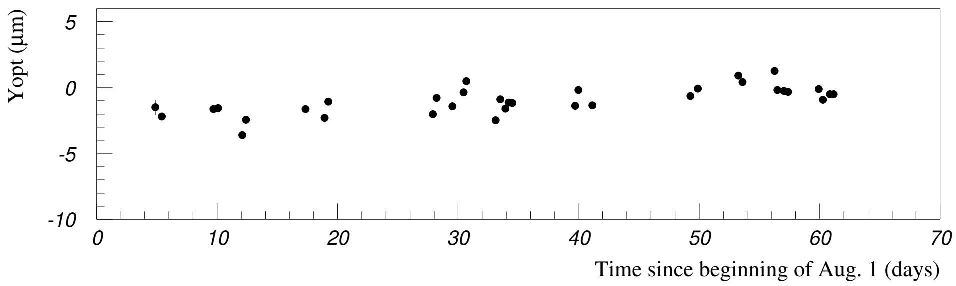

Figure 6.10: *The stability of the optimal vernier position at IP2 (P-2) during the 95 energy scan. The RMS scatter is approximately 1 μm. The reproducibility is of the same order as for all other IPs. This figure is taken from [91].*

6.2.3 Luminosity Feedback

A different approach to control the vernier settings and to minimise the dispersion effect is an automatic feedback acting on the beam offsets, which is based on luminosity measurements. A feedback like this was proposed before the start of the 1995 energy scan simultaneously to the vernier scans [92]. It was developed and finally successfully used for a period of about one week at the end of the 1995 energy scan. The feedback technique and results are presented in this section.

6.2.3.1 The Method

The idea of the feedback is based on the fact that the collision offset is minimised when the luminosity is maximised. The feedback procedure, illustrated in Fig. 6.12, consists of several steps:

(1) Measure the luminosity for a certain time at the interaction points at two different settings of the vernier separators, y_1 and y_2. The distance $d = |y_1 - y_2|$ is set to a fixed value of 0.8 μm.

(2) Compute the difference luminosity of the measurements at both positions $L_1 = \mathcal{L}(y_1)$ and $L_2 = \mathcal{L}(y_2)$ respectively:

$$dL = L_2 - L_1 \qquad . \tag{6.7}$$

(3) If $dL < 0$ the luminosity at position y_1 is higher than the luminosity at position y_2. Move the vernier settings by $y_{step} = 0.4$ μm towards position y_1. If $dL > 0$ change the vernier settings by y_{step} towards y_2.

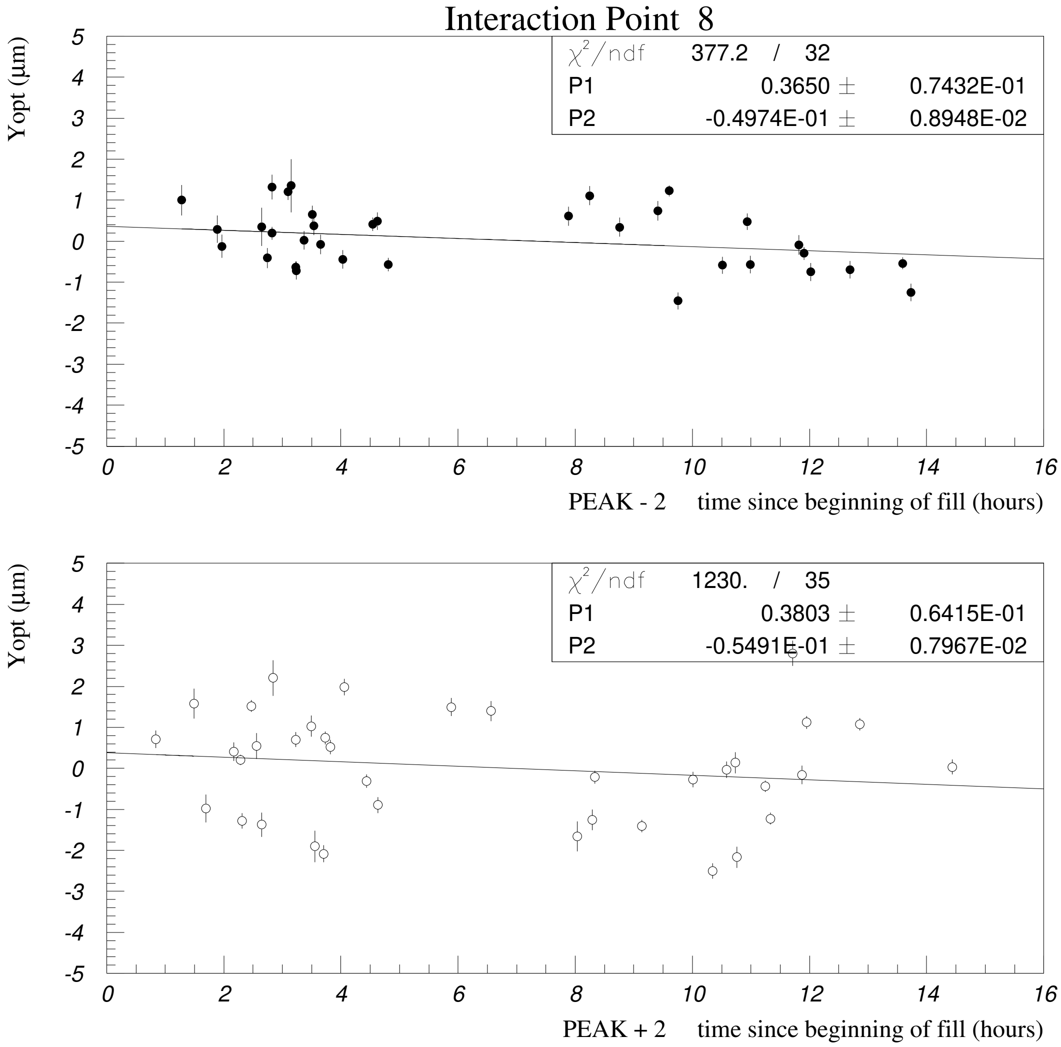

Figure 6.11: *The drift of the optimal vernier setting at IP8 as a function of time in the fill. The figures are taken from [91]. The bad χ^2 values indicate an underestimation of the fit parameter errors. A rescaling of the errors leads to a reduction of the significance of the fitted slope by a factor of 12 and 35 respectively.*

(4) Repeat the procedure and start with point (1).

y_{step} and d are free parameters of the feedback. The choice of y_{step} is given by the minimal possible step of the high voltage DAC [92]. The duration of an individual luminosity measurement was set to 100 s to ensure a statistical error below 1.5 % [92, 93]. It is imaginable that the choice of the parameters can still be tuned and be adjusted to different start configurations. The feedback provides continuous measurements. No

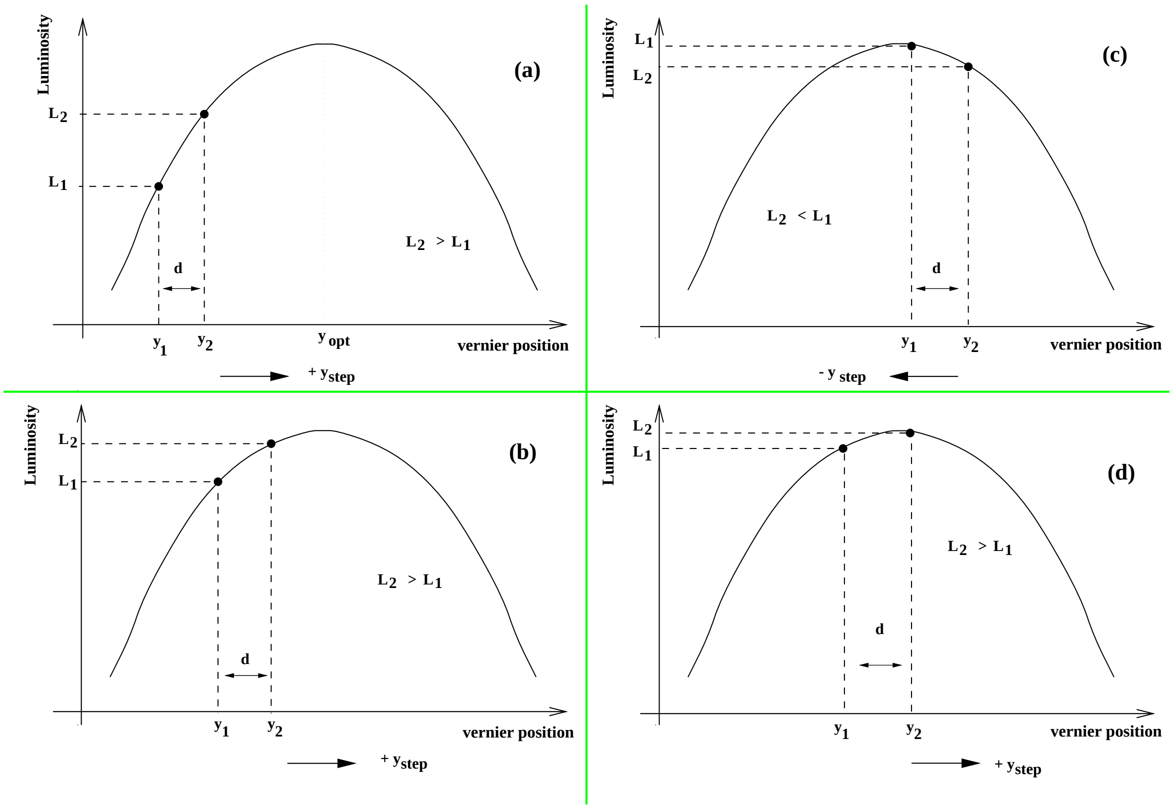

Figure 6.12: *Illustration of the principle of the luminosity feedback. (a) The feedback is started with a certain offset from the optimal position y_{opt}. The luminosity measurements at the two positions y_1 and y_2 results in $L_2 > L_1$. The feedback moves the two vertical positions by $+y_{step}$ towards y_{opt}. (b) The difference between L_2 and L_1 is smaller than before but still giving $L_2 > L_1$. Thus the two vertical positions are again moved by $+y_{step}$. (c) The luminosity measurements result in $L_2 < L_1$. Consequently the vertical positions are moved back by $-y_{step}$. (d) Close to the optimal position, the luminosity measurement results periodically in $L_2 > L_1$ or $L_2 < L_1$. The positions are moved according to the current result keeping them close to the optimal position.*

operation time is lost for data taking with high luminosity. In case of an unexpected change of the optimal position the feedback automatically moves the beams to the new optimal setting.

6.2.3.2 Simulation of the Feedback

The feedback simulation was based on bunch currents and beam size data from various 1994 physics fills [93, 94]. The luminosity was calculated according Eq. 6.6. $\mathcal{L}_0$ was computed from the variation of the bunch currents I_b and the vertical beam size σ_b as a function of time during the input fill. In order to study the worst case, fills with large fluctuations in the beam size were selected, leading to luminosity changes of up to 10 % due to beam size variations. Tab. 6.5 summarises the parameter settings for the feedback simulation [93]. In the simulation the energy shift, which is related to vertical

quantity	value	remark
ΔD_y	2 mm	vertical opposite sign dispersion at IP
σ_E	$1 \cdot 10^{-3}$	energy spread
Δt	100 s	time interval to measure L_1, L_2
y_{step}	0.4 μm	step size of vernier position changes
y_0	0.2 - 4 μm	range of initial vertical displacements
d	0.8 μm	distance between y_1 and y_2
σ_b	7 - 3.5 μm	range of vertical bunch sizes for physics fills

Table 6.5: *List of quantities and assigned values which are used in the feedback simulation.*

displacements, ΔE_{CM}, is obtained from Eq. 6.5, using the simulated vertical position $y - y_{opt}$. The shift in E_{CM} was calculated for one input fill assuming the feedback being ON or OFF for a range of initial values y_0. Tab. 6.6 shows the results, expressed as the average energy variation over the fill [93]. The reduction of ΔE_{CM} due to the feedback

y_0 (μm)	feedback OFF $<\Delta E_{CM}>_{OFF}$ (MeV)	feedback ON $<\Delta E_{CM}>_{ON}$ (MeV)
0.2	0.6	0.1
0.4	1.3	0.6
0.6	1.9	0.6
0.8	2.6	0.4
1.0	3.2	0.2
1.5	4.8	0.8
2.0	6.4	0.7

Table 6.6: *Mean centre-of-mass energy shift (absolute value) as a function of initial collision offsets for a simulated fill with feedback ON or OFF.*

is obvious. When the feedback is not used, the initial collision offset is not changed during the entire fill. With feedback the collision offset is continuously reduced and the mean energy shift is uncorrelated with the choice of y_0. Fig. 6.13 shows ΔE_{CM} as a function of time assuming an initial vertical displacement y_0 of 1.5 μm before the feedback is started. The time which is needed to reduce the initial energy shift to 50%, is defined as $\tau_{1/2}$. It is obtained from an exponential fit to the simulation data. The fit result is superimposed on the plot as a solid line. In Fig. 6.14 $\tau_{1/2}$ is plotted as a function of y_0. The simulation shows that even for relatively large initial collision offset of 4 μm the energy shifts are reduced within less than 1 hour to 50% of the start value. The observed fill-to-fill reproducibility of the optimal position is about 1 μm at

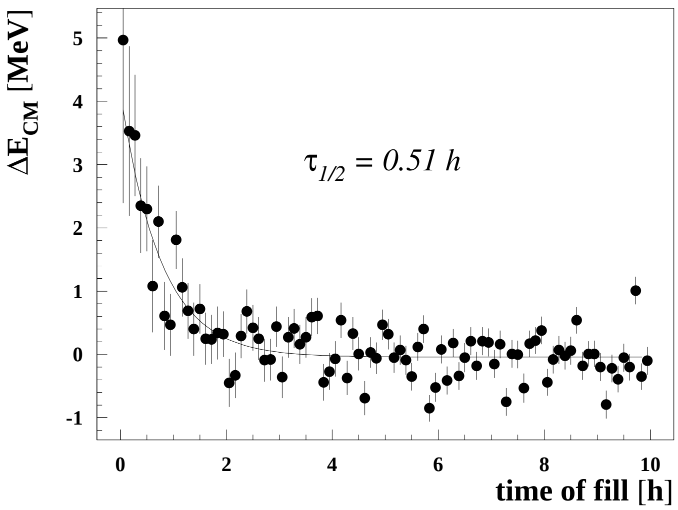

Figure 6.13: *Centre-of-mass energy shifts due to the simulated vertical displacement of the colliding bunches as a function of time in a fill. The solid line shows an exponential fit to the simulation data.*

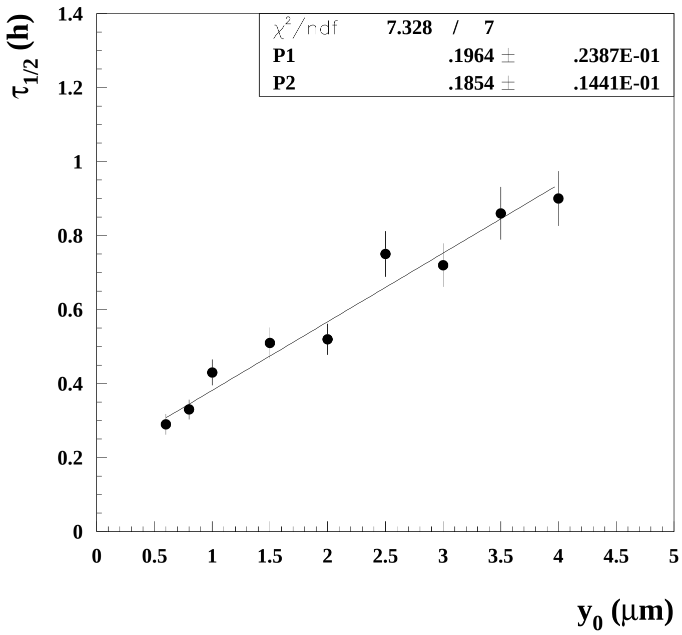

Figure 6.14: *The time required by the feedback to reduce the initial energy shift by 50% as a function of the initial collision offset y_0.*

all IPs [91, 95]. Therefore, once the optimal position is known, the vernier separators can be set to this value at the start of a new fill. Thus in practice initial collision offsets of much more than 1 μm are unlikely and it can be expected that the feedback reaches the optimal position after 20 minutes [94].

Another important requirement on the performance of the feedback is the accuracy to which the optimal position is known. As mentioned above, the typical statistical error of the optimal position using the vernier scan technique is 0.2 to 0.3 μm. This error was calculated in the simulation for various start values y_0. Fig. 6.15 shows the error as a function of time in a simulated fill. The initial collision offset is set to 1.5 μm, which is considered to be a typical value. After about 1 hour feedback operation the optimal

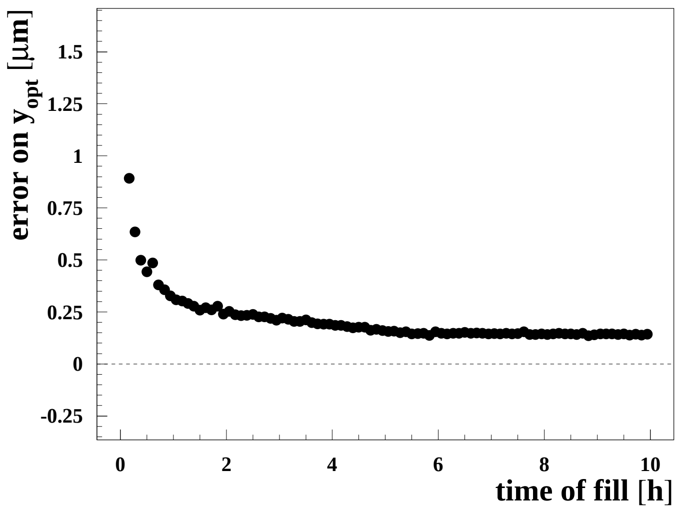

Figure 6.15: *Error on the optimal vertical position as a function of time in a fill when the feedback is used. y_0 is set to 1.5 μm.*

position is known to an accuracy smaller than 0.25 μm [94]. Hence the error on the optimal position expected for the luminosity feedback matches the accuracy achieved using vernier scans.

6.2.3.3 Performance during LEP Operation

After two successful tests of the feedback in the peak fills 2866 and 2932 [96], the feedback was used in the last week of the 95 energy scan on a sample of 7 off-peak fills: 3019, 3022, 3024, 3025, 3027, 3032, 3036. For these fills at least 2 vernier scans at each IP were performed.

The feedback was implemented into the LEP operation software [97] and could be controlled by the operator in the control room. Fig. 6.16 shows a flowchart of one cycle in the feedback software. In this simple picture one complete cycle consists of 11 steps. The feedback software acts as an interface between the vernier separator control, the LEP logging database and an output unit (memory). The memory is used for later analysis of the feedback data. The feedback was performed in four consecutive cycles such that it was active at one IP at the time, while it was paused at the others. Whenever a vernier scan was performed, the feedback was interrupted to avoid interferences.

The analysis of the feedback performance is based on the specific luminosity $\mathcal{L}_{spec}$:

$$\mathcal{L}_{spec} = \frac{\mathcal{L}}{I_{e^+} \cdot I_{e^-}} \qquad . \tag{6.8}$$

I_{e^+} and I_{e^-} are the total positron and electron beam currents. $\mathcal{L}_{spec}$ is used to disentangle effects due to beam current variations and due to the feedback. Fig. 6.17 shows the specific luminosity, measured by the luminosity monitors of the experiments, as a

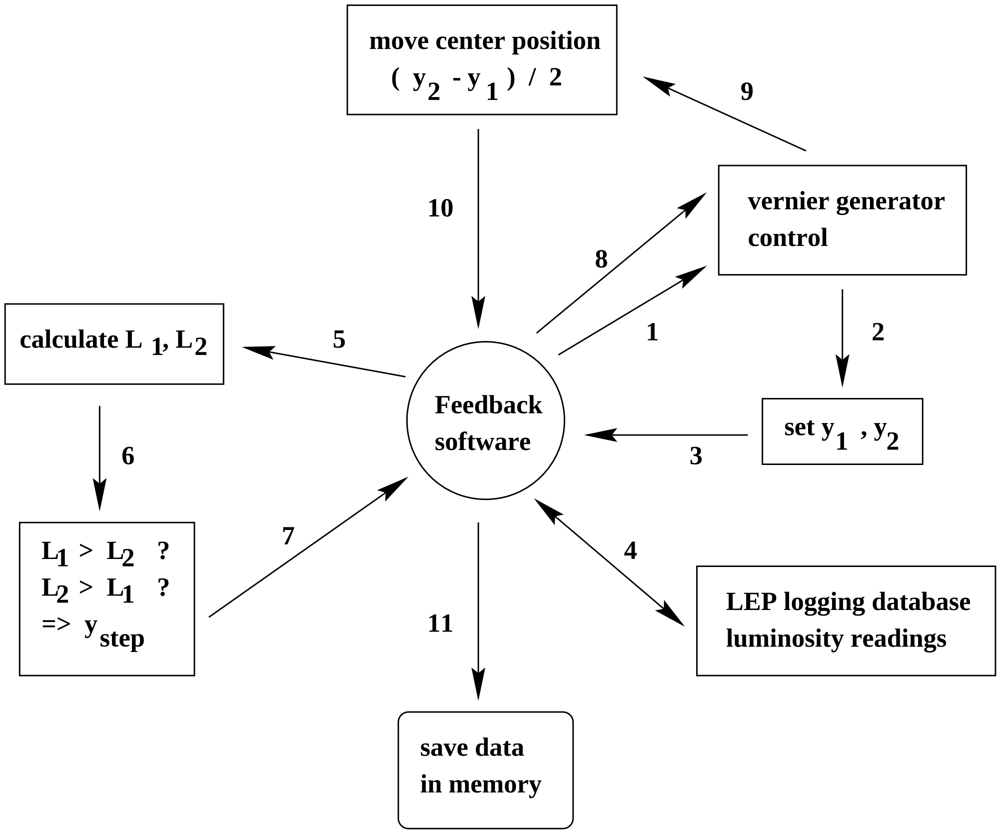

Figure 6.16: *Flowchart of the working principle of the luminosity feedback.*

function of time at the four interaction regions. The on-line luminosity data of the four experiments were taken from the LEP logging database. $\mathcal{L}_{spec}$ as a function of time can be approximated with a linear function. For equal electron and positron beam sizes, the luminosity is proportional to the beam currents and the horizontal and vertical beam sizes at the IP, $\sigma^*_{x,y}$:

$$\mathcal{L} \sim \frac{I_{e^+} \cdot I_{e^-}}{\sigma^*_x \cdot \sigma^*_y} \quad . \tag{6.9}$$

Since the beam size decreases linearly during a fill due to the beam-beam effect, the specific luminosity increases with time. Linear fits to the data give reasonable χ^2/ndf spanning values between 0.9 and 2.4. The agreement with the linear approximation is fairly good for the first 10 hours of a fill, while discrepancies appear for elapsed times > 10 h, when the luminosity is no longer beam-beam limited. Within about 10% the slope is the same in all IPs: (0.1 ± 0.01) in units of $\mathcal{L}_{spec}$/h. Fig. B.1 to Fig. B.14 in Appendix B show $\mathcal{L}_{spec}$ derived from the feedback data as a function of time. A linear fit is applied to the feedback data. Superimposed on all plots is the maximum specific luminosity deduced from the vernier scans. The specific luminosity measured by the luminosity detectors of the experiments is also shown. The luminosity readings

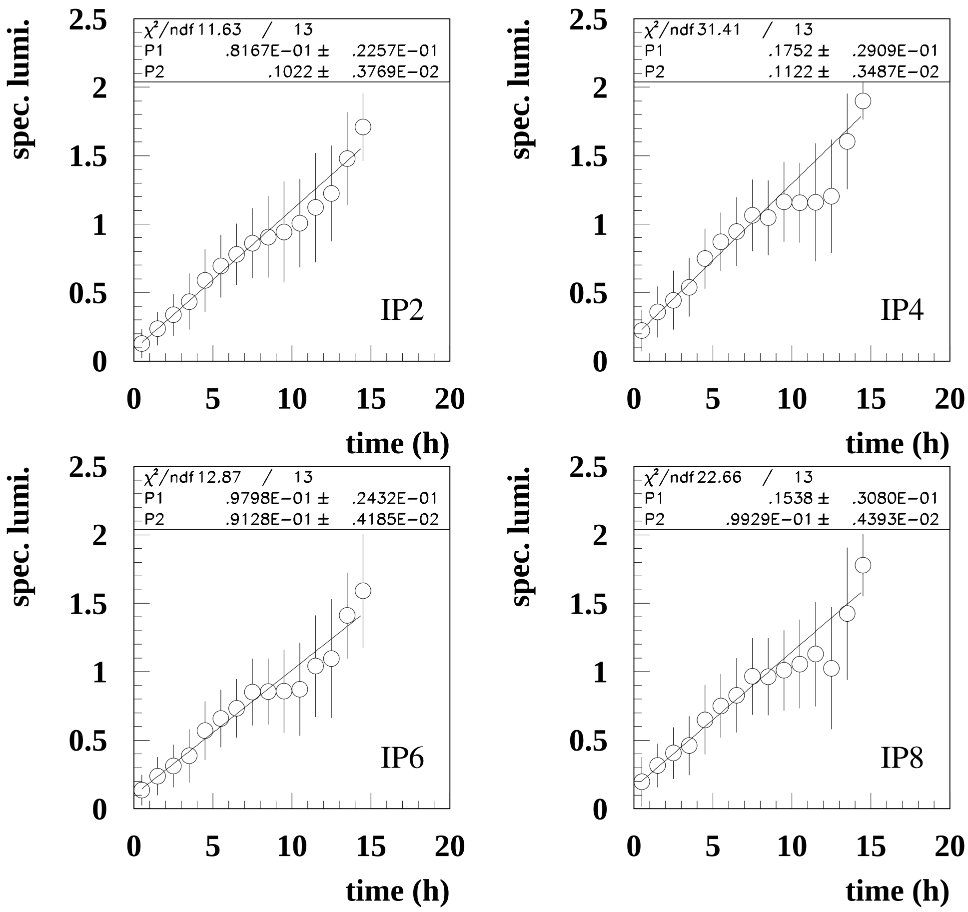

Figure 6.17: *Specific luminosity $\mathcal{L}_{spec}$ from the luminosity detectors of the experiments as a function of the time in a fill. The data are normalised to the first reading in a fill. The mean $\mathcal{L}_{spec}$ was averaged over 15 fills (> 3008) including the fills with feedback. The error bars correspond to the RMS scatter. A linear fit ($P_1 + P_2 \cdot t$) and the fit parameters are superimposed on each plot.*

are normalised to the first readings, which are constraint to 1. The offsets between the LEP data and experimental data are due to the imperfect absolute calibration of the LEP luminosity monitors. The RMS scatter of the feedback data around the linear fit vary from 0.03 to 0.21 (in units of specific luminosity) corresponding to 1.5% to 7%. The fairly small RMS indicates the good stabilisation of the luminosity around the optimal value by the feedback. In all cases where feedback and vernier scan data exist within a short time interval the optimal position found by the feedback agrees well with the result of the vernier scan.

An undesirable side-effect of the Vernier Scans is easily visible in the experimental $\mathcal{L}_{spec}$ data: in most cases around the time of the vernier scan a reduction of the specific luminosity can be seen. Often the reduction at a particular IP occurs shortly before or after the time of the vernier scan, indicating a cross-talk between the IPs. The reduction then occurs due to the vernier adjustment at one IP, which influences the crossing of the beams at the other IPs. The cross-talk was predicted to be roughly 10% [91]. It was tested in an experiment leading to a measured reduction of 15% [91]. The determination of the optimal position and hence ΔE_{CM} is not affected by the cross-talk. Furthermore it can be seen in Fig. B.1 to B.14 that the maximum luminosity derived from the Vernier Scans is on average lower than that derived from the feedback. It reflects a known change of the vertical beam size at the time of a vernier scan [91]. The blow up increases the width of the luminosity distribution, which is related to the vertical beam size. In general, the blow up might affect the maximum luminosity derived from the fit to the data since the Gaussian shape of the luminosity distribution is distorted. This effect has been studied and it was found that the correction to the optimal vernier setting is less than 0.1 μm for all IPs [98]. The mean blow up of the vertical beam size, derived from the distribution width and averaged over the three families, is shown in Tab. 6.7. The feedback allows to study the effect of the distorted Gaussian shape by comparing the maximum specific luminosity from the Vernier Scans with the expected specific luminosity derived from the fit to the feedback data. The ratio ϵ of both is given by:

$$\epsilon = \mathcal{L}^{fit}_{spec} \,/\, \mathcal{L}^{scan}_{spec} \quad . \tag{6.10}$$

The valued of ϵ were averaged over all vernier scan data from the 7 fills excluding the second sets of vernier scans in fill 3022 and 3027. In fill 3022, the specific luminosity starts decreasing significantly at 04:30. At this time a computer network problem occurred causing a loss of control and a decreasing luminosity. The second set of Vernier Scans gives results, which are much below the expectation from the fit. The effect is due to a real reduction of the luminosity and not caused by a beam blow up. Therefore this second set of Vernier Scans is excluded from the analysis. In fill 3027 the logging of the experimental luminosity data crashed. It cannot be judged if the results of the second vernier scans, which are again much below the prediction from the linear fit, are related to a true decrease of the specific luminosity. Thus they are also excluded from the analysis. The results of the feedback data analysis are shown in Tab. 6.7. The effect is stronger in IP2 and IP8 than in IP4 and IP6. This is consistent with the result from the analysis of the entire vernier scan data sample. In this analysis, the blow up of the beam sizes was obtained from a measurement of the width of the luminosity distribution while the feedback analysis used the reduction of the fitted maximum luminosity. Hence the absolute values are not comparable.

One important advantage of the feedback is the continuity of the measurements. In general, the feedback guarantees a vertical position close to the optimal one in any fill almost from the beginning. No dedicated operation time, which is lost when using the Vernier Scan technique, is needed. However, the optimal positions found by the feedback could be confirmed by the vernier scans. A further important advantage of the feedback technique is the absence of large offsets from the optimal position. Vernier Scans require significant offsets from the optimal position which lead to a blow up of

IP	$< \epsilon >$	mean blow up
2	1.10 ± 0.01	1.38 ± 0.03
4	1.03 ± 0.02	1.15 ± 0.02
6	1.0 ± 0.03	1.18 ± 0.03
8	1.08 ± 0.01	1.32 ± 0.03

Table 6.7: *The distortion of the Gaussian shape of the luminosity data due to a beam blow up affects the maximum value and the width, which are derived from a fit assuming a Gaussian distribution. The genuine maximum value remains unchanged. While ϵ is a measure of the reduced maximum value, the mean blow up is obtained from the wings of the Gauss-distribution. The first column shows results from the feedback data analysis, while the second column presents results from an analysis of the entire vernier scan data sample. Statistical errors are taken into account only.*

the beams and cause a luminosity decrease at all IPs due to a cross-talk. Since large offsets are avoided by the feedback, no temporary reduction of the luminosity, which is an intrinsic feature of the Vernier Scans, appears. It can be concluded that the feedback technique is at least a powerful complement or even superior to the Vernier Scan method although it is interfered by luminosity tuning of the machine.

6.2.4 Dispersion Measurements

The knowledge of Δy, the deviation from y_{opt}, can only be related to shifts of the centre-of-mass energy if the dispersion at the IPs is known. Two different methods have been used to derive the vertical dispersion for 1993 [89] and 1995 [91].

1993 Two orbits are acquired with different settings of the RF frequency. From the known difference in energy and the measured orbit position change at the beam orbit monitors, the dispersion at the position s of the orbit monitors is extracted using:

$$\Delta y_d(s) \;=\; D_y(s)\frac{\Delta E}{E_0} \qquad , \tag{6.11}$$

where $\Delta y_d(s)$ is the measured orbit shift of a particle with nominal energy. ΔE is the change of energy, typical was a change of $\Delta E/E = 1.6 \cdot 10^{-3}$. The dispersion at the IP ΔD_y^* is then extrapolated from the position of the orbit monitors to the interaction point using the properties of the dispersion function. 17 measurements from 1993 are available.

1995 The dispersion is directly measured at the interaction points. The shift of the optimal Vernier setting Δy_{opt} is measured for a certain RF frequency change

Δf_{RF}. The shift in the optimal setting is directly proportional to ΔD_y^*:

$$\Delta D_y^* = -\alpha_c \frac{f_{RF}}{\Delta f_{RF}} \Delta y_{opt} \qquad , \tag{6.12}$$

where α_c is the momentum compaction factor. Dispersion measurements at the even IPs were performed at least once at each energy setting. In the example of Fig. 6.18, the dispersion computed from -50 Hz to +50 Hz is consistent with the one computed using only one off frequency scan and the three nominal frequency scans. However, this was not the case for all 23 measurements and in some cases the vertical position offsets are not symmetrically arranged with respect to the nominal frequency. For that reason, an additional error was introduced. This error corresponds to the variation of the mean dispersion rejecting the sets of measurements where the dispersion was not consistent between the three computed values.

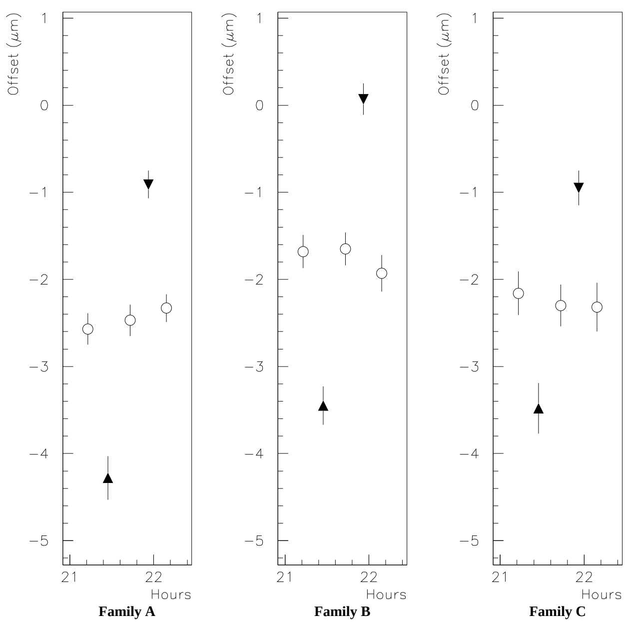

Figure 6.18: *Example of a dispersion measurement at IP2 for the three bunch families. The vertical position offsets for the three energies at -50 Hz (upright triangle), nominal frequency (open circles) and +50 Hz (inverse triangle) are displayed. The Figure is taken from [91].*

The dispersion values, obtained in 1993 [89] and 1995 [91] respectively, are presented in Tab. 6.8 together with the predictions for the 1995 Bunch Train configuration. As expected, the results for the bunch train scheme are about a factor of 5 larger than the values measured for the 1993 Pretzel operation. The measured size of the vertical dispersion in 1995 agrees reasonably well with the predicted values from theoretical calculations.

IP	ΔD_y^* 1993 [mm]	ΔD_y^* 1995 [mm]	$\Delta D_y^{pred.}$ 1995 [mm]
IP2	0.4 ± 0.3	2.0 ± 0.4	1.8
IP4	0.4 ± 0.4	-2.0 ± 0.7	-2.8
IP6	0.2 ± 0.4	1.8 ± 0.8	1.9
IP8	0.6 ± 0.4	-1.5 ± 0.7	-1.9

Table 6.8: *Summary of average difference dispersion at the four IPs in the years 93/95 and the prediction for the Bunch Train configuration used in 1995. The errors include systematic and statistical components.*

6.2.5 Energy Shifts and Systematic Errors

The recorded Vernier settings and the results from the dispersion measurements can be used to evaluate the impact of the Vernier Effect on the CM energy. Eq. 6.5 is used to derive CM energy shifts for typical values of the energy spread and the vertical beam sizes. For the 1993 data, due to the limited accuracy of the beam orbit monitors, the collision offset could be estimated only. The resulting CM energy shift is estimated to be 0.4 MeV for all IPs, assuming that the average collision offset has not exceeded 1 μm [89]. The dispersion effect was not taken into account in the evaluation of the errors for the 1993 scan in [33]. The value gives the systematic error due to the Vernier effect for the 1993 energies and is small compared to the ± 1.5 MeV calibration error coming from the complete 1993 analysis [33]. For 1995 the CM energy corrections could be computed for all IPs at each energy setting [91]. Table 6.9 shows the results. Fewer Vernier Scans were performed at peak settings, leading to larger uncertainties

	ΔE_{cm} (MeV)		
IP	P-2	Peak	P+2
IP2	-1.0 ± 0.4	-0.55 ± 0.8	0.1 ± 0.4
IP4	0.7 ± 0.2	0.1 ± 0.4	-0.5 ± 0.2
IP6	-0.5 ± 0.3	-0.2 ± 0.4	-0.2 ± 0.4
IP8	0.3 ± 0.25	0.9 ± 0.5	-0.3 ± 0.4

Table 6.9: *The 1995 centre-of-mass energy corrections ΔE_{cm} due to the Vernier effect. Errors include the uncertainty due to the determination of the collision offset.*

for that point. The accuracy of the peak data is less relevant for the Z mass and the width than that of the off-peak data. To evaluate the total systematic error on the CM energy shift, various studies have been performed:

- Vernier scans were performed in the opposite direction rather than the standard direction.
- The difference between the optimal position for the bunch families a,b,c were measured.
- The influence of the Vernier adjustment at one IP on the other IPs (cross-talk) has been studied.
- Systematic drifts of the optimal position within a fill have been investigated.
- The variation of the optimal position with the vertical beam size has been studied.
- Systematic effects arising from the fit procedure have been taken into account.

These studies lead to averaged errors $\sigma(\Delta E_{cm})$ for the four experiments, where in all cases the systematic errors are larger than the statistical ones. This is mainly due to the limited statistics available for the study of each of the systematic effects described above. The errors, combining the mean statistical and the correlated and uncorrelated systematic errors, are listed in Tab. 6.10. The errors are relatively small and the

IP	$\sigma(\Delta E_{cm})$ (MeV)
IP2	0.68
IP4	0.46
IP6	0.54
IP8	0.54

Table 6.10: *Mean error on the CM energy shifts $\sigma(\Delta E_{cm})$ in MeV per interaction point.*

program of adjusting the Vernier settings with Vernier scans was successful in keeping the effect on the CM energies small. Hence the expected error on the Z mass and width is < 0.4 MeV combining all experiments.

Chapter 7

Further Studies

In addition to the effects discussed so far, other possible effects on the beam energies were studied in 1993, 1994 and 1995: energy differences between electrons and positrons and energy differences between bunchlets in a train. The results obtained in chapter 5 were compared to variations of the hadronic cross section data acquired by ALEPH, DELPHI and L3.

7.1 Energy Differences between Beams and between Bunches

At the end of the 1993 running period the LEP beam energy was calibrated for the first time by depolarising positrons rather than electrons [52]. This experiment revealed an unexpectedly large energy difference between the electron and positron beam of $0.5\,\mathrm{MeV} < \Delta E = E_{e^+} - E_{e^-} < 3.2\,\mathrm{MeV}$. An energy difference of that size would lead to an additional systematic error of $\pm$ 1.7 MeV on the Z mass. Therefore possible differences between electron and positron energy were studied more carefully in 1994 [99]. Imperfections of the LEP lattice such as misalignment of quadrupoles, imperfections of the quadrupole and sextupole fields, asymmetries in the optical sequence and the pretzel scheme combined with the energy sawtooth can cause horizontal deviations from the ideal orbit, which are different for electrons and positrons. Theoretical calculations combined with simulations of the LEP machine lead to an energy difference of less than 0.3 MeV at a 90% confidence level [99]. Additionally, two further experiments were performed during the 94 run and one experiment during the 95 run. Fig. 7.1 shows the energy calibration measurements including both, electrons and positrons, from the 1995 fill 3024 at September 26, 1995. This experiment was performed with the bunch train optics. Tab. 7.1 lists the results of all four experiments (1993-1995). Except the 1993 experiment, all results are compatible with zero and agree well with the expected value from theoretical calculations. The reason for the deviation of the 1993 result

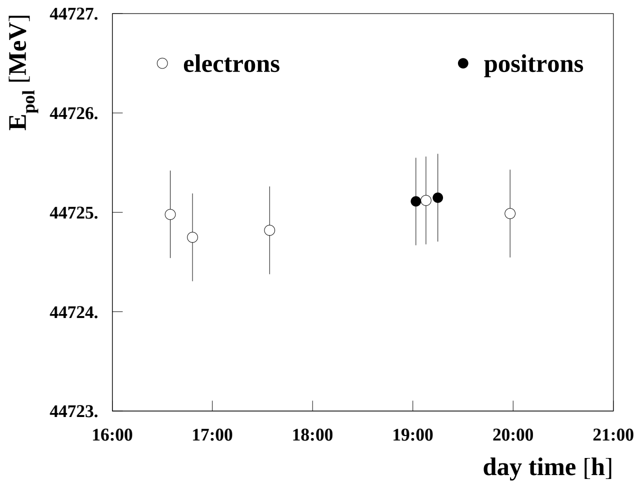

Figure 7.1: *Energy calibration measurements with resonant depolarisation in fill 3024 as a function of time. In this fill electron and positron energy was measured subsequently giving an estimate of possible differences between electron and positron energies of 0.1 ± 0.25 MeV.*

from the other experimental results as well as from the theoretical expectation remains unclear since it could be shown that even slightly different optics cannot cause such a deviation [99]. Therefore, the result of this experiment was not included into the error

year	experiment	$\Delta E(e^+ - e^-)$ (MeV)	operation scheme
1993	Nov. 15^{th}	1.9 ± 0.8	Pretzel
1994	Jul. 15^{th}	0.4 ± 0.4	Pretzel
	Aug. 1^{st}	0.0 ± 0.2	Pretzel
1995	Sep. 26^{th}	0.1 ± 0.25	Bunch Train

Table 7.1: *Energy difference $\Delta E = E_{e^+} - E_{e^-}$ as measured in 1993, 1994 and 1995.*

estimation. For both scans, a correction of 0.3 MeV to the energy of the positron beam with respect to the electron beam with an error of ± 0.3 MeV was taken into account. This uncertainty leads to an additional systematic error of ± 0.3 MeV on the mass and the width of the Z particle.

Since LEP is operated in the Bunch Train mode eventual energy differences between the bunchlets in a train enter the game. During the 1995 energy scan trains with three bunchlets A,B and C collided. The spacing between the bunches in a train is much less than the spacing between two bunches in the Pretzel mode or between two trains. Because of the small distance bunchlet B (C) is usually depolarised together with bunchlet A (B) when a resonant depolarisation is performed. Therefore, subsequent depolarisations are possible for bunchlet A and C only. The energy difference between bunchlet A and C, $\Delta E_{A-C} = E_A - E_C$, was determined five times during an on-going energy calibration in 1995 [100]. Fig. 7.2 shows the results from the five measurements. A constant fit applied to the data leads to an averaged energy difference of $\Delta E_{A-C} = -0.1 \pm 0.1$ MeV, which is compatible with zero. A conservative error estimate leads to an additional uncertainty of ± 0.2 MeV on the mass and the width of the Z particle.

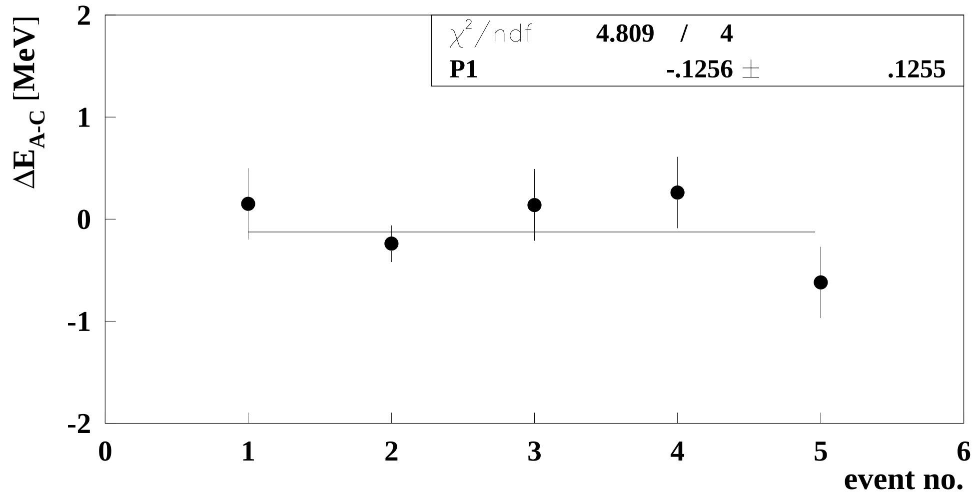

Figure 7.2: *Energy difference ΔE_{A-C} between bunchlet A and C in a train. In total, 5 measurements were done during the 1995 scan. The results of the 5 events are combined to derive an error estimate for possible energy differences between bunchlets in a train.*

7.2 Hadronic Cross Sections

In this chapter the time dependence of the hadronic cross sections, as measured by the experiments, will be compared to the expected change due to the described beam energy variations. Luminosity measurements and numbers of hadronic Z events were available from three experiments, ALEPH [101], DELPHI [102] and L3 [103] for the two off-peak points in 1993 and 1995. Tab. 7.2 summarises the number of hadronic Z events, which were used in the following study. Each data set consists of many

year		ALEPH	DELPHI	L3
93	P-2	76682	62379	83449
	P+2	111845	102169	121753
95	P-2	77369	80728	76407
	P+2	118266	130261	114097

Table 7.2: *Statistics of hadronic Z events for the 1993 and 1995 off-peak points.*

measurement in time intervals of approximately 15 to 20 minutes with the associated statistical errors only. For the data quoted here no systematic errors were given. Thus the numbers are educated guesses and do not necessarily correspond to the final values, which will be published by the experiments.

The approximate size of the energy rise ΔE_{model} can be estimated with a simplified model, which takes into account only the most important contributions:

$$\Delta E_{model}(t) = \frac{5}{8}(\Delta E_{NMR4} - \Delta E^{OCT4}_{Tmod})(t) + \frac{3}{8}(\Delta E_{NMR8} - \Delta E^{OCT8}_{Tmod})(t) + \Delta E^{RING}_{Tmod}(t). \quad (7.1)$$

The constituents are:

- $\Delta E_{NMRi} - \Delta E^{OCTi}_{Tmod}$ (i=4,8) accounts for the energy rise due to the Train Effect. The contribution of each branch of LEP is calculated separately.
- ΔE^{RING}_{Tmod} describes the part of the energy rise, which is caused by temperature changes. It is based on the new temperature parametrisation and averaged over the eight octants (Eq. 5.18).

Other contributions like the horizontal corrector settings can be neglected for this purpose. Fig. 7.3 shows the modelled rise and the two contributions from the net Train Effect and core temperature changes averaged over all NMR and temperature data of the entire scan. The two contributions to the energy rise are approximately

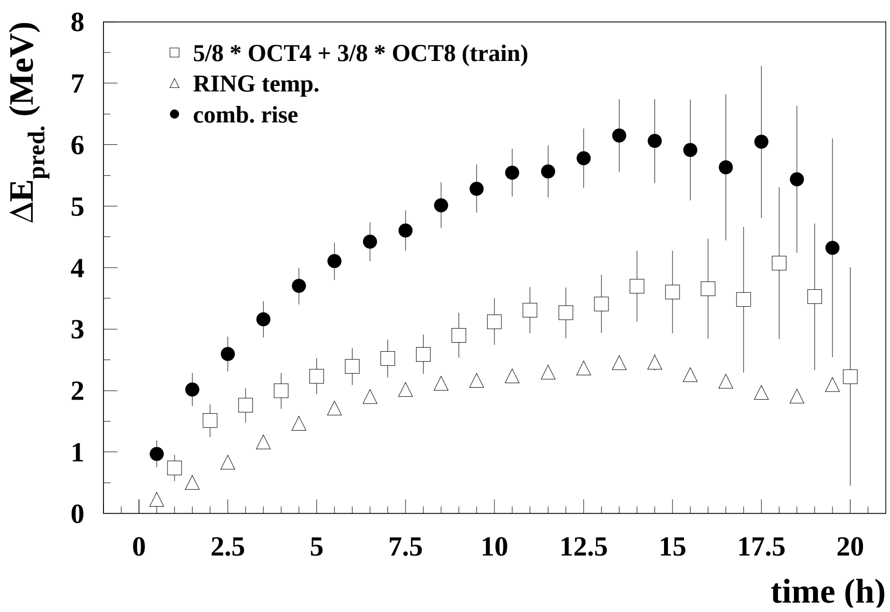

Figure 7.3: *The prediction of the mean beam energy rise (comb. rise) in a fill consisting of the NMR and temperature data. The contributions from the net Train Effect (train) and from the core temperature (RING temp.) according to the new temperature model are also shown.*

equal. The rise has to be multiplied by 2 to obtain the effect on the CM energy.

The CM energy rises by about 12 MeV over 12 h. Fig. 7.4 shows cross sections as a function of the CM energy for the relevant energy ranges around the P-2 and P+2 points. The cross section can be fairly well approximated by a linear function. The

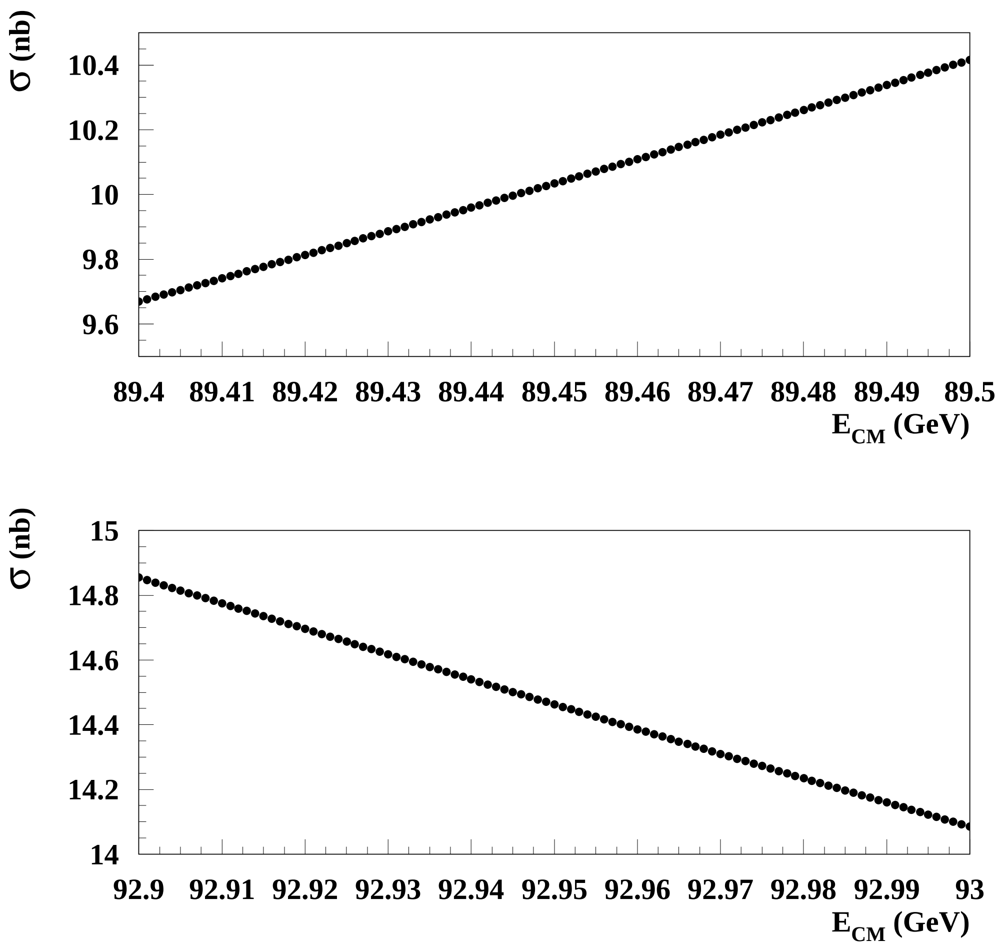

Figure 7.4: *Cross sections calculated with ZFITTER [12] as a function of the centre-of-mass energy around the two off-peak settings. The distribution is adequately linear inside a range of 100 MeV. Top: Cross section around the P-2 setting. Bottom: Cross sections around the P+2 setting.*

gradients at the two off-peak points have opposite sign whereas the values of the slope are approximately the same:

$$\text{P-2} \quad : \qquad 1\ \text{MeV} \equiv 7.31\ \text{pb}, \tag{7.2}$$
$$\text{P+2} \quad : \qquad 1\ \text{MeV} \equiv -7.66\ \text{pb}. \tag{7.3}$$

The gradient of the Breit-Wigner-Curve around the resonance peak is essentially zero, which reduces the sensitivity of the peak data to energy changes significantly. Therefore peak data cannot be used in this study. For a 12 MeV CM energy change the cross section is expected to vary by approximately 100 pb. In principle it should be possible to see this increase in the experimental cross sections. In Fig. 7.5 the cross section per data tape (approximately 15 minutes each) is shown for one data set acquired by the DELPHI experiment in 1993. The expected cross section change of the order of 0.1 nb

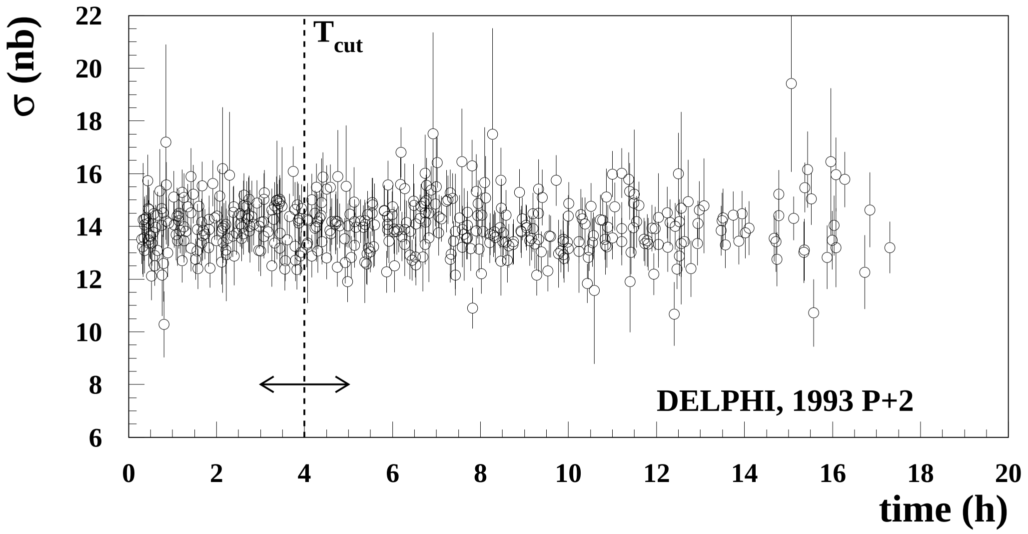

Figure 7.5: *The cross section per data tape measured at P+2 by the DELPHI experiment during the 1993 scan as a function of time in a fill.*

is equivalent to the size of the data points. Such a small effect cannot be seen from the cross section distribution without further effort. In fact, even after combining all data samples the statistical errors are too large to divide the data into more than 2 subsamples. Therefore each data sample is split into two time intervals only:

- period I:
  cross sections measured at a time $t < T_{cut}$
- period II:
  cross sections measured at a time $t > T_{cut}$

The optimum cut value T_{cut}, which divides the data sets into two periods with statistical errors of the same size, is indicated by a dashed line in Fig. 7.5. The mean cross section is calculated averaging period I and period II resulting in σ_I and σ_{II}. The sign and the size of the difference $\Delta\sigma = \sigma_{II} - \sigma_I$ is then determined for each data set. Since only relative differences between the two periods are of interest, any absolute corrections like the precise background cross sections, which were not subtracted in the provided data samples, can be ignored. Systematic errors, which are usually correlated, should cancel. The error of the difference, $d\Delta\sigma$, depends strongly on the cut value T_{cut}. The significance of the analysis depends on the error of $\Delta\sigma$ relative to the size of the energy rise. Fig. 7.6 shows the error of the cross section difference $\sigma_{II}-\sigma_I$ after the combination of all data samples (solid line) and for one individual experiment (dashed line) as a function of T_{cut}. The expected cross section change due to the CM energy rise, has been

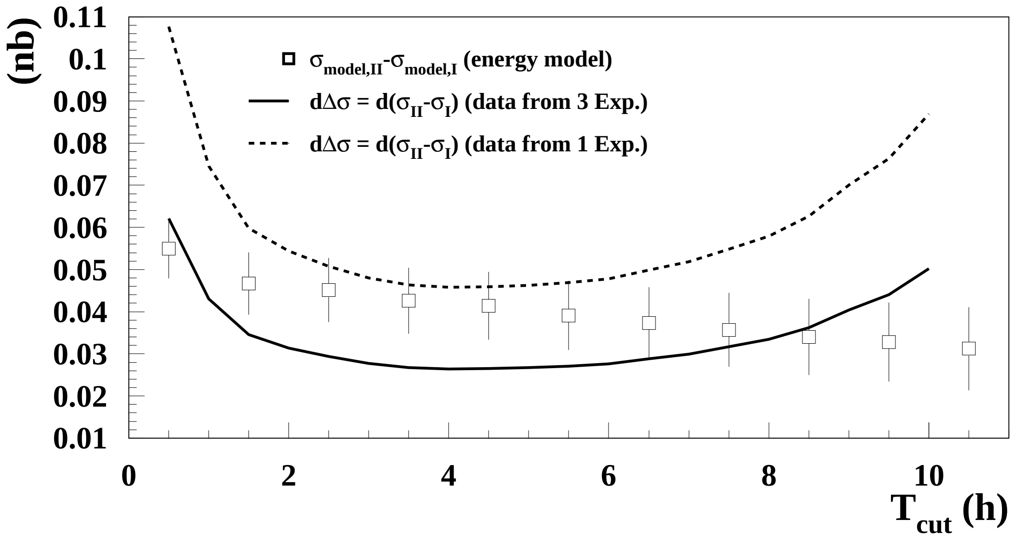

Figure 7.6: *The error of the difference between $\sigma_I(t < T_{cut})$ and $\sigma_{II}(t > T_{cut})$ and the expected difference in the cross sections as a function of T_{cut}. The error function (solid line) is based on the combined data of the 3 experiments. The error function for one individual experiment (dashed line)is superimposed to illustrate the gain in the achieved precision.*

split into the same two periods depending on the cut value T_{cut} as it was done with the cross section data from the experiments. The difference between the average of period I and period II, $\sigma_{model,II} - \sigma_{model,I}$ is superimposed in Fig. 7.6. The difference $\Delta\sigma_{model}$ exceeds the achievable error for the three combined experiments at $2\,h \leq T_{cut} \leq 8\,h$. The cut value was set to $T_{cut} = 4\,h$, because it represents the minimum of the error function and guarantees the statistical balance of σ_I and σ_{II} for all data sets.

For $T_{cut} = 4$ h, ΔE_{CM} calculated from the energy model is 5.7 MeV. This corresponds to a 0.0426 nb cross section difference. Tab. 7.3 shows the cross section difference separated for P-2 and P+2 for the three experiments in 1993 and 1995. In the two bottom lines the combined results in terms of cross sections and CM energy are given. Some of the individual results deviate rather significantly from the expected difference. However, the average $\Delta\sigma$ values, though within errors compatible with zero, have the expected sign. The corresponding ΔE_{CM} values are also given in the table. Combining these results gives a value of:

		$\Delta\sigma \pm d\Delta\sigma$ (nb)	
	year	P-2	P+2
ALEPH	1993	0.157 ± 0.076	-0.070 ± 0.091
	1995	0.153 ± 0.087	-0.133 ± 0.107
DELPHI	1993	-0.181 ± 0.084	-0.046 ± 0.096
	1995	0.063 ± 0.078	-0.006 ± 0.090
L3	1993	0.035 ± 0.077	-0.006 ± 0.092
	1995	-0.102 ± 0.081	0.040 ± 0.095
comb.		0.0258 ± 0.0332	-0.0336 ± 0.0391
ΔE_{CM} (MeV)		3.5 ± 4.5	4.4 ± 5.1

Table 7.3: *The difference cross sections at P-2 and P+2 for all individual data samples with the associated errors. The last two lines show the result for the combined experiments at P-2 and P+2 respectively in nb and converted into MeV.*

$$\Delta E_{CM} = 4.0 \pm 3.4 \text{ MeV}.$$

Within the large statistical errors the expected effect of 5.7 MeV can be confirmed by a combination of the cross sections measured by the three experiments. The result implies that at a confidence level of 90 % the beam energy does not change by more than 4.1 MeV between $t_I = 1.9$ h and $t_{II} = 8.0$ h, where t_I and t_{II} correspond to the luminosity weighted mean time of the two periods.

Chapter 8

LEP Center-of-Mass Energies and the Z Mass and Z Width

8.1 The Energy Model

The work of the LEP Energy Working Group over the past two years resulted in a new model to calculate the LEP energy variation inside a fill. The LEP energy is a function of the time t from the start of the fill and a function of the interaction points. In general the new 1995 energy model is similar to the old model used in 1993 [33]. Two effects, which were not known in 1993, have now been included: "train,rise"-term and the "h.c."-term. In addition some corrections were modified following the new insight gained after the 1993 scan. The new model can be expressed by the following formula:

$$\begin{aligned} E_{CM}/2(t,IP) \quad = \quad & C_{norm}(fill) \cdot E_{NMR}(t=0) \cdot (1+C_T(t)) \cdot (1+C_{tide}(t)) \cdot \\ & (1+C_{orbit}(fill)) \cdot (1+C_{h.c.}(t)) \cdot (1+C_{train,rise}(t)) \cdot \\ & (1+C_{RF}(t)) \cdot (1+C_{disp}(t)) \qquad . \end{aligned} \tag{8.1}$$

$E_{CM}/2$ denotes the center-of-mass energy, which divided by 2 gives the beam energy equivalent. The calibration of the energy at the end of a fill determines the absolute energy scale. The meaning of the individual terms is explained below:

- $C_{norm}(fill)$ determines the absolute energy normalisation. If the fill was calibrated, the energy calculated by the model is constrained to be equal to the calibrated energy. If it was not, this term is equal to the mean normalisation factor of all the calibrated fills at that energy point.

- $E_{NMR}(t=0)$ accounts for the beam energy measured by the NMR probes at the start of a fill. The start time is given by the time of the ramp to the final energy.

In 1993 and 1994 the NMR readings in the reference magnet are used. In 1995, $E_{NMR}(t)$ has to be composed of $E_{NMR4}(t)$ and $E_{NMR8}(t)$ to obtain a reasonable description of the energy for the whole ring (i.e. NMR_{48}).

- $C_T(t)$ denotes the dependence of the beam energy on the dipole core temperature. Two different parametrisations of the temperature dependence exist, which were discussed previously. The parametrisation used in [33] is referred to as "classical temperature model". The model, which is developed in 1995, uses the new temperature parametrisation according to Eq. 5.7.

- $C_{tide}(t)$ describes the effect of the earth tides. The tide effect can be predicted by a tide model [77] with an uncertainty such that its contribution to the total error on the LEP energy is negligible.

- $C_{orbit}(fill)$ corrects for the horizontal position of the orbit derived from BOM data. It is determined according to Eq. 4.12. Two different approaches are possible: (i) Orbit drifts during fills after correction of tidal effects are taken into account. A risk of double-counting of some effects exist (see section 5.3). (ii) An average orbit position of each fill is calculated. C_{orbit} does not change inside a fill. The second approach was used in both, the old and the new model. A systematic error has to be assigned to the ambiguity of the two approaches.

- $C_{h.c.}(t)$ is the correction for different settings of the horizontal correctors. Usually the correction is negligible since during standard fills the corrector settings are not changed. However, it is important for the interpretation of the long term energy calibration experiments (see section 5.3).
  A new consideration concerned this effect: In the old model the effect was ignored for the determination of the central values and a systematic error was assigned to it only. Following the results of the experiment in 1996, the new energy model corrects for changes of the horizontal corrector settings. Corrector magnet data are available for both energy scans.

- $C_{train,rise}(t)$ accounts for the drifts of the magnetic field due to train leakage currents. The variable t can be replaced by t_{day} and t_{fill} since the rise of the magnetic field can be parametrised as a function of the day-time t_{day} and the time after the ramp to the final energy t_{fill}.
  In 1993 half of the rise observed in the reference magnet, which cannot be caused by the trains, was included. The new model neglects the NMRREF drifts since all studies except the analysis of fill 1849 indicate that a correction for reference magnet drifts is meaningless. However, for fill 1849 - one of the three tide experiments - the evidence for true field drifts can scarcely be neglected. Thus an additional systematic error has to be assigned to this uncertainty.

- $C_{RF}(t, IP)$ corresponds to the energy offsets, which have to be added at the individual IPs to implement RF corrections. They have to be calculated according to the appropriate RF model.

- $C_{disp}(t, IP)$ takes centre-of-mass energy shifts arising from the dispersion effect into account. The correction is IP dependent. It can be neglected for the 1993 scan, since the pretzel scheme was used for the LEP operation. In 1995 the vernier position data, which are stored in the LEP logging database, are used to calculate the dispersion correction.

For the analysis of the 1995 data two different basic concepts are possible:
(i) The model prediction is based on the first NMR measurements and extrapolated by using averaged drifts due to temperature and trains. The energy model according to formula 8.2 corresponds to this concept.
(ii) The model could use the tunnel NMR data directly regardless the source of the observed changes. C_T and $C_{train,rise}$ have then both to be replaced by a correction, which is similar to the simplified model presented in section 7.2.

A modified version of the first approach is appropriate for the revisal of the 1993 data. The first NMR measurements have to be replaced by NMRREF data. A parametrisation of the averaged rise derived from the 1995 data and adjusted to the results of the 1993 long term experiments will be used to model the energy rise throughout the 1993 fills.

8.2 Summary of the Systematic Errors on the Collision Energies

The individual contributions to the systematic error of the off-peak CM energies are summarised in Tab. 8.1. The main part of the errors were already published in [104, 105], labelled to be preliminary. Most of them still changed since this first preliminary publication. All errors have been reevaluated for the definitive publication of the LEP Energy Working Group [106], which summarises all the performed studies and their results.

- **Mean fill energy**
  This error accounts for the energy uncertainty in the uncalibrated fills. The dominant error in the old analysis of the 1993 data was the knowledge of the mean fill energy: the scatter of the model with respect to the energy calibration data is used to derive the uncertainty in the mean energy at the off-peak points. For 1995 the error from this source on Γ_Z and M_Z is approximately half of that assigned in 1993 or even smaller. The improvement is mainly due to the significant increase of the luminosity weighted fraction of calibrated off-peak fills in 1995 and due to the modelling demonstrated in section 5.3.

- **Horizontal correctors**
  The difference between the settings of the horizontal corrector magnets used to correct the orbit between physics and calibration mode contributes to the energy uncertainty. This error has been evaluated by simulating the accelerator optics

	1993		1995	
source	Peak-2	Peak+2	Peak-2	Peak+2
Mean fill energy	1.7	0.9	0.8	0.5
Corrector settings	< 0.1	0.4	0.2	0.2
Tide	0.0	0.2	0.2	< 0.1
Ring temperature	0.1	0.4	0.4	0.4
Energy rise	2.9	2.6	1.2	1.2
Bending modulation	-	-	< 0.1	0.3
Energy calibration	0.5	0.5	0.5	0.5
e^+/e^- energy difference	0.3	0.3	0.3	0.3
Bunchlet energy difference	-	-	0.1	0.1
total common	3.4	2.9	1.6	1.5
RF corrections (comb.)	0.5	0.5	0.7	0.7
Dispersion correction (comb.)	0.4	0.4	0.3	0.3
overall error	3.5	3.0	1.8	1.7

Table 8.1: *Summary of errors (MeV) on the LEP energy determination. The errors summarised in the upper part of the table apply to the energies at each interaction point. The errors in the lower part apply, respectively, to the energies at the individual interaction points.*

with a simulation program [82]. For both years the uncertainty is of the same order and results in an error around 0.5 MeV on Γ_Z and M_Z [106]. These errors have been evaluated using the data from the experiments where the effect of the horizontal corrector settings has been tested.

- **Tide**
  The systematic errors induced by the tidal correction have been reevaluated for 1993 and calculated for 1995 using the meanwhile established new energy model [106].

- **Ring temperature**
  Various fits of the magnetic field as a function of the temperature were made for the mean of all 16 dipoles, which were in 1996 equipped with NMR probes. The results of these fits showed significant variations indicating the presence of systematic effects and the difficulty of separating the parasitic current and temperature driven behaviour. The error associated to these variations amounts 0.2 to 0.4 MeV for 1993 and 1995 respectively.

- **Uncertainties of the energy rise**
  The knowledge of the energy rise due to the Train Effect and temperature changes in a fill has associated errors. The uncertainty on the absolute energy rise results in an error on M_Z, whereas the assumption that this rise is the same at P-2 and

P+2 is accompanied by a systematic uncertainty which translates into an error on Γ_Z. The predictions of the energy model (Eq. 8.2) can be compared with calibration data (Long Term Experiments) directly. They induce an error of 0.6 MeV for 1995 and about 2.5 MeV for 1993 on the average energy rise for either energy setting. To what degree the rise term has the same magnitude and shape at the two off-peak points was quantified from the NMR data itself. The data indicated that the error on Γ_Z arising from this assumption is less than 0.6 MeV for both years [106]. An additional error of approximately 1 MeV (in 1995) and 0.6 MeV (in 1993) for all four energy points accounts for the variations observed when different assumptions were used constructing the NMR part of the energy model and in particular for different temperature coefficients and models.

- **Bending modulation jump**
  The large scatter of the measured field jump at NMR4 and NMR8 due to the magnet conditioning induces an error, which differs slightly for the two energy points in 1995. Since bending modulations were performed during the 1995 scan only no error has to be assigned to this source for the 1993 data. For both energy points in 1995 this error is less than 0.3 MeV

- **Energy calibration**
  The energy calibration with the resonant depolarisation technique has an intrinsic systematic error. This has been calculated in the 1993 analysis [33]. The same value has been used here as an educated guess for the 1995 error.

- **Uncertainties of energy differences**
  The energy differences between electrons and positrons and between the bunches in a train as well as the associated errors have been discussed in section 7.1. In 1993 no energy difference between the bunches in a train occurred, since LEP was operated with pretzel optics.

- **IP Dependent errors**
  The contribution from the RF corrections has been estimated by comparing the observables mentioned in the RF chapter in this dissertation and the RF model. All contributions are well below 1 MeV. In particular the error at IP2 is dominant as IP2 is the interaction point where the largest uncertainty for the individual bunchlet z vertex position occurred. The detailed systematic errors associated with the RF corrections were presented in section 6.1 in this dissertation.
  The errors arising from a finite vertical dispersion of opposite sign between the two beams are small. The systematic errors, which are related to the dispersion correction, were discussed in section 6.2. They induce a $\sim$ 0.3 MeV error on the two energy points in 1995, which is even slightly smaller than the accordant error assigned for the 1993 pretzel operation. This indicates the success of the Vernier Scan programme in coping with this potentially troublesome source of uncertainty.

Tab. 8.1 contains also averaged values for the combined errors. Note that these are meant to illustrate the size of the errors. They should not be used for the error estimate of M_Z and Γ_Z since one would overestimate the error.

Many of the systematic errors on the collision energy are correlated at the four IPs, the two energy settings as well as for 1993 and 1995. In order to take these correlations correctly into account, the LEP Energy Working Group calculated an error matrix which contains all errors common to all IPs [106]. This formalism allows to determine the errors on the Z line shape parameters for the combined data of all LEP experiments. In general, correlated errors contribute to an uncertainty of M_Z while uncorrelated ones determine the systematic error associated to Γ_Z.

8.3 LEP Contribution to the Error of M_Z and Γ_Z

During the two Z resonance scans, which were performed in 1993 and 1995, the LEP contribution to the error of the mass and the width of the Z particle could be reduced significantly with respect to the precision achieved after the energy scan in 1991. This is illustrated in Tab. 8.2, which summarises the errors as they were evaluated after the 1991 scan [31], after the 1993 energy scan [33] and the preliminary values from 1995 [104, 105], which were given at the ICHEP96 conference in Warsaw, 25-31 July 1996. The final error evaluation is published in [106] The old energy model from

year	ΔM_Z	$\Delta \Gamma_Z$
1991	6.3	4.9
1993, old	1.4	1.5
1995, ICHEP96	1.5	1.7
1995, final	1.5	1.5

Table 8.2: *LEP error contribution to the error of M_Z and Γ_Z after the scans in 1991, 1993 and 1995, where preliminary (ICHEP96) and final results are given. Note that the 1995 result includes the contribution from the previous years, in particular from 1993, which had to be revised.*

1993 and the new one from 1995 differ mainly in the prediction of the energy rise in a fill, leading to increased LEP contributions (Tab. 8.2) to ΔM_Z and $\Delta \Gamma_Z$ as well as to expected changes in the mean energy values after the application of the new and modified model to the 1993 and 1995 data. The 1993 errors are increased significantly with respect to those published earlier. The energy rise term had been underestimated by about 4 MeV causing an overestimated mean CM energy because energy calibrations were especially performed at the end of fills. The reduction of the mean energy values is reflected in a decrease of the M_Z value. This can be seen in Fig. 8.1. The results from 1991 with their large errors are supplied for illustration only. The 1993 results, which combine the data acquired from the four experiments between 1989 and 1993, were derived without the knowledge of the true size of the energy rise. The averaged value of M_Z from the data of the four LEP experiments at that time was 91.1888 ± 0.0044 GeV [107]. The error included a common LEP error of $\Delta M_Z = 1.4$ MeV. Taking into

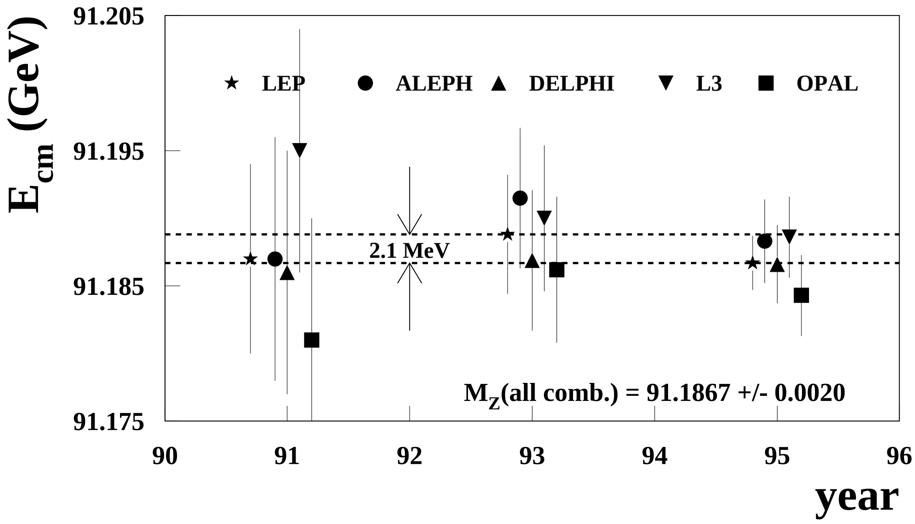

Figure 8.1: The mass of the Z particle measured by the four LEP experiments as a function of the year. All fits from a certain year include the data from the years before. The numbers are taken from [8], [107] and [108].

account the additional 1995 data and after application of the modified energy model, the averaged result for M_Z is 91.1867 ± 0.0020 GeV [108]. M_Z is lower by 2.1 MeV compared to the 1993 (old) value indicating the overestimation of the mean CM energy. The error on the Z mass contains a LEP CM energy contribution of 1.5 MeV arising from the combined 1993 and 1995 studies. The instance that the 1995 final LEP error contribution to ΔM_Z could not be lowered but increased slightly with respect to the old 1993 value is due to the revisal of the 1993 data in the light of the new insight gained in 1995. However, this 1.5 MeV error is a significant reduction compared to the 6.3 MeV in 1991. Today the error on M_Z due to the uncertainty of the LEP CM energies is of the same order as the error arising from the cross section measurements at the experiments ($\simeq 1.3$ MeV). The notable reduction of the LEP error results to a large extend from the improved knowledge about LEP, which was gained over the last three years. The work presented in this thesis was a major contribution to this gain.

Chapter 9

Summary

The calibration of the LEP collision energy is of particular importance for the precise determination of the Z mass and width. After the 1991 Z resonance scan a combination of the data from the four LEP experiments gave an error on M_Z of 7.5 MeV and on Γ_Z of about 8 MeV. The contribution of the LEP energy uncertainty to the error on the Z mass of 6.3 MeV dominated the achieved precision. Hence it was decided to perform another energy scan in 1993 in order to reduce the LEP contribution to the error on M_Z and Γ_Z and to simultaneously increase the available data statistic. The analysis of the 1993 scan resulted in a combined error on M_Z of 4.4 MeV including an error of 1.4 MeV arising from the energy uncertainty. But during this scan some of the observed properties of the dipole field remained unexplained. This lack of understanding motivated another Z resonance scan with improved instrumentation. In particular for the first time the dipole field was monitored with two NMR probes in the LEP tunnel. The aim of this so far last Z resonance scan at LEP was not only to improve further the accuracy on the Z mass and width but also to confirm the results achieved in the 1993 scan.

During the 1995 scan quite some effort was made to calibrate off-peak fills at the end of physics conditions. About 70 % of the 1995 off-peak luminosity consists of calibrated fills, compared to approximately 35 % achieved in 1993. The tunnel NMR probes revealed significant increases of the dipole field superimposed by day-time dependent fluctuations on a minute time scale. These unexpected features could be explained by earth currents produced by trains circulating in the Geneva area, which are captured by the LEP vacuum chamber, and by a new understanding of the temperature variations of the dipole field. The averaged energy increase during an operation time of about 12 hours was measured to be approximately 6 MeV. The measurements of the NMR probes were confirmed by data from fills with either frequent calibrations (machine developments) or energy measurements at the beginning. The notable large drifts implied an overestimation of the mean CM energy by about 4 MeV in the earlier 1993 analysis, where only a rise of approximately 2 MeV was taken into account.

Interaction point specific corrections arise from the RF system and from opposite sign vertical dispersion at the IPs induced by the bunch train mode of LEP operation. Such a vertical dispersion was not present in earlier scans, which were performed with the pretzel operation mode. In contrary to earlier scans, in 1995 LEP was operated with numerous new super conducting cavities. Large alignment uncertainties of these cavities implied a significant increase of the error assigned to the energy offset at IP6. However, the errors on the interaction point specific corrections are comparatively small and do not dominate the LEP errors on M_Z and Γ_Z.

Because of the insight gained from the 1995 energy scan the value of M_Z, deduced in 1993, had to be lowered by 2.1 MeV taking into account the overestimation of the mean CM energy. Additionally, the LEP errors on M_Z and Γ_Z had to be increased slightly compared to the 1993 values resulting in new values of [106, 108]:

$$\begin{aligned} \Delta M_Z &= 1.5 \text{ MeV}, \\ \Delta \Gamma_Z &= 1.5 \text{ MeV}. \end{aligned}$$

These errors are a significant reduction of the 1991 value and are of the same order as the errors arising from statistical and experimental uncertainties.

Appendix A

Long Term Calibration Measurements

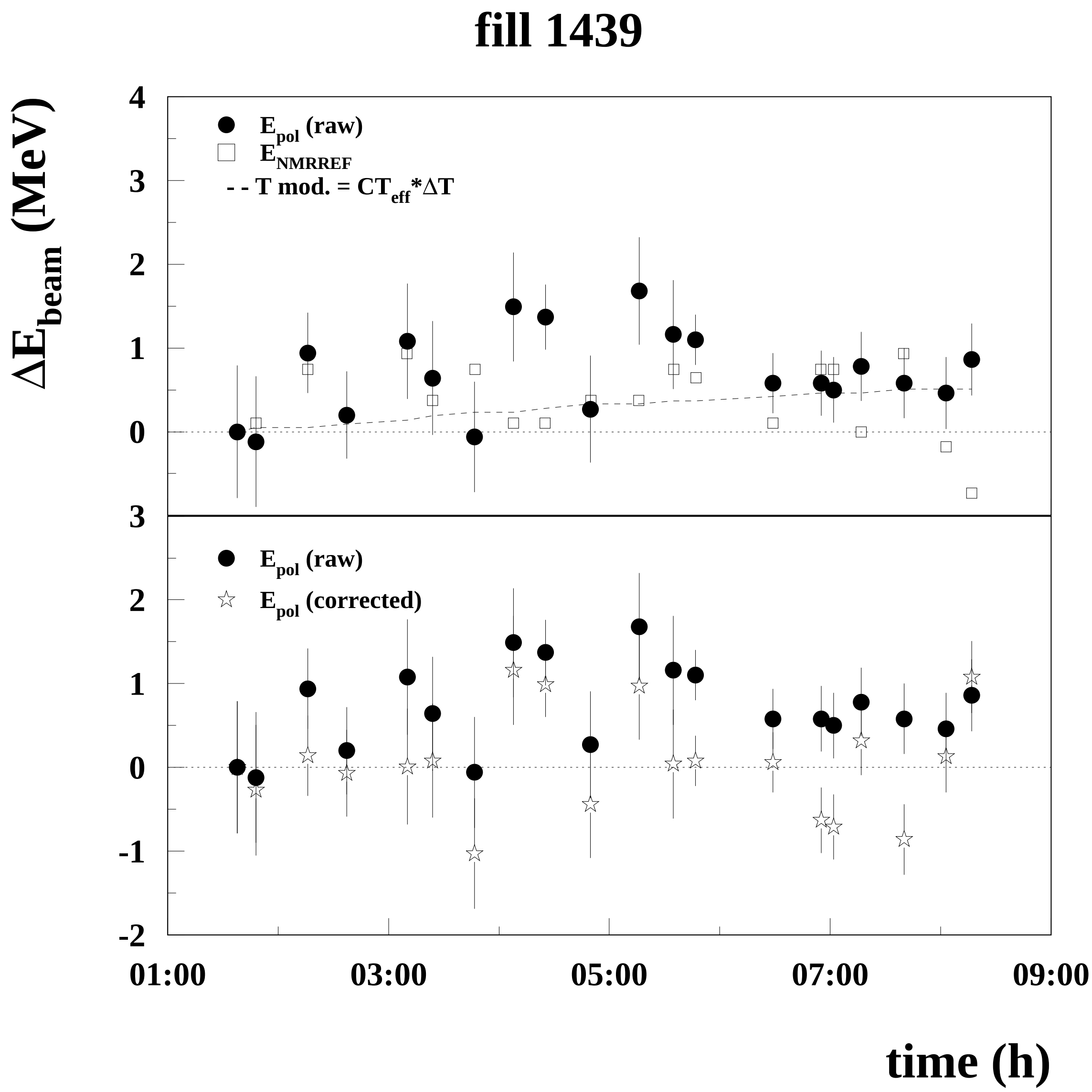

Figure A.1: *Top: Energy calibration measurements, the prediction from a temperature based model and B-field measurements from the NMRREF probe as a function of time in fill 1439. The temperature predicition is based on an effective coefficient $C_{T_{eff}}$ acting on the mean temperature of the ring. Energy calibration measurements are corrected for tidal effects only (raw). The RMS scatter of the E_{pol} data around zero (dotted line) amounts 0.5 MeV. Bottom: Raw energy calibration measurements and corrected measurements as a function of time. The corrected measurements take NMRREF drifts and temperature effects into account. The RMS scatter of the corrected energy measurements around zero is 0.6 MeV. All data points are normalised to the first energy calibration reading and presented as a difference from the initial value.*

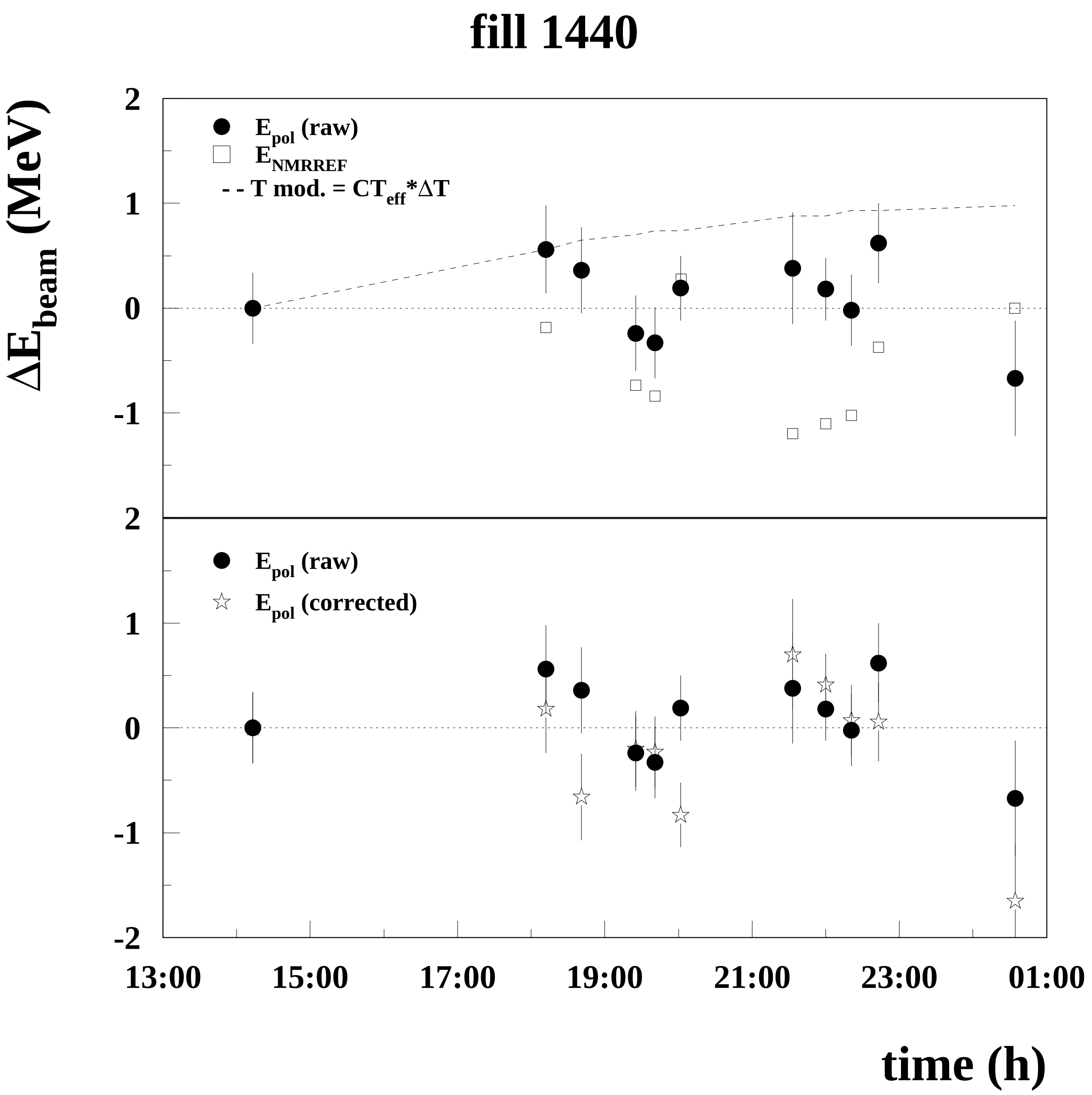

Figure A.2: *Top: Energy calibration measurements, the prediction from a temperature based model and B-field measurements from the NMRREF probe as a function of time in fill 1440. The temperature predicition is based on an effective coefficient $C_{T_{eff}}$ acting on the mean temperature of the ring. Energy calibration measurements are corrected for tidal effects only (raw). The RMS scatter of the E_{pol} data around zero (dotted line) amounts 0.4 MeV. Bottom: Raw energy calibration measurements and corrected measurements as a function of time. The corrected measurements take NMRREF drifts and temperature effects into account. The RMS scatter of the corrected energy measurements around zero is 0.6 MeV. All data points are normalised to the first energy calibration reading and presented as a difference from the initial value.*

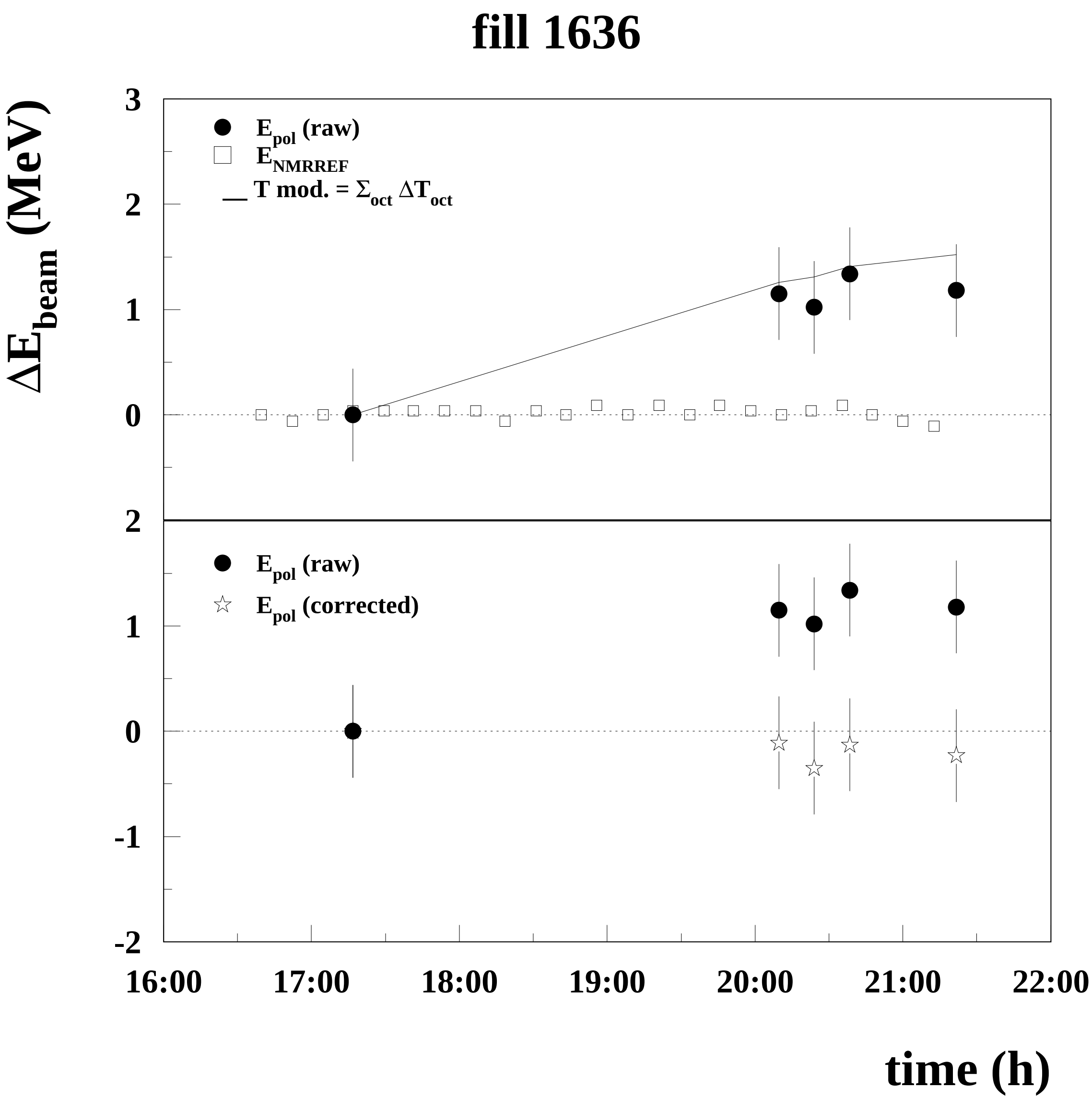

Figure A.3: *Top: Energy calibration measurements, the prediction from a temperature based model and B-field measurements from the NMRREF probe as a function of time in fill 1636. The temperature predicition is based on a 5-coefficient model according to Eq 5.7, acting on the mean temperatures per octant. Energy calibration measurements are corrected for tidal effects only (raw). The RMS scatter of the E_{pol} data around zero (dotted line) amounts 0.5 MeV. Bottom: Raw energy calibration measurements and corrected measurements as a function of time. The corrected measurements take NMRREF drifts and temperature effects into account. The RMS scatter of the corrected energy measurements around zero is 0.1 MeV. All data points are normalised to the first energy calibration reading and presented as a difference from the initial value.*

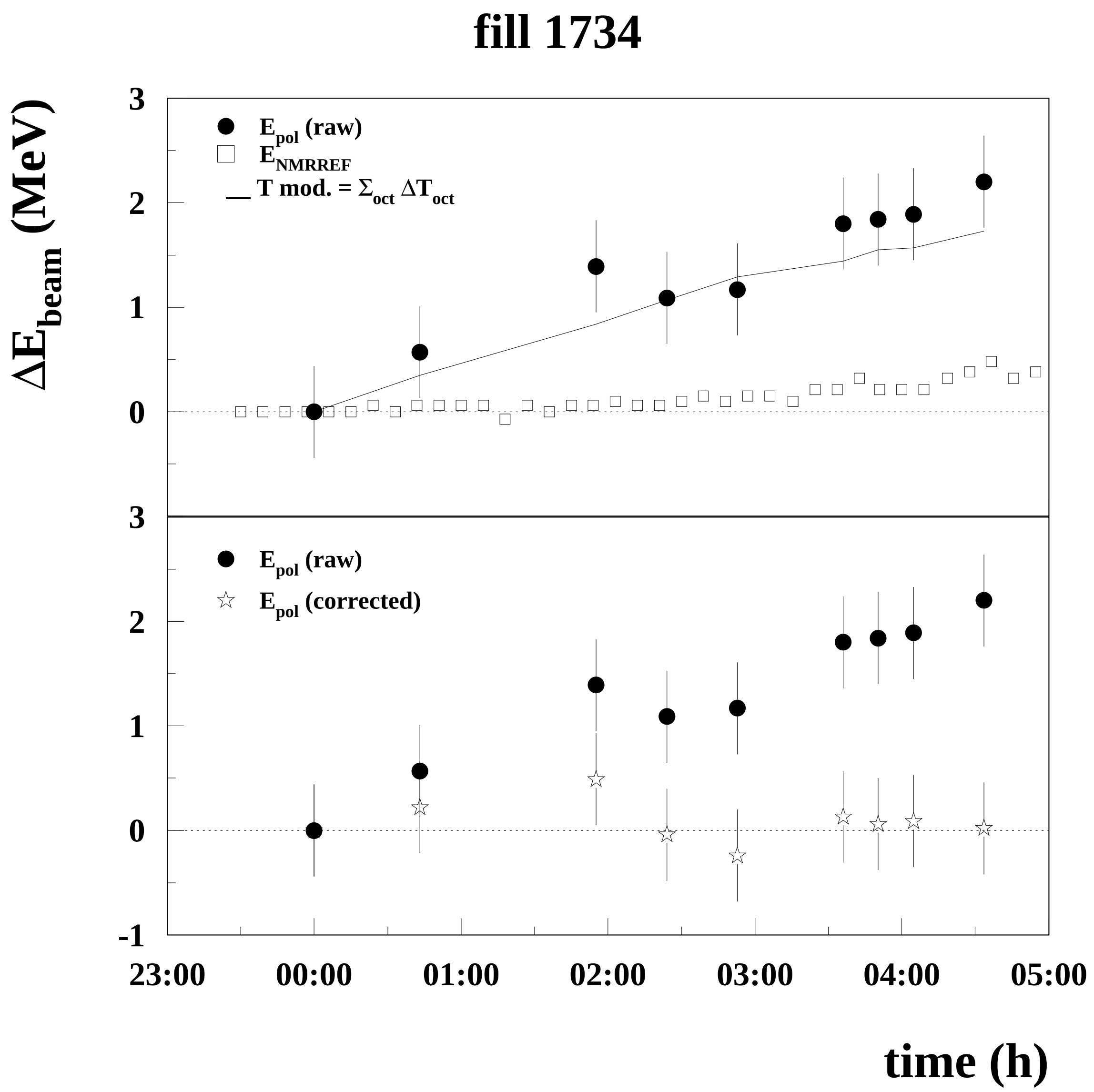

Figure A.4: *Top: Energy calibration measurements, the prediction from a temperature based model and B-field measurements from the NMRREF probe as a function of time in fill 1734. The temperature predicition is based on a 5-coefficient model according to Eq 5.7, acting on the mean temperatures per octant. Energy calibration measurements are corrected for tidal effects only (raw). The RMS scatter of the E_{pol} data around zero (dotted line) amounts 0.7 MeV. Bottom: Raw energy calibration measurements and corrected measurements as a function of time. The corrected measurements take NMRREF drifts and temperature effects into account. The RMS scatter of the corrected energy measurements around zero is 0.2 MeV. All data points are normalised to the first energy calibration reading and presented as a difference from the initial value.*

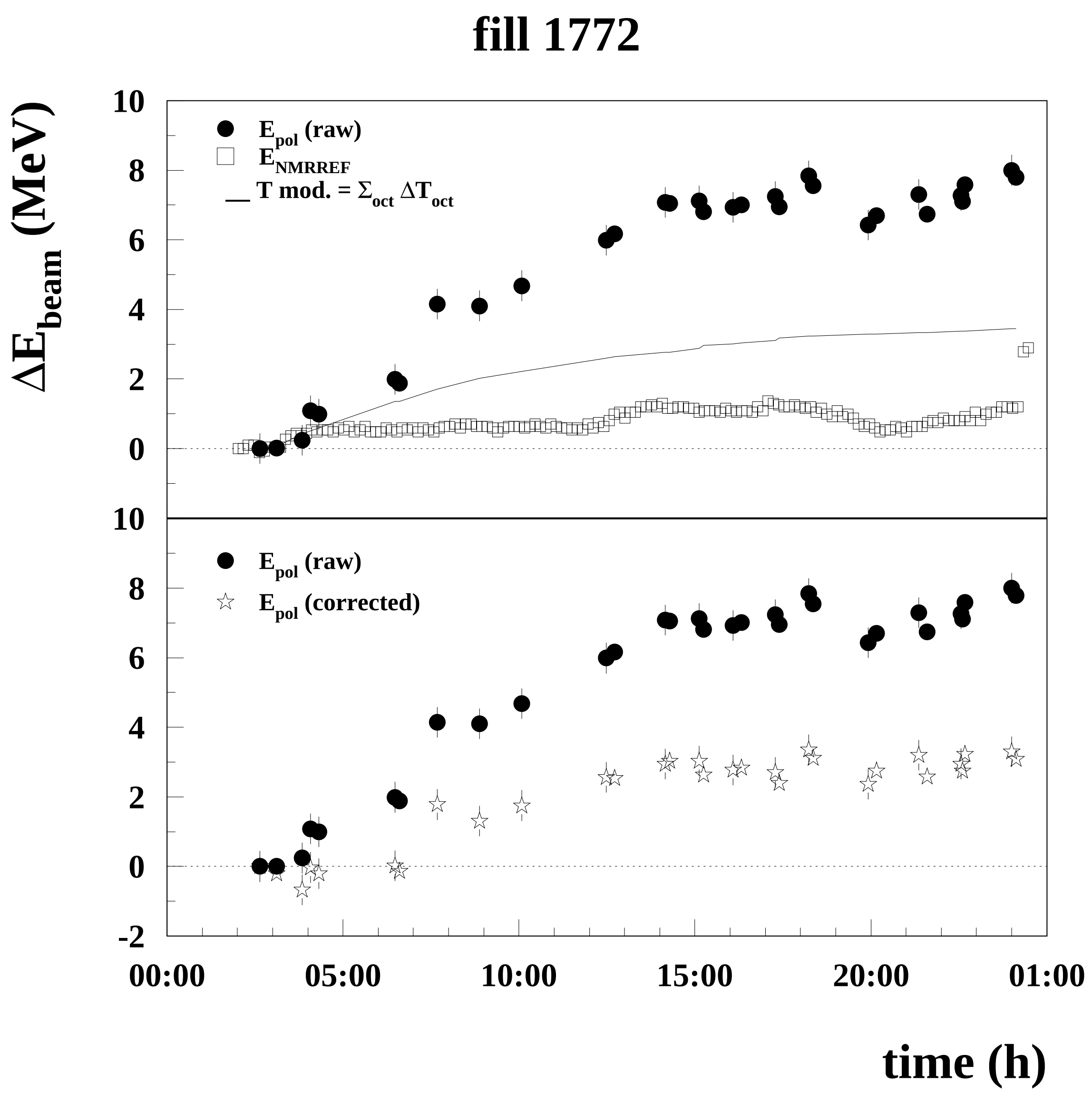

Figure A.5: *Top: Energy calibration measurements, the prediction from a temperature based model and B-field measurements from the NMRREF probe as a function of time in fill 1772. The temperature predicition is based on a 5-coefficient model according to Eq 5.7, acting on the mean temperatures per octant. Energy calibration measurements are corrected for tidal effects only (raw). The RMS scatter of the E_{pol} data around zero (dotted line) amounts 2.6 MeV. Bottom: Raw energy calibration measurements and corrected measurements as a function of time. The corrected measurements take NMRREF drifts and temperature effects into account. The RMS scatter of the corrected energy measurements around zero is 1.3 MeV. All data points are normalised to the first energy calibration reading and presented as a difference from the initial value. This fill is the only one with a clear evidence for jumps, which can be deduced from the Train Effect.*

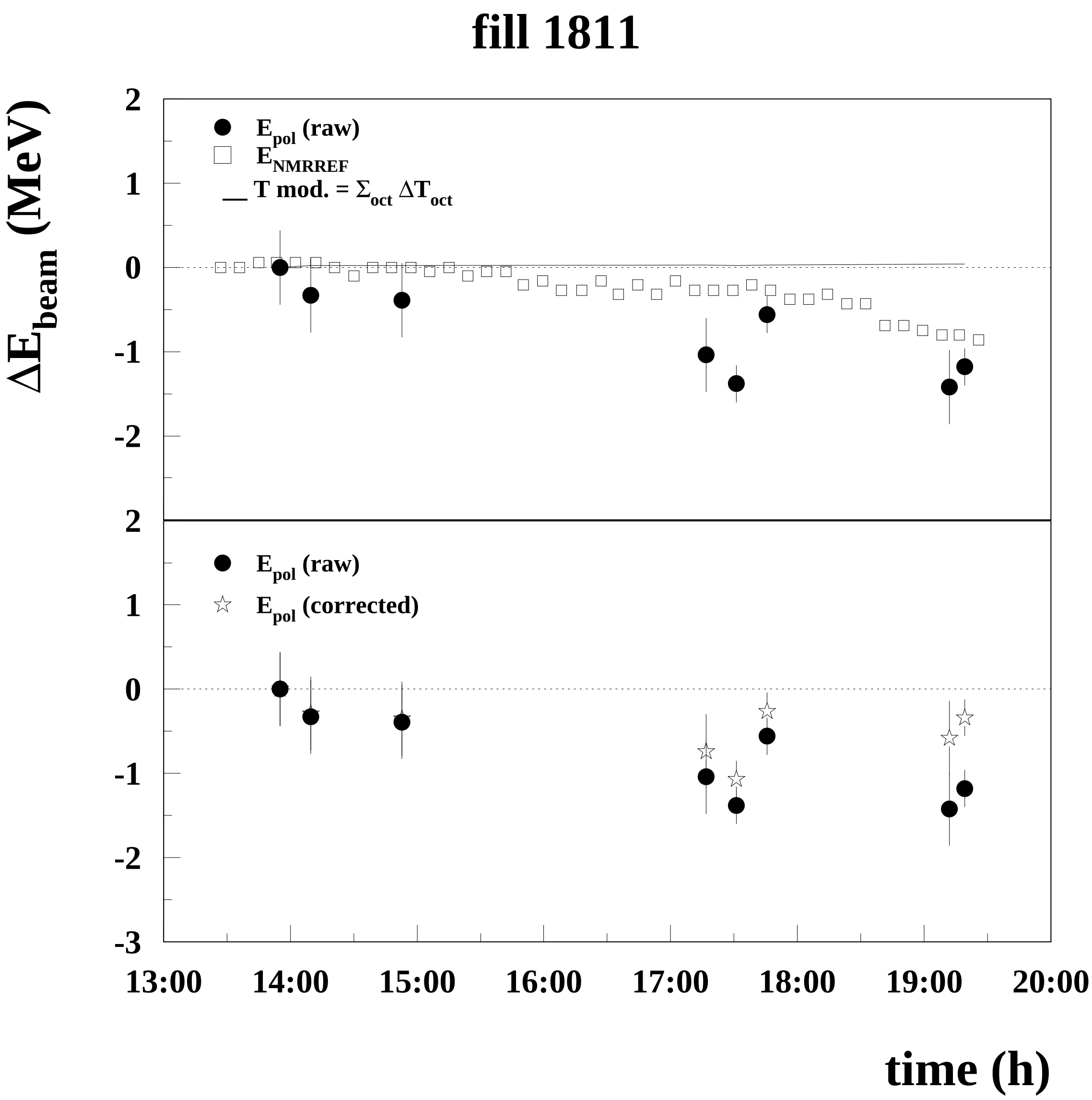

Figure A.6: *Top: Energy calibration measurements, the prediction from a temperature based model and B-field measurements from the NMRREF probe as a function of time in fill 1811. The temperature predicition is based on a 5-coefficient model according to Eq 5.7, acting on the mean temperatures per octant. Energy calibration measurements are corrected for tidal effects only (raw). The RMS scatter of the E_{pol} data around zero (dotted line) amounts 0.5 MeV. Bottom: Raw energy calibration measurements and corrected measurements as a function of time. The corrected measurements take NMRREF drifts and temperature effects into account. The RMS scatter of the corrected energy measurements around zero is 0.3 MeV. All data points are normalised to the first energy calibration reading and presented as a difference from the initial value.*

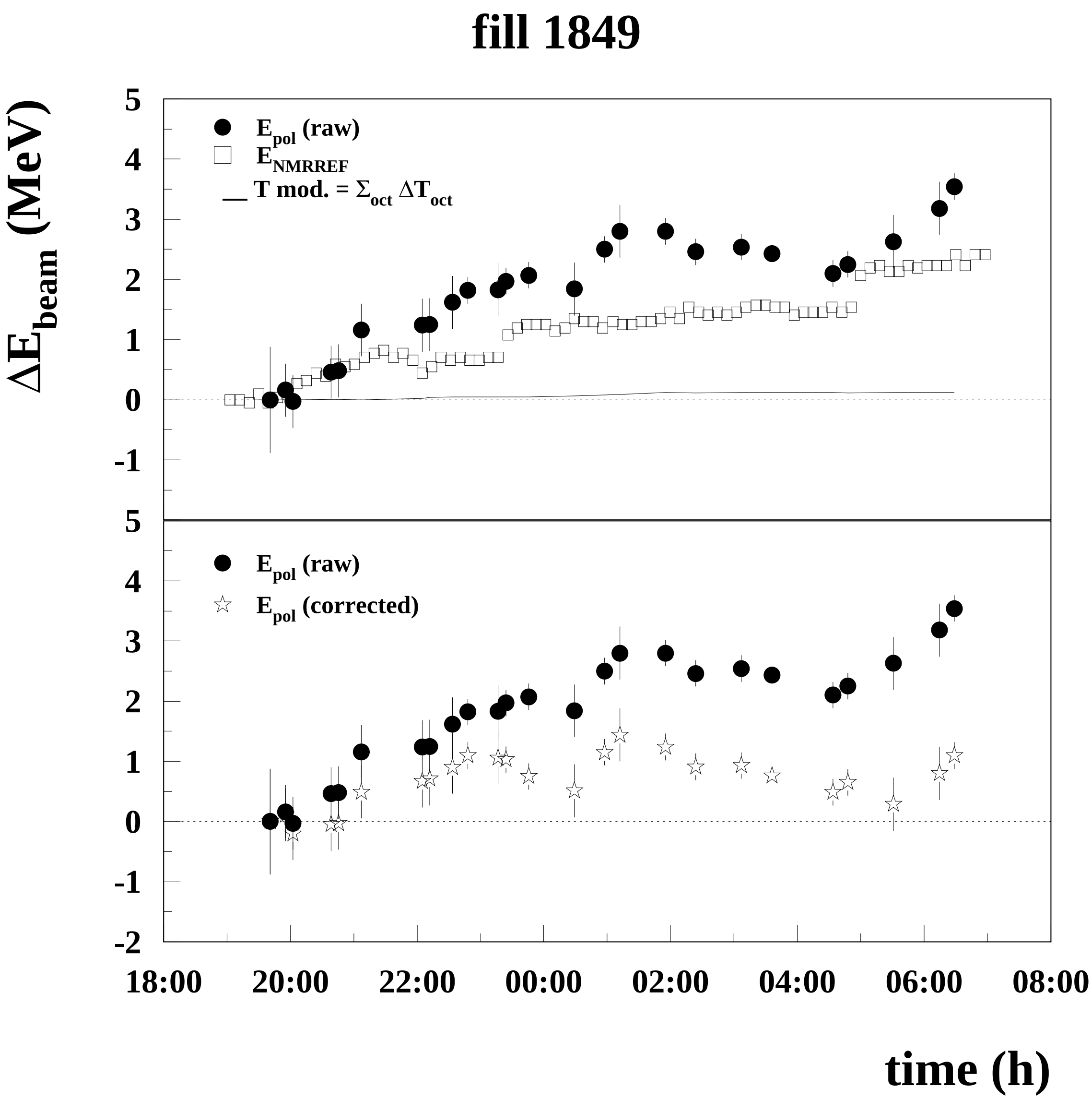

Figure A.7: *Top: Energy calibration measurements, the prediction from a temperature based model and B-field measurements from the NMRREF probe as a function of time in fill 1849. The temperature predicition is based on a 5-coefficient model according to Eq 5.7, acting on the mean temperatures per octant. Energy calibration measurements are corrected for tidal effects only (raw). The RMS scatter of the E_{pol} data around zero (dotted line) amounts 1.0 MeV. Bottom: Raw energy calibration measurements and corrected measurements as a function of time. The corrected measurements take NMRREF drifts and temperature effects into account. The RMS scatter of the corrected energy measurements around zero is 0.4 MeV. All data points are normalised to the first energy calibration reading and presented as a difference from the initial value.*

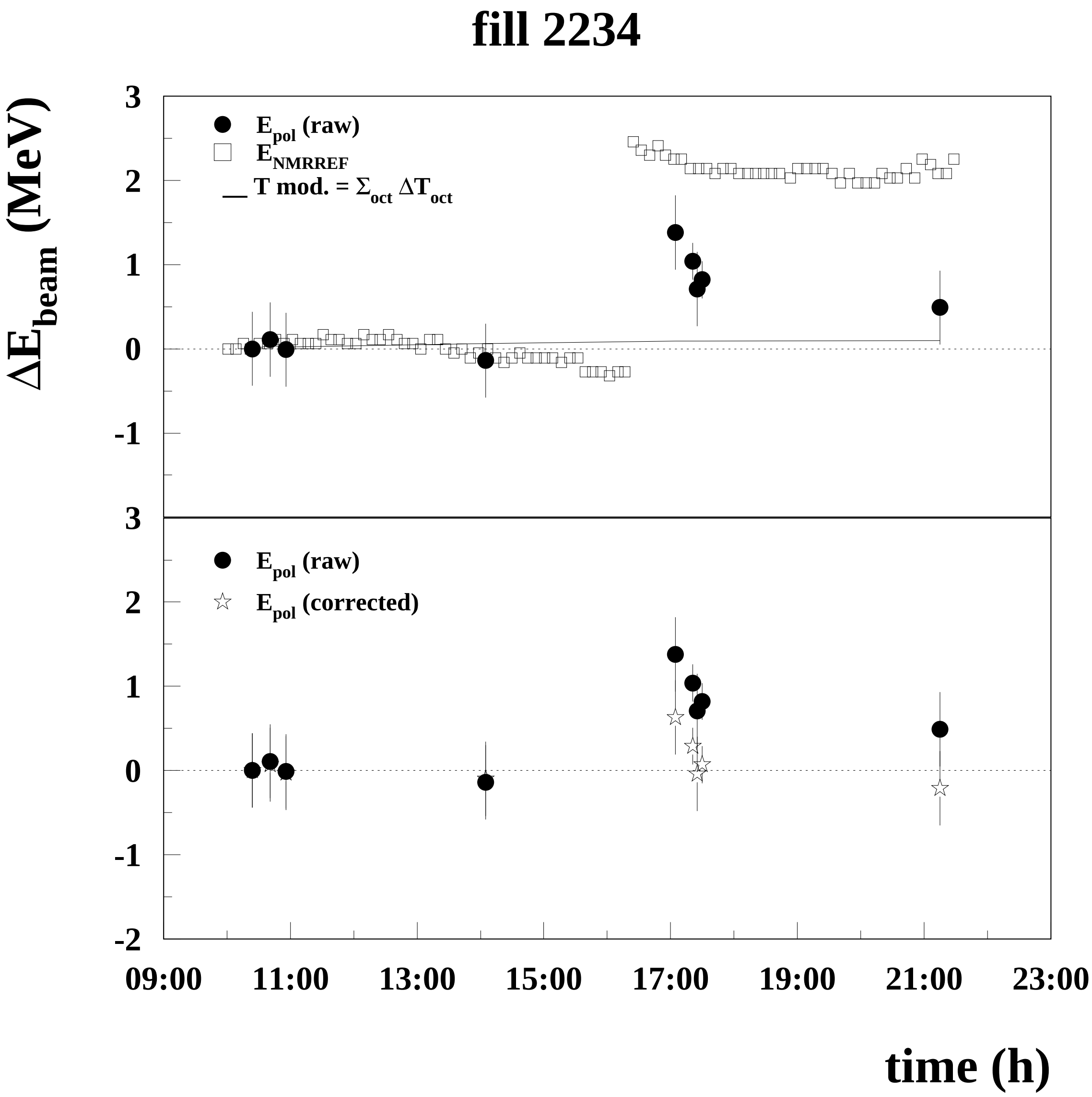

Figure A.8: *Top: Energy calibration measurements, the prediction from a temperature based model and B-field measurements from the NMRREF probe as a function of time in fill 2234 (1994). The temperature predicition is based on a 5-coefficient model according to Eq 5.7, acting on the mean temperatures per octant. Energy calibration measurements are corrected for tidal effects only (raw). The RMS scatter of the E_{pol} data around zero (dotted line) amounts 0.5 MeV. Bottom: Raw energy calibration measurements and corrected measurements as a function of time. The corrected measurements take 30 % of the jump in the NMRREF readings and temperature effects into account. The RMS scatter of the corrected energy measurements around zero is 0.2 MeV. All data points are normalised to the first energy calibration reading and presented as a difference from the initial value.*

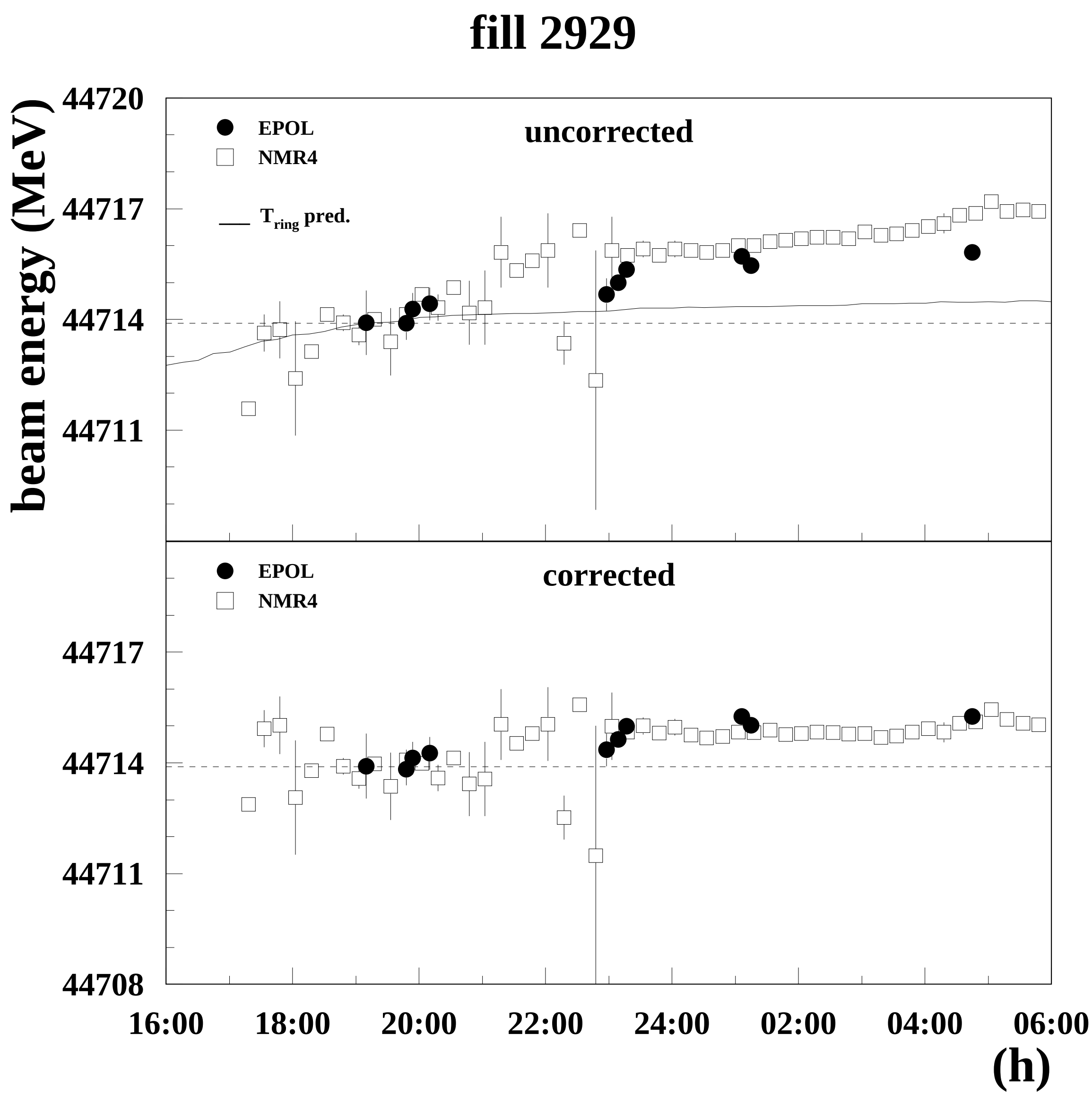

Figure A.9: *Beam energy measurements and NMR data as a function of time. Top: NMR data are uncorrected, energy measurements are corrected for tide effects only. The solid line corresponds to the prediction of the new temperature parametrisation for the whole ring. Bottom: NMR readings and energy measurements are corrected for temperature effects. The errors of the NMR readings correspond to the RMS scatter in the time interval, which is equivalent to one bin. In this fill no NMR8 data were recorded.*

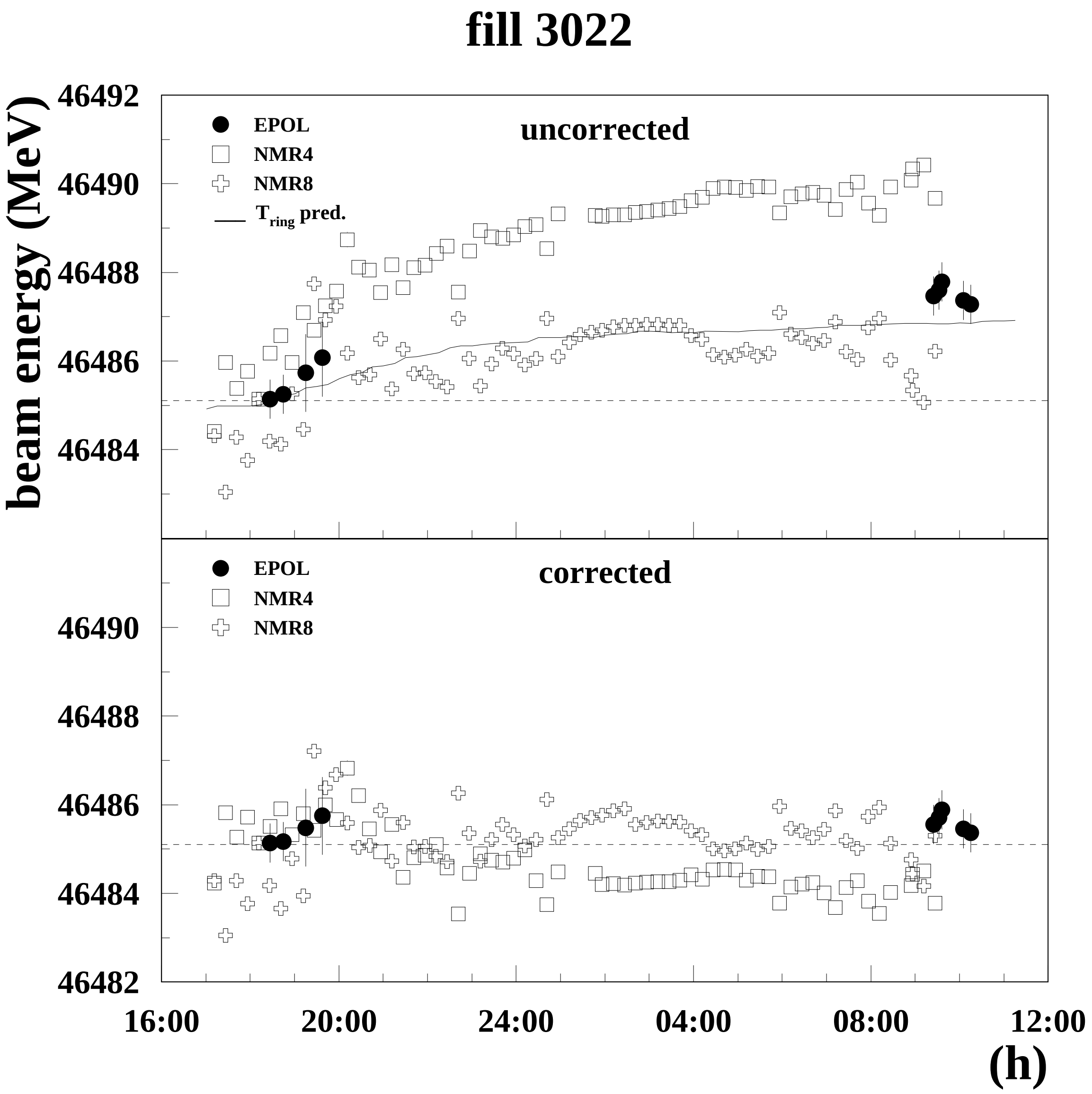

Figure A.10: *Beam energy measurements and NMR data as a function of time. Top: NMR data are uncorrected, energy measurements are corrected for tide effects only. The solid line corresponds to the prediction of the new temperature parametrisation for the whole ring. Bottom: NMR readings and energy measurements are corrected for temperature effects and for the bending modulation at 20:05. The beam energy measurements are corrected for the horizontal corrector settings. The errors of the NMR readings correspond to the RMS scatter in the time interval, which is equivalent to one bin.*

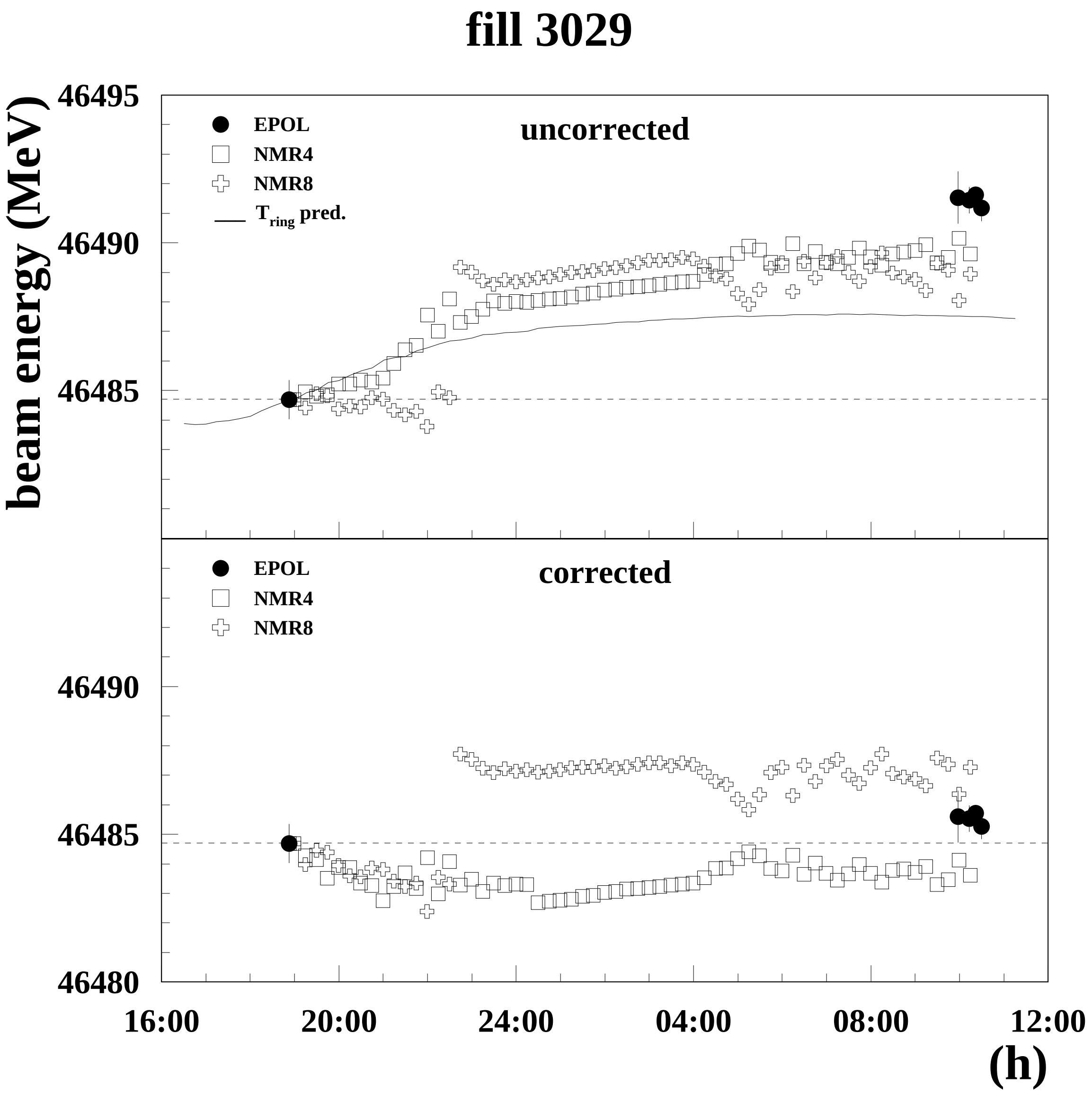

Figure A.11: *Beam energy measurements and NMR data as a function of time. The errors of the NMR readings correspond to the RMS scatter in the time interval, which is equivalent to one bin. Top: NMR data are uncorrected, energy measurements are corrected for tide effects only. The solid line corresponds to the prediction of the new temperature parametrisation for the whole ring. Bottom: NMR readings and energy measurements are corrected for temperature effects. The beam energy measurements are corrected for the horizontal corrector settings.*

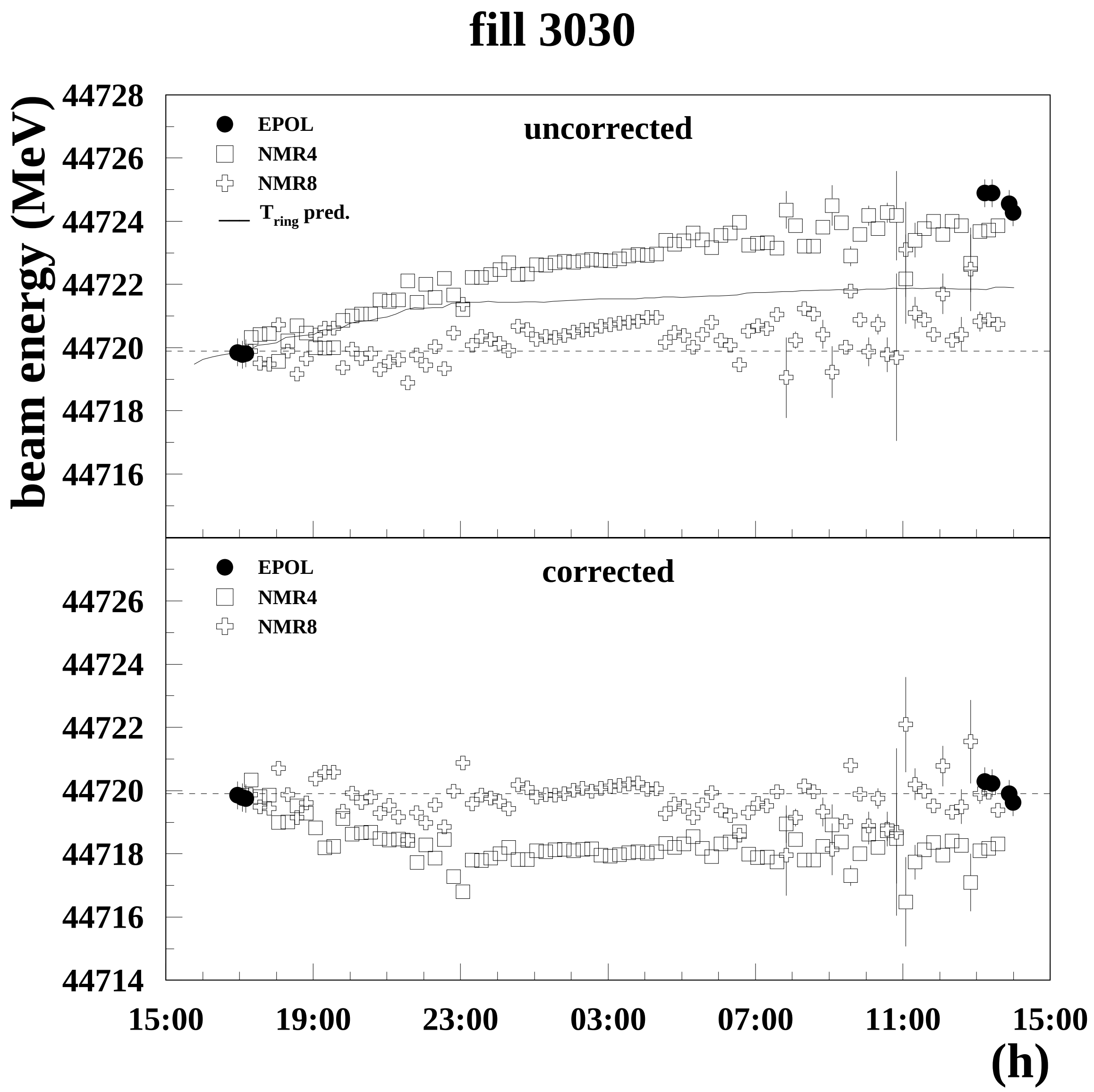

Figure A.12: *Beam energy measurements and NMR data as a function of time. The errors of the NMR readings correspond to the RMS scatter in the time interval, which corresponds to one bin. Top: NMR data are uncorrected, energy measurements are corrected for tide effects only. The solid line corresponds to the prediction of the new temperature parametrisation for the whole ring. Bottom: NMR readings and energy measurements are corrected for temperature effects. The beam energy measurements are corrected for the horizontal corrector settings.*

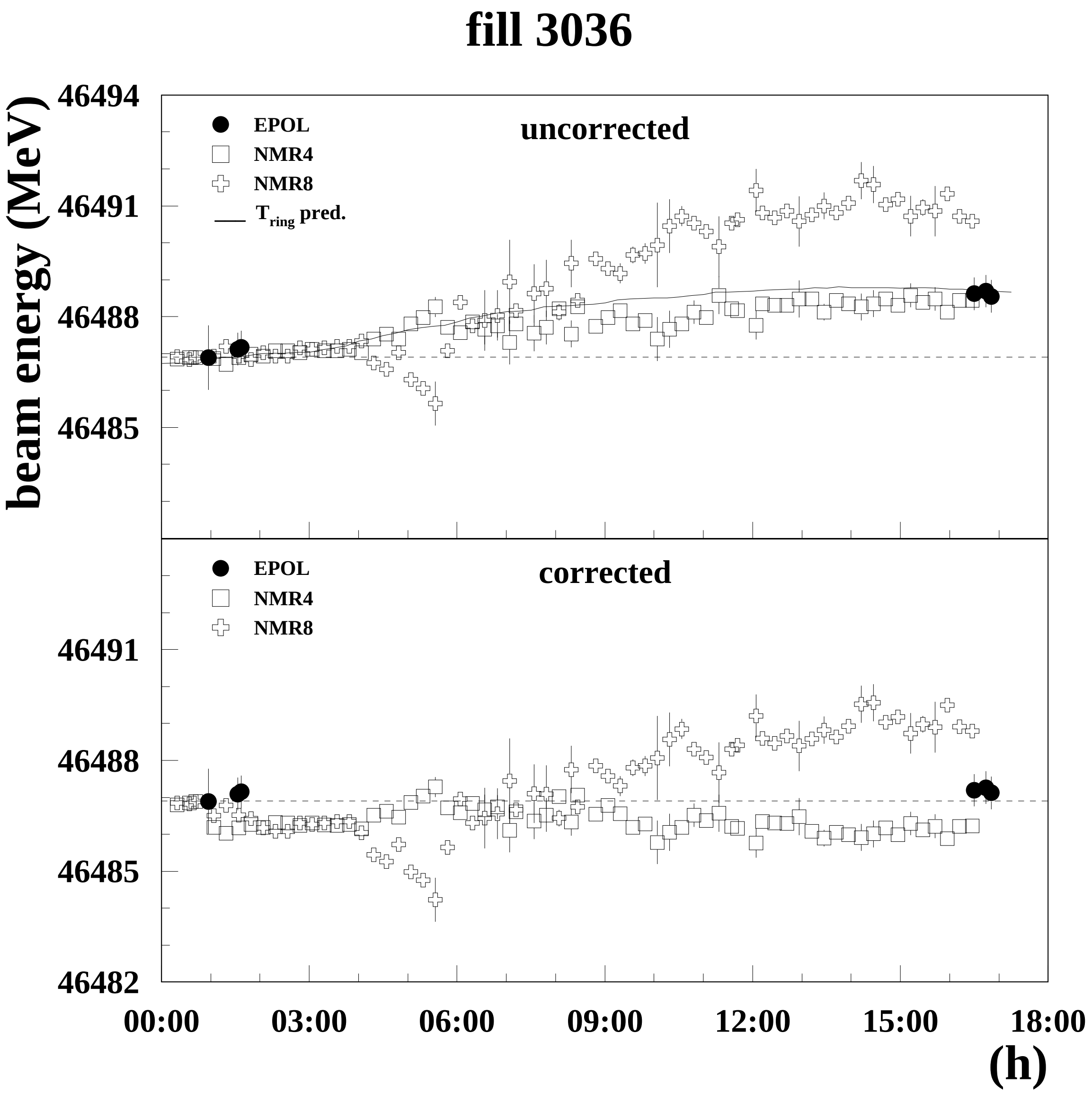

Figure A.13: *Beam energy measurements and NMR data as a function of time. The errors of the NMR readings correspond to the RMS scatter in the time interval, which is equivalent to one bin. Top: NMR data are uncorrected, energy measurements are corrected for tide effects only. The solid line corresponds to the prediction of the new temperature parametrisation for the whole ring. Bottom: NMR readings and energy measurements are corrected for temperature effects. The beam energy measurements are corrected for the horizontal corrector settings.*

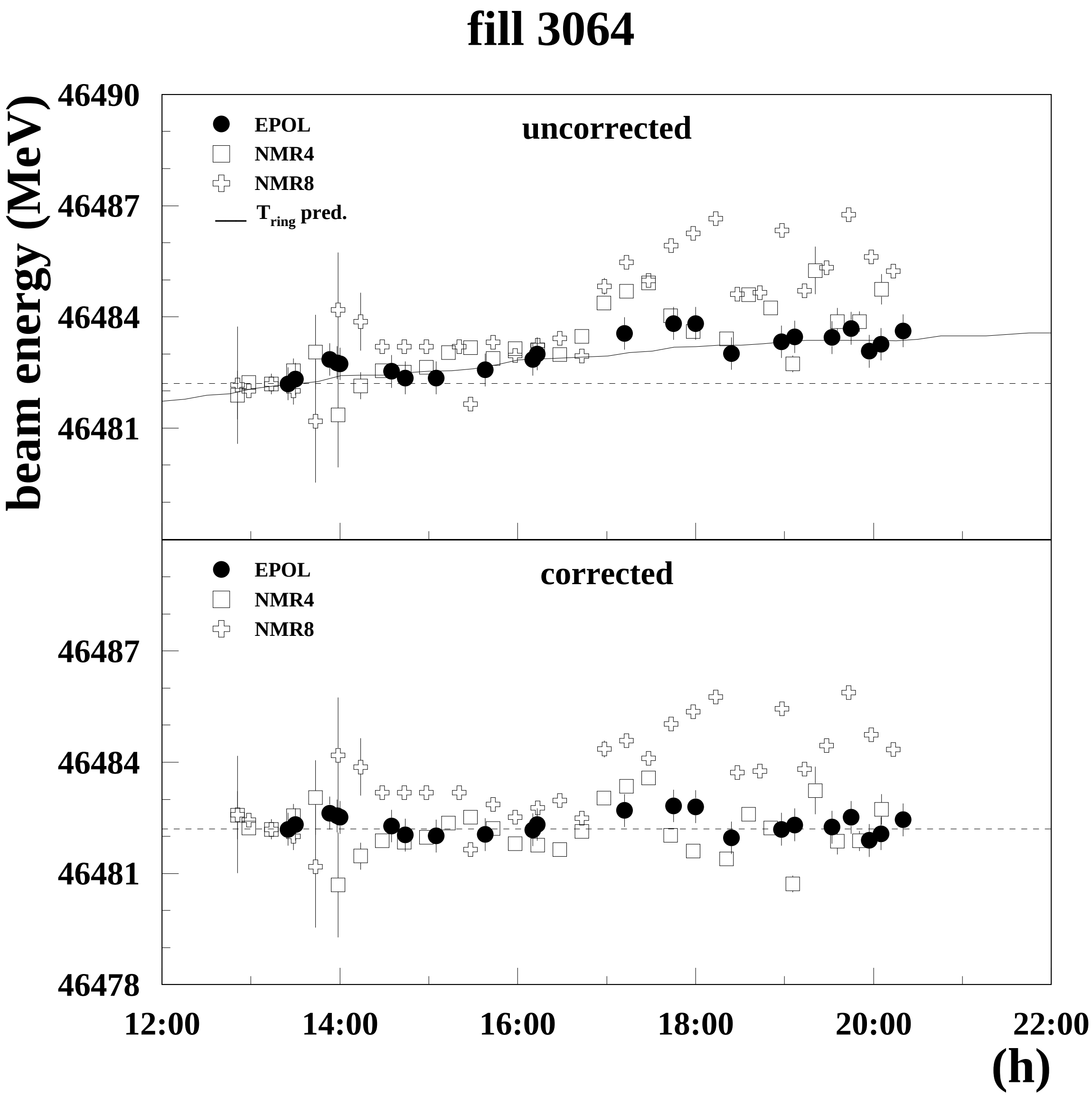

Figure A.14: *Beam energy measurements and NMR data as a function of time. The errors of the NMR readings correspond to the RMS scatter in the time interval, which is equivalent to one bin. Top: NMR data are uncorrected, energy measurements are corrected for tide effects only. The solid line corresponds to the prediction of the energy variation according to the new parametrisation. Bottom: NMR readings and energy measurements are corrected for temperature effects.*

Appendix B

Fills with Luminosity Feedback

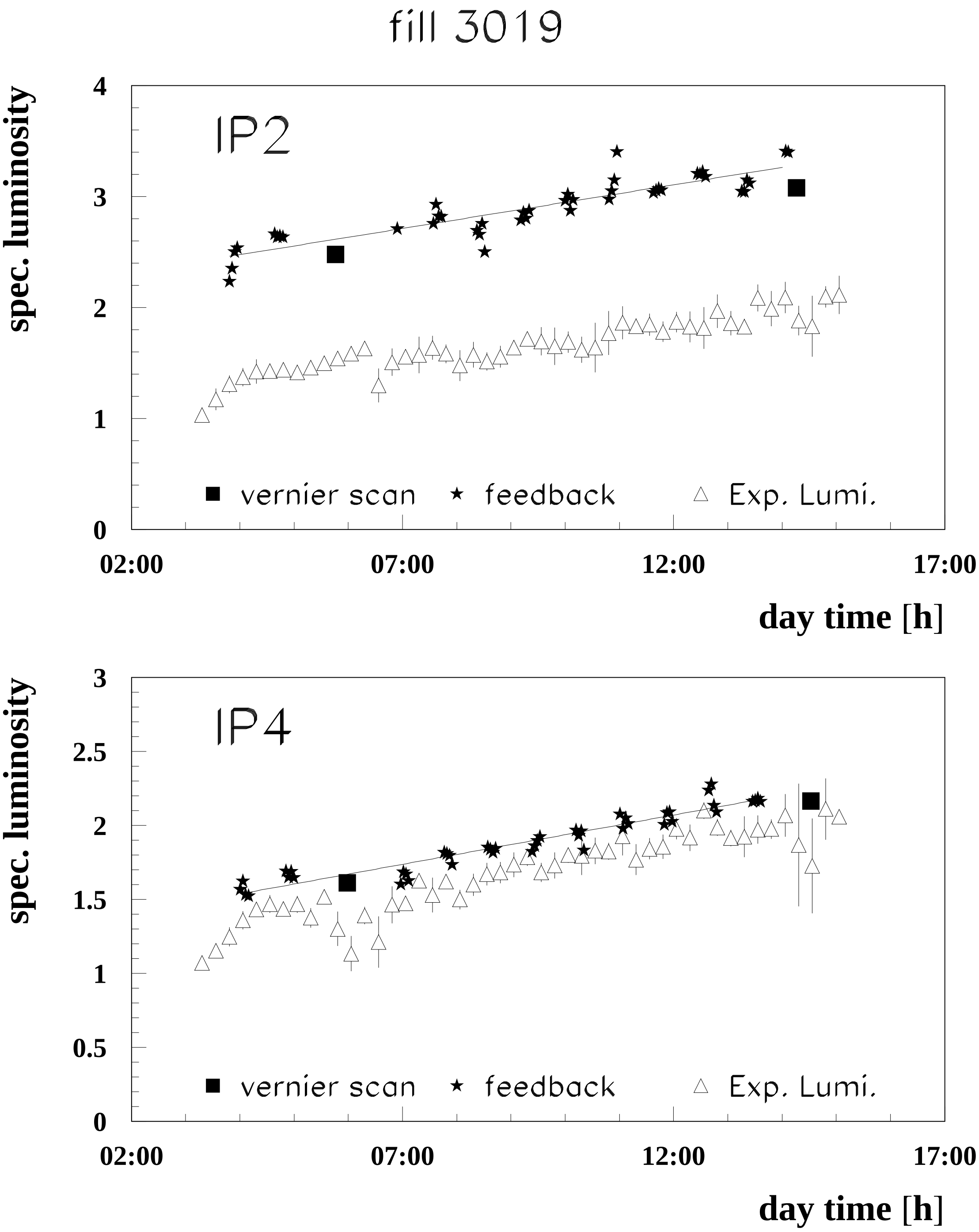

Figure B.1: *$\mathcal{L}_{spec}$ determined by the luminosity feedback, vernier scans and the experimental luminosity monitors. The scale is abritrary. Statistical errors are assigned to the data. The RMS scatter of the feedback data in units of $\mathcal{L}_{spec}$ around the linear fit (solid line) amounts 0.12 at IP2 and 0.06 at IP4.*

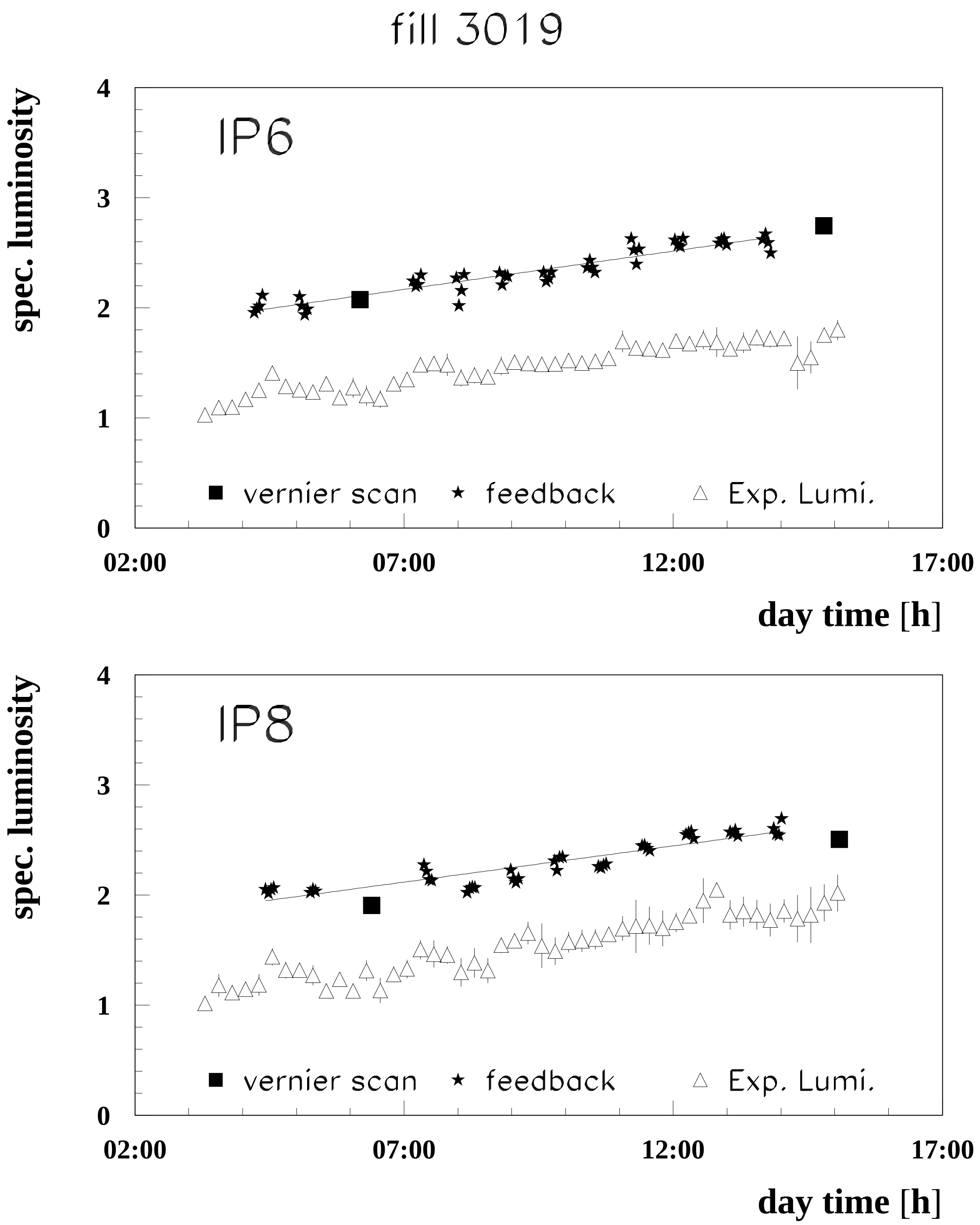

Figure B.2: *$\mathcal{L}_{spec}$ determined by the luminosity feedback, vernier scans and the experimental luminosity monitors. The scale is abritrary. Statistical errors are assigned to the data. The RMS scatter of the feedback data in units of $\mathcal{L}_{spec}$ around the linear fit (solid line) amounts 0.07 at IP6 and 0.08 at IP8.*

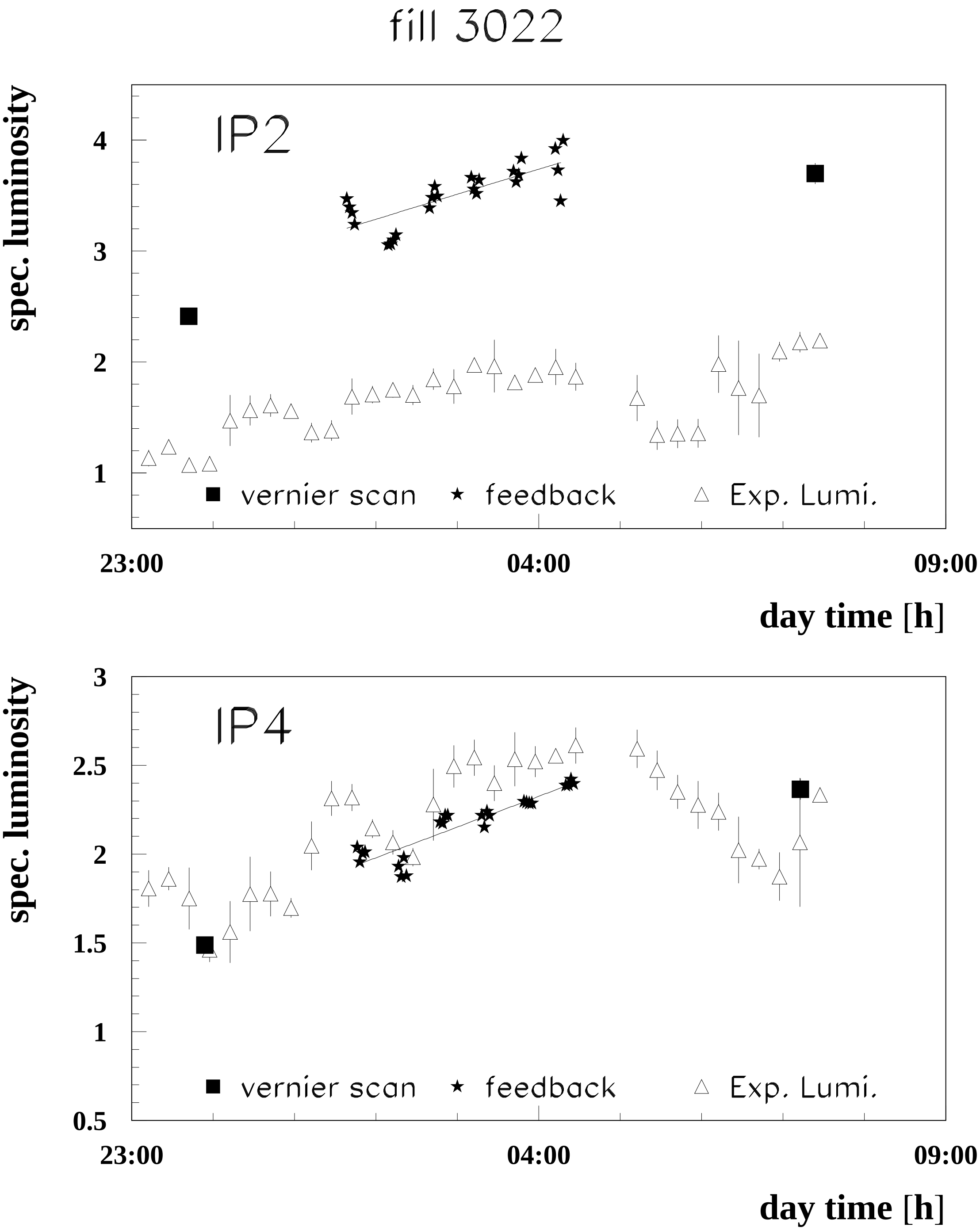

Figure B.3: *$\mathcal{L}_{spec}$ determined by the luminosity feedback, vernier scans and the experimental luminosity monitors. The scale is abritrary. Statistical errors are assigned to the data. The RMS scatter of the feedback data in units of $\mathcal{L}_{spec}$ around the linear fit (solid line) amounts 0.16 at IP2 and 0.07 at IP4. At 04:30 a computer network problem occured leading to a loss of control of the machine. This caused a significant luminosity decrease.*

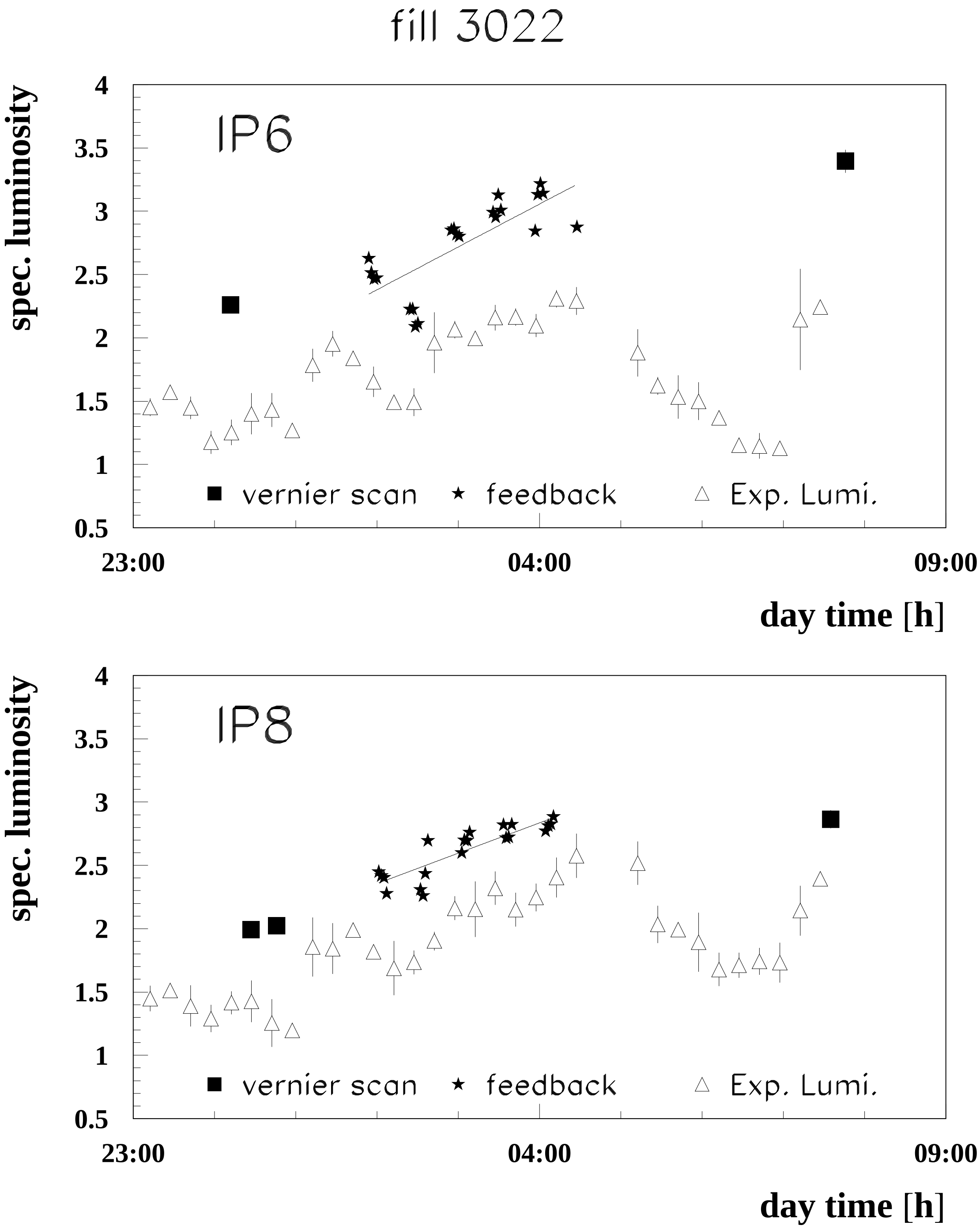

Figure B.4: *$\mathcal{L}_{spec}$ determined by the luminosity feedback, vernier scans and the experimental luminosity monitors. The scale is abritrary. Statistical errors are assigned to the data. The RMS scatter of the feedback data in units of $\mathcal{L}_{spec}$ around the linear fit (solid line) amounts 0.21 at IP6 and 0.10 at IP8. At 04:30 a computer network problem occured leading to a loss of control of the machine. This caused a significant luminosity decrease.*

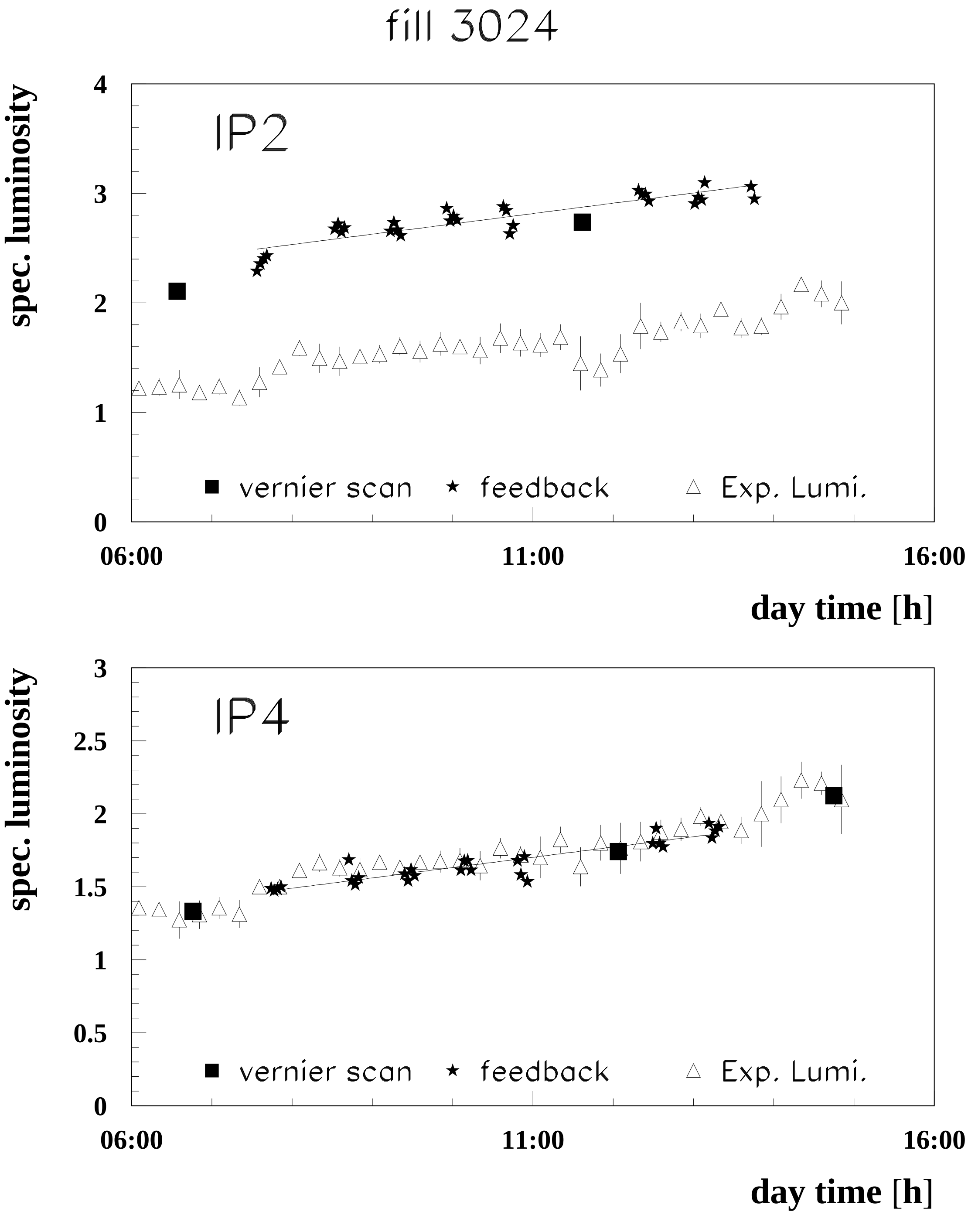

Figure B.5: *$\mathcal{L}_{spec}$ determined by the luminosity feedback, vernier scans and the experimental luminosity monitors. The scale is abritrary. Statistical errors are assigned to the data. The RMS scatter of the feedback data in units of $\mathcal{L}_{spec}$ around the linear fit (solid line) amounts 0.09 at IP2 and 0.06 at IP4.*

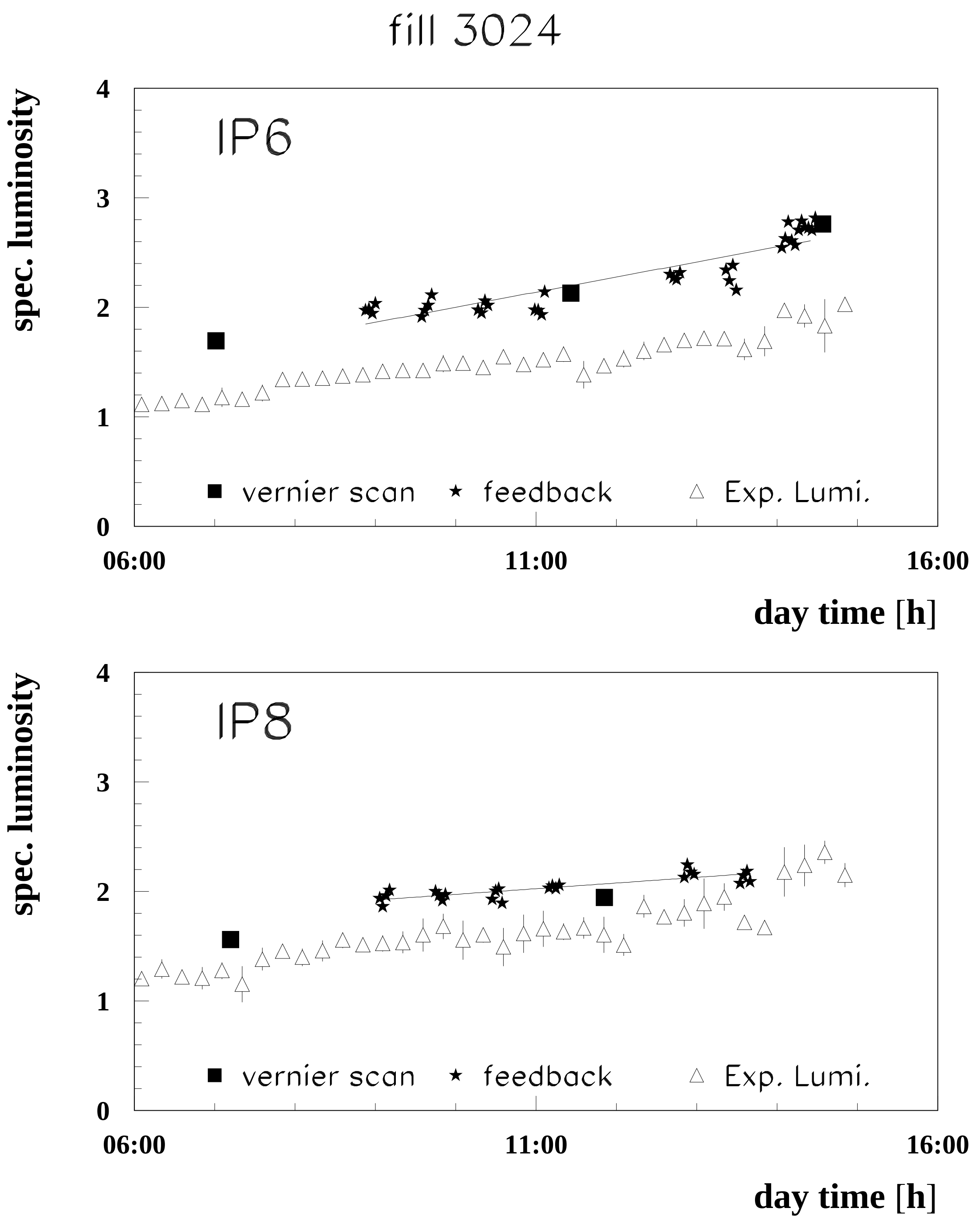

Figure B.6: *$\mathcal{L}_{spec}$ determined by the luminosity feedback, vernier scans and the experimental luminosity monitors. The scale is abritrary. Statistical errors are assigned to the data. The RMS scatter of the feedback data in units of $\mathcal{L}_{spec}$ around the linear fit (solid line) amounts 0.13 at IP6 and 0.06 at IP8.*

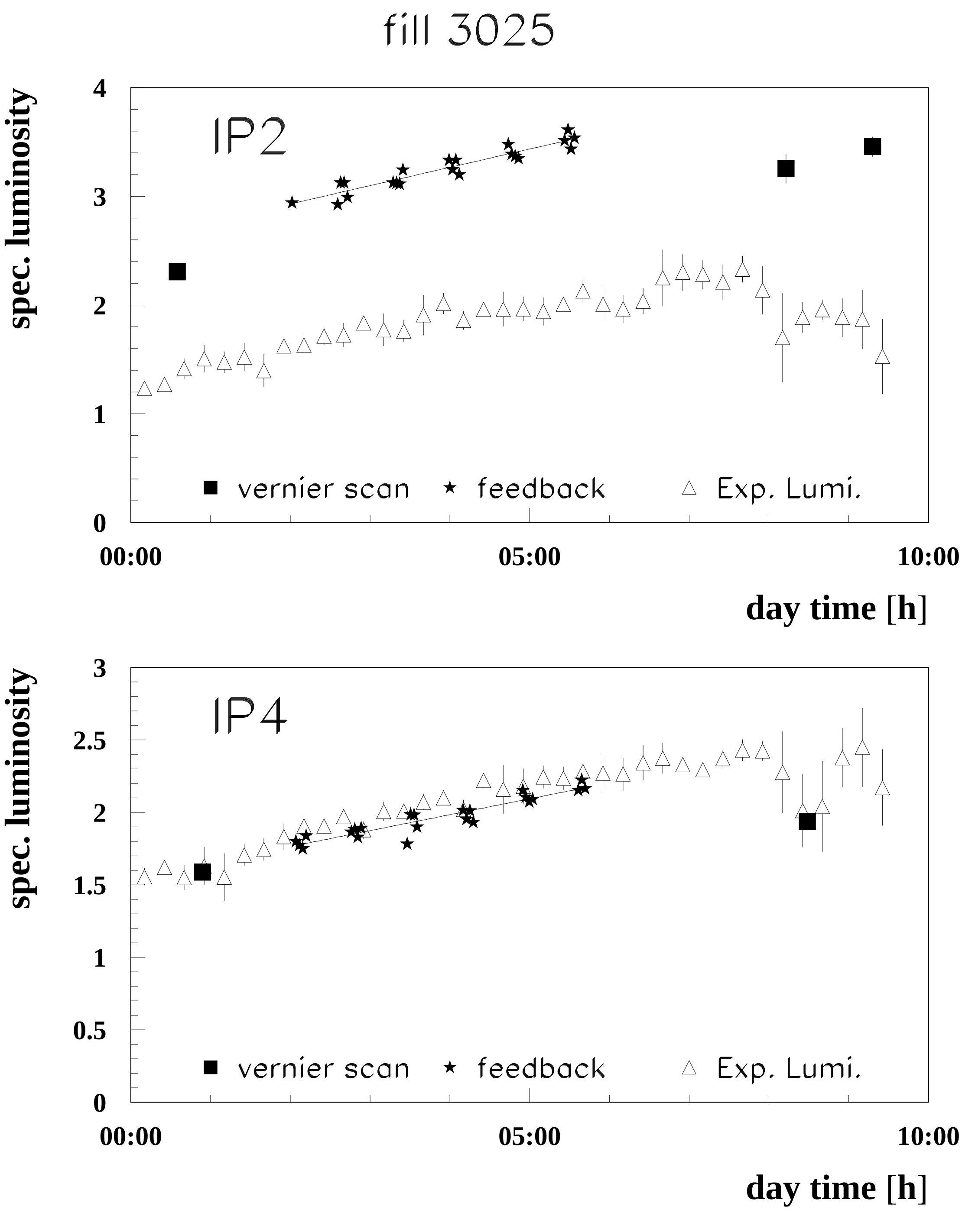

Figure B.7: *$\mathcal{L}_{spec}$ determined by the luminosity feedback, vernier scans and the experimental luminosity monitors. The scale is abritrary. Statistical errors are assigned to the data. The RMS scatter of the feedback data in units of $\mathcal{L}_{spec}$ around the linear fit (solid line) amounts 0.06 at IP2 and 0.05 at IP4.*

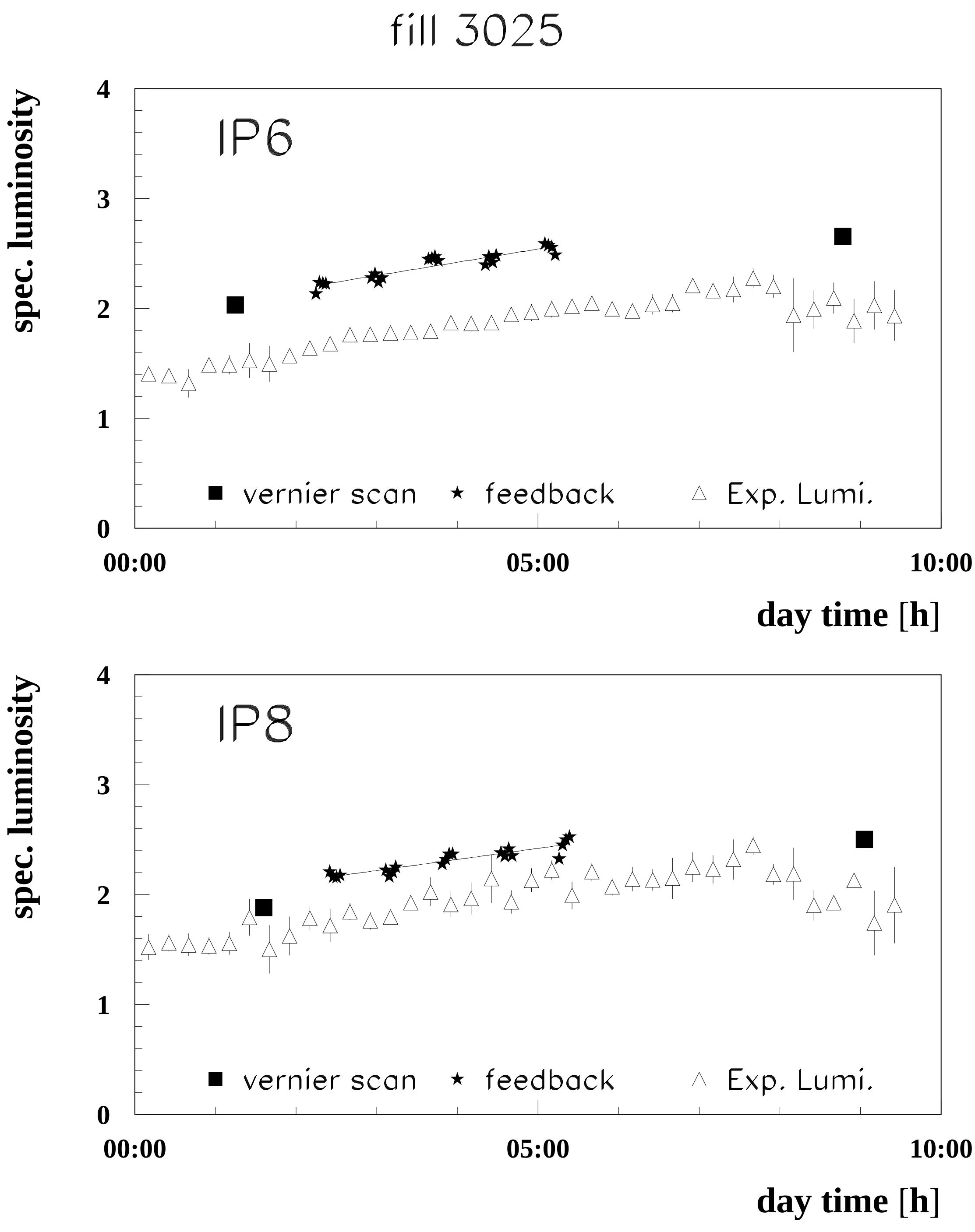

Figure B.8: *$\mathcal{L}_{spec}$ determined by the luminosity feedback, vernier scans and the experimental luminosity monitors. The scale is abritrary. Statistical errors are assigned to the data. The RMS scatter of the feedback data in units of $\mathcal{L}_{spec}$ around the linear fit (solid line) amounts 0.05 at IP6 and 0.05 at IP8.*

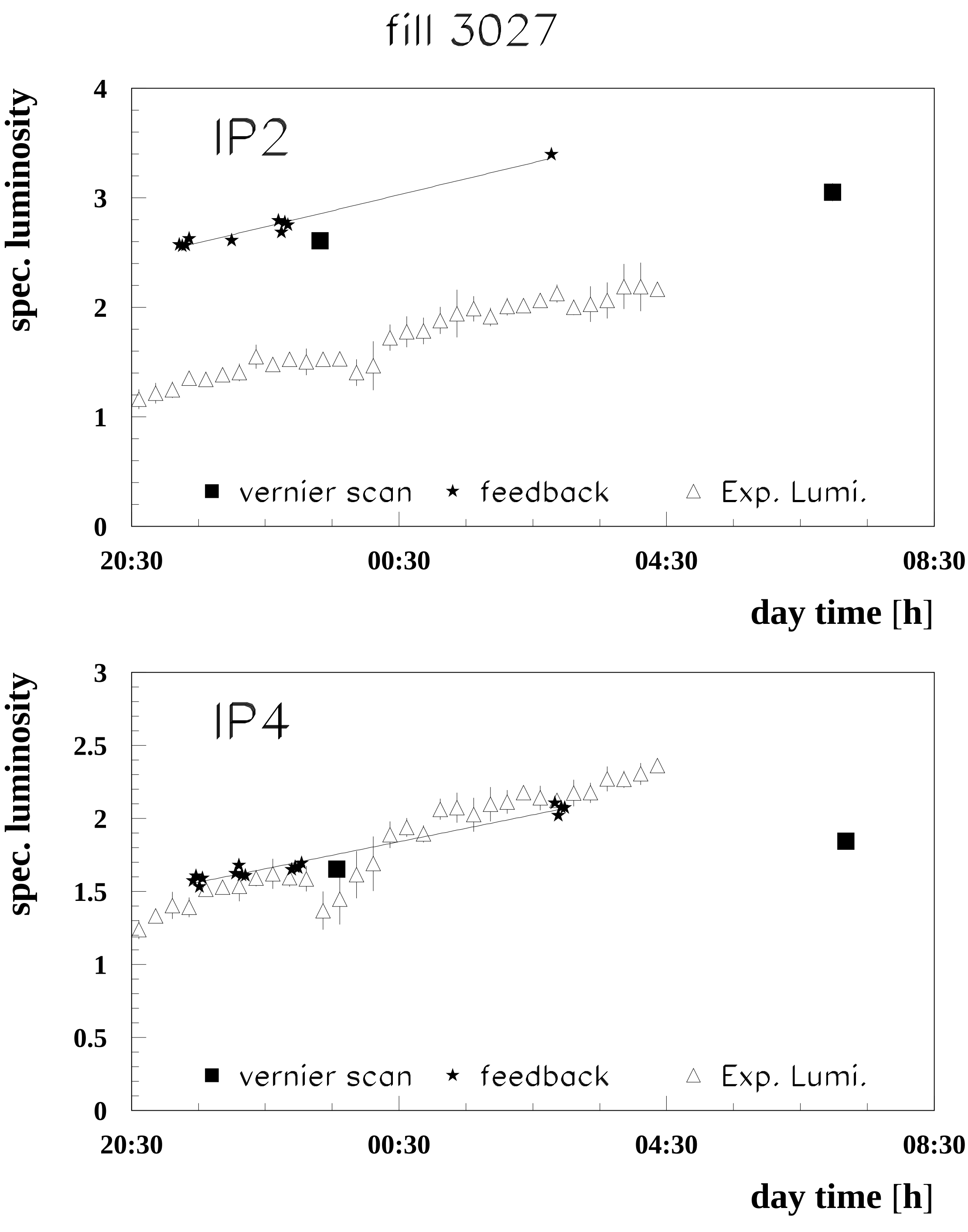

Figure B.9: *$\mathcal{L}_{spec}$ determined by the luminosity feedback, vernier scans and the experimental luminosity monitors. The scale is abritrary. Statistical errors are assigned to the data. The RMS scatter of the feedback data in units of $\mathcal{L}_{spec}$ around the linear fit (solid line) amounts 0.04 at IP2 and 0.03 at IP4.*

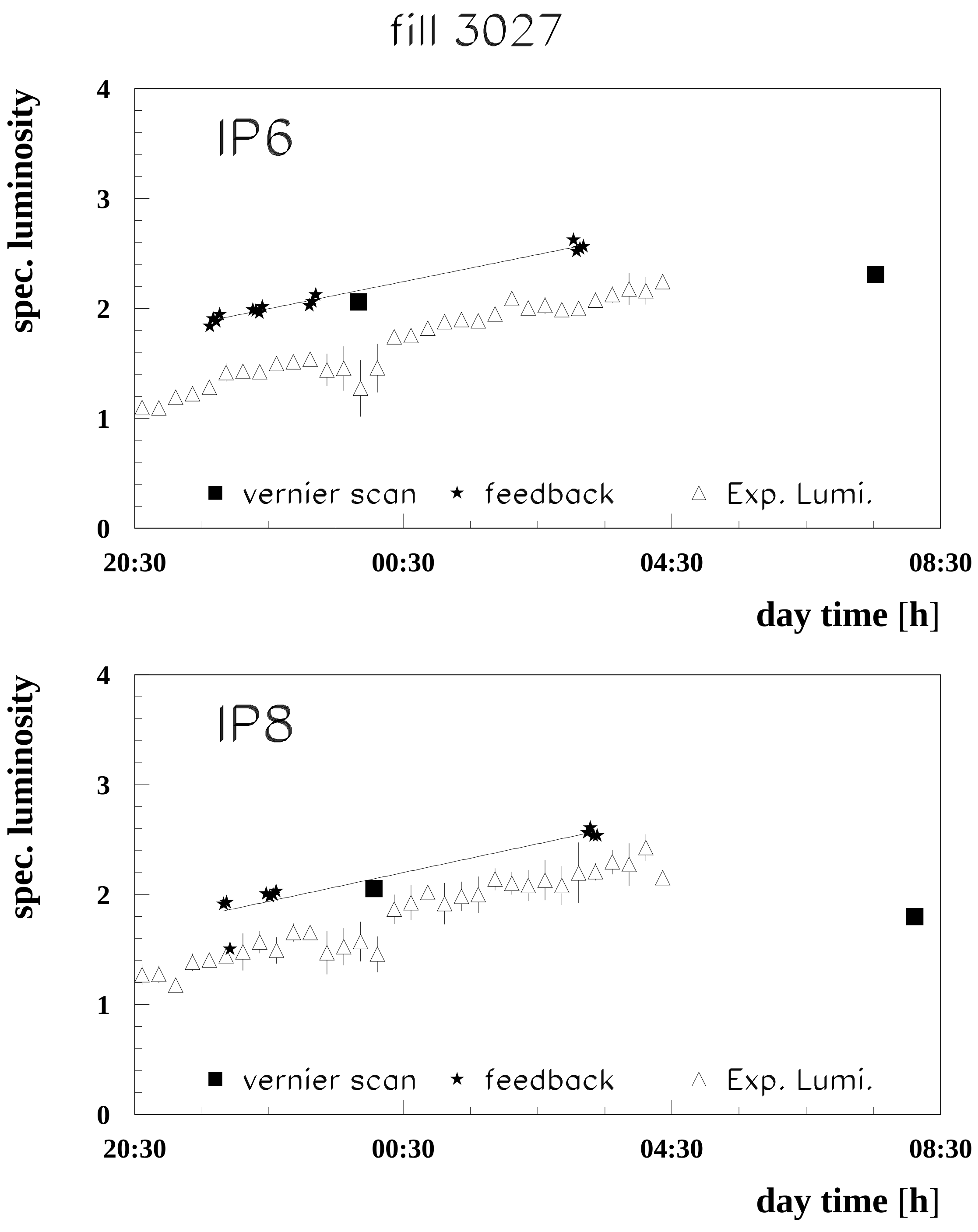

Figure B.10: *$\mathcal{L}_{spec}$ determined by the luminosity feedback, vernier scans and the experimental luminosity monitors. The scale is abritrary. Statistical errors are assigned to the data. The RMS scatter of the feedback data in units of $\mathcal{L}_{spec}$ around the linear fit (solid line) amounts 0.03 at IP6 and 0.12 at IP8.*

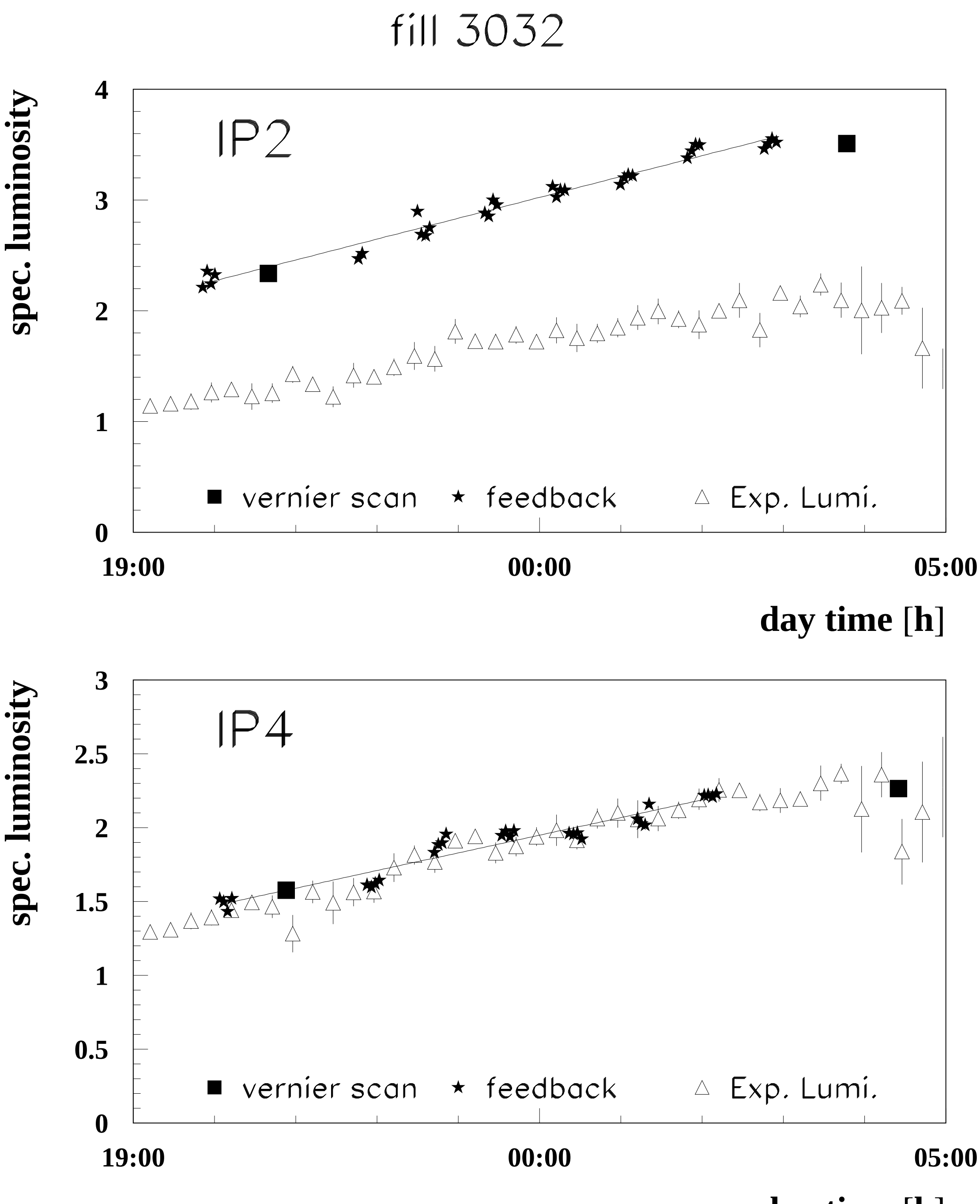

Figure B.11: *$\mathcal{L}_{spec}$ determined by the luminosity feedback, vernier scans and the experimental luminosity monitors. The scale is abritrary. Statistical errors are assigned to the data. The RMS scatter of the feedback data in units of $\mathcal{L}_{spec}$ around the linear fit (solid line) amounts 0.07 at IP2 and 0.06 at IP4.*

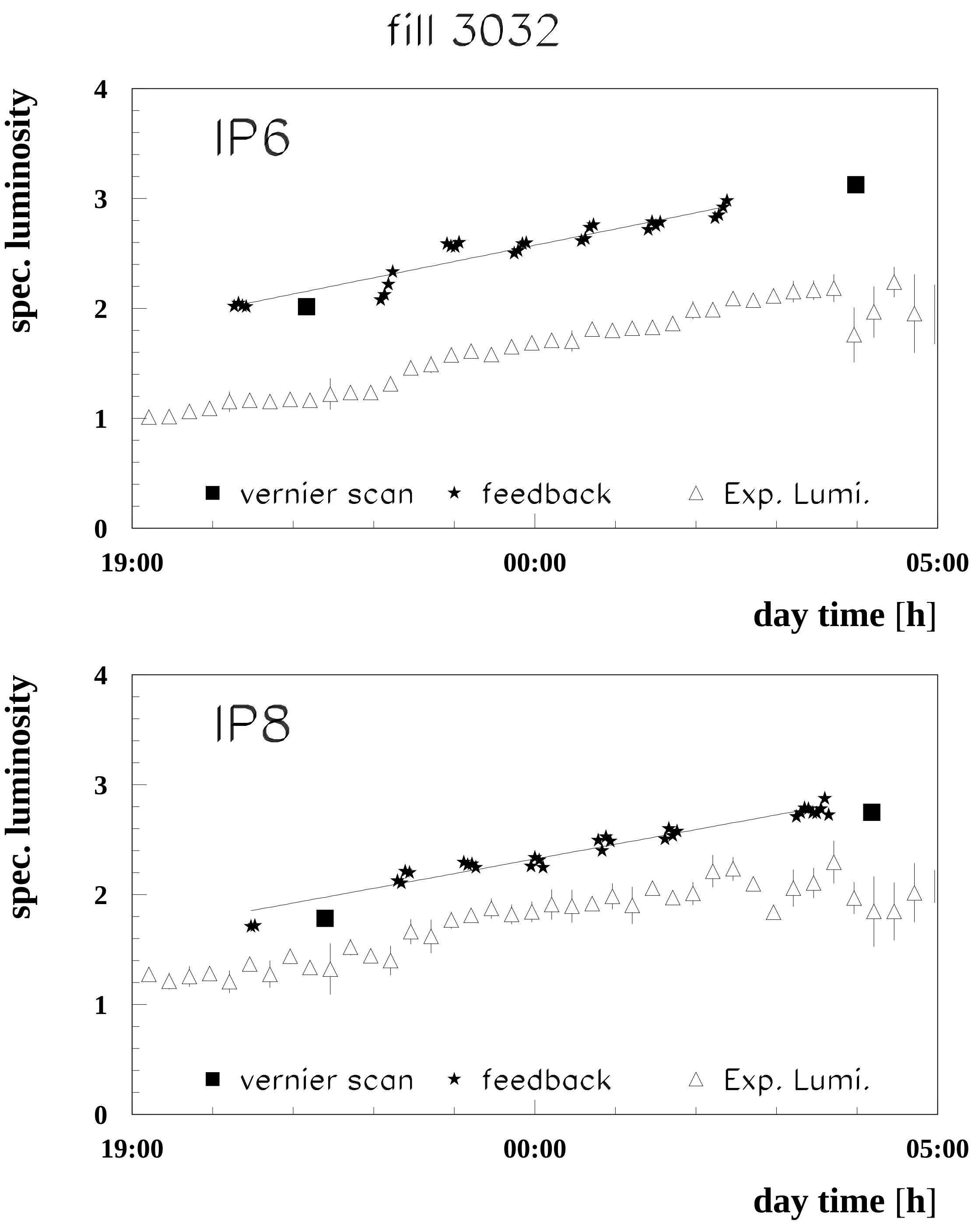

Figure B.12: *$\mathcal{L}_{spec}$ determined by the luminosity feedback, vernier scans and the experimental luminosity monitors. The scale is abritrary. Statistical errors are assigned to the data. The RMS scatter of the feedback data in units of $\mathcal{L}_{spec}$ around the linear fit (solid line) amounts 0.09 at IP6 and 0.06 at IP8.*

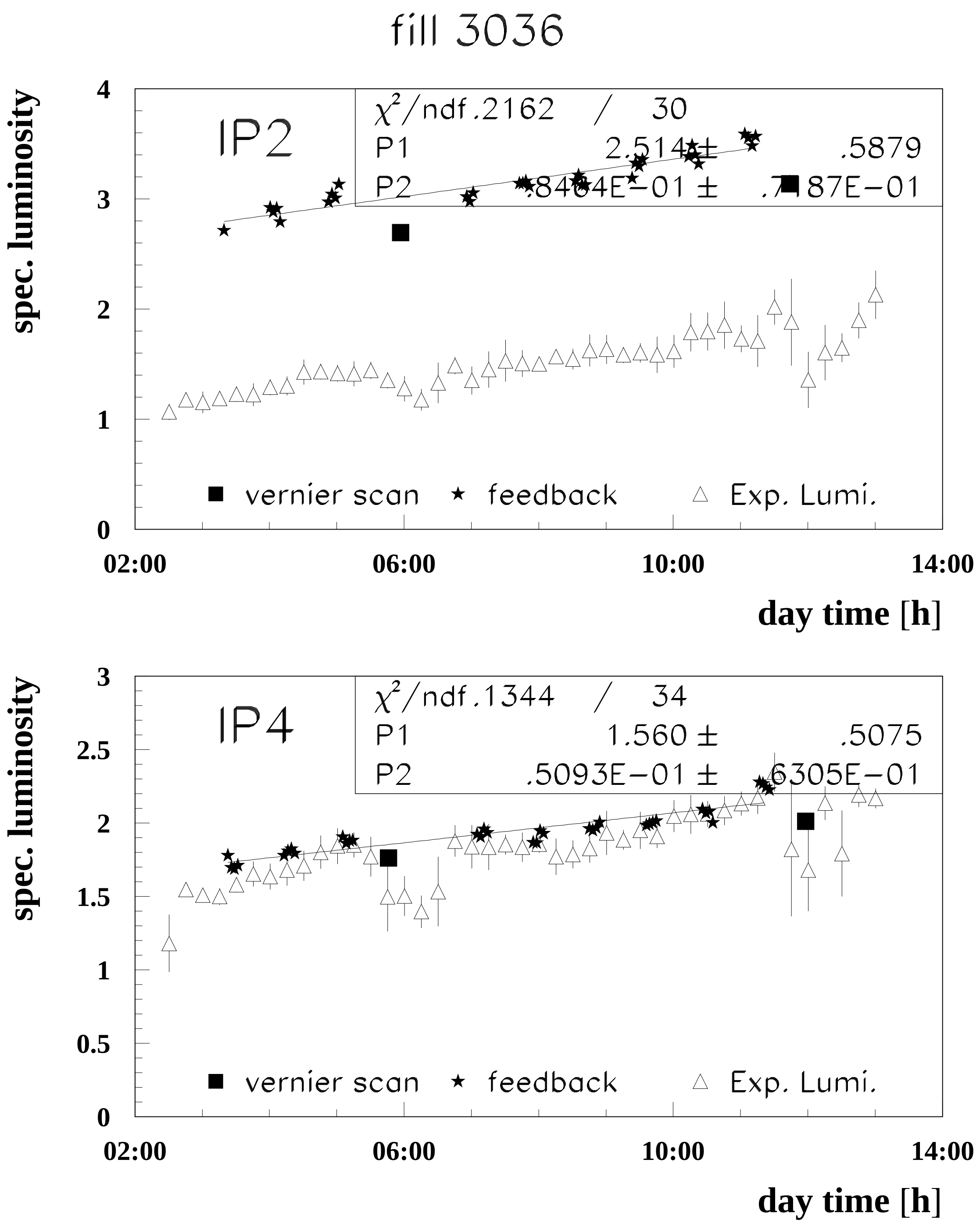

Figure B.13: *$\mathcal{L}_{spec}$ determined by the luminosity feedback, vernier scans and the experimental luminosity monitors. The scale is abritrary. Statistical errors are assigned to the data. The RMS scatter of the feedback data in units of $\mathcal{L}_{spec}$ around the linear fit (solid line) amounts 0.08 at IP2 and 0.06 at IP4.*

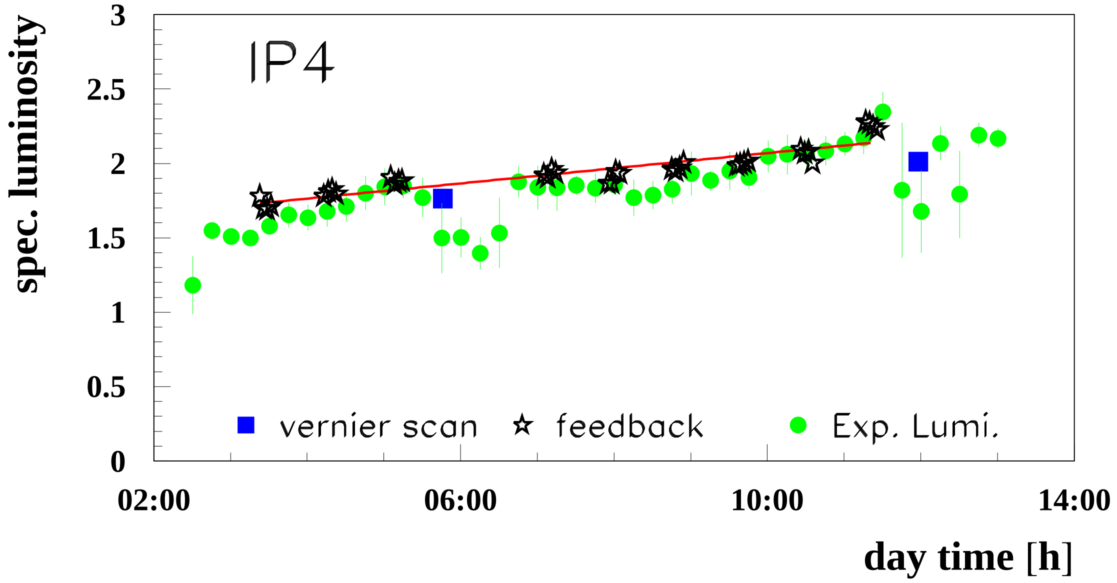

Figure B.14: *$\mathcal{L}_{spec}$ determined by the luminosity feedback, vernier scans and the experimental luminosity monitors. The scale is abritrary. Statistical errors are assigned to the data. The RMS scatter of the feedback data in units of $\mathcal{L}_{spec}$ around the linear fit (solid line) amounts 0.07 at IP6 and 0.15 at IP4.*

Bibliography

[1] ALEPH collaboration, D. Decamp et al., Nucl. Instr. and Meth. **A294** (1990) 121.

[2] DELPHI collaboration, P. Aarnio et al., Nucl. Instr. and Meth. **A303** (1991) 233.

[3] L3 collaboration, B. Adeva et al., Nucl. Instr. and Meth. **A289** (1990) 35.

[4] OPAL collaboration, K. Ahmet et al., Nucl. Instr. and Meth. **A305** (1991) 275.

[5] F. J. Hasert et al., Phys. Lett. 46B (1973) 138.

[6] UA1 Collaboration, G. Arnison et al., Phys. Lett. 126B (1983) 398;
UA2 Collaboration, M. Banner et al., Phys. Lett. 129B (1983) 130.

[7] G. Altarelli et al., "Precision Tests of Electroweak Theory at the Z^0", Physics at LEP, Vol. 1, CERN 86-02 (1986).

[8] The LEP Collaborations and The LEP Electroweak Working Group, Phys. Lett. B 307 (1993) 187.

[9] D. Schaile, "Tests of the Electroweak Theory at LEP", CERN-PPE/93-213 (1993).

[10] S. L. Glashow, Nucl. Phys. A 22 (1961) 579.
S. Weinberg, Phys. Rev. Lett. 19 (1967) 1264.
A. Salam, "Elementary Particle Theory", Ed. N. Svartholm, Stockholm, "Almquist and Wiksell" (1968), 367.

[11] R. Kleiss, "Electroweak Interaction", Lectures given at CERN, (1990).

[12] D. Bardin et al., FORTRAN package ZFITTER, Preprint CERN TH 6443/92 (1992);
D. Bardin et al., Z. Phys. C 44 (1989) 493;
D. Bardin et al., Nucl. Phys. B 351 (1991) 1;
D. Bardin et al., Phys. Lett. B 255 (1991) 290.

[13] M. Martinez et al. Z. Phys. C 49 (1991) 645;
S. Jadach et al., Phys. Lett. B 280 (1992) 129.

[14] J. Mnich, "Experimental Tests of the Standard Model in $e^+e^- \to f\bar{f}$at the Z Resonance", Phys. Rep. 271 (1996) 181-266.

[15] S. Jadach et al. Phys. Lett. B 353 (1995) 349;
S. Jadach et al. Phys. Lett. B 353 (1995) 362.

[16] ALEPH Collab., D. Decamp et al., Phys. Lett. B 231 (1989) 519.

[17] ALEPH Collab., D. Decamp et al., Z. Phys. C53 (1992) 1.

[18] ALEPH Collab., D. Buskulic et al., Z. Phys. C60 (1993) 71.

[19] DELPHI Collab., P. Aarnio et al., Phys. Lett. B 231 (1989) 539.

[20] DELPHI Collab., P. Abreu et al., Nucl. Phys. B 367 (1991) 511.

[21] DELPHI Collab., P. Abreu et al., Nucl. Phys. B 417 (1994) 3.

[22] L3 Collaboration, B. Adeva et al., Phys. Lett. B231 (1989) 509.

[23] L3 Collaboration, B. Adeva et al., "Measurement of Electroweak Parameters from Hadronic and Leptonic Decays of the Z^0", Zeit. Phys. C51 (1991) 179.

[24] L3 Collaboration, "Results from the L3 Experiment at LEP", Phys. Rep. 236 (1993) 1.

[25] OPAL Collab., M. Z. Akrawy et al., Phys. Lett. B 231 (1989) 530.

[26] OPAL Collab., G. Alexander et al., Z. Phys. C 52 (1991) 175.

[27] OPAL Collab., P. D. Acton et al., Z. Phys. C 58 (1993) 219.

[28] The LEP Collaborations: ALEPH, DELPHI, L3 and OPAL, Phys. Lett. B 276 (1992) 247.

[29] A. Hofmann and T. Risselda, "Injection of Protons into LEP for Diagnostics Experiments and Absolute Energy Calibration", LEP Note 282 (1982);
J. Billan et al., "Calibration of Beam Momentum", LEP Commissioning Note 12

[30] V. Hatton et al., "LEP absolute Energy in 1990", LEP Performance Note 12 (1990).

[31] The Working Group on LEP Energy, "The Energy Calibration of LEP in 1991", CERN-SL/92-37(DI) (1992).

[32] The LEP Polarization Collaboration, "First Observation of Transverse Beam Polarization in LEP", Phys. Lett. B 270 (1991) 97.

[33] The Working Group on LEP Energy, "The Energy Calibration of LEP in the 1993 Scan", Zeit. Phys. C66 (1995) 567-582.

[34] L. Arnaudon et al., "Measurement of LEP Beam Energy by Resonant Spin Depolarisation", Phys. Lett. B 284 (1992) 431.

[35] Matthew Sands, “The Physics of Electron Storage Rings, An Introduction”, prepared for the U.S. Atomic Energy Commission under contract No. AT(04-3)-515 (1970).

[36] Helmut Wiedemann, “Particle Accelerator Physics, Vol. I”, Springer Verlag (1993).

[37] “LEP Design Report Vol. 2”, CERN-LEP/84-01, 1984.

[38] H. Grote, C. Iselin, “The MAD program V8.10”, CERN-SL/90-13 Rev. 3 (AP) 1990.

[39] C. Bovet et al., “Final Report of the 1994 Bunch Train Study Group” CERN-SL/94-95 (AP) (1994).

[40] E. Keil, “Truly Self-Consistent Treatment of the Side Effects with Bunch Trains”, CERN SL/95-75 (1995).

[41] H. Schmickler, “Measssurements of the Central Frequency of LEP”, LEP MD Note 89 (1993).

[42] V. Bargmann, L. Michel and V. L. Telegdi, Phys. Rev. Lett. 10 (1959) 435.

[43] M. Placidi and R. Rossmanith, Nucl. Instr. Meth. A274 (1989) 79.

[44] R. Assmann et al., “Polarization Studies at LEP in 1993”, CERN-SL/94-08 (AP) 1994.

[45] A. A. Sokolov and I. M. Ternov, Sov. Phys. Dokl. 8 (1964) 1203.

[46] R. Assmann, “Transversale Strahlpolarisation und ihre Anwendung für Präzisionsmessungen bei LEP”, PhD thesis at the Ludwigs-Maximilians-Universität, 1994.

[47] A. Blondel, “Compensation of Integer Spin Resonances Created by Experimental Solenoids”, LEP Note 629 (1990).

[48] J. P. Koutchouk, “Spin Tune Shifts due to Solenoids”, CERN SL-Note / 93-26 (AP) (1993).

[49] R. Assmann and J. P. Koutchouk, “Spin Tune Shifts due to Optics Imperfections”, CERN-SL/94-13 (AP) (1994).

[50] R. Jacobson, “1993 LEP Energy Spread and Variation from Spot Size Measurements”, ALEPH 94-060, April 1994 (1994).

[51] D. Strom, “Determination of the LEP Energy Spread from the Longitudinal Beam Size in OPAL”, Opal Technical Note TN264, November 1994 (1994).

[52] L. Arnaudon et al., “Accurate Determination of the LEP Beam Energy by Resonant Depolarization”, Z. Phys. C66 (1995) 45.

[53] M. Geitz, "Investigation of Environmental Effects on the LEP Beam Energy - Magnetic Field Perturbations", Diploma Work, PITHA 96/14, RWTH Aachen, Germany.

[54] W. Weber, "Über die Anwendung der magnetischen Induktion auf Messung der Inclination mit dem Magnetometer", Ann. der Physik 2 (1853) 209-247;
J. M. B. Kellogg,I. I. Rabi, N. F. Ramsey and J. R. Zacharias, "The magnetic moments of the proton and the deuteron", Phys. Rev. 56 (1939) 728-743.

[55] F. Bloch, W. W. Hansen and M. Packard, "Nuclear induction", Phys. Rev. 69 (1946) 127;
F. Bloch, W. W. Hansen and M. Packard, "The nuclear induction experiment", Phys. Rev. 70 (1946) 474-485.

[56] E. M. Purcell, H. C. Torrey and R. V. Pound, "Resonant absorption by nuclear magnetic moments in a solid", Phys. Rev. 69 (1946) 37-38.

[57] Technical Manual, Bruker, "Bruker Microprocessor controlled NMR Gaussmeter ER035 M", 1992 (1992).

[58] J. Billan et al., "Magnetic Performance of the LEP Bending Magnets", CERN LEP-MA/89-04 (1989);
J. Billan et al., "Determination of the Particle Momentum in LEP from precise Magnet Measurements", CERN/AT-MA/91-03 (1991);
J. Billan et al., "Long Term Magnetic Performance of the Steel Concrete Dipole in LEP", CERN AT/93-32 (MA) (1994).

[59] J. Billan, J.P. Gourber, K.N. Henrichsen, L. Walckiers, "Field Display System for the Forecast of Beam Momentum and Betatron Frequencies in LEP", LEP-MA/89-41 (1989);
J. Billan, J.P. Gourber, K.N. Henrichsen, L. Walckiers, "Field Display System for the Forecast of Beam Momentum and Betatron Frequencies in LEP", Particle Accelerators 29 (1990) 215-220.

[60] J. Borer, "BOM system hardware status", Proc. f the Third Workshop on LEP Performance, CERN-SL/93-19 (DI) (1993) 219.

[61] G. Vismara, "The new front-end Narrow-Band electronics for the LEP Beam Orbit Measurement System", Contribution to the 1994 European Particle Accelerator Conference, London, July 1994.

[62] Jörg Wenninger, "Radial Deformations of the LEP Ring", CERN-SL/ Note 95-21 (OP)

[63] J. Wenninger, "Study of the LEP Beam Energy with Beam Orbits and Tunes", CERN-SL/94-14 (BI), 1994

[64] R. Forest, "Main Bend Power converter Current Stability", proc. of the Third Workshop on LEP Performance, CERN-SL/93-19 (DI) 325, 1993

[65] P. Galbraith, R. Genand, Y. Jacquemard, A. Beuret, "Jumps in the Magnetic Field induced by Current Spikes", Minutes of the 39th ECWG Meeting, 01.10.1993, 1993.

[66] F. Brailsford, "Magnetic Materials", Methuen & CO. LTD, London, 1960

[67] B. Dehning, A. Drees, M. Geitz, "A Study of the Magnetic Dipole Field of LEP during the 1995 Energy Scan", CERN SL/96-54 (BI) (1996).

[68] E. Bravin,G. Brun,B. Dehning,A. Drees,P. Galbraith,M. Geitz,K. Henrichsen, M. Koratzinos,G. Mugnai, "The Influence of Train Leakage Currents on the LEP Dipole Field", CERN SL/97-47 (BI), to be submitted to NIM (1997).

[69] Ch. Fleury, Laboratoire d'essais Service de L'electricite, SIG, private communication,
J. M. Jolidon, CFF, private communication

[70] R. Bräunlich, "Die messtechnische Überprüfung von grossen Erdungsanlagen", Bulletin SEV/VSE 23/95 (1995).

[71] J. Billan, J. P. Gourber, K. N. Henrichsen, H. Laeger, L. Resegotti, "Influence of Mortar-Induced Stresses on the Magnetic Characteristics of the LEP Dipole Cores", CERN LEP-MA/87-53 (1987);
J. P. Gourber, "Properties of the LEP magnets", Workshop of LEP Performance, Chamonix 1992.

[72] J. Gascon et al. , "The Temperature Dependence of the Energy Calibration of LEP Beams by Flux Loop Measurements", LEP Performance Note 74, CERN, 1991

[73] A. Drees, "Polarization Experiment Analysis and NMR Corrections", contribution to the 83rd Meeting of the Energy Calibration WG, Nov. 24, 1995.

[74] E. Bravin, "New Temperature Model", Contribution to the 106th Energy Calibration Meeting, Sep. 27, 1996;
E. Bravin, private communication 1996.

[75] G. Wilkinson, P. Renton, K. Yip, contribution to the 113th Energy Calibration Meeting at Dec. 6th, 1996.
G. Wilkinson, P. Renton, K. Yip, contribution to the Energy Calibration Meeting at Jan. 20th, 1997.

[76] J. Billan, "Influence of Humidity on the LEP Dipole Field", contribution to the LEP Energy Meeting 19.4.96.

[77] G. Fisher and A. Hofmann, Proc. of the Second Workshop on LEP performance, CERN SL/92-29 (1992) 337;
L. Arnaudon et al., "Effects of terrestrial tides on the LEP beam energy", Nucl. Instr. Meth. A357 (1995) 249-252.

[78] Model provided by Prof. P. Melchior from the International Center for Earth Tides in bruxelles, Belgium;
P. Melchior, "The Tides of the Planet Earth", 2nd Edition, Pergamon Press (1983).

[79] J. Wenninger, "Measurement of Tidal Deformations of the LEP Ring with Closed Orbits", CERN SL-Note/96-22 (OP) (1996).

[80] K. Lindemann, "Rain and ground water effects of LEP", CERN SL-MD note 89 (1993).

[81] J. Wenninger, private communication.

[82] J. Wenninger, "Orbit Corrector Magnets and Beam Energy", CERN SL-Note 97-06 (OP) (1997).

[83] G. Quast, "Uncertainties on the Energy Correction due to RF Effects in 1993", Memo to the Energy Working Group 93-??, December 20 (1993).

[84] M. D. Hildreth et al., "Preliminary RF Corrections to the LEP Energy for the 95 Scan", LEP Energy Group 96/02 (1996).

[85] M. D. Hildreth, "A Study of RF Effects on Bunch Trains in the 1995 Running", LEP Energy Group 97/02 (1997);
M. D. Hildreth, "A Systematic Check of SC Cavity Alignment Using LEP Beams", LEP Energy Group 97/03 (1997).

[86] J. M. Jowett, J. Wenninger, J. Yamartino, "Influence of Dispersion and Collision Offsets on the Center-of-Mass Energy at LEP", CERN-SL/95-46 (OP) (1995).

[87] A. Drees, "How does the bunch train scheme effect E_{CM}?", Memorandum to the DELPHI Superteam 1 meeting at 24.04.95 (1995).

[88] The LEP Energy Working Group, "LEP Center-of-Mass Energies in Presence of Opposite Sign Vertical Dispersion in Bunch Train Operation", CERN-SL/95-77 (BI) (1995)

[89] J. Wenninger, "Center-of-Mass Energy Shifts from Difference Dispersion and Collision Offsets in Pretzel Operation at LEP", CERN-SL/95-64 (OP) (1995).

[90] P. Castro, "Luminosity and Beta Function Measurement at the Electron-Positron Collider ring LEP", Doctoral Thesis, Universitat de Valencia, May 17, 1996.

[91] P. Puzo, J. Yamartino, "Preliminary Center-of-Mass Energy Corrections from Dispersion and Collision Offsets for the 1995 Scan", LEP Energy Working Group / 96-01 (1996).

[92] A. Drees and R. Schmidt, "Correction of Vertical Offsets during Energy Scanning", contribution to the 67th Energy Calibration WG Meeting, May 12, 1995.

[93] A. Drees, “Feedback Simulation”, contribution to the 68th Energy Calibration WG meeting, May 29, 1995.

[94] A. Drees, “Status of Feedback Simulation”, contribution to the 70th Energy Calibration WG meeting, July 3, 1995.

[95] A. Drees, contribution to the 81st Energy Calibration WG meeting, Sep. 29, 1995.

[96] A. Drees, “Status of the Luminosity Feedback”, contribution to the 76th Energy Calibration WG meeting, Aug. 18, 1995 and contribution to the 77th Energy Calibration WG meeting, Sep. 1, 1995.

[97] J. Wenninger, M. Lamont, private communication (1995).

[98] P. Puzo, “Beam Blow Up Correction during Vernier Scans”, contribution to the 81st Energy Calibration WG Meeting, Oct. 10, 1995.

[99] A. Drees, “Energy Difference of Electron and Positron Beam”, CERN SL/Note 94-100 (BI) (1994).

[100] A. Drees, contribution to the 95th and 96th LEP Energy Meeting on 14 June 1996 and 21 June 1996.

[101] A. Lucotte, ALEPH collaboration, private communication (1996).

[102] H. Wahlen, M. Winter, F. Glege, DELPHI collaboration, private communication (1996).

[103] J. Mnich, L3 collaboration, private collaboration (1996).

[104] G. Wilkinson, representing the LEP Energy Working Group, “The Determination of the LEP Energy in the 1995 Z^0 Scan”, talk presented at the ICHEP96, Warsaw, 25-31 July 1996.

[105] The Working Group on LEP Energy, “LEP Energy Calibration in 1993, 1994 and 1995”, LEP Energy Group/96-05 (1996).

[106] The Working Group on LEP Energy, “The Energy of the LEP Beams during the Z Runs”, to be submitted to Z. Phys. C (1997).

[107] The LEP Collaborations and The LEP Electroweak Working Group, “Combined Preliminary Data on Z Parameters form the LEP Experiments and Constraints on the Standard Model”, Preprint CERN PPE/94-187, CERN, 1994.

[108] The LEP Electroweak Working Group and the SLD Heavy Flavour Group, “A Combination of Preliminary LEP and SLD Electroweak Measurments and Constraints on the Standard Model”, Internal Note, CERN LEPEWWG/97-02 (1997).

Acknowledgements

Many people and special circumstances enabled the success of this dissertation. Even a shepherd, Hel aus dem Weinsbergtal, contributed to it. Its patience and obedience allowed it to become an unofficial member of the DELPHI collaboration and me to enjoy its pleasant accompaniment every day.

Once I became attracted to the LEP energy calibration challenge and volunteered to collaborate with the LEP polarimeter team, a kind of migration from the DELPHI experiment - where I have started to work in the team of the line shape analysis - to the LEP Energy Working Group started. Fortunately my university advisor, Dr. Karl-Heinz Becks, was flexible enough to look after a phd student who decided to work not exactly in the field where she was supposed to. Since the results of the LEP Energy Working Group are a substantial part of the line shape measurements and since all four LEP experiments, including DELPHI, profit from these results, Prof. Dr. Becks and Prof. Dr. Drees accepted my migration to accelerator physics as a natural expansion of the studies in the Wuppertal High Energy Physics group. Helmut Wahlen, who is most involved from the Wuppertal group in the DELPHI line shape analysis, quickly became attracted by the LEP energy calibration aspect of the electroweak studies at CERN. I appreciated his enduring support and many helpful suggestions and discussions.

On the initiation of Bernd Dehning and Massimo Placidi, I was friendly supported by Claude Bovet, the group leader of the Beam Instrumentation (BI), which is part of the SPS/LEP division at CERN. He welcomed me as a new colleague in his BI group and provided the necessary environment such as a new office and a computer. Massimo Placidi as the project leader of the LEP polarimeter and Bernd Dehning as a section leader in BI integrated me into the LEP Energy Working Group, the LEP polarimeter team and introduced me to many questions related to the energy calibration task. I profited most from the instructions and suggestions of Jörg Wenninger and of active discussions with him. He became my advisor in all aspects of my work, which were related to the LEP collider and accelerator physics. Albert Hofmann and Rüdiger Schmidt, who inspired the automatic feedback described in this dissertation, were always available to me for questions and discussions. I enjoyed the amicable atmosphere provided by my colleagues Frank Tecker, Marc Geitz, Enrico Bravin and Markus Elsing as well as the daily lunch, coffee, conversation and discussions with them.

Last but not least my husband Axel Drees contributed to this thesis with his patience and many, many helpful discussions and motivating contentions anytime. He became my favourite and most critical reader. And with the help of my well beloved son Florian I could recover from all the painful programming, boring editing and the discussions, which I used to have with my colleagues, advisors and cooperators. He managed that I did not miss to enjoy life.